

UNIVERSITY OF CALIFORNIA
RIVERSIDE

Measurement of Identified Charged Hadron Anisotropic Flow in d+Au Collisions

A Dissertation submitted in partial satisfaction
of the requirements for the degree of

Doctor of Philosophy

in

Physics

by

Matthew Mendoza

September 2016

Dissertation Committee:

Dr. Richard Seto , Chairperson
Dr. Kenneth Barish
Dr. John Ellison

Copyright by
Matthew Mendoza
2016

The Dissertation of Matthew Mendoza is approved:

Committee Chairperson

University of California, Riverside

Acknowledgments

I am grateful to my advisor, without whose help, I would not have been here.

To my parents for all the support.

ABSTRACT OF THE DISSERTATION

Measurement of Identified Charged Hadron Anisotropic Flow in d+Au Collisions

by

Matthew Mendoza

Doctor of Philosophy, Graduate Program in Physics

University of California, Riverside, September 2016

Dr. Richard Seto , Chairperson

Collective flow has historically been an indicator that nuclear matter created in heavy ion collisions has undergone a phase change to a novel state where its constituent particles are deconfined. This phase called a *Quark-Gluon Plasma* has many characteristics that are signature of its creation. Among these are the increase in the baryon to meson ratio at mid- p_T and the enhancement of strange quark containing particles above binary scaling expectations. Recent results from CMS at the LHC show evidence of collective flow in the simpler p+Pb system, implying that a QGP may be formed in smaller systems than previously thought. An elliptic flow measurement with identified particles in d+Au collisions could reveal more about the nuclear matter created in these simpler systems. PHENIX's Time of Flight detector used in conjunction with its Aerogel Cherenkov Counter can provide particle identification with good proton/kaon/pion separation for $p_T < 10$ GeV/c. I will present studies of particle identified elliptic flow using these detectors which could help to elucidate the underlying physics of the baryon excess and strangeness enhancement anomalies that may be evidence of new physics in the d+Au system.

Contents

List of Figures	x
List of Tables	xiii
1 Introduction	1
1.1 Introduction	1
1.2 Early Experiments: An Overview	3
2 Nuclear Matter: Hot and Cold	6
2.1 Hot versus Cold Nuclear Matter	6
2.2 The Cronin Effect	7
2.2.1 Initial State Multiple Scattering	8
2.2.2 Final State Multiple Scattering	10
2.3 Hot Nuclear Matter: QGP	12
2.3.1 Baryon Enhancement	13
2.3.2 Theoretical Models of Baryon Enhancement	13
Recombination	13
Fragmentation	15
2.4 Flow at the LHC	17
2.5 Recombination and Fragmentation for All?	19
3 Experimental Apparatus	22
3.1 The Relativistic Heavy Ion Collider	22
3.2 From Start to Finish	23
3.3 The PHENIX Detector	25
3.3.1 Central Arm	27
Drift and Pad Chambers	27
TOF: Time Of Flight Detectors	29
ACC: Aerogel Cherenkov Counter	34
EMCal and RICH: Electromagnetic Calorimeter and Ring Imaging Cherenkov Counter	37
3.3.2 Forward and Global Detectors	40

BBC: Beam-Beam Counter	41
ZDC/SMD: Zero Degree Calorimeter and Shower Max Detectors	42
MPC: Muon Piston Calorimeter	44
RXNP: Reaction Plane Detector	44
3.4 The DAQ	45
4 Heavy Ion Collisions: A Primer	49
4.1 Measurable Quantities	49
4.2 Event Characterization	50
4.2.1 Centrality	50
4.2.2 Event Vertex and Timing	53
4.3 Track Reconstruction	55
4.3.1 Variables for Track Selection	55
Track Matching: DC and PC1	55
Track Matching: TOF and PC3	57
4.3.2 Particle Identification	58
5 Anisotropic Flow	62
6 Event Plane	66
6.1 Determination of Event Plane	66
6.2 Event Plane “Flattening”	68
6.3 Event Plane Resolution Correction	70
7 Results	72
7.1 Charged Track v_2	72
7.2 Separating Particle Signals	75
7.2.1 Single Gaussians	75
7.2.2 Gaussian Mixing	76
7.2.3 ACC as a Particle Discriminator	76
7.2.4 High p_T : Fixed Width and Mean	78
7.3 Identified Particle v_2	78
8 Error Analysis and Quality Assurance	80
8.1 Event Plane Resolution	82
8.2 Centrality Resolution	83
8.3 Particle Identification Methods	84
8.3.1 Momentum Uncertainty	84
8.3.2 TOF Timing	85
8.3.3 Uncertainties from Gaussian Models	88
Single and Mixed Gaussians, no ACC, $p_T \leq 2.1$ GeV/c	88
ACC Meson Separation and Gaussian Tail Cross Contamination, $2.1 \leq p_T \leq 2.9$	89

Fixed Width/Mean Gaussians and Background Effects	89
8.4 Detector Acceptance	90
8.5 Summary	91
9 Summary and Conclusions	94
9.1 Discussion	94
9.2 Conclusions	94
A PHENIX Coordinate System	95
B Nuclear Modification Factor	97
C Event and Track Selection Cuts	99
D Analysis Data and Plots	100
D.1 Charged Track Elliptic Flow	101
D.2 Particle Identification: TOFW	105
D.2.1 Single Gaussian fits, $p_T=0.5\text{-}1.3 \text{ GeV}/c$, TOF.W, negative charged tracks	105
D.2.2 Single Gaussian fits, $p_T=0.5\text{-}1.3 \text{ GeV}/c$, TOF.W, positive charged tracks	109
D.2.3 Mixed Gaussian fits, $p_T=1.3\text{-}2.1 \text{ GeV}/c$, TOF.W, negative charged tracks	113
Mixed Gaussian fits, $p_T=1.3\text{-}2.1 \text{ GeV}/c$, TOF.W, positive charged tracks	117
D.2.4 TOF.W and ACC, $p_T=2.1\text{-}3.5 \text{ GeV}$, negative charged tracks	121
D.2.5 TOF.W and ACC, $p_T=2.1\text{-}3.5 \text{ GeV}$, positive charged tracks	142

List of Figures

2.1	Proton vs pion yield ratio from the Cronin paper	7
2.2	Illustration of Initial State Multiple Scattering	9
2.3	Feynman diagram of Drell-Yan production of dileptons.	9
2.4	Planarity of jets created with protons incident on Pb targets vs H targets.	11
2.5	Illustration of Final State Multiple Scattering	12
2.6	Evidence of Baryon Enhancement in Au+Au collisions	14
2.7	Recombination model compared with Au+Au data	16
2.8	Illustration of an example hard scatter resulting in fragmentation to two pions	17
2.9	Elliptic Flow in p+Pb at the LHC	18
2.10	p/ π ratios compared for central d+Au and peripheral Au+Au	19
2.11	Pion transverse momentum distribution from d+Au collisions compared to one created with the recombination model	20
3.1	An Aerial view of BNL	22
3.2	Illustration of all the accelerators used to boost ions to relativistic speeds at RHIC	23
3.3	PHENIX Detector Configuration for RHIC Run 8 (2008)	26
3.4	Wire net configuration in the DC	29
3.5	Schematic of the Pad Chambers	30
3.6	A schematic of the slat layout in the TOFE	31
3.7	An illustration of a single slat in the TOFE	32
3.8	Diagram of a basic RPC	33
3.9	Cross sectional diagram of the MRPCs used in the TOFW	34
3.10	A schematic of the Aerogel Cherenkov Counter	35
3.11	A schematic of one tile in the ACC	36
3.12	Chart of Particle Identification capabilities over a range of transverse momentum	37
3.13	A diagram of the RICH	38
3.14	Schematics of EMCAL components	39
3.15	A drawing of example ERT events	41
3.16	The Beam Beam Counter	42

3.17	Schematic showing the layout of fiber optics in the ZDC	42
3.18	Centrality bins as determined by ZDC energy versus BBC charge sum	43
3.19	Schematic of the MPC	45
3.20	Cross sectional diagram of RXNP layers	46
3.21	A diagram of the data flow of PHENIX data through the DAQ	48
4.1	Central versus peripheral ion collisions, BBC vs ZDC determination of	52
4.2	Diagram of BBC event characterization	54
4.3	Event Vertex Distribution	54
4.4	Hits in the DC matched to tracks using a Hough transform	56
4.5	Distribution of track quality.	57
4.6	Diagram of track reconstruction by the DC/PC1 projected linearly onto the TOF/PC3	58
4.7	Particle separation in the TOF	59
4.8	m^2 vs p_T showing clear constant separation of particle signatures.	61
5.1	Plots of the first four harmonics of a cosine series	64
6.1	Illustrations of the event plane in heavy ion collisions	67
6.2	Cartoon of Event Plane determination with forward detectors	68
6.3	Flattened event plane distributions in the BBC, MPC, and RXNP	69
7.1	Charged track elliptic flow, $\sqrt{s_{NN}} = 200$ GeV d+Au collisions	74
7.2	Number of ACC photoelectrons vs m^2 in bins of p_T	77
7.3	$\pi^\pm, k^\pm, p/\bar{p}$ elliptic flow, $\sqrt{s_{NN}} = 200$ GeV d+Au collisions	79
8.1	Centrality uncertainty contribution to Systematic Error	84
8.2	Timing QA in the TOF.W	86
8.3	Systematic Offset in TOF.W	87
8.4	Effects of Systematic Shifts in Yield on v_2	93
A.1	PHENIX coordinate system	95
D.1	$\frac{dN}{d\phi}$ vs $d\phi$, 0-5% centrality.	101
D.2	$\frac{dN}{d\phi}$ vs $d\phi$, 5-10% centrality.	102
D.3	$\frac{dN}{d\phi}$ vs $d\phi$, 10-15% centrality.	103
D.4	$\frac{dN}{d\phi}$ vs $d\phi$, 15-25% centrality.	104
D.5	PID fits and Yield vs $d\phi$ for $p_T=0.5-0.7$ GeV/c, TOF.W, negative particles	105
D.6	PID fits and Yield vs $d\phi$ for $p_T=0.7-0.9$ GeV/c, TOF.W, negative particles	106
D.7	PID fits and Yield vs $d\phi$ for $p_T=0.9-1.1$ GeV/c, TOF.W, negative particles	107
D.8	PID fits and Yield vs $d\phi$ for $p_T=1.1-1.3$ GeV/c, TOF.W, negative particles	108
D.9	PID fits and Yield vs $d\phi$ for $p_T=0.5-0.7$ GeV/c, TOF.W, positive particles	109
D.10	PID fits and Yield vs $d\phi$ for $p_T=0.7-0.9$ GeV/c, TOF.W, positive particles	110

D.11 PID fits and Yield vs $d\phi$ for $p_T=0.9\text{-}1.1 \text{ GeV}/c$, TOF.W, positive particles	111
D.12 PID fits and Yield vs $d\phi$ for $p_T=1.1\text{-}1.3 \text{ GeV}/c$, TOF.W, positive particles	112
D.13 PID fits and Yield vs $d\phi$ for $p_T=1.3\text{-}1.5 \text{ GeV}/c$, TOF.W, negative particles	113
D.14 PID fits and Yield vs $d\phi$ for $p_T=1.5\text{-}1.7 \text{ GeV}/c$, TOF.W, negative particles	114
D.15 PID fits and Yield vs $d\phi$ for $p_T=1.7\text{-}1.9 \text{ GeV}/c$, TOF.W, negative particles	115
D.16 PID fits and Yield vs $d\phi$ for $p_T=1.9\text{-}2.1 \text{ GeV}/c$, TOF.W, negative particles	116
D.17 PID fits and Yield vs $d\phi$ for $p_T=1.3\text{-}1.5 \text{ GeV}/c$, TOF.W, positive particles	117
D.18 PID fits and Yield vs $d\phi$ for $p_T=1.5\text{-}1.7 \text{ GeV}/c$, TOF.W, positive particles	118
D.19 PID fits and Yield vs $d\phi$ for $p_T=1.7\text{-}1.9 \text{ GeV}/c$, TOF.W, positive particles	119
D.20 PID fits and Yield vs $d\phi$ for $p_T=1.9\text{-}2.1 \text{ GeV}/c$, TOF.W, positive particles	120
D.21 ACC $N_{p.e.}$ vs m_2 , PID fits, and Yield vs $d\phi$ for $p_T=2.1\text{-}2.3 \text{ GeV}/c$, TOF.W, negative particles	123
D.22 ACC $N_{p.e.}$ vs m_2 , PID fits, and Yield vs $d\phi$ for $p_T=2.3\text{-}2.5 \text{ GeV}/c$, TOF.W, negative particles	126
D.23 ACC $N_{p.e.}$ vs m_2 , PID fits, and Yield vs $d\phi$ for $p_T=2.5\text{-}2.7 \text{ GeV}/c$, TOF.W, negative particles	129
D.24 ACC $N_{p.e.}$ vs m_2 , PID fits, and Yield vs $d\phi$ for $p_T=2.7\text{-}2.9 \text{ GeV}/c$, TOF.W, negative particles	132
D.25 ACC $N_{p.e.}$ vs m_2 , PID fits, and Yield vs $d\phi$ for $p_T=3.0\text{-}3.5 \text{ GeV}/c$, TOF.W, negative particles	135
D.26 ACC $N_{p.e.}$ vs m_2 , PID fits, and Yield vs $d\phi$ for $p_T=3.5\text{-}4.0 \text{ GeV}/c$, TOF.W, negative particles	138
D.27 ACC $N_{p.e.}$ vs m_2 , PID fits, and Yield vs $d\phi$ for $p_T=4.0\text{-}4.5 \text{ GeV}/c$, TOF.W, negative particles	141
D.28 ACC $N_{p.e.}$ vs m_2 , PID fits, and Yield vs $d\phi$ for $p_T=2.1\text{-}2.3 \text{ GeV}/c$, TOF.W, positive particles	144
D.29 ACC $N_{p.e.}$ vs m_2 , PID fits, and Yield vs $d\phi$ for $p_T=2.3\text{-}2.5 \text{ GeV}/c$, TOF.W, positive particles	147
D.30 ACC $N_{p.e.}$ vs m_2 , PID fits, and Yield vs $d\phi$ for $p_T=2.5\text{-}2.7 \text{ GeV}/c$, TOF.W, negative particles	150
D.31 ACC $N_{p.e.}$ vs m_2 , PID fits, and Yield vs $d\phi$ for $p_T=2.7\text{-}2.9 \text{ GeV}/c$, TOF.W, positive particles	153
D.32 ACC $N_{p.e.}$ vs m_2 , PID fits, and Yield vs $d\phi$ for $p_T=3.0\text{-}3.5 \text{ GeV}/c$, TOF.W, positive particles	156
D.33 ACC $N_{p.e.}$ vs m_2 , PID fits, and Yield vs $d\phi$ for $p_T=3.5\text{-}4.0 \text{ GeV}/c$, TOF.W, positive particles	159
D.34 ACC $N_{p.e.}$ vs m_2 , PID fits, and Yield vs $d\phi$ for $p_T=4.0\text{-}4.5 \text{ GeV}/c$, TOF.W, positive particles	162

List of Tables

8.1 Event Plane Resolution for MPC, 0-5% centrality	82
---------------------------------------------------------------	----

Chapter 1

Introduction

1.1 Introduction

Humanity is set apart from the rest of creation by its tenacity to explore and discover and it's no surprise that the driving force for this discovery is our constant desire to better understand the universe around us. From the deepest distances of outer space to the infinitesimally small structures of the atoms that comprise the matter we interact with everyday, our growing understanding of the intricacies of our world has revealed such amazing complexities we never could have thought possible. Over the last century, one such exploration that has uncovered many unforeseen phenomena is the study of the building blocks of matter and the forces that hold it together. From Planck's discovery that the world of the incredibly small is not smooth and continuous but rather comprised of discrete quanta, extending to Bohr's model of the atom showing that even the orbital dynamics of electrons

were non classical, to the discovery of the neutron leading the way to the discovery of new fundamental forces of nature, field theories to describe them, and eventually the venerable standard model of particle physics, our ever increasing understanding of the workings of the atom has revealed many discoveries that were surprising to those who sought them. In the last few decades one such investigation into the makings of the atomic nucleus seeks to study the properties of this nuclear material under temperature and density extrema, namely the search for phenomena where quarks and gluons that make up a solid phase of nuclear matter like protons and neutrons in a nucleus would become deconfined and melt into a novel state of matter called the *Quark Gluon Plasma* (QGP) at said extrema. First discussions of this deconfinement were found when Collins and Perry [17] said that at small distances the coupling constant would decrease implying that dense nuclear matter would comprise of deconfined quarks and gluons. Though their inferences pertained to low temperature, high density systems, they noted that similar phenomena could occur in high temperature systems like that of the early universe. The first to coin the term "Quark-Gluon Plasma" was Shuryak in 1980 [46] who wrote:

"When the energy density ϵ exceeds some typical hadronic value (~ 1 GeV/fm 3), matter no longer consists of separate hadrons (protons, neutrons, etc.), but as their fundamental constituents, quarks and gluons. Because of the apparent analogy with similar phenomena in atomic physics we may call this phase of matter the QCD (or quarkgluon) plasma."

With this theoretical framework, we have set out to develop an understanding of

this phase transition whose resulting deconfinement of quarks and gluons has led to a new era of physics discoveries.

1.2 Early Experiments: An Overview

The earliest experiments that utilized collisions of two ions to study nuclear matter were largely re-purposing existing accelerators that were used for elementary particle physics. Whereas the general goal of an accelerator setup to study elementary particle physics is to study the production of exotic single particles created in specific Quantum Field Theory processes (baryons, mesons, force carrier bosons, leptons) an accelerator used for Heavy Ion Physics is used to study larger nuclear matter systems which result in higher track multiplicity consisting of particles created by more common processes.

Examples of this include the re-purposing of the weak focusing proton synchrotron called the Bevatron at Lawrence Berkeley National Laboratory when it was joined with the SuperHiLac, a linear accelerator capable of accelerating ions to relativistic energies of up to 2 GeV per nucleon and became the only machine in the world capable of accelerating all of the elements in the periodic table to relativistic speeds. This capability allowed researchers to pioneer the study of "quark matter" [25] the crowning achievement of this epoch being the discovery that nuclear matter could be compressed to high temperature [43], made evident by the observation of collective flow in Niobium + Niobium ions at 400 MeV/nucleon [26] which paved the way for the search for other phases of nuclear matter, namely the Quark Gluon Plasma.

The first step into the "ultra-relativistic" energy regime (> 10 GeV/nucleon) took place at Brookhaven National Lab in the mid 80's with the Alternating Gradient Synchrotron which initially was able to reach 14 GeV per nucleon with Silicon ions. Concurrently across the ocean, the European Organization for Nuclear Research (Conseil Europen pour la Recherche Nuclaire, CERN) had the Super Proton Synchrotron accelerated Oxygen and Sulfur ions up to 200 GeV per nucleon. By the mid 90's both had seen their own upgrades that allowed them to create larger systems with the use of so called "Heavy" ions. At the AGS, Gold ions accelerated to 11 GeV per nucleon, and at the SPS, Lead ions accelerated to 158 GeV per nucleon[51]. Both accelerators set the stage for RHIC, each with their own prolific periods of discovery.

At the AGS, the observation of directed and elliptic flow in 11.5 GeV Au + Au collisions at the AGS by the E877 collaboration [9] showed that quark matter behaved collectively, that it was indeed a new state of matter not just a conglomerate of independent nuclei. The E802 collaboration compared the production of charged kaons compared to charged pions in 14.6 GeV Si + Au collisions and saw the "strange" result that the production of kaons was enhanced compared to proton + proton collisions showing that the collective behavior of this quark matter produced a different spectrum of particles than the simpler p + p collisions [1].

At the SPS, this strangeness enhancement was also studied by the NA49[28] collaboration through a similar measurement of the charged kaon to pion ratio and the WA97[8] collaboration measuring the production of multi-strange baryons ($\Lambda, \bar{\Lambda}, \Xi^\pm$, and Ω^\pm). Mean-

while the NA50 collaboration was finding not enhancement but suppression of J/Ψ mesons (which decay to $l^+ + l^-$ pairs) when compared to $l^+ + l^-$ pairs created through Drell-Yan processes (see fig 2.3) [3].

Concurrently, the teams at the two accelerators used two particle correlations to study the evolving collision volume and saw that the energy density of the quark matter was considerably higher, an order of magnitude greater, than naturally stable laboratory nuclei [27] and found the conditions for thermal freeze out [12], i.e. the re-confinement of quarks and gluons into hadronic states, a process called *hadronization*.

These various phenomena were signatures of new physics that could not be explained by solely scaling up $p + p$ collisions, they were signs that the nuclear material had undergone a transformation, more specifically, a phase transition and a sign of quark-gluon deconfinement.

Chapter 2

Nuclear Matter: Hot and Cold

2.1 Hot versus Cold Nuclear Matter

Because the deconfinement corresponds to a condition where the temperature of the system is above some critical temperature it is often called "Hot Nuclear Matter." Therefore, the region of the nuclear matter phase diagram where quarks and gluons are confined to baryon and meson states is often called "Cold Nuclear Matter." Historically, "Hot" QGP systems were those created by colliding two large nuclei such as in Au+Au collisions and "Cold Nuclear Matter" systems were made by colliding large nuclei with smaller ones such as in d+Au collisions and in beam collisions with fixed nuclear targets.

2.2 The Cronin Effect

The seminal paper titled **Production of hadrons at large transverse momentum at 200, 300, and 400 GeV** by J.W. Cronin, et al. detailed a fixed target experiment that collided protons with a tungsten target and underpinned a phenomenon found in cold nuclear matter systems. Later dubbed the *Cronin Effect* after the paper's first author, the experiment found that the production of protons at mid p_T ($2 \leq p_T \leq 4$) was enhanced when compared to the production of pions [19].

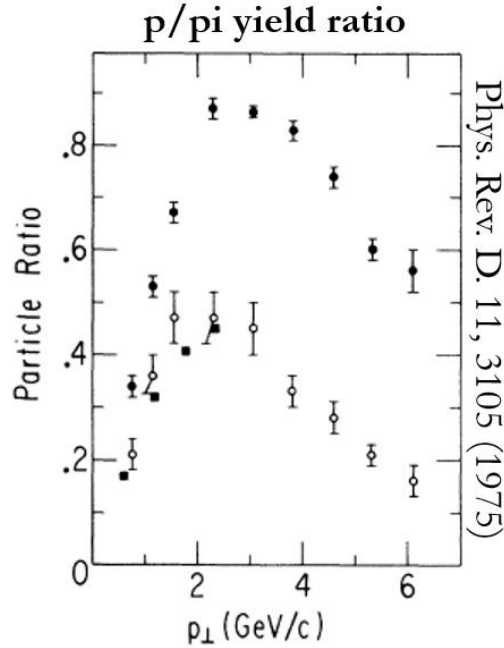


Figure 2.1: Proton vs pion yield ratio from the Cronin paper. Closed circles are the ratio obtained by colliding $23.7 \text{ GeV}/c^2$ protons on tungsten ($A=110$). Open circles are the same data extrapolated ($A=1$).

After this discovery many set out to come up with theoretical mechanisms that

could explain this baryon production preference. These mechanisms can largely be categorized into two types: those where the incoming partons interact with the nuclear medium and those where outgoing partons created after an incoming nucleon hard scatters interacts with the nuclear medium. These two categories are called *Initial State Interactions* and *Final State Interactions*.

2.2.1 Initial State Multiple Scattering

The first attempts at explaining the Cronin Effect were made using initial state interactions. Khn in 1975 described a mechanism where incoming quarks scatter with nuclear quarks which randomize the direction of the incoming parton before finally colliding with another quark to produce an event similar to a proton-proton collision[33]. Since it is unclear how many "soft scatters" happen before the final hard scatter the p_T spectrum is broadened which could account for the increase of particle production for the mid p_T range.

The NA10 collaboration at CERN set out to use back to back lepton probes to study the effect of the nucleus on jets. They collided 140 GeV and 258 GeV negative pions on tungsten targets of various thicknesses and looked for muon pairs produced via a Drell-Yan Process.

They found that the mean squared p_T did not vary much at all as a function of target thickness which implies that incident partons are not affected by the thickness of

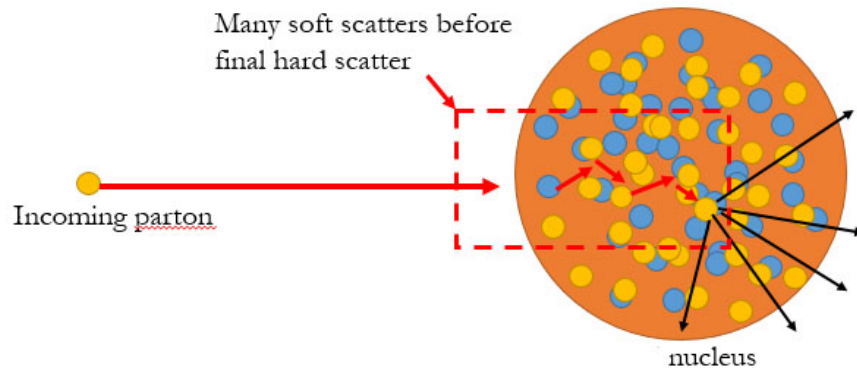


Figure 2.2: Illustration of Initial State Multiple Scattering.

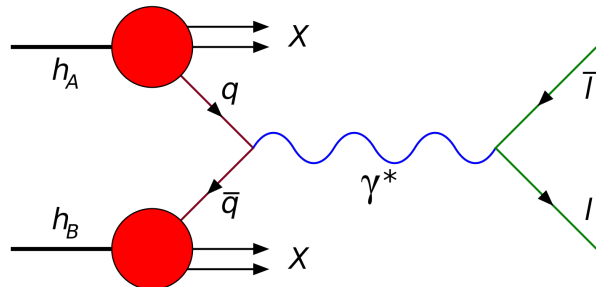


Figure 2.3: Feynman diagram of Drell-Yan production of dileptons. Quark-Antiquark annihilation produces a lepton-antilepton pair through the exchange of a virtual photon.[20]

the target and therefore that the path length of soft collisions that would broaden the p_T spectrum is very short. Furthermore, the E772 collaboration, with an experiment colliding 800 GeV protons on H₂, C, Ca, Fe, and W targets, showed that Drell-Yan produced dileptons mean squared p_T did not vary much between the nuclear targets of varying nucleon number.[7] i.e. increasing the number of nucleons does not change the net p_T much, further showing that initial state contributions to p_T broadening is minimal.

2.2.2 Final State Multiple Scattering

In 1991 the E609 collaboration at Fermilab studied dijets produced in fixed target experiments colliding 400 GeV/c protons with targets made of various nuclear materials including hydrogen and lead[18]. The conditions of interest to them were the creation of two back to back jets produced after an incoming parton hard scattered with a target nucleon. They defined a quantity called *planarity* which measured how *back-to-back* two jets are. In their words:

”An axis is found which maximizes the sum of the squares of all momentum components (b_{max}) along that axis while minimizing the sum of the squares of momentum components perpendicular to that axis (b_{min}). Planarity is then defined as:

$$P = \frac{b_{max} - b_{min}}{b_{max} + b_{min}}. \quad (2.1)$$

For two narrow back-to-back jets P approaches 1, while for a circularly symmetric

event P is 0.”

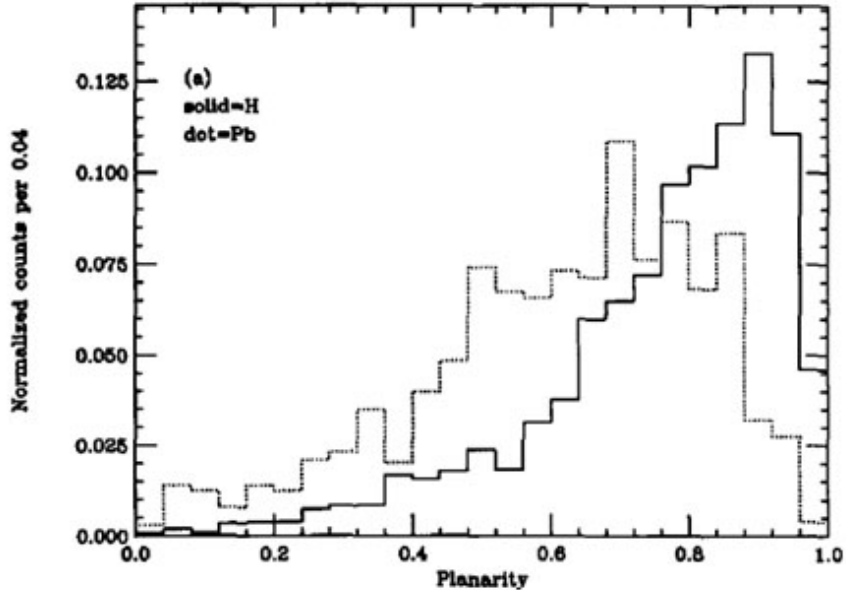


Figure 2.4: Planarity of jets created with protons incident on Pb targets vs H targets.

Their measurement compared the planarity of dijets created from protons colliding with a hydrogen target with the planarity of those created with collisions on a lead target. They noticed a downward shift in planarity and broadening of the spectrum for Pb dijets compared to H although both had very similar jet widths. This measurement led to a paper in 1993 where they concluded that Parton hard scatterings within nuclei involve very little nuclear scattering of the incident parton, but that there is substantial nuclear rescattering of outgoing hard scattered partons.[22] Because of this, we call this type of mechanism a *Final State Interaction*. While it is true that this could account for the increase in particle

production it does not effectively explain why the effect is stronger for baryons than for mesons and why this preference disappears for at high p_T

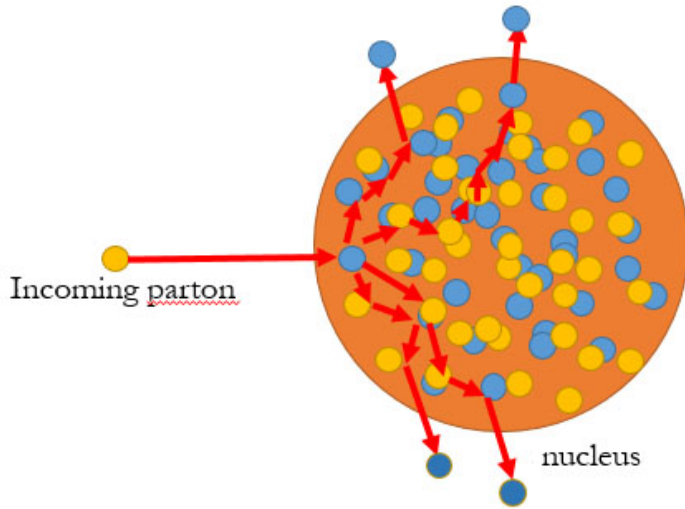


Figure 2.5: Illustration of Final State Multiple Scattering.

2.3 Hot Nuclear Matter: QGP

So far this discussion has stayed within the temperature regime where quarks and gluons are confined to hadronic states. As summarized in the previous chapter, physicists had already seen enough hints that new physics was taking place when the energy density reached some critical value and consequently RHIC was commissioned to study this phase change.

2.3.1 Baryon Enhancement

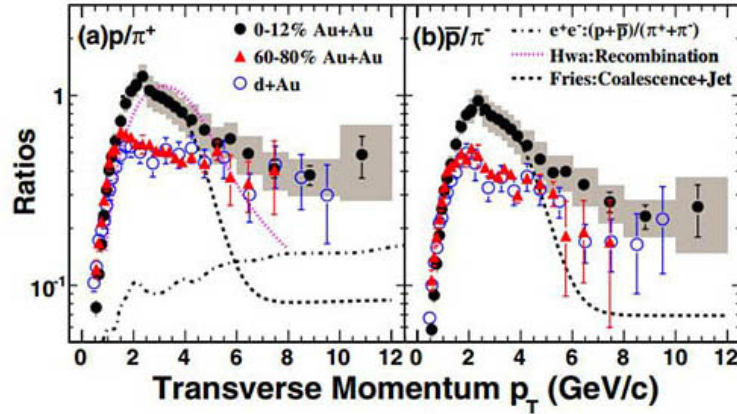
One of the surprises encountered when studying this new phase of matter was that the production of particles seemed to have a different mechanism compared to p+p collisions. One experimental signature of this was the so called *baryon enhancement* for peripheral Au+Au collisions [2]. This result is shown in figure 3.16a which shows the comparative yield between protons and pions in bins of p_T . The phenomena of interest is the apparent baryon excess in central collision data set for the mid p_T range which is strongest at around $p_T \approx 2$ GeV/c and disappears at around $p_T \approx 4$ GeV/c. Similarly, the Nuclear Modification factor for Central and Peripheral collisions also shows this enhancement in the same range (shown in figure 3.16b).

2.3.2 Theoretical Models of Baryon Enhancement

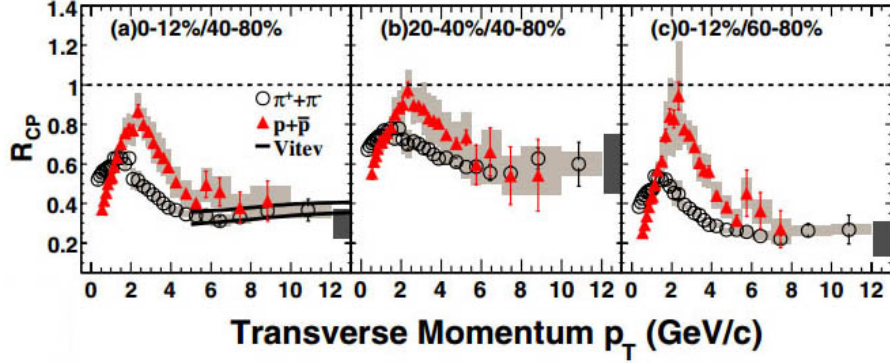
Though many have proposed models to describe this baryon enhancement, I will focus this discussion on the two leading models.

Recombination

Following the idea that a phase change in nuclear matter happens when a critical energy density causes deconfinement of quarks and gluons from their bound states as neutrons and protons and that the post-collision evolutionary behavior of this QGP is one that expands rapidly, Rudolph Hwa and C.B. Yang postulated that the enhancement of particle production could be explained by the ways in which the outgoing partons interacted[30].



(a) p/π^+ and \bar{p}/π^- ratios for central and peripheral 200 GeV $Au+Au$ collisions. Two leading models are compared to the data as well as the same ratio for 200 GeV $d+Au$ collisions.



(b) Nuclear modification factor, R_{CP} , comparing nuclear effects on particle production in central versus peripheral $Au+Au$ collisions compared to production in binary scaled $p+p$ collisions (see appendix B for a summary on nuclear modification factors)

Figure 2.6: p/π production ratio and R_{CP} as evidence of Baryon Enhancement in central $Au+Au$

They defined two types of partons, those with low transverse momentum created by the hydrodynamic outward expansion of the QGP referred to as *soft* and/or *thermal* partons and those with high transverse momentum created by *hard* nuclear scattering processes or *shower* partons. The production of particles could then be described by the way these partons combined combinatorically, i.e. the way thermal partons combined with other thermal partons, the way they combined with shower partons, and the way shower partons combined with other shower partons. This mechanism was termed *recombination* since it relied on the recombining of quarks in partons created from the nuclear collision.

Fragmentation

Fries, Müller, Nonaka, and Bass postulated that the reason why protons were produced in abundance was simply that following a collision, the building blocks of protons: up and down quarks, are plentiful and that they simply recombine back into their confined states. This mechanism dominates for low p_T since outgoing partons are traveling slowly which allows the constituent quarks to remain connected by a color string. In contrast to the soft thermal partons, partons created with hard scattering processes are more likely to break the color string creating quark/anti-quark pairs, i.e. mesons. Because this range of p_T causes individual quarks in the QGP to fragment out, the lone quarks scatter off with enough energy to create quark antiquark pairs from the vacuum which pair up with the nuclear quarks . This two regime model naturally creates a baryon preference for low p_T partons that is met with proportional meson production when the parton p_T is adequately

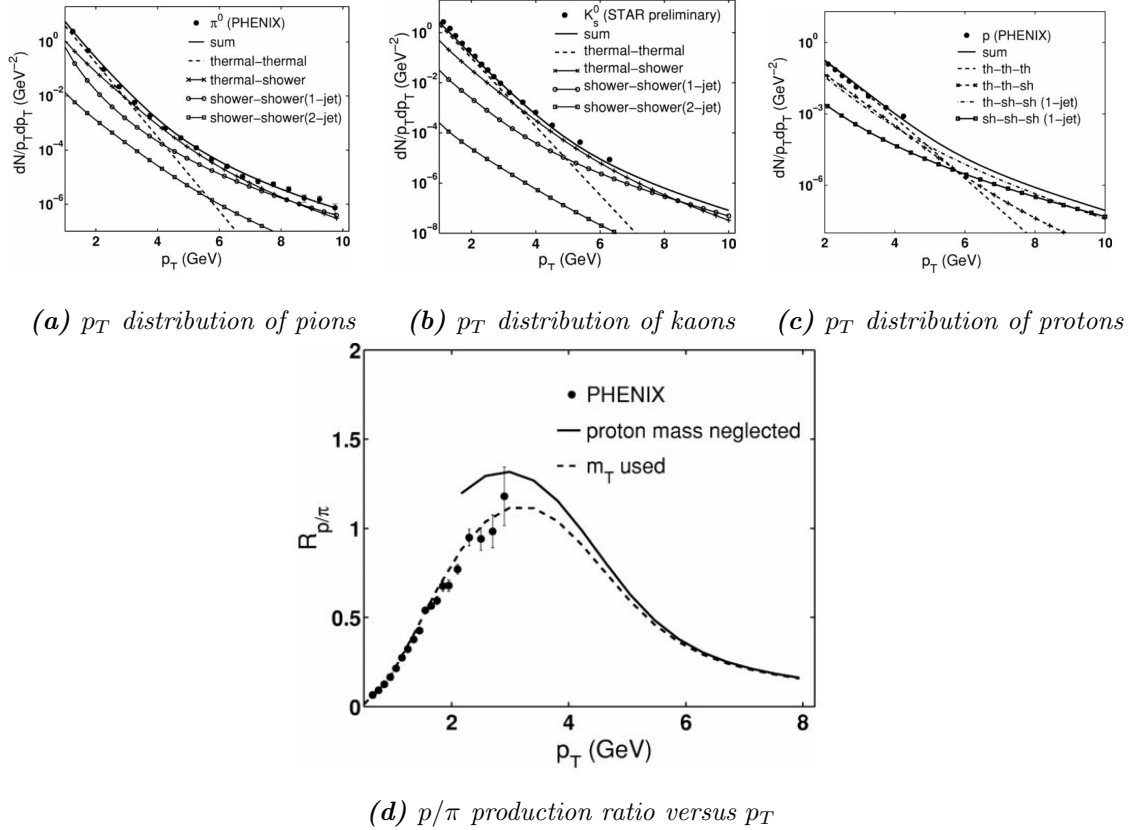


Figure 2.7: $Au+Au$ identified particle measurements compared with recombination model predictions. For the p_T distributions we see three distinct regions of recombination, the low p_T range where soft thermal parton recombination dominates, the high p_T range where hard shower parton recombination dominates, and the middle range where thermal-shower recombination best describes the data.

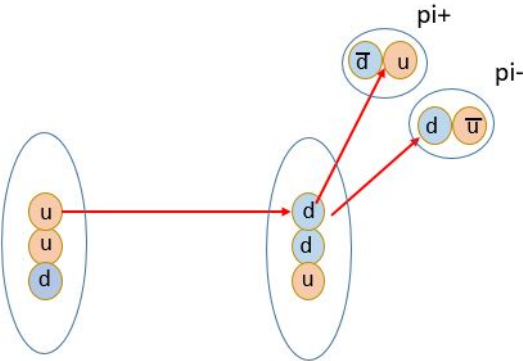


Figure 2.8: Illustration of an example hard scatter resulting in fragmentation to two pions. Here an up quark scatters with enough energy to scatter and release the down quark from being bound in another nucleon. This occurs with enough energy to create antiparticle partners from the vacuum resulting in the formation of charged pions.

high enough.

2.4 Flow at the LHC

Up till now it appeared that the lines in the proverbial sand were clear with respect to nuclear matter phase changing and that we had two distinct ways to measure the properties of these two states. There is cold hadronic matter which has its own experimental signatures that are measured with beam on fixed target experiments and with small ion (protons and deuterons) on heavy ion collisions and hot deconfined quark matter which flows and behaves another way and studied using collisions of two heavy nuclei. This notion that the two experimental methods allowed the temperature dependent phenomena to be studied separately was brought into question in 2015 when the Large Hadron Collider

(LHC) at CERN turned on and entered its second era of measurements. At the Compact Muon Solenoid (CMS) they collected data from p+Pb collisions at 5.02 TeV and compared it to Pb+Pb collisions at 2.76 TeV. While hydrodynamic phenomena like collective flow was expected in the Pb+Pb data, they found the unexpected when a nonzero elliptic flow was measured in p+Pb (see fig 2.9).

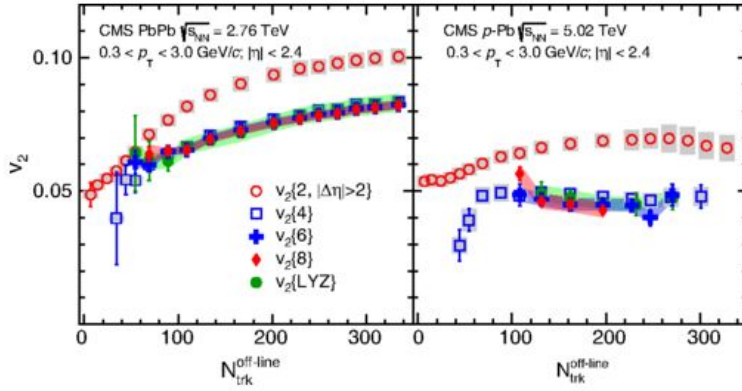


Figure 2.9: CMS result from 5.02 TeV p+Pb collisions showing a nonzero elliptic flow signal versus track multiplicity

The appearance of flow in systems previously thought of as "cold" was a sign that perhaps the QGP forms much easier than previously expected and that perhaps some phenomena found in cold systems, such as baryon enhancement, could be attributed to mechanisms that found favor in explaining similar phenomena in hot heavy ion systems.

2.5 Recombination and Fragmentation for All?

Furthermore, experimental evidence that the two systems behave quite similarly has been found. In fig. 2.11 particle production ratios (p/π) are compared and we see that the baryon enhancement which was indicative of the QGP formation in peripheral Au+Au collisions is followed extremely closely by data from central d+Au.

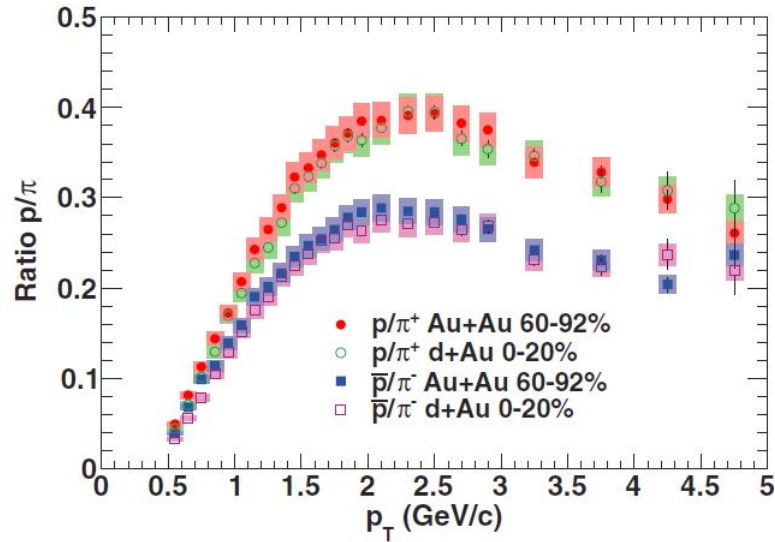


Figure 2.10: p/π ratios compared for central d+Au and peripheral Au+Au[4]

It may seem that the behavior of the two are contradicting since one is central and the other peripheral but we can see that the geometries of the collisions for the two cases are similar. The glancing peripheral Au+Au collisions create an "almond-like" QGP fireball whereas peripheral collisions in d+Au would behave such as a p+p collision since the number of participants is at a minimum when the collision is maximally peripheral. If we

make the hypothesis that QGP formation is most likely with a higher number of participants then it follows that central d+Au collisions would be most likely to form a QGP. And so since physicists love reductionism and unification, and that the evidence makes one wonder if a QGP is formed in simpler systems, it would be advantageous to be able to describe the two systems with a singular mechanism.

But are there even the building blocks to support such a notion that QGP is created in such a simple system as d+Au? Recombination is easy to justify in Au+Au since the large number of participants makes the formation of the QGP easily achieved and leaves a great abundance of free quarks that are able to recombine. What if we apply the same ideas to d+Au? Hwa and Yang asserted [29] that since hard scattering creates jets, jet formation generates a lot of soft outgoing partons. Furthermore, soft partons behave like an expanding QGP, that is to say, they behave like thermal partons. Thermal parton baryon

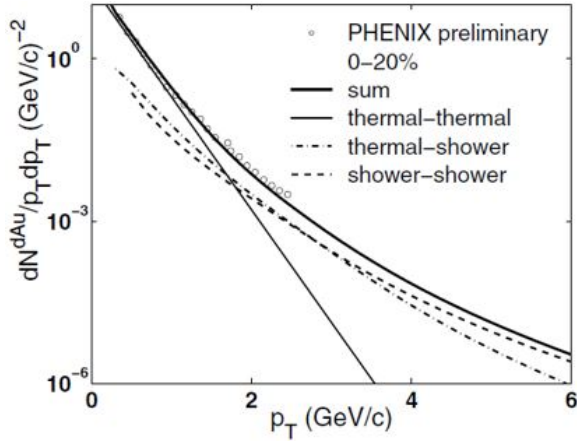


Figure 2.11: Pion transverse momentum distribution from d+Au collisions compared to one created with the recombination model

enhancement is due to recombination. Since soft partons behave like thermal partons, could there recombination in d+Au, and if there is, could it be a sign that we should see other signs of QGP formation such as collective flow?

I postulate that there is sufficient evidence to say that the nuclear matter created by d+Au behaves collectively and that there should be a non-zero elliptic flow measurement. Furthermore, this elliptic flow is dependent on particle species in that it exhibits baryon enhancement in the mid p_T range indicative of the formation of a QGP. Unknown phenomena of interest is the enhancement of strangeness. Proton and pion flow is an indicator of first generation quark recombination however strange quarks are not part of the initial conditions and are rather created “fresh” from the QGP. Evidence of strangeness enhancement via kaon flow independent of quark scaling may be further evidence of QGP formation in the previously thought-to-be cold d+Au system. Due to system geometry, flow effects should be maximal with the most central collisions since they create the most interaction of nuclear material. Furthermore, as the collisions become more peripheral, the behavior of the system should become more p+p like.

Chapter 3

Experimental Apparatus

3.1 The Relativistic Heavy Ion Collider

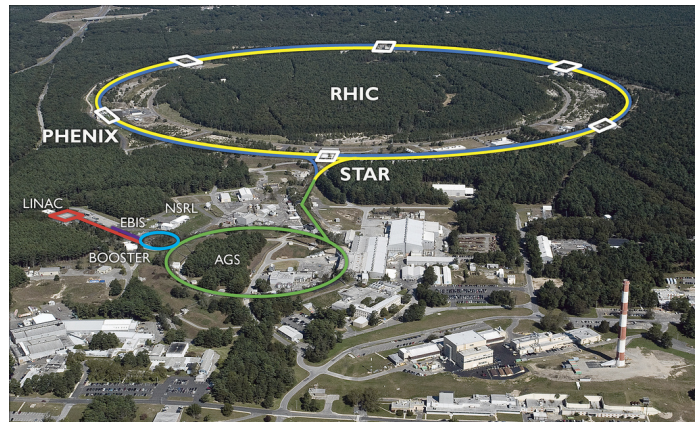


Figure 3.1: An Aerial view of BNL with RHIC and the AGS outlined and the locations of PHENIX and STAR mapped

Based at Brookhaven National Lab (BNL) on the east end of Long Island, New York, the Relativistic Heavy Ion Collider (RHIC) is a particle accelerator and storage ring

that is used to study the properties of nuclear matter, specifically the properties, formation of, and phase transition of nuclear matter into a novel state called the Quark Gluon Plasma (QGP). RHIC accelerates nuclei which are stripped of their electrons (heavy ions) to almost the speed of light and collides them together with enough energy to raise the system's temperature to that which is required to create the QGP.

3.2 From Start to Finish

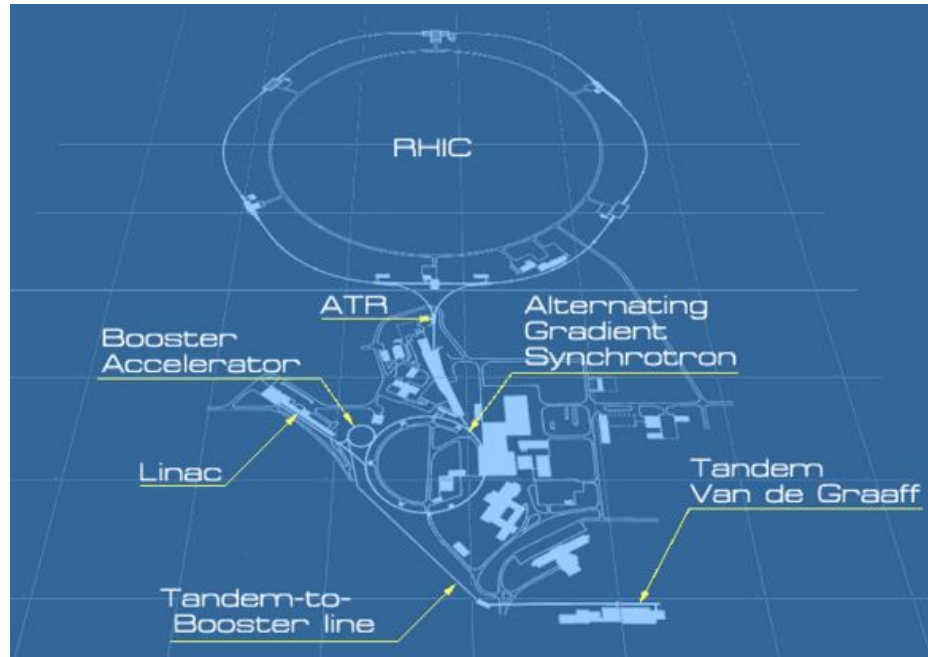


Figure 3.2: Illustration of all the smaller accelerators which are used together in order to boost ions to relativistic speeds at RHIC

The speeds achieved at RHIC is the result of many smaller accelerators working in concert in order to boost the ions' speed faster and faster [11]. Ions begin their journey

at a compact source and heavy ion accelerator called the Electron Beam Ion Source (EBIS) (located by the Linear Accelerator (LINAC) in figure 3.2). From there they are transferred to the a circular accelerator called the Booster Synchrotron which utilizes long-wavelength radio frequency electromagnetic waves allowing the ions to "surf" on their downward slope. The ions are then fed into the Alternating Gradient Synchrotron (AGS). No slouch in and of itself, the AGS was once the proverbial end-of-the-line where experiments took place and were studied and is responsible for three Nobel Prizes itself: the discovery of the muon neutrino in 1962, the discovery of charge-parity violation in 1963, and the joint discovery of the J/Ψ in 1976. The AGS uses the magnetic field gradients of 240 magnets, alternating them in order to boost the ions to 99.7% the speed of light after which it is transferred to the AGS-to-RHIC transfer line (AtR). The AtR is like a train switch yard wherein bunches of ions are fed into the RHIC rings. Bunches of ions are sent through either clockwise in one ring or counterclockwise in the other using a switching magnet.

RHIC is comprised of two concentric rings which are 3.8 kilometers in circumference. These rings use 1,740 helium cooled superconducting magnets to hold beams of these heavy ions which circulate in opposite directions within the two rings. Along the circumference of RHIC there are six points where the counter-circulating beams can be steered to collide (Interaction Regions or IR). Of these six IR, four have been used to house different detectors: the smaller, now defunct PHOBOS and BRAHMS experiments, and the larger still operational PHENIX and STAR experiments.

RHIC is an incredibly flexible machine capable of colliding various species of nuclei

from protons to Uranium [21] at a wide range of energies. Heavy ions such as Au can be accelerated as low as $3.85 \text{ GeV}/c^2$ and as high as $100 \text{ GeV}/c^2$ [34] with a combined center of mass energy of $200 \text{ GeV}/c^2$. When accelerating protons, RHIC is able to achieve up to $250 \text{ GeV}/u$ since the mass/charge ratio is smaller and is able to do so with polarized beams. It is also able to do this asymmetrically, that is to say, with two different species of nuclei, one in each ring. The system studied in this thesis is one such asymmetric system wherein a deuteron is collided with a gold ion with a center of mass energy of $200 \text{ GeV}/c^2$ (this system is referred to shorthand as "d+Au").

3.3 The PHENIX Detector

The analysis described in this thesis was made using the PHENIX detector which stands for: *Pioneering High Energy Nuclear Interaction eXperiment*. PHENIX is the largest of the experiments at RHIC and was designed specifically to study the QGP using a wide variety of particle probes at a very high rate with high accuracy.

It consists of a collection of various detectors assembled into four spectrometers called arms. The muon arms are used for studying physics phenomena at forward rapidity ($\eta = |1.1 - 2.4|$)[23] but the system of detectors used for the reconstruction of event tracks of import for this analysis are contained in the *Central Arm*.

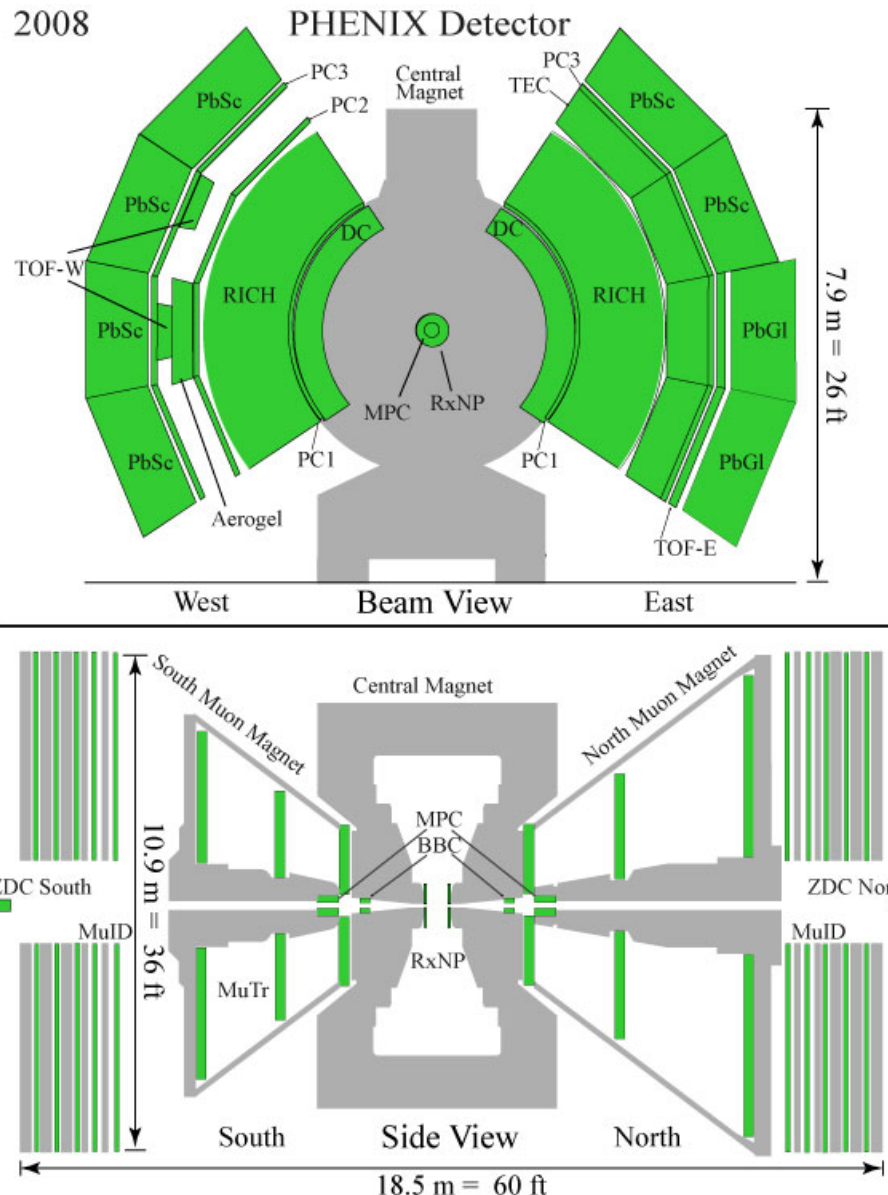


Figure 3.3: The configuration of the PHENIX detector for Run 8 (2008)

3.3.1 Central Arm

Covering a rapidity range of $\eta = < |0.375|$, the central arm consists of an east and a west arm that cover the azimuth 90° each [13] and is a complex, multi-layered, multi-system spectrometer capable of measuring a variety of particle probes. It is shown on the upper image labeled "Beam View" on figure 3.3 with individual subsystem detectors labeled. No single device is ideal for measuring every aspect of a collision event and as such, particle physicists design these complex detector systems such that different device technologies that are ideal for measuring specific quantities can all be used in concert to gather clean and precise data. Here I will discuss the various individual detectors in the central arm that I use in this analysis.

Drift and Pad Chambers

Particle trajectories are tracked using the Drift Chamber (DC) and the Pad Chambers (PC 1,2, and 3). The DC is a multiwire jet-type drift chamber with 12,800 readout channels. It is constructed from 6x80 wire nets in each arm. In principle the DC is similar to a wire chamber; When a charged particle travels through the gas in the DC the gas atoms are ionized and these ions and electrons are accelerated to anode wires which collect this ionization and sends a signal proportional to the ionization effect of the traveling particle. The DC is filled with a gas that is selected to have a uniform drift velocity close to the anode wires, i.e. a gas such that the traveling ions and electrons in the ionized gas have a linear relation in position and time such that $x(t) = v_{drift} * t$ within the active region [14], this

gas is a mixture of equal parts Argon and Methane also chosen for the mixture's high gas gain amplification and low diffusion coefficient. In doing so and when combined with high accuracy timing calculation we are able to achieve a more accurate position and trajectory of outgoing particles. The wire nets in the DC are arranged in different predetermined ways with respect to the beam axis. The six nets are designated names: X1, U1, V1, X2, U2, and V2. There are 12 anode wires in each X net and the wires are configured to be parallel to the beam axis so that they can be used to measure the azimuthal angle: ϕ . The U and V nets are stereo pairs with 4 anode wires in each net and are oriented such that they are tilted by an angle of 4.5° with respect to the beam axis. This angular bias allows us to use these nets to measure the track's z-component with high resolution. Furthermore, all wire nets are oriented in layers radially such that outgoing tracks deposit linear, correlatable signals in the DC. Additionally, since the DC is the first detector subsystem that outgoing particles created in a collision pass through, it is also used in conjunction with other detectors in order to accurately determine track trajectory through all of the detectors in the central arm. I will discuss the method of track reconstruction in section 4.3.

The Pad Chambers are three individual layers of pixel detectors. These pixels are arranged in 9 pixel clusters called "pads" that are readout by a single channel [39]. The pads in the closest-to-collision PC (PC1) are 8.4 mm x 8.45 mm and the pads in PC2 and PC3 are sized to maintain the same angular resolution at farther radial distances. The PC and DC have the same azimuthal coverage as the rest of the central arm and are located at increasing concentric distances from the collision vertex, the DC being the inner most

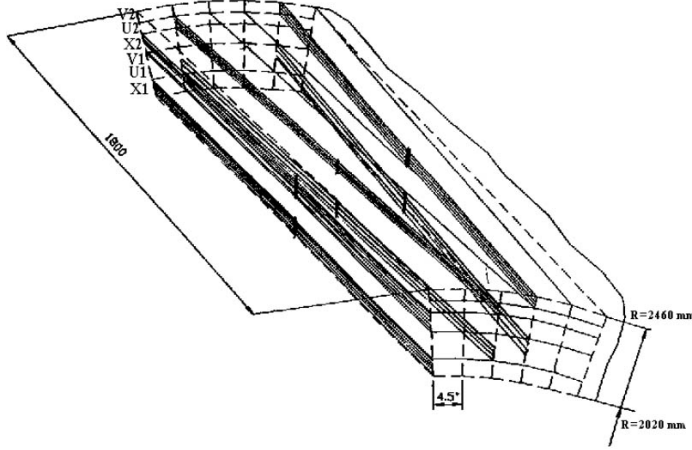


Figure 3.4: A diagram showing the configuration of the wire nets in the DC

detector, followed immediately by PC1. PC2 only exists in the west arm however PC3 exists in both arms. The small size of the individual pads allows for a large pixel density important for maintaining the separation of individual track signals in a high luminosity, high multiplicity event such as that of central heavy ion collisions. Since we can use these detectors to accurately determine particle track trajectories, and since charged particles under the influence of a magnetic field curve, the determined curvature can be used to determine track momentum. This track location data is also used to match with other detector data such as calorimetry, time of flight, and Cherenkov counters.

TOF: Time Of Flight Detectors

In addition to the track matching detectors this analysis utilizes the Time of Flight (TOF) detectors which are high accuracy timing detectors that measure the time it takes

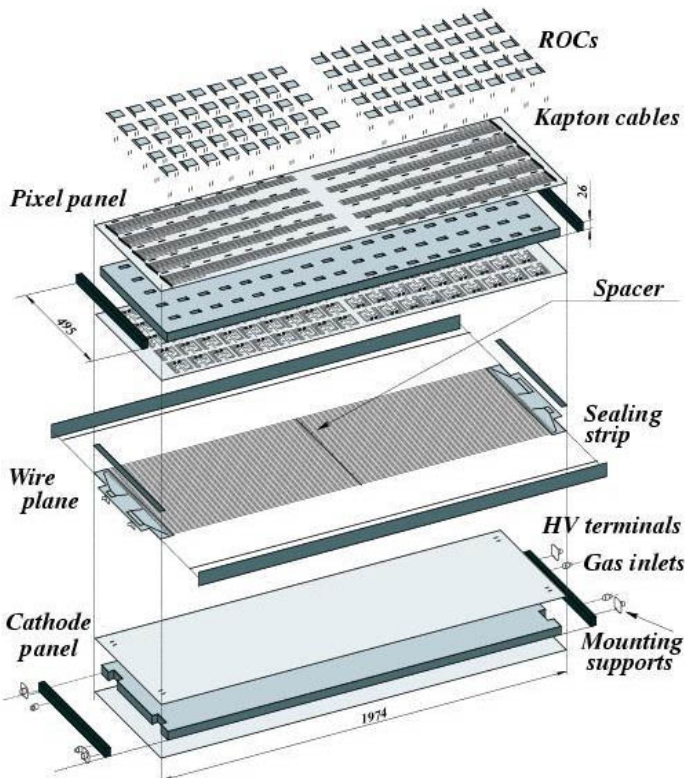


Figure 3.5: A blown up schematic showing the anatomy of the Pad Chambers.

for charged particles traveling through the central arm to go from the event vertex to the detector[35]. There are two TOF detectors in PHENIX, one on the east DC arm and one on the west arm. Located 5 meters away from the collision vertex and in the lower two sectors of the east arm, the TOF East (TOFE) is a scintillation detector with a timing resolution of $\Delta t_{res} \sim 80ps$. It covers $\Delta\phi = \pi/4$ and $\eta < |0.35|$.

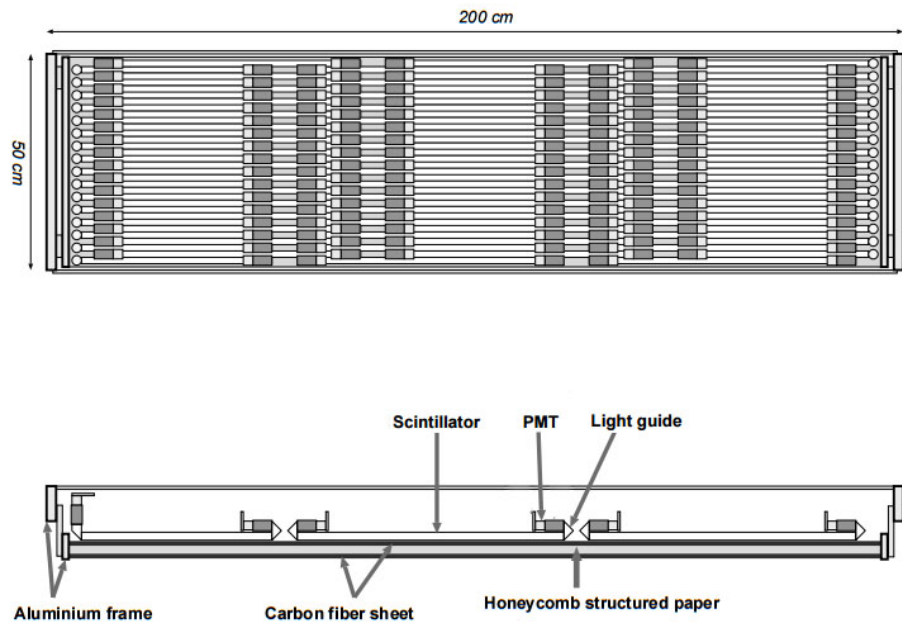


Figure 3.6: A schematic of the slat layout in the TOFE

Scintillators are a special type of material that fluoresces when it absorbs radiation. The TOFE is comprised of 1000 "slats" of plastic scintillation material with two photomultiplier tubes (PMT) on either end of the slats which amplify the fluorescing photons caused by charged particles that pass through the scintillators. Since we know the

length of the slat and the speed of light in the scintillation material we can easily calculate both the time when the particle first hit the slat (T_0) and the position where the particle hit the slat (y).

$$T_0 = \frac{(T_1 + T_2) - L/v}{2}, \quad y = \frac{T_1 - T_2}{2}v \quad (3.1)$$

Where T_1 and T_2 are the times measured by PMTs 1 and 2 respectively, L is the length of the slat, and v is the speed of light in the scintillator.

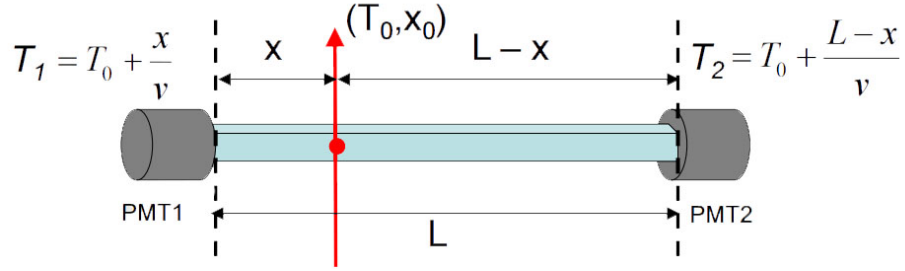


Figure 3.7: An illustration of a single slat in the TOFE

In the west arm, the TOF West (TOFW) is a 1024 channel Multi-gap Resistive Plate Chamber (MRPC) detector with a timing resolution of $\Delta t_{res} < 100ps$, located 4.85 m from the collision vertex and also covering $\Delta\phi = \pi/4$ and $\eta < |0.35|$. The MRPC works on the same principle as a basic Resistive Plate Chamber which is comprised of two high resistivity plastic (bakelite) plates separated by a volume of gas. On one resistive plate is a sheet of conducting material which is used to maintain a constant electric field across the gas gap. The other resistive plate has an array of conducting readout strips. When

a charged particle travels through the gas it causes an electron avalanche similar to what happens in a drift chamber. This electron avalanche is accelerated under the influence of an externally applied electric field toward one of the readout strips resulting in a "hit" signal which is then amplified by electronics.

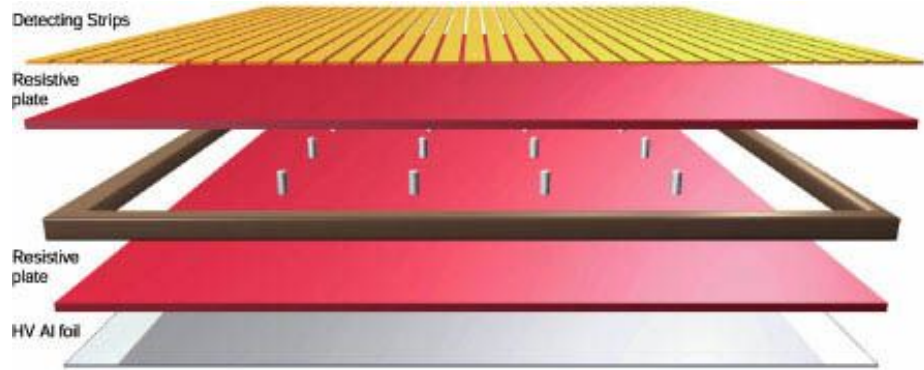


Figure 3.8: Diagram of a basic RPC [48]

A MRPC is a version of an RPC with alternating layers of the resistive material and gas gaps sandwiched together with the high voltage surface and readout strips on the outermost sides of the device [6]. The resistive plates inside the sandwich are electrically isolated and are transparent to the fast signals of incoming particles. Initially the externally applied electric field induces charges on the surfaces of the resistive plates causing each of the small gas gaps to be held at the same potential, and since each incoming particle ionizes the gas and deposits the same amount of one charge on one side of the plate and the opposite charge on the other, the potential in each individual gap is held constant. This means that the total signal the strips see is the *sum* of all of the electrical activity in each of small gaps. By using this configuration a greater precision is allowed than conventional RPC designs

and lends itself well to high precision timing detectors.

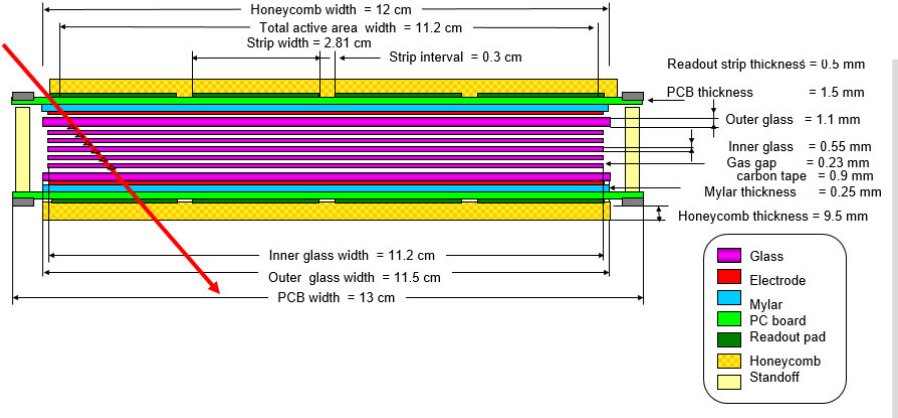


Figure 3.9: Cross sectional diagram of the MRPCs used in the TOFW

ACC: Aerogel Cherenkov Counter

As track momentum increases the signal width of the particle masses increases. The high resolution capabilities of the TOF detectors only allows them to be able to separate π^\pm , k^\pm , and p / \bar{p} signals up to certain transverse momentum p_T thresholds. The distinct masses of the particles of interest do provide an additional method of separating particle signals since if you were to give two particles of different mass the same momentum they would have distinct velocities. This is the principle with which a Cherenkov detector works. Cherenkov radiation is light that is emitted in a material when a charged particle travels through it with a velocity faster than the speed of light in that medium. This medium, called a Cherenkov radiator, can be carefully selected such that its intrinsic speed of light is such that lighter particles with higher velocities cause Cherenkov radiation but heavier

particles which travel slower given the same momentum will not. This threshold is given by:

$$E_{threshold} = \frac{nm}{\sqrt{n^2 - 1}} \quad (3.2)$$

where n is the index of refraction in the Cherenkov radiator and m is the mass of the particle. Using this, a Cherenkov detector acts as a logic detector categorizing tracks as those that either "fire" or "veto", that is to say tracks that radiate versus tracks that don't. In the case of separating π^\pm mesons from k^\pm mesons for p_T tracks where their mass signals overlap so strongly that they cannot be uncorrelated, the radiator was chosen such that the pions will fire the detector and the kaons will not. Pions and kaons are indistinguishable for $p_T > 2.8$ GeV/c, so the radiator chosen to separate the signals is a silica aerogel ($n \approx 1.011$).

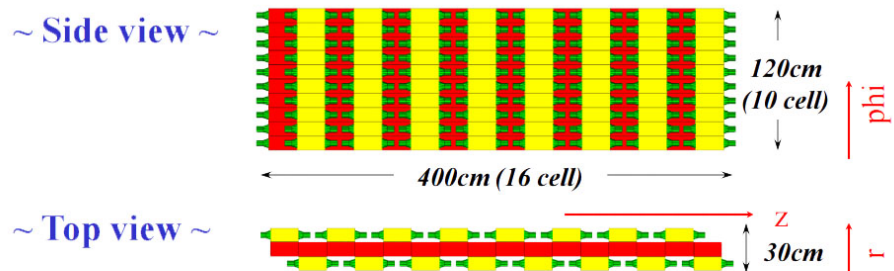


Figure 3.10: A schematic of the Aerogel Cherenkov Counter

The Aerogel Cherenkov Counter (ACC) is comprised of 160 tiles of silica aerogel. Each tile is affixed to an integration cube which allows for radiated cherenkov photons to

reflect internally until they hit a PMT. Each integration cube is filled with air and is covered on all exposed sides by a goretex reflector except for the "front" facing aerogel tile side and the two cutouts where the PMTs attach. There are two PMTs located opposite from each other for each cube. To account for the space taken by PMTs on the ends of the tiles the ACC is two sided and the tiles are oriented such that the opposite side tile occupies the gap where PMTs would be situated. There are 10 rows of 8 tiles on each side for a total of 160 tiles.

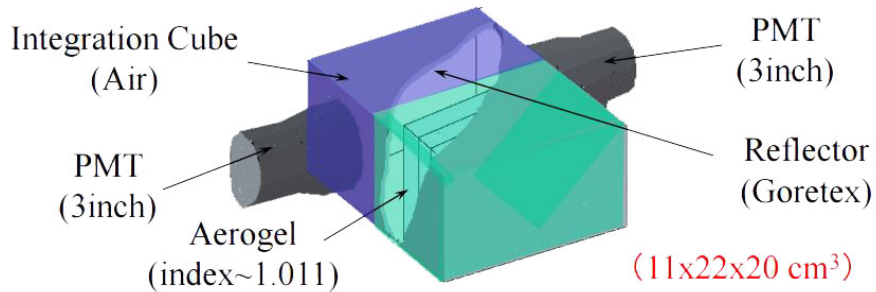


Figure 3.11: A schematic of one tile in the ACC

The ACC is located in the west arm covering the half of the azimuthal coverage that the TOFW covers and with the same rapidity coverage. When used in conjunction with the TOFW it can provide pion/kaon separation for $p_T < 4 \text{ GeV}/c$ and can discriminate protons for $p_T < 7 \text{ GeV}/c$. The total capabilities of the combination of the TOFW + ACC is shown in the following chart.

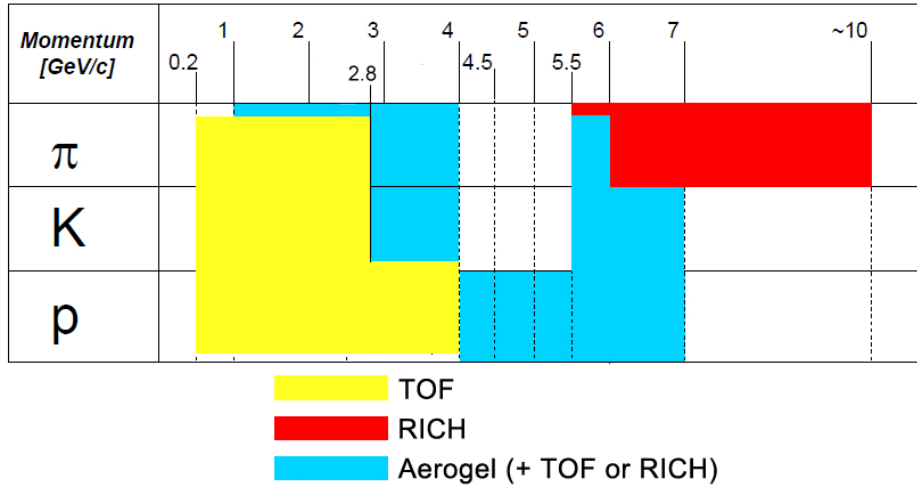


Figure 3.12: Chart of Particle Identification capabilities over a range of transverse momentum

EMCal and RICH: Electromagnetic Calorimeter and Ring Imaging Cherenkov Counter

Two other detectors that provide important track data are the *Electromagnetic Calorimeter* (EMCal) and the *Ring Imaging Cherenkov Counter* (RICH). Each arm has full coverage with both the RICH and the EMCal and they are often used together in order to study electrons via the EMCal/RICH Trigger (ERT).

As evident from it's name, the RICH is a Cherenkov counter that is used in a similar fashion as the ACC: to discriminate between particle species using Cherenkov radiation as a logic trigger. In the case of RICH, we are interested in separating pion and electron signals. It is filled with CO₂ which was chosen because it would allow electrons to radiate at very low p_T (> 0.018 GeV/c) while pions will not until the relatively high p_T of 4.87 GeV/c. Cherenkov radiated photons are emmited parallel to each other along the

track path as electrons move through the detector. The outer surface of the RICH is a series of mirrors arranged to form a spherical mirror which focusses that Cherenkov light onto the 2560 PMTs/arm which line the inner surface of the RICH. This results in a ring shaped Cherenkov signature as measured by the PMTs, hence the name: Ring Imaging Cherenkov Counter.

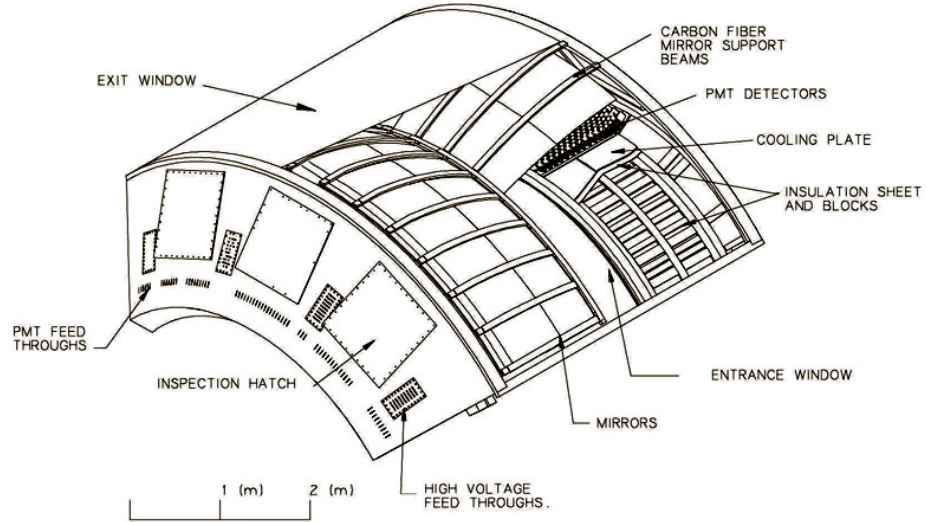
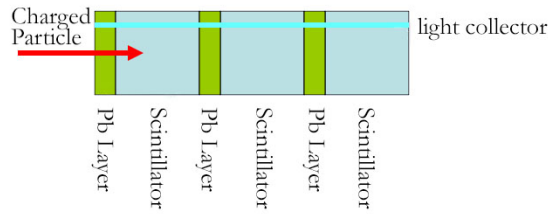
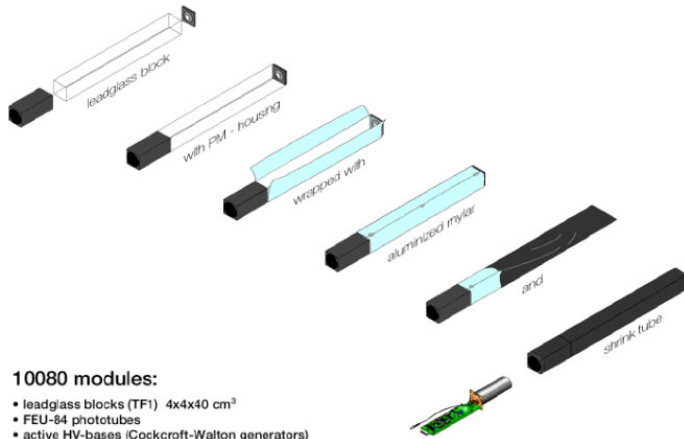


Figure 3.13: A diagram of the RICH

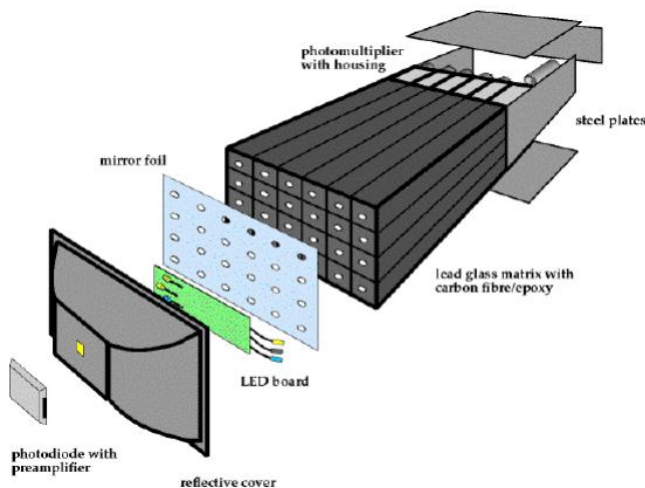
The EMCal provides an energy measurement for charged tracks and is broken up into eight sectors, four sectors in each arm [13]. Six of the sectors (all four of the west arm and the top two in the east arm) are made of channels comprised of alternating layers of lead and scintillator (PbSc) material. The lead layers cause incoming particles to shower into the scintillator layers which generate light that is detected by PMTs. The lower two sectors in the east arm are comprised of 10,080 uniform lead glass Cherenkov radiator towers (PbGl).



(a) Schematic of a PbSc module. Pb layers cause EM showers which create light in the scintillators and are detected by the light collectors.



(b) Construction of PbGl modules.



(c) One PbGl super module

Figure 3.14: Schematics of EMCAL components

These towers have PMTs attached on one end and are wrapped individually in reflective mylar and shrink wrapped to form *modules*. They are then placed in grid-like networks and each 16 module x 12 module structure is read out by one photodiode/preamplifier combination.

Though it may seem odd to have two types of detectors in the EMCAL, there is a method to the madness. Both have their own strengths, PbSc is more linear in response and is better at timing than PbGl thanks to its alternating layers, whereas PbGl is a tried and true design used in previous experiments such as WA98 at the SPS at CERN for its exceptional granularity and accurate energy measurement. Because they are two separate systems, they have different systematics and therefore we have a higher confidence level for the physics results from the EMCAL.

As mentioned, the EMCAL and RICH are used together to form a level 1 trigger to classify charged tracks. Since the RICH is tuned to radiate with electron tracks and the EMCAL measures all charged tracks, we know that tracks that result in signals in both the EMCAL and the RICH are most likely electrons, whereas tracks that only have signals in the EMCAL are likely charged hadrons.

3.3.2 Forward and Global Detectors

Though the bulk of this analysis is dependent on the central arm detectors, many aspects of reconstruction, namely event characterization (start of the event timer, the event vertex, centrality, and event reaction plane) is dependent on a handful of forward detectors

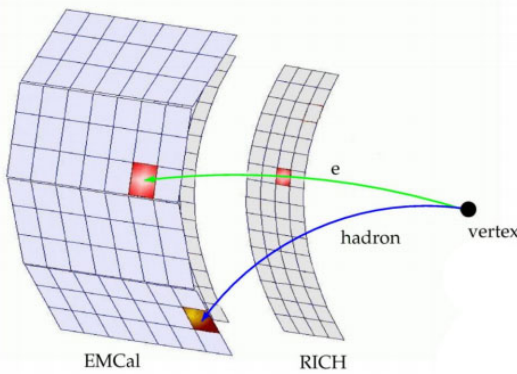
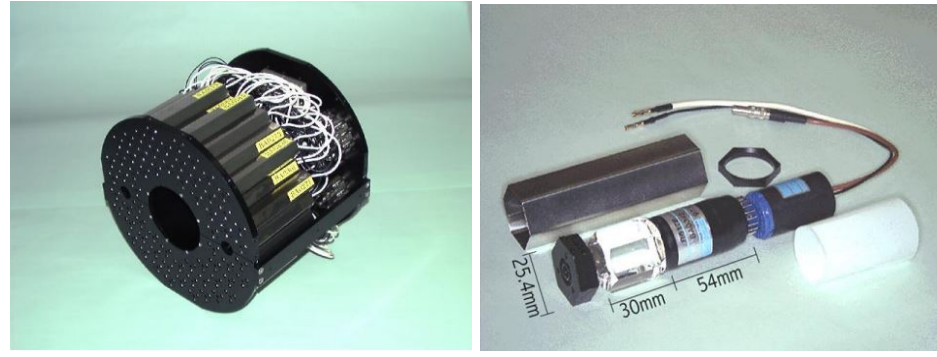


Figure 3.15: A drawing of example ERT events

which I will briefly discuss here.

BBC: Beam-Beam Counter

Of the forward detectors, the *Beam-Beam Counter* (BBC) is probably the most important because of its ability to measure the various global event parameters. There are two BBCs, one on the north side and one on the south side of PHENIX both equidistant from the center of the interaction region (IR). The constituent detector elements are made of quartz Cherenkov radiators attached to meshed dynode PMTs housed in hexagonal encasement. These elements are arranged in a toroidal shape in order to allow the ion beams to pass through the center while still getting full 2π azimuthal coverage. The BBCs cover $3.1 \leq \Delta\eta \leq <4$ in pseudorapidity.



(a) An illustration of a BBC

(b) A single element of the BBC

Figure 3.16: The Beam Beam Counter

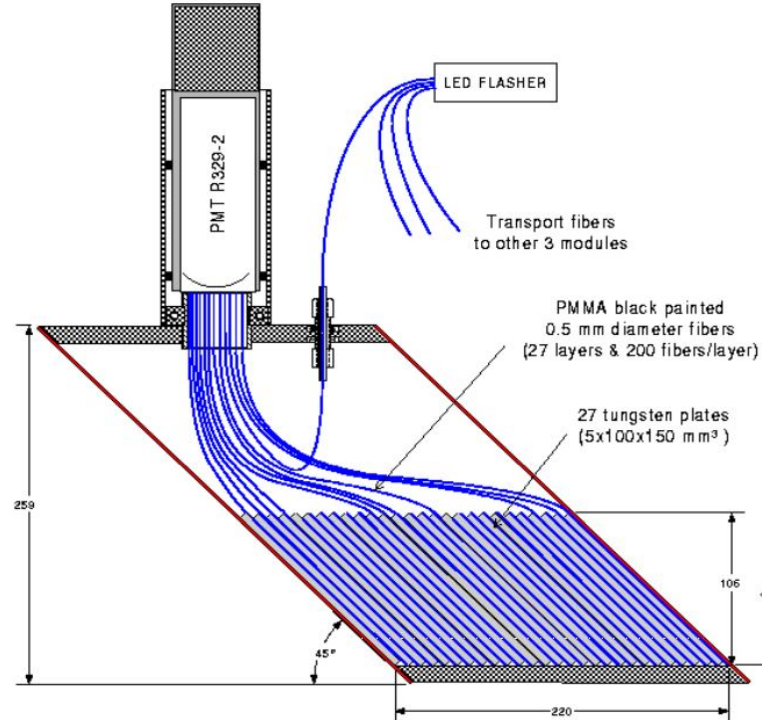


Figure 3.17: Schematic showing the layout of fiber optics in the ZDC

ZDC/SMD: Zero Degree Calorimeter and Shower Max Detectors

Crucial to the determination of event centrality is the ability to count the number of spectator particles. Since neutrons are have no charge we can place a calorimeter at high

rapidity behind an IR dipole magnet which we can use to "sweep" away charged particles like proton spectators and other charged track noise. The *Zero Degree Calorimeter*[16] is comprised of a ribbon of acrylic fiber optic strands sandwiched between two tungsten plates. The tungsten plates act as a dense absorber for the neutrons to hit and shower into resulting in detectable photon yield in the fiber optic ribbon. Sandwiched between modules of the ZDC is a hodoscope called the *Shower Max Detector* (SMD). The SMD is comprised of 21 0.5 cm x 0.5 cm scintillators and is used to measure the centroid of the shower in cartesian coordinates since the ZDC only measures energy[50]. The ZDC is used in conjunction with the BBC in order to determine centrality. Since more peripheral collisions mean more spectators and therefore more neutrons to hit the ZDC, the higher the energy measured by the ZDC the more peripheral the event (see fig 3.18[24]).

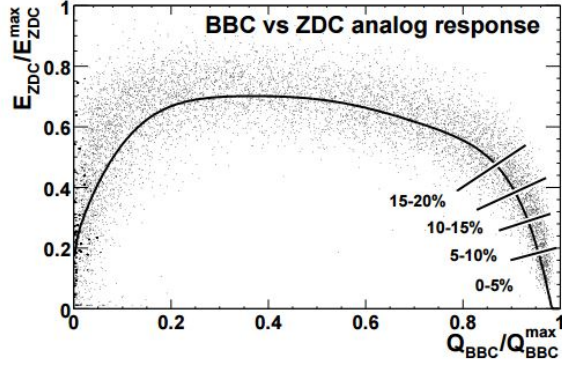


Figure 3.18: Centrality bins as determined by ZDC energy versus BBC charge sum[24]

MPC: Muon Piston Calorimeter

The *Muon Piston Calorimeter* (MPC) was a needed upgrade to PHENIX that provided calorimetry at very high rapidity[32]. It was installed in two parts: first in the south in 2005, then in the north in 2006 and was commisioned to reconstruct π^0 and η mesons for various forward physics analyses. Nestled in a gap in the piston of the Muon Magnet Arms, it provides full azimuthal coverage at $3.1 \leq |\eta| \leq 3.7$ (3.9 in the north) and is comprised of 196 (220 in the north) Lead Tungstate $PbWO_4$ crystal scintillator towers attached to avalanche photodiodes with preamplifiers to measure the electromagnetic shower photons. For this analysis, the MPC is used as a another measurement point for determining the reaction plane resolution correction.

RXNP: Reaction Plane Detector

Of particular interest for this analysis is the determination of the reaction plane. This will be discussed in further detail in a later chapter but I will cover the basics of the technical specifications here. The *Reaction Plane Detector* (RXNP) is a forward detector subsystem [10] with full azimuthal coverage in 12 segments. It has two segments in rapidity: an inner segment that covers $1.5 \leq \eta \leq 2.8$ and an outer segment that covers $1.0 \leq \eta \leq 1.5$. There are two RXNP detectors, one on each muon arm and all the segments are made of 2 cm thick plastic scintillators with a 2 cm layer of lead placed directly in front that acts as a converter causing all tracks to shower before hitting the scintillators [42].

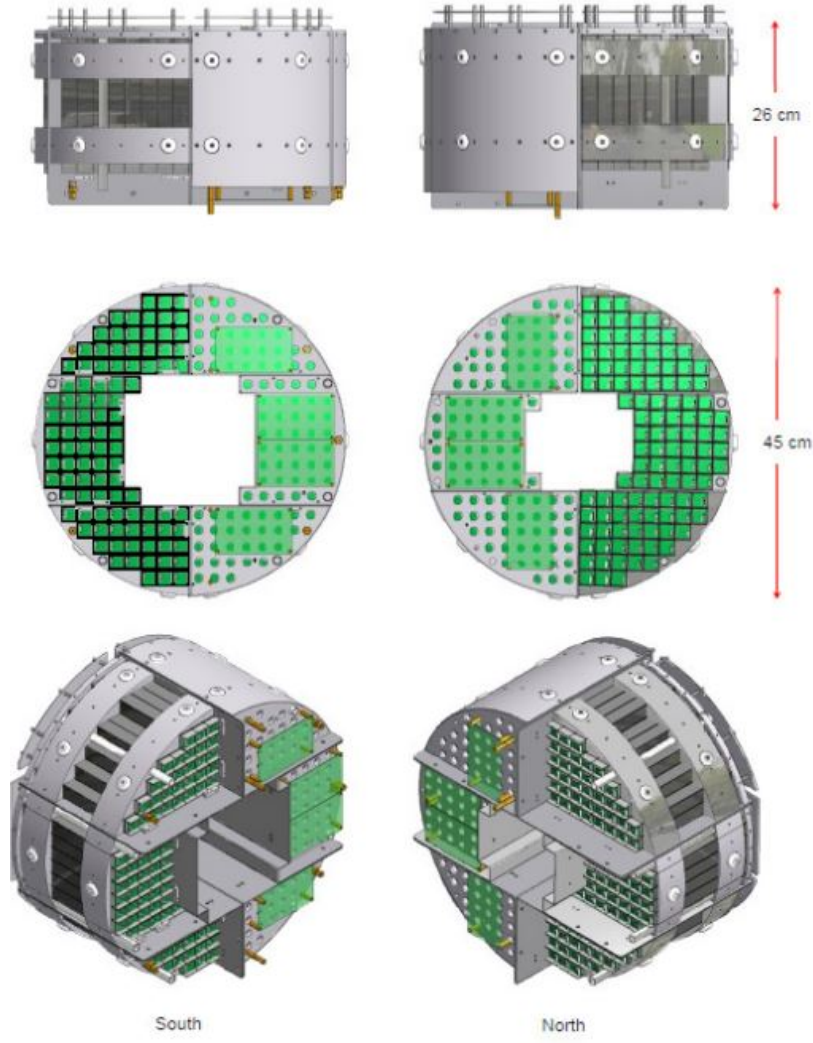


Figure 3.19: Schematic of the MPC

3.4 The DAQ

Each of these detector subsystems captures large amounts of data per event, and with the high luminosity of RHIC collisions in the millions of events per second, the events don't stop and wait for our computation systems, reconstruction, or network storage capabilities to catch up. The process of optimizing data collection created from a high-event-rate,

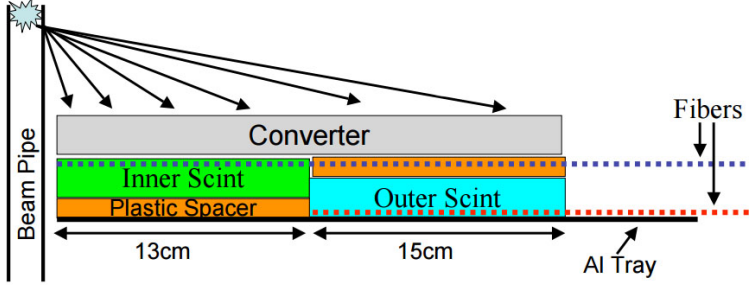


Figure 3.20: Cross sectional diagram of RXNP layers

high track multiplicity experiment, in the form of dozens and dozens of event and track variables collected by thousands of individual readout channels in a handful of individual subsystems, all funneled through a single data acquisition system that organizes everything and prepares the data for analysis is an intricate and chaotic symphony [41]. In order to do this, the DAQ breaks up the dataflow into smaller groups called *partitions* which are assembled from the smallest collection of data channels that can collect coherent data which we call *granules*. This partition model with granules allows PHENIX to collect even if some subsystems are down for whatever reason, an ability of great importance since funding for RHIC runs only allows us to have collisions for a few months a year, meaning that during data taking runs it is of utmost importance that we collect as much data as possible, stopping only to maintain the machinery. In practice this results in three 8 hour manned shifts a day, 7 days a week, for the duration of the run, where data taking only stops to re-inject RHIC with ions or on machine-wide agreed upon "access days" where all collaborations and the Collider-Accelerator Department agree to do their maintenance and repair work with no beam in RHIC.

Each granule consists of a Granule Timing Module (GTM), a Front End Module (FEM), and a Data Collection Module (DCM). The GTM synchronizes with the overall DAQ clock which is also synchronized with the RHIC clocks. These clocks optimize the amount of time the DAQ is actively processing data (called its *livetime*) so that the DAQ is live when bunches of ions are colliding at a maximum rate. The FEMs take the raw output from the preamplifiers in the individual readout channels of a detector subsystem and organizes them into coherent data packets which are transferred over fiber optics to the DCMs which act as a sort of stop light regulating the flow of data into buffers with the GTM clock so that data packets from various subsystems are in sync with each other from the same event as they go into the buffer boxes before being transferred to storage. Even with this timing and granule optimization, RHIC's event rate is so high that it is impossible to collect every track that passes through its subsystems. The means of making sure the only events we capture are events that contain rare processes is called *triggering*. There are many triggers at different levels of the DAQ, for example the aforementioned ERT is a trigger that allows us to only collect data on electron events, events that are of interest for dilepton analyses such as Drell-Yan and J/Psi measurements. The master trigger that sets the timing for the whole DAQ is called the Global Level 1 trigger or the GL1. It synchronizes large track multiplicity signal coincidence collected by the ZDC to the start of the event and checks to see if the buffers in each granule are clear. Other triggers such as *Local Level 1* (LL1) utilize data from the BBCs to ensure the event vertex happens within a region that will result in acceptable track acceptance.

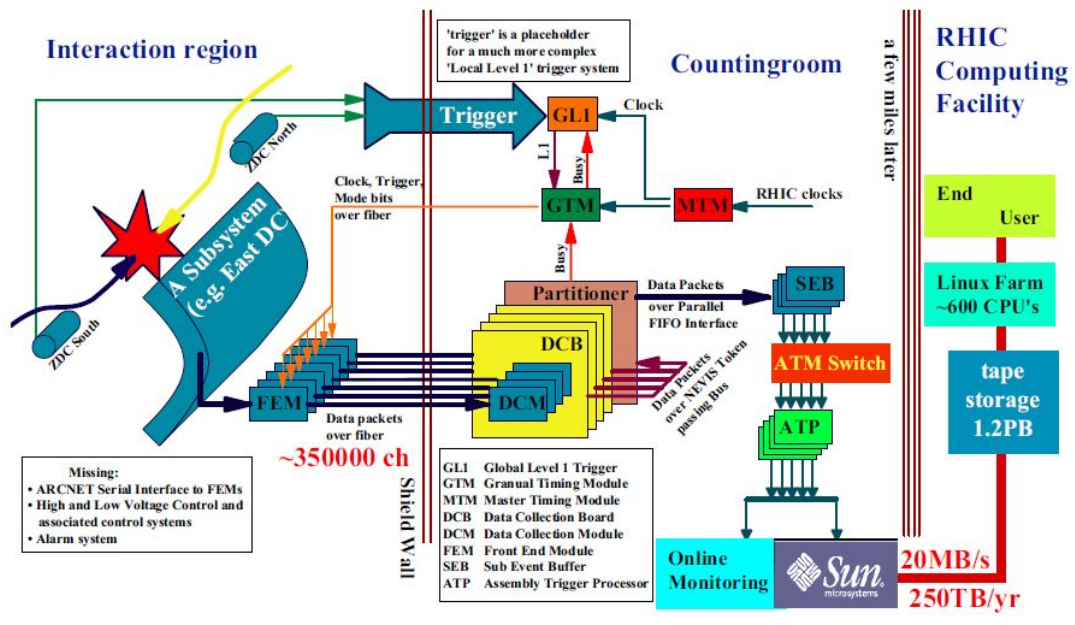


Figure 3.21: A diagram of the data flow of PHENIX data through the DAQ

Chapter 4

Heavy Ion Collisions: A Primer

4.1 Measurable Quantities

Due to the complexity inherent in colliding large nuclei containing a large number of nucleons (for instance 197 nucleons in Au) there is a multitude of metrics we can use to quantify the collision and the evolution of what happens after. For clarification, when talking about high energy physics analyses we refer to all data gathered from a single collision of two nucleons as an *event*. The location where the collision takes place is called the *event vertex* or often in collaboration literature since the z-axis is along the beam axis, the *z vertex*. The high luminosity of heavy ion collisions (437 nb^{-1} in 9 weeks for the data used in this analysis: Run 8 d+Au), produces a plethora of particles. As these particles travel from the event vertex through the various layers of detectors under the influence of the PHENIX magnetic field it leaves its own signature on each detector it passes through.

These signatures for each given particle can be matched to form a trajectory from the event vertex through PHENIX. The set of data corresponding to location, kinematic, and detector specific variables (i.e. charge deposited, clusters fired, Cherenkov photons, etc) is called a *track*. The determination of these variables is the topic of this chapter.

4.2 Event Characterization

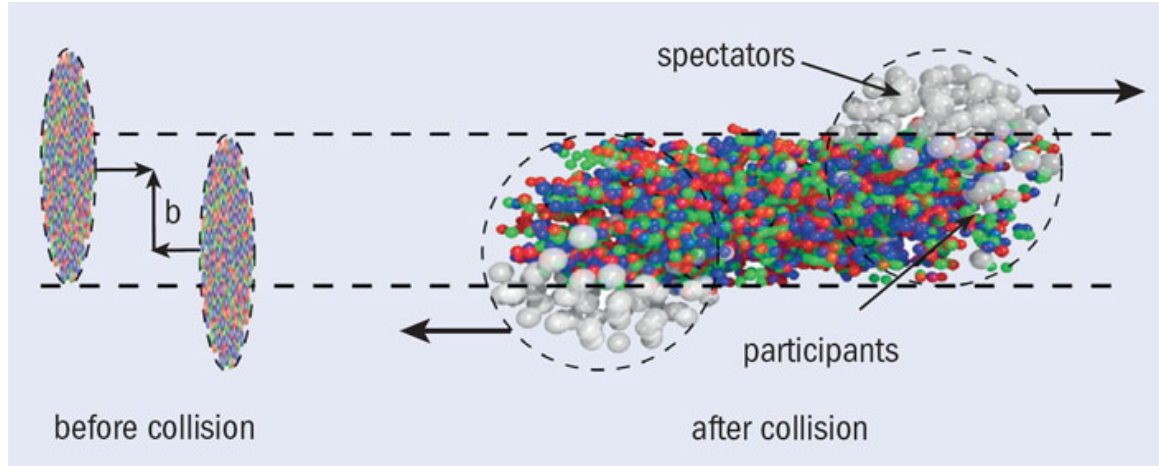
When describing a heavy ion collision it is useful to introduce quantities that describe the initial conditions of the interacting nucleons. The set of variables that correspond to these conditions are called the *event* or *global* variables. They are used to accurately locate where the event took place inside the detector and the geometric configuration of the nuclei at the time of collision. Since we are accelerating the ions to ultra relativistic speeds, by Heisenberg uncertainty we have very little idea before the collision what event parameters such as centrality and event plane will be. In practice, we use the remnants of the collisions to determine these event parameters and since the particles that are largely unperturbed by the collision are the ones that do not interact but rather continue down the beam pipe, these event variables reconstructed mostly by the extremely forward detectors: the *Beam-Beam Counters* (BBC) and the *Zero Degree Calorimeters*.

4.2.1 Centrality

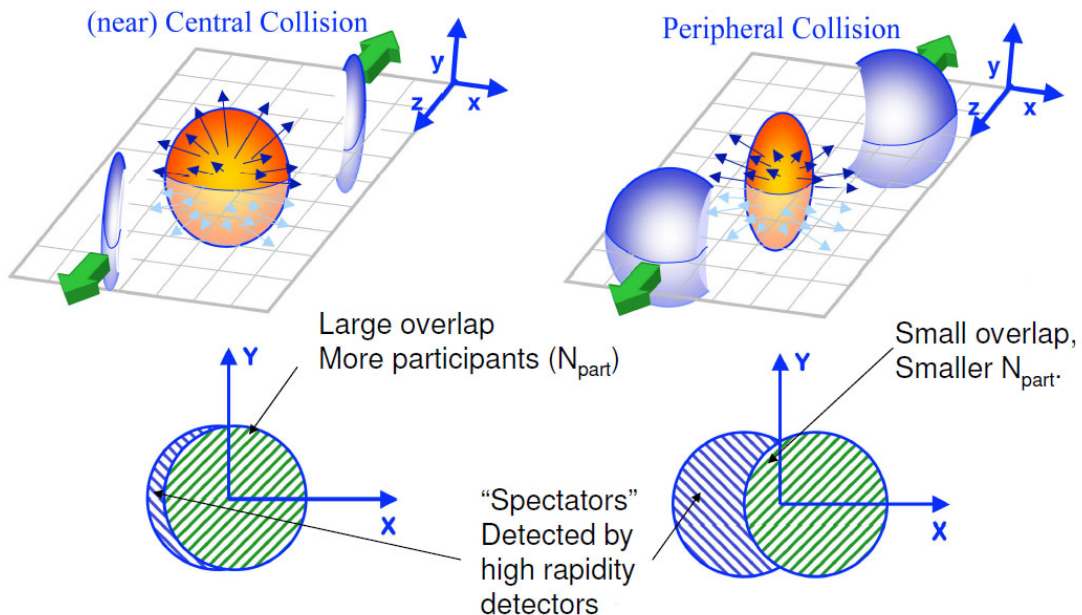
One such variable is *centrality* and is used to describe how "head-on" two ions collide, that is, do they collide with complete cross sectional overlap or do they just barely

glance each other. It is useful to quantify this overlap with a quantity called the *impact parameter*, \mathbf{b} . We define this impact parameter by measuring the distance between ion centers as depicted on the left-hand side of figure 6.1a. Note that the ions in this illustration appear squished in the x axis due to Lorentz contraction. Therefore, small impact parameters correspond to large ion-ion overlap in the collision and large impact parameters refer to glancing collisions. In heavy ion physics we call collisions with small impact parameters *central collisions* and those with large impact parameters *peripheral collisions*. Experimentally it is impossible to measure the distance between the two ion centers. In practice, centrality can also be quantified by the number of *participants*, or the number of nucleons that collide/interact with each other, versus the number of *spectators*, or the number of nucleons that do not collide. Since we know the number of total nucleons in each ion we can determine the number of participants by counting the number of spectators and subtracting them from the total number of nucleons. Colliding nucleons will produce particles in all directions however spectating nucleons will continue to travel down the beam pipe. We therefore can count the number of spectators by placing detectors at very high rapidity.

Extending the terminology from impact parameters, we then define a collision with a large number of participants to be a *central* collision and a collision with a small number of participants: a *peripheral* collision. These are quantified in percents, 0% being most central collisions i.e. highest number of participants, $b = 0$, two colliding ions overlap completely, and 100%: ions completely miss each other, i.e. there are no participants,



(a) Diagram showing impact parameter versus $N_{\text{spectators}}$ and $N_{\text{participants}}$ [49]



(b) Central vs Peripheral collisions, geometry of initial conditions.

Figure 4.1: Central versus peripheral ion collisions, BBC vs ZDC determination of

$b > R_{nucleus}$. Since ions are spherical in shape, centrality can be used as a way of describing the geometry of the collision region, central collisions have a more circular shape whereas peripheral collisions have a more almond-like shape.

4.2.2 Event Vertex and Timing

The event vertex is the location along the beam axis where the collision happened relative to the equidistant point between the two beam beam counters. That is, an event vertex value of 0 would be exactly in the center of the PHENIX detector, at equal distance from both BBCs. When a collision happens, the non colliding nucleons (spectators) continue to travel through the interaction region and are detected on the other side by the two BBCs. The time at which each cluster of spectators hits an individual BBC is measured. These two times, T_1 and T_2 respectively, can be used to calculate both the event vertex (z_{vtx}) and the initial time the collision takes place (T_0) as follows[36]:

$$z_{vtx} = \frac{T_1 - T_2}{2c} \quad \text{and} \quad T_0 = \frac{T_1 + T_2}{2} \quad (4.1)$$

This initial time is used to start the stopwatch of the event and is used in conjunction with other detectors to find the time a produced particle takes to travel from the vertex to a detector.

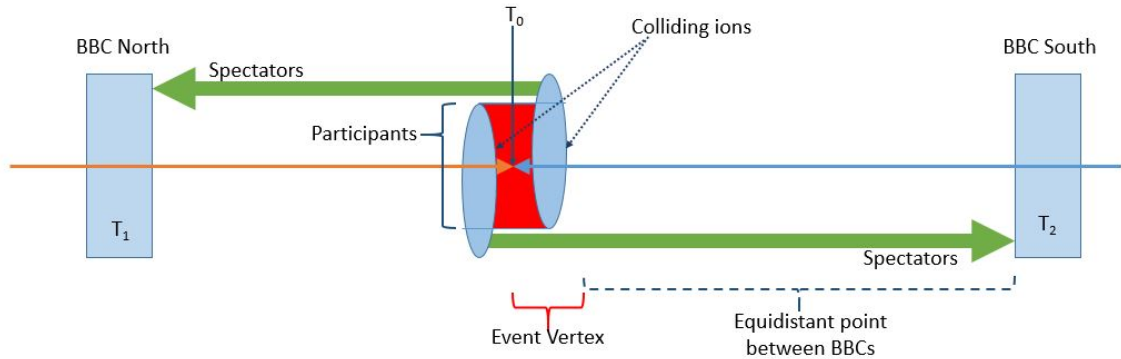


Figure 4.2: Diagram of BBC event characterization

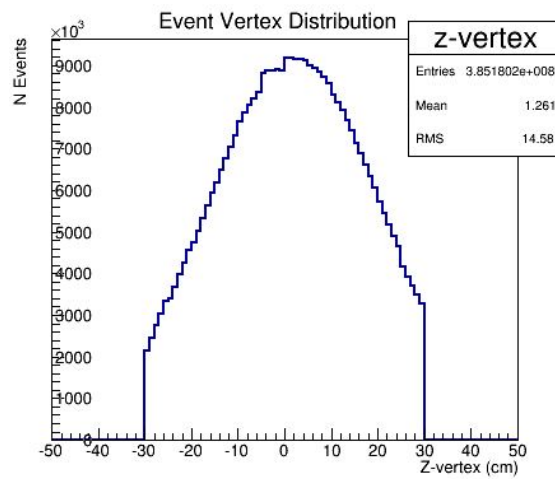


Figure 4.3: Event vertex distribution, there is an applied cut for all events to be $|z_{vtx}| \geq 30 \text{ cm}$.

4.3 Track Reconstruction

4.3.1 Variables for Track Selection

After the collision, particles fly outward from the vertex under the various mechanisms that take place within the formation and evolution of the QGP. Due to the high multiplicity of tracks resulting from a heavy ion collision and the various complexities that arise when using a multifaceted complicated detector system to reconstruct track trajectories, it is important to come up with a metric by which to measure the quality of the tracks in order to discern which tracks are able to be reconstructed cleanly versus those which, for whatever anomalous reasons, would not be advantageous to analyze.

Track Matching: DC and PC1

The process of determining the track trajectory through the PHENIX detector is called *track matching* and it utilizes the various layers of the Drift Chamber and Pad Chambers in concert to determine track momentum due to the varying curvature of tracks of different momenta traveling through a magnetic field. Tracks are reconstructed in the DC and PC1 using an algorithm called a *combinatorial Hough Transform* (CHT) which works very well for particles whose p_T is >200 MeV/c [36]. CHT is a methodical continuation of a *Hough Transform* which is a reconstruction algorithm used on a set of points that we know were created by single linear tracks in order to fit them with likely linear track candidates[38]. We use a parameter called track *quality* in order to quantify our confidence

that a CHT reconstructed track is a likely fit and it is a function of how well a reconstruction fits hits in the different tracking detector layers (X1, X2, and UVs in the DC, PC1). Since this is a combinatorial reconstruction, and since PHENIX doesn't exist in a vacuum, it is possible that other tracks such as cosmic events and background events are reconstructed. Because of this we also make the assumption that the origin of all probable tracks is the event vertex as determined by the BBC. This analysis uses tracks whose quality is > 10 which means that the accepted reconstructions contain at least one hit in X1 and X2 nets in the DC and a hit in PC1.

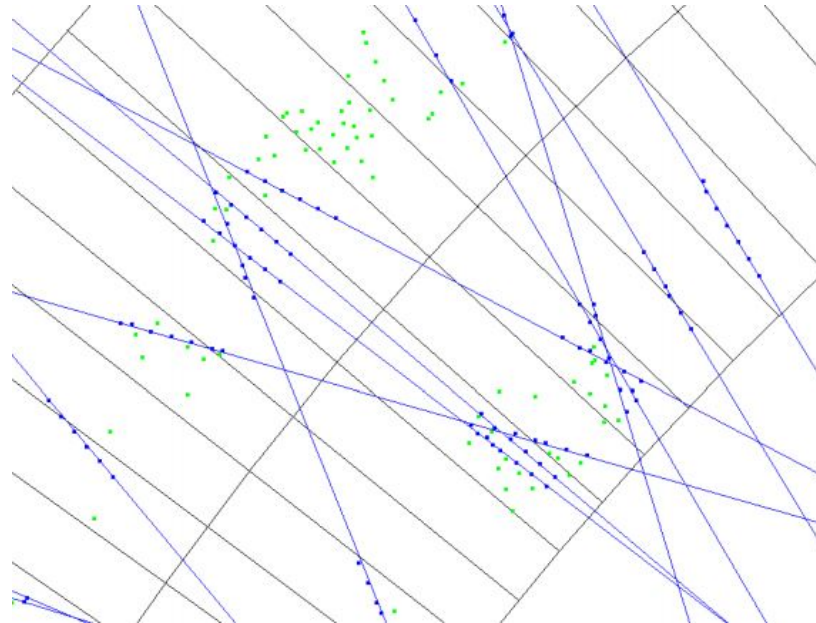


Figure 4.4: Hits in the DC matched to tracks using a Hough transform. Note that if we were to ignore the track lines it would just be a collection of points. CHT aims to provide these matched track lines by weighting combinatoric solutions by probability of it being a physical track.

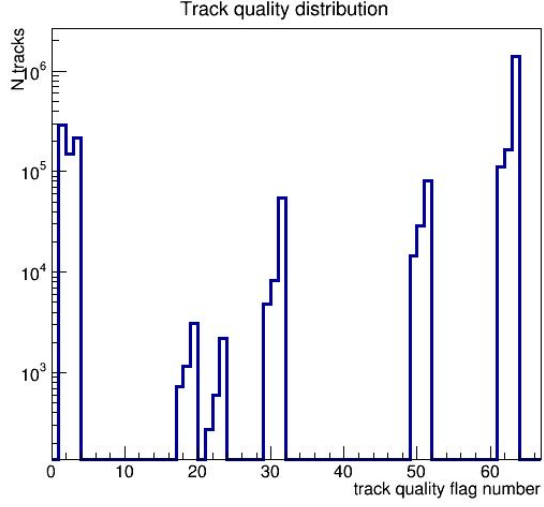


Figure 4.5: Distribution of track quality by track quality flag designation.

Track Matching: TOF and PC3

The magnetic field in PHENIX is strongest in the IR where $R < 2$ and negligible within the central arms[44]. Therefore once tracks are matched in the DC and through the PC1 we can project the track linearly through the rest of the central arms. We can then match these projections with hits in the PC3 and TOF as illustrated in figure 4.6 and assign variables (called *residuals*) to the difference between where a hit landed in the TOF/PC3 versus where it was projected to be, one in azimuthal angle ($d\phi$) and one along beam axis (dz). Therefore, track purity can be increased by setting limits to how large a track's residuals can be, usually in multiples of standard deviations from a probability distribution around the projected TOF/PC3 hit. For this analysis, the maximum residual allowed for both TOF and PC3 in both z and ϕ is three standard deviations (3σ) to allow for more statistics needed due to the lower multiplicity d+Au system (compared to larger

systems) while still maintaining good track reconstruction purity.

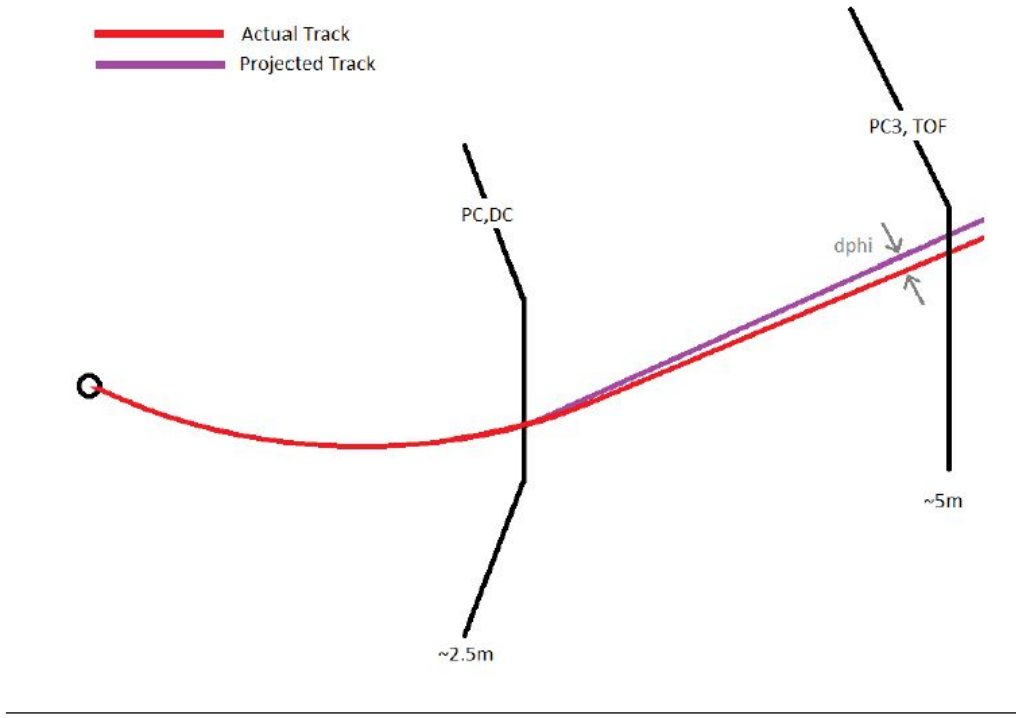


Figure 4.6: Diagram of track reconstruction by the DC/PC1 projected linearly onto the TOF/PC3. [45]

4.3.2 Particle Identification

Using the TOF detectors' high resolution timing measurements I am able to identify particles which have long lifetime relative to the event duration i.e. particles whose lifetimes are long enough such that they do not decay before leaving the detector. For this analysis, these particles of interest are the charged pions (π^\pm), charged kaons (k^\pm), and protons/antiprotons (p/\bar{p}). Since the masses of these particles are distinct, plotting

the momentum vs time of flight can show clear separation between pion, kaon, and proton signals (see fig 4.7).

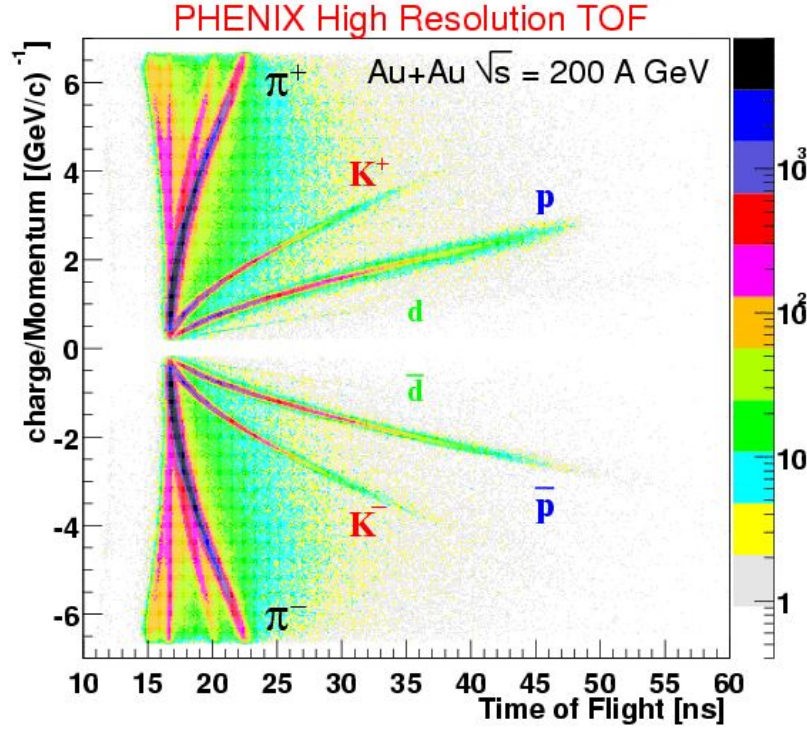


Figure 4.7: Particle separation in the TOF [31]

While visually the individual particle signatures are easily identifiable in this plot, computationally it is advantageous to convert units so that the signatures only depend on a single variable. After the collision, the QGP fireball is expanding rapidly however the constituent outgoing tracks traversing the distance scales in the detector do not experience appreciable deceleration. We know from basic kinematics that we can calculate the velocity, v , of an object traveling at a constant speed:

$$v = \frac{L}{t} \implies t = \frac{L}{v}, \quad (4.2)$$

where t is the time it takes to travel some path length, L . It is useful to define the relative speed of the particle compared to the speed of light, c , as $\beta = v/c$ and substitute it in for v . We also know from the relativistic identities that $\beta = p/E$ and $E^2 = p^2 + m^2$. The equation is then:

$$t = \frac{L}{v} = t = \frac{L}{c\beta} = \frac{L}{c} \frac{E}{p} = \frac{L}{c} \frac{\sqrt{p^2 + m^2}}{p}. \quad (4.3)$$

which can be solved for m^2 to give the mass vs time relation:

$$m^2 = p^2 \left\{ \frac{t^2}{L^2} - 1 \right\}. \quad (4.4)$$

Note that since the distance from the event vertex to the detector is constant and for that distance scale the velocity, and therefore also the momentum, can be treated as constant, m^2 depends on two constant terms if we take measurements in bins of p . Since we are talking about radially outward traveling tracks, this p is, in practice, p_T . Therefore if we do arithmetic on the track variables we are able to plot m^2 vs p_T which gives us a much easier to analyze representation of the individual particle signatures.

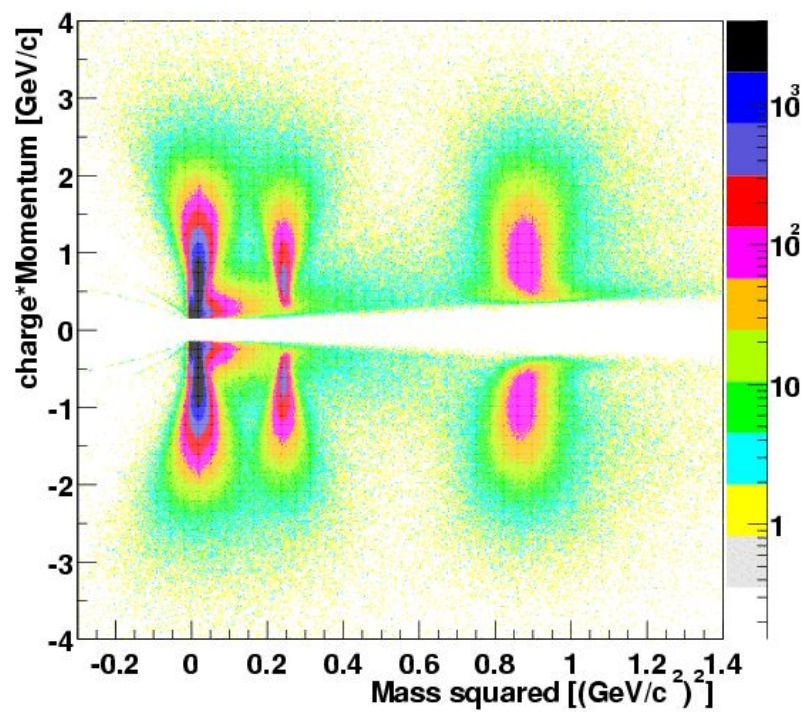


Figure 4.8: m^2 vs p_T showing clear constant separation of particle signatures. [31]

Chapter 5

Anisotropic Flow

In the moments immediately after a collision event, the outwardly expanding behavior of the newly formed QGP can be studied to better understand the QCD processes that take place both during formation as well what happens as this QGP dissipates. Though it expands in all directions it is the expansion about the azimuth that best describes the behavior of this fluid. Often physicists like to describe the behavior of phenomena using a series expansion of orthogonal functions. Since the azimuthal angle runs from 0 to 2π , this azimuthal expansion can be treated as a harmonic function which lends itself well to parameterization using a Fourier series. Recall that a Fourier series can approximate a function $f(x)$:

$$f(x) = \sum_{n=-\infty}^{\infty} A_n e^{i(2\pi n x/L)} \quad (5.1)$$

where

$$A_n = \frac{1}{L} \int_0^L f(x) e^{-i(2\pi n x/L)} dx \quad (5.2)$$

are said to be the Fourier **coefficients** or often, since they approximate harmonic functions, Fourier **harmonics**. It is a tautology that the exponential term can be written as the sum of a real cosine term and an imaginary sine term:

$$f(x) = \sum_{n=1}^{\infty} A_n \cos(2\pi n x/L) + i \sum_{n=1}^{\infty} B_n \sin(2\pi n x/L) \quad (5.3)$$

where

$$A_n = \frac{1}{L} \int_0^L f(x) \cos(2\pi n x/L) dx \quad (5.4)$$

and

$$B_n = \frac{1}{L} \int_0^L f(x) \sin(2\pi n x/L) dx \quad (5.5)$$

Since we define $\phi = 0$ to be along the waist of the ellipsoidal shaped QGP and not at the poles, odd function contributions (sine terms, B_n) to the Fourier series can all be ignored. Therefore if we wish to approximate the shape of the outgoing flow from the QGP we can define the rate of change of outgoing particle tracks vs transverse momentum and approximate it with a Fourier series. Flow anisotropy of the QGP can then be written as:

$$E \frac{d^3 N}{dp^3} = \frac{1}{2\pi} \frac{d^2 N}{p_T dp_T dy} \left(1 + \sum_{n=1}^{\infty} 2v_n \cos(n(\phi - \Psi_r)) \right), \quad (5.6)$$

where:

$$v_n = \left\langle \cos(n[\phi - \Psi_{RP}]) \right\rangle \quad (5.7)$$

are the n-th order Fourier coefficients that describe the azimuthal shape of the QGP's outward expansion and ϕ is the azimuthal angle with respect to the reaction plane. Each n-th order coefficient scales the amount of expansion that behaves like $\cos nx$.

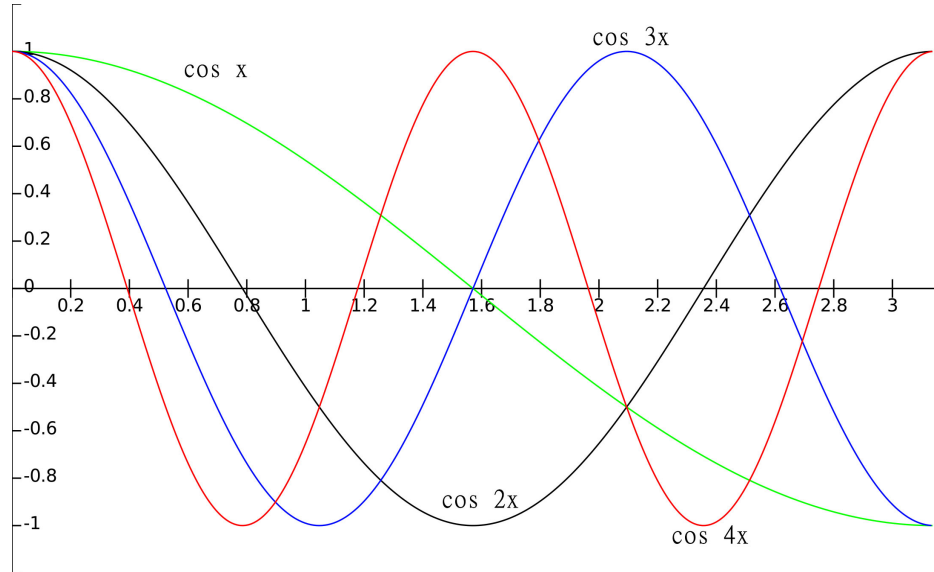


Figure 5.1: Plots of the first four harmonics of a cosine series

From studying the behavior of these various harmonics we can see that for $n = 1$, $\cos x$ is a maximum at $\phi = 0$ and a minimum at $\phi = \pi$ which would correspond to a preferential flow in the $\phi = 0$ direction. Therefore the $n = 1$ flow coefficient is often called *directed flow*. For the case of $n = 2$ we see that again there is a maximum at $\phi = 0$ and again at $\phi = \pi$ which corresponds to maximal flow at the waist of the ellipsoidal QGP. This expansion about the waist of the collision region results in an elliptical preferential flow,

a term which is shortened to *elliptic flow*. There are higher order harmonics which can describe various other phenomena of QGP flow which are beyond the scope of this analysis.

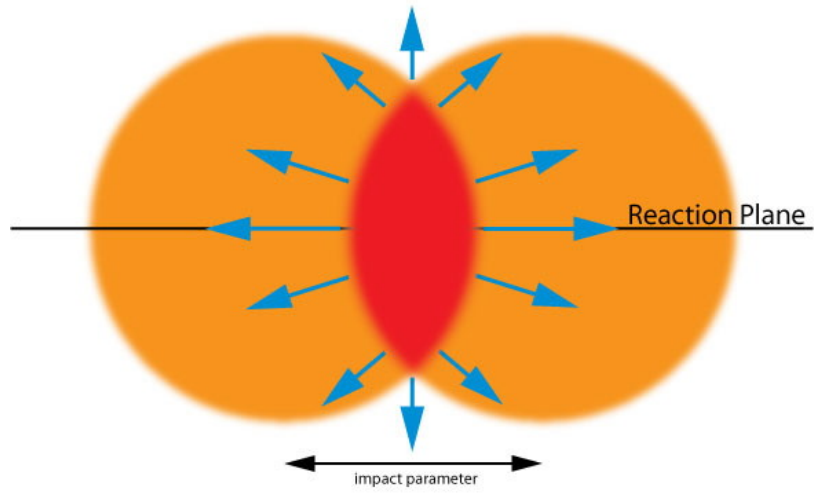
Chapter 6

Event Plane

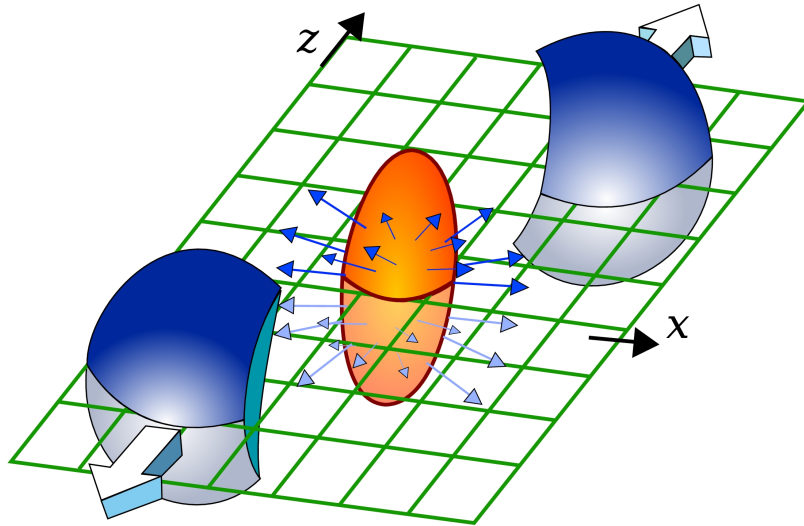
6.1 Determination of Event Plane

Pivotal to this analysis is the ability to determine an event characterization variable called the *Reaction* or *Event Plane*. Given the geometry of a heavy ion collision, we define the event plane as the two dimensional plane that bisects both ions equally through their centers as shown in 6.3. If we recall that the impact parameter is the distance between the two colliding ions' centers and we were to create a vector from this distance and we have a vector that represents the direction one of the ions is traveling down the beam axis, the plane containing both of these vectors is the Reaction/Event plane (it is irrelevant which direction the impact parameter vector points and which direction we pick to point the beam axis vector, this is merely for creating a plane).

In practice this plane is determined by detecting the spectator nucleons or high



(a) Two dimensional representation of the event/reaction plane. Recall the impact parameter is the distance between the two colliding ions' centers. In this illustration the orange spheres represent the ions, one is going into the page and one is coming out of and the red overlap is the matter created by the participant nucleons.



(b) A three dimensional render of the initial conditions just after a collision. The two blue spheres are the remnant spectator nucleons from the colliding ions, the orange/yellow ellipsoid is the nuclear matter created by the collision of participant nucleons. The green grid here represents the plane that bisects all three of these bodies which we call the event plane

Figure 6.1: Illustrations of the event plane in heavy ion collisions

multiplicity track signals at high rapidity using a detector with full azimuthal coverage. Ideal candidates for this are the BBC, the SMD, and the RXNP. Particle signals would appear in the Northern detector as a cluster of hits on one side in azimuth and in the Southern detector as a cluster of hits 180° azimuthal degrees across. The event plane can therefore be constructed using the locations of these signal clusters and creating a plane that bisects them (see fig. 6.2).

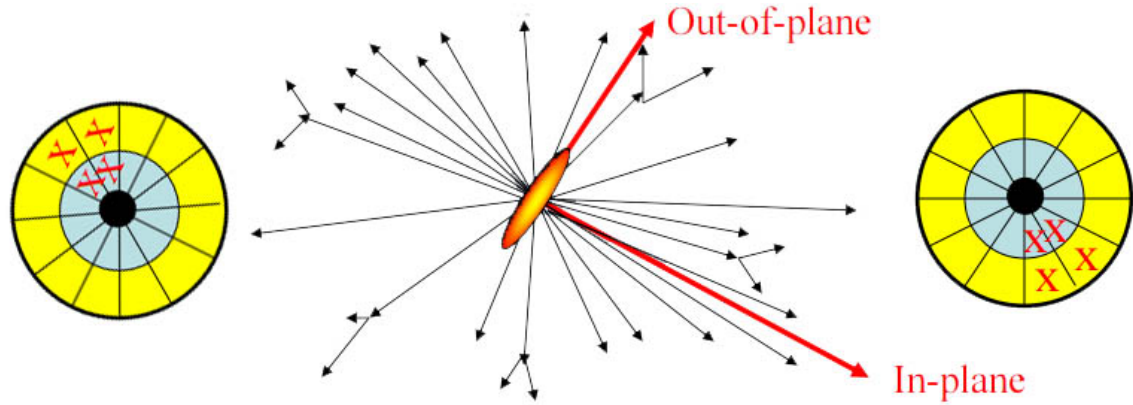


Figure 6.2: Cartoon of Event Plane determination with forward detectors [10]

6.2 Event Plane “Flattening”

Since we have little control over the precise impact parameter and event plane orientation for each collision, instead, data is taken and event plane orientations populate a distribution statistically and this distribution is non uniform. The process of making this distribution uniform in azimuth is called *flattening*.

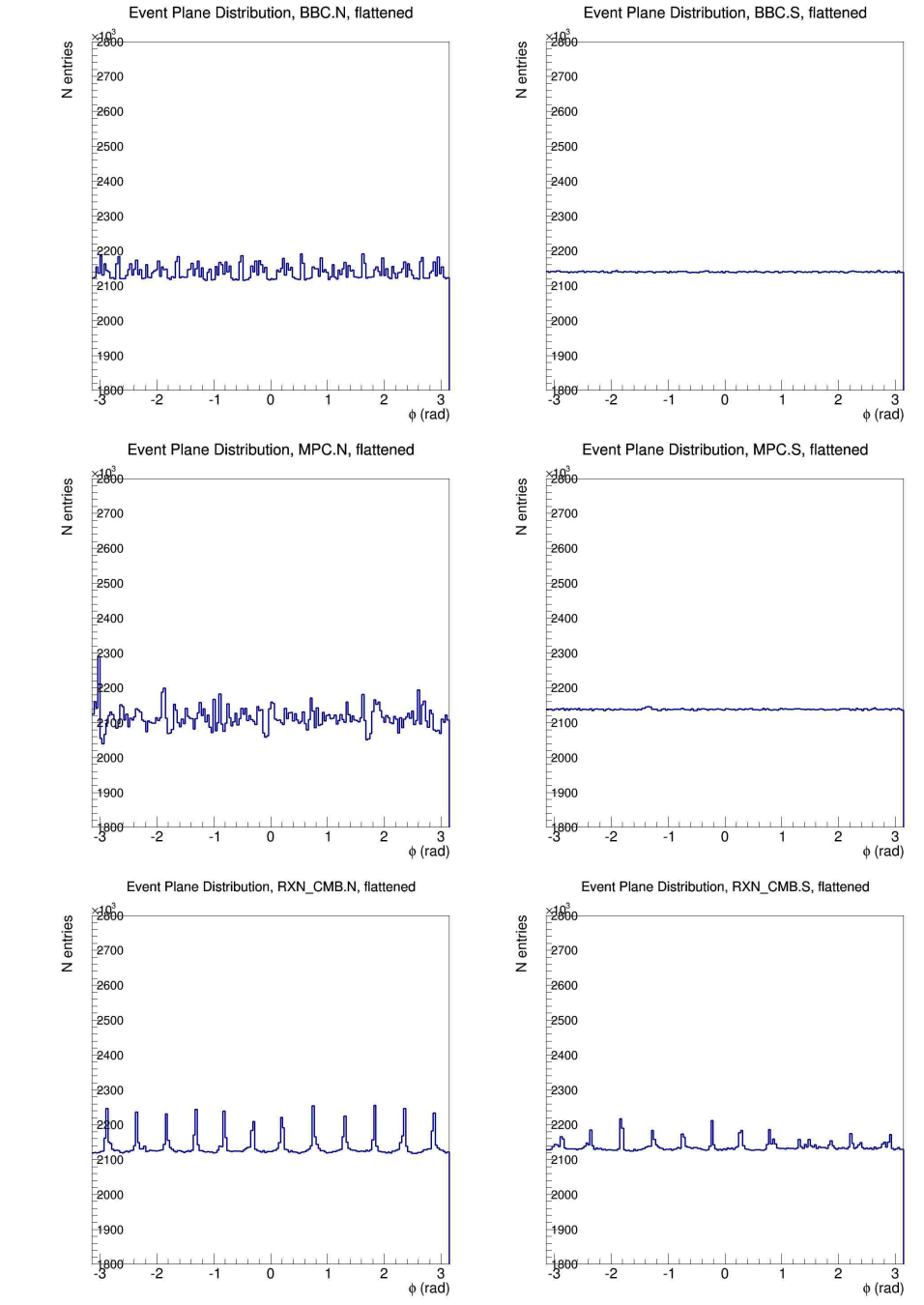


Figure 6.3: Flattened event plane distributions in the BBC, MPC, and RXNP. Note that this flattening is significantly better in the “gold-going” south arm.

Because the d+Au system is asymmetric by construction, track multiplicities on the north and south detectors are not the same. Rather, since gold ions have a considerably larger amount of nucleons than deuterons, it therefore has higher forward track multiplicity, and its event plane signature in the forward detectors is much stronger. In practice, the north side is the deuteron going side, and the south side is the gold going side. This can be seen clearly in figure 6.3 where the event plane is much easier to flatten in the south than in the north regardless of which detector subsystem is chosen.

6.3 Event Plane Resolution Correction

Since we have a finite number of readout channels in any of the chosen detectors capable of measuring the event plane, our track multiplicity distribution is not smooth and continuous, rather there is an associated resolution limitation for each measurement made with a specific detector. This resolution limitation affects how well we can measure flow anisotropies, and because of the nature and shape of various Fourier harmonics, higher harmonics are more strongly affected by resolution limitations since their shape is quickly varying over the azimuthal distribution compared to lower harmonics. Because of this, resolution corrections must be calculated for each harmonic separately. The apparatus make different measurements of the event plane using different Fourier harmonics and so the resolution corrections made for each detector are coupled to the Fourier harmonic used by the detector to find the event plane, that is to say, the Harmonic dependence and detector resolution dependence of the resolution correction are not separable. Additionally, by col-

lision geometry, the ability to determine each correction is dependent on event centrality, implying that these corrections must be made for each centrality bin as well. The measured flow anisotropy decreases as the ability to resolve changes in flow decreases so we correct this resolution error by defining some multiplicative scaling such that:

$$v_n = \frac{v_n^A}{Res(\Psi_n^A)} \quad (6.1)$$

where v_n^A is the n^{th} order anisotropic flow coefficient measured with some detector, arbitrarily designated A, and $Res(\Psi_n^A)$ is a single valued correction factor for the v_n measurement using a specific detector and a single bin in centrality. Since device resolution is independent of particle species, we do not need to calculate a different correction for each particle flow.

The method of determining resolution correction used for this analysis is called the *Three Subevent Method* and can be calculated by comparing the event plane measured with one detector with measurements made by two other detectors, let's call the detector of interest: detector A, and the other two detectors B and C respectively. It can be shown [40] that we can define this correction as:

$$Res\{n\Psi_n^A\} = \sqrt{\frac{\langle \cos(n[\Psi_n^A - \Psi_n^B]) \rangle \langle \cos(n[\Psi_n^A - \Psi_n^C]) \rangle}{\langle \cos(n[\Psi_n^B - \Psi_n^C]) \rangle}} \quad (6.2)$$

where Ψ_n^X is the event plane as measured with detector X using the n^{th} Fourier harmonic.

Chapter 7

Results

7.1 Charged Track v_2

Here I present measurements of elliptic flow in $\sqrt{s_{NN}} = 200$ GeV d+Au collisions.

Since the flattening the event plane redistributes the event plane distribution, the unidentified charged track flow can be measured directly from plots of $d\phi$. Recall that the Fourier coefficients parameterize the shape of the azimuthal hydrodynamic flow by describing it as a superposition of cosine harmonics:

$$\frac{d^2N}{dp^2} \propto v_0 + v_1 \cos(\phi - \Psi_r) + v_2 \cos(2(\phi - \Psi_r)) + v_3 \cos(3(\phi - \Psi_r)) \dots \quad (7.1)$$

where v_0 , v_1 , v_2 , and v_3 are the values that scale the amount of spherical, directed, elliptic, and triangular flow respectively, and are indicative of collective behavior of the nuclear matter. To measure the elliptic flow we count number of tracks in bins of $d\phi$ and fit this

with a function of the form:

$$f(x) = A[1 + B \cos 2x] \quad (7.2)$$

where A is a term that accounts for an overall shift in the number of tracks due to statistics and B is our v_2 . Due to the asymmetric nature of d+Au collisions, event plane calculations are significantly better on the Au going side, because of this, the plots (figures D.1-D.4 in Appendix D) were made using the BBC South determination of the event plane. They are binned in 5% bins of centrality up to 15%, at which point statistics requires the remainder of data to be binned 10%-25%. This $d\phi$ plot can then be fit with the aforementioned cosine function to calculate the elliptic flow measurements vs centrality for all charged tracks which is shown in figure 7.1.

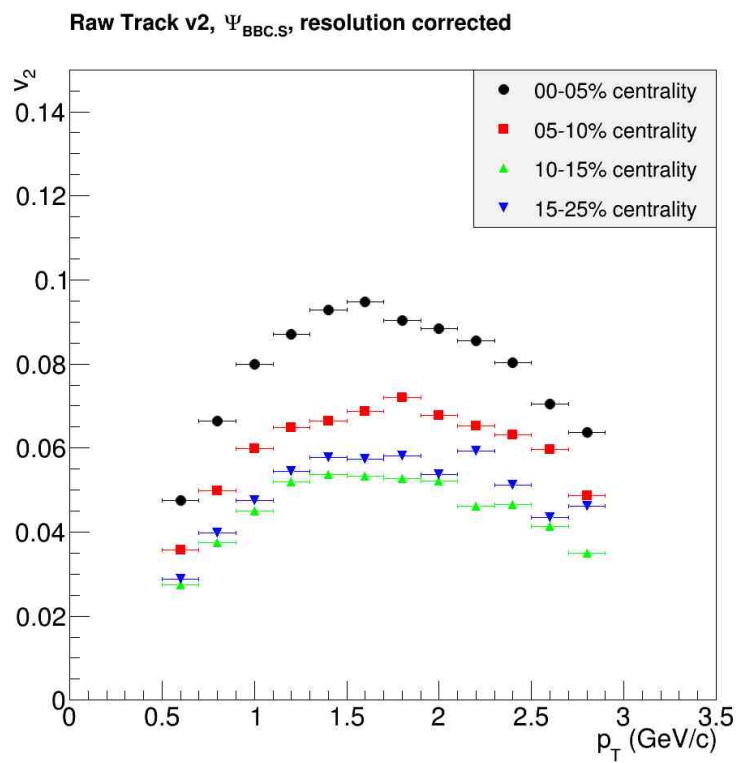


Figure 7.1: Charged track elliptic flow, $\sqrt{s_{NN}} = 200$ GeV $d + Au$ collisions

7.2 Separating Particle Signals

Following the flattening of the event plane and checking for calibration of the TOF detector, I can plot a 2-d histogram of p_T vs m^2 following the method described in section 4.3.2 to identify the species of charged track hits in the TOF. In order to do a statistical analysis, these 2-d histograms will need to be “sliced” into a series of 1-d histograms in small bins of p_T which will give a 3-peak histogram showing the signatures of the pion, kaon, and proton which are Gaussian in shape. The widths and heights of these particle peaks will change and overlap in various ways over the variance of p_t , because of this I will divide the p_T range into three ranges which will be analyzed with different methods. The Gaussians are then integrated to calculate the particle yield for each species. Integration bounds can be set to increase track ID purity at the expense of statistics and vice versa. As a QA tool means and widths across each bin in $d\phi$ are plotted and set to be flat as there should not be a shift in either of those for a set bin of p_T . The yields from the integrated Gaussians are then fit with the Fourier function to determine the 2nd harmonic coefficient as per equation 7.2.

7.2.1 Single Gaussians

For $p_T < 1.3$, there is enough separation between the pion, kaon, and proton signals to fit each particle peak with a single Gaussian. This will take the form:

$$f(x) = \frac{N_0}{\sqrt{2\pi}\sigma^2} e^{-\frac{(x-\mu)^2}{2\sigma^2}}, \quad (7.3)$$

where σ is the width of the identified particle peak, μ is the location of the peak's mean along the x-axis, and N_0 is the height of the peak. The Gaussians are then integrated from $\mu - 2\sigma$ to $\mu + 2\sigma$ for each particle distribution, i.e. the number of particles of each type are counted out to two standard deviations around their mean mass. (full fits and data in Appendix D.2.1)

7.2.2 Gaussian Mixing

For $1.3 < p_T < 2.1$, kaon and pion mass distributions become overlapped. To decouple the two I use a mixed Gaussian model in order to fit the tails of the distributions without over counting. This function takes the form:

$$f(x) = \frac{1}{\sqrt{2\pi}} \left(\frac{N_\pi}{\sigma_\pi} e^{-\frac{(x-\mu_\pi)^2}{2\sigma_\pi^2}} + \frac{N_k}{\sigma_\pi - \sigma_k} e^{-\frac{(x-\mu_k)^2}{2(\sigma_\pi - \sigma_k)^2}} \right), \quad (7.4)$$

where N_x , μ_x , and σ_x are the parameters that describe the shape of particle x 's (π/k) distribution. These parameters can then be used to reconstruct single Gaussian distributions which are then integrated out to 2σ as mentioned in the previous section. (full fits and data in Appendix D.2.3)

7.2.3 ACC as a Particle Discriminator

Above $p_T = 2.3$ pion/kaon mixing becomes inseparable. In this region I utilize the

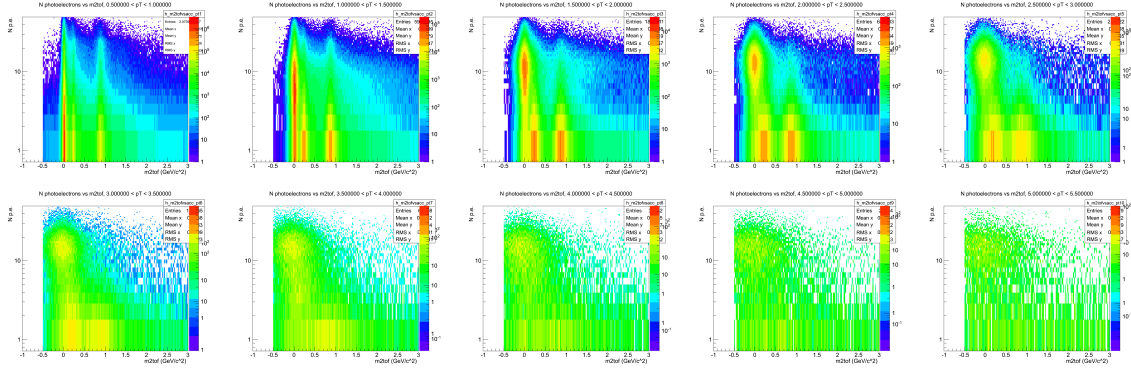


Figure 7.2: Number of ACC photoelectrons vs m^2 in bins of p_T

ACC to trigger and veto pion and kaon events respectively by setting Cherenkov radiation threshold which is done by counting the number of photoelectrons collected by the two PMTs on each channel of the ACC. This utilization of the ACC therefore sorts tracks into two separate histograms, one with an *ACC fire* condition that contains mostly pions with minimal kaon contamination, and another with an *ACC veto* condition that contains the remaining kaons and protons with minimal pion contamination. These two histograms can then be analyzed with single Gaussians since the distributions are now separate. This ACC threshold is the sum of the number of photoelectrons ($N_{p.e.}$) in both PMTs. The total number of $N_{p.e.}$ is plotted versus m^2 in a 2-d histogram and a threshold is set in order for there to be a maximum separation between pion and kaon signals. This 2-d histogram is then projected from the threshold up to the highest $N_{p.e.}$ bin for the pions and projected from the threshold down to the lowest $N_{p.e.}$ bin for kaons and protons. These 1-d projections can then be modeled with either single Gaussians (pions) or mixed Gaussians (kaons and protons). (full fits and data in Appendix D.2.4)

7.2.4 High p_T : Fixed Width and Mean

Above $p_T=3.5$, the strength of particle signatures decreases, approaching level of the background, making individual peaks hard to fit. Though statistics may be very low in the six bins of $d\phi$, there are still enough statistics if all the bins are combined. Means and widths of particle signals should only depend on p_T and not on $d\phi$, therefore I can merge all $d\phi$ bins to calculate the statistical mean and width for each particle species at a given p_T and fix these means and widths as constant for each bin in $d\phi$ and allow the heights of the Gaussians to dictate the yield.

7.3 Identified Particle v_2

The end result of each of these particle identification methods is a Yield vs $d\phi$ plot for the three particle species. These plots can be treated like the $dN/d\phi$ vs $d\phi$ plots that provided the charged track v_2 measurement which was acquired by fitting with the functional form of equation 7.2. The parameters of this Fourier fit are the uncorrected v_2 coefficients. Dividing by the event plane resolution gives the corrected v_2

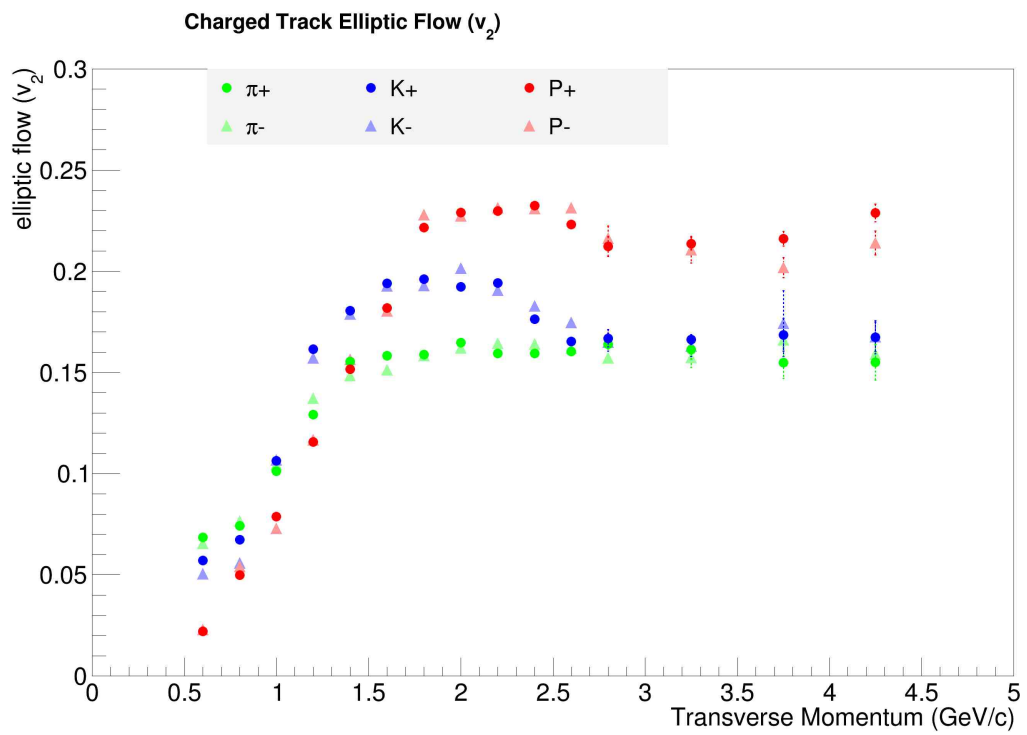


Figure 7.3: π^\pm , k^\pm , p/\bar{p} elliptic flow

Chapter 8

Error Analysis and Quality

Assurance

There are various sources of systematic error that could contribute to uncertainty in this measurement. These include certainty in how the event plane was determined (sect. 8.1), how well the event centrality can be determined (sect. 8.2), various uncertainties pertaining to the identification of the particles (sect. 8.3), and the effects of detector acceptance (sect. 8.4). In this chapter I will quantify the uncertainty for each of these contributions and then use these values to find the possible variance in the flow measurement due to these uncertainties. It will be shown that event plane resolution and PID systematics due to Gaussian fitting dominate and other errors are negligible.

Any uncertainty that would affect the value of this flow measurement would do so in one of two ways: either by shifting individual v_2 data points (changing inherent shape

of the data set) or by changing the overall scaling of the whole measurement in a net direction (simple scaling of entire data set). Errors that would simply shift the value of v_2 are the event plane resolution and centrality determination errors. Errors that would shift individual points consist of the various PID uncertainties and detector acceptance effects. The way the uncertainties in this category would shift individual data points is by changing the shape of the particle yield distribution in $d\phi$. Recall that there are two terms that parametrize the shape of the yield in $d\phi$:

$$yield(d\phi) = v_0[1 + v_2 \cos 2d\phi] \quad (8.1)$$

In this equation, v_0 corresponds to an overall shift in the function, that is to say it describes the up-and-down displacement of the whole curve and doesn't affect the general shape of it. The remaining parameter, v_2 , describes the shape of the yield distribution in $d\phi$. Changes to the shape of this distribution happen when yield values are perturbed up or down in individual bins of $d\phi$ which results in a change in the associated v_2 . In order to study the strength of v_2 -affecting uncertainties I will apply the variances discussed in this chapter to individual points in the yield vs $d\phi$ distribution and re-fit in order to see the variances' effect on the flow coefficient.

Table 8.1: Event Plane Resolution for MPC, 0-5% centrality

Detectors Used	$\Psi_{RES.3SE}$
MPC, SMD, RXNIN	0.200718 ± 0.0001312
MPC, SMD, RXNOUT	0.261658 ± 0.0001312
MPC, SMD, RXNCMB	0.241446 ± 0.0001311
$\langle \Psi_{RES.MPC} \rangle$	0.234607
$\sigma_{RES.MPC}$	0.03104

8.1 Event Plane Resolution

As mentioned in section 6.3, the limitations of the detectors to precisely resolve the event plane result in a weaker anisotropic flow measurement which is exacerbated by the asymmetric nature of the d+Au system. By RHIC convention and PHENIX construction, the north arm is the “deuteron-going” side and the south side is the “gold-going” side, i.e. spectators from the deuteron beam hit the north arm and spectators from the gold beam hit the south arm. The significant increase in the number of nucleons in a gold nucleus result in higher track multiplicity which is used to determine the event plane. Because of this, the event plane determination using south arm detectors is significantly easier and more accurate, as evident in fig 6.3. This combination of higher track multiplicity in the south arm and a smooth flattened event plane distribution in the MPC makes it a good choice for event plane determination. Furthermore, a combinatoric calculation of the event plane resolution in the various detectors shows that the MPC has the best resolution of all the detectors possible. Additional independent measurements of the event plane are used to correct further resolution limitations in the MPC (using the Three Subevent Method, eqn. 6.2). The Event Plane resolution measurements displayed in table 8.1 were determined

using 5 detectors: the SMD, MPC, inner RXNP, outer RXNP, and the combined RXNP. Since any 3 detectors can be used to determine an event plane resolution correction, this correction can be calculated for the MPC using various detectors as subevent comparisons. Doing so gives a 3% variance on the MPC resolution correction.

8.2 Centrality Resolution

Flow is at its strongest in most central collisions and uncertainty in the determination of centrality could affect the flow measurement. Collaborators have addressed the centrality categorization in Run 8 d+Au[37] by correlating the charge sum in the BBC to the number of binary collisions ($\langle N_{coll} \rangle$). They found a systematic uncertainty of 7% on the determination of $\langle N_{coll} \rangle$ for this data set for centralities from 0-20%. Furthermore, centrality systematic do little to change the shape of the yield vs $d\phi$ distribution and only increase the statistics. As a check, I performed the flow measurement on a centrality range from 0-4% and 0-6% to see if the value was changed appreciably or not. In figure 8.1 I have plotted the fractional deviation:

$$\sigma_{sys}^{centrality} = \left| \frac{v_2^{0-5\%} - v_2^{0-4\%(6\%)}}{v_2^{0-5\%}} \right|, \quad (8.2)$$

as a measure of the effect of varying size of the centrality bin on the flow measurement. This deviation was maximally 5% and appeared to have no correlation to the p_T of the tracks.

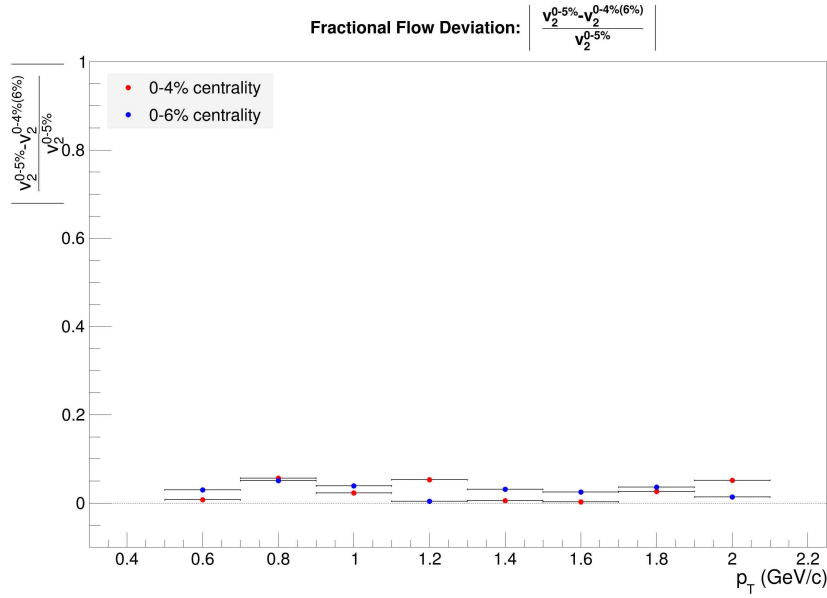


Figure 8.1: Centrality uncertainty contribution to Systematic Error

8.3 Particle Identification Methods

There are three sources of error that can come from the identification of these particle species. Since the separation of signals is dependent on the time of flight and the momentum, uncertainty in either of these propagates to the error in identification. Furthermore, imperfections in the goodness of fit for the Gaussian models can systematically miscount particles contributing to further uncertainty in flow coefficients.

8.3.1 Momentum Uncertainty

Track momentum is determined by track curvature in the DC/PC1 as described in section 4.3. Track curvature and certainty of this calculation is correlated to the ability to match hits in the DC and PC which is quantified by the *track quality* designation. As

mentioned, only tracks which have at least 3 hits in the DC and PC1 are accepted for analysis. Additionally, TOF and PC3 tracking adds additional confidence to the tracing of individual hits to reconstructed tracks. Track projections that pass the quality cut in the PC1 are projected onto the TOF and PC3 and only hits that fall within 3σ of the projected hit are accepted for analysis. Furthermore momentum reconstruction resolution has been studied with single particle simulations[36]. This resolution was shown to be linear in p_T with the highest p_T bin used in this analysis (5 GeV/c) having a resolution of 2%.

8.3.2 TOF Timing

Since the TOF boasts a very high timing resolution and since the preamplifier gains, cable lengths, and various other systematics can affect the timing measurement from strip to strip, it is important to calibrate the response across all the strips in the TOF. Conventionally, the tracks are shifted to some expected value. Since pions are by far the most plentiful particles created in heavy ion collisions, we pick them to be our normalization. Specifically the track time distribution is plotted for each strip individually. We know the start of the event time as given by the BBC and we know the expected time of flight for a pion (t_π) of mass m_π with a measured momentum, p :

$$t_\pi = \sqrt{\frac{m_\pi}{p^2} + \frac{1}{c^2}}. \quad (8.3)$$

Each strip is then fit with a normal distribution and the distance from the mean to $t = 0$ is the timing offset () for the strip. This offset is then applied to each track's

measured time:

$$\Delta t = t_{TOF\ measured} - t_{collision/BBC} - t_\pi \quad (8.4)$$

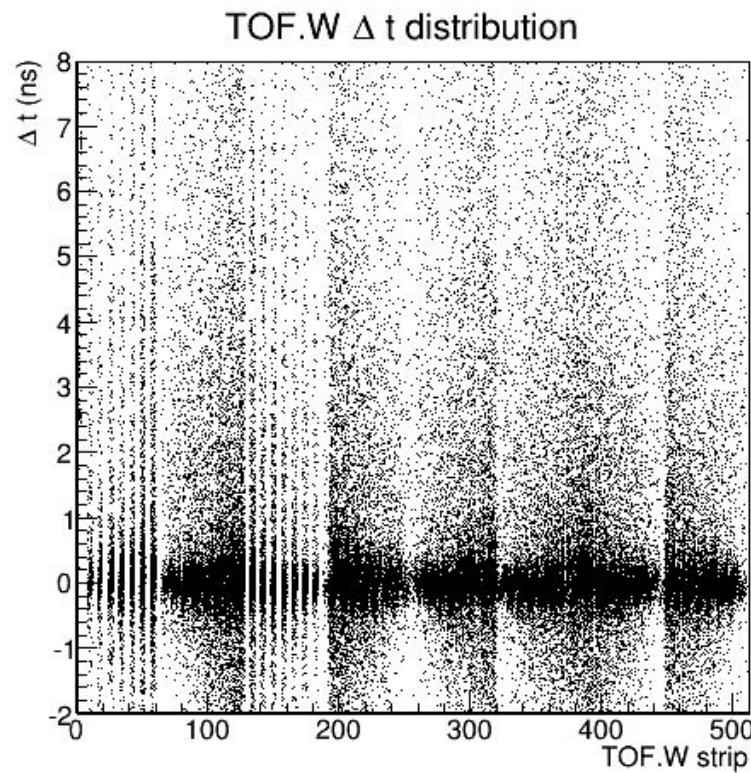


Figure 8.2: Timing QA in the TOF.W, Δt vs TOF.W strip id

Given the TOFW's known resolution of $\sim 80ps$, if we propagate this error through eqn. 4.4 with the known distance from the vertex of the TOF.W and a maximal p_T value for this analysis of 5 GeV/c, the maximum variance in m due to resolution is ± 2 eV/c²) which, when compared to the smallest mass measured ($m_\pi \approx 139$ MeV/c²), is negligible.

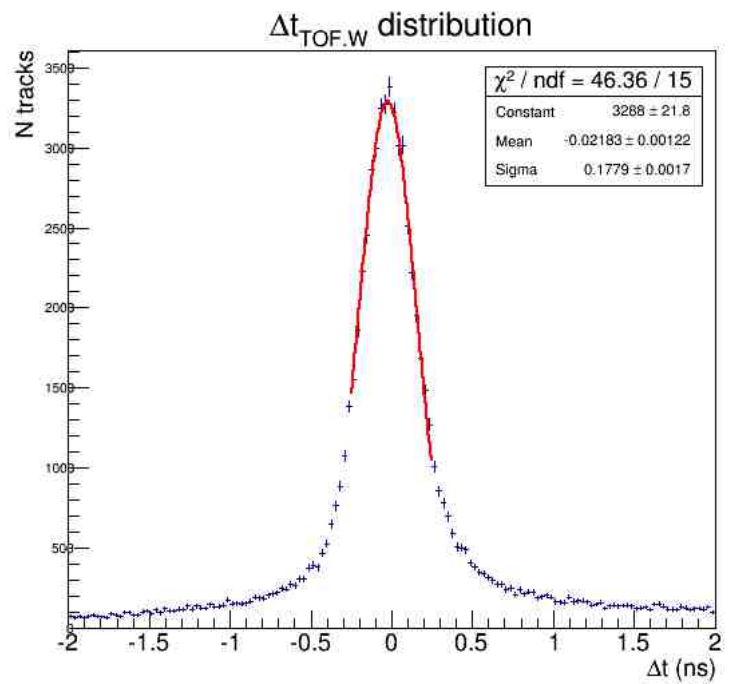


Figure 8.3: Systematic Timing Offset in the TOF.W

Furthermore, the systematic offset of the detector after calibration is 21 ps, well below the TOFW's resolution limitation (fig. 8.3).

8.3.3 Uncertainties from Gaussian Models

Single and Mixed Gaussians, no ACC, $p_T \leq 2.1 \text{ GeV}/c$

Species purity is integrated out to 2σ which accounts for 95.45% of particles about the mean of their distribution. Therefore systematics due to mixing in the tails of the particle distributions is at most 4.55%. Gaussian distributions do not perfectly match the particle distributions, often there is a trade off between fitting the shape of the peak or the shape of the tails. Given the the $2 - \sigma$ integration of the Gaussians, fitting the shape of the peaks took priority as the tails would contribute very minimally. This systematic uncertainty in the tails always *under* counts the number of particles in a distribution, however it can be seen from inspection (see App. D) that and over and under counting done by the models is uniform across each bin in $d\phi$ for within the same bin of p_T . Any systematic over/under counting such as this only serves to shift the y-position of the flow curve a net value up or down without changing the value of the harmonic. This appears to remain true for $p_T \leq 2.1 \text{ GeV}/c$. There are a few instances where fitting algorithms appear to have not matched the shape of the peaks perfectly but the functions fit nicely through the waist of the distribution. Each of these bins were inspected and allowed to vary by hand to fit various misshapen regions of the distributions. The maximal variance in the yield from the fit functions was 2% for the pions and kaons and <1% for the protons in this

range of p_T .

ACC Meson Separation and Gaussian Tail Cross Contamination, $2.1 \leq p_T \leq 2.9$

For $p_T \geq 2.1 GeV/c$, the ACC is used to separate pions from kaons and protons. Over/under counting in the tails is still the most likely place for systematic errors to accrue and this effect is strongest in the kaons since the ACC threshold still allows some pion contamination. Because of this, fitting the peaks and the right side waist and tail of the kaon distributions for ACC vetoed tracks took priority. In the lower bound of this p_T range, kaons maintain good separation from protons, however as the p_T increases there is some species contamination in the tails. This is accounted for in two ways. Firstly, as with the low $p_T \pi/k$, mixing happens in the extremes of the tails and particle counting stops at $2 - \sigma$. Secondly. A two peak, Mixed Gaussian model is used to fit the kaon and proton peaks which allows for the additive overlap in the tails to be visualized and accounted for. This accounts for a 5% maximum systematic error for the kaons and 2% max for the protons. Since the ACC operates on Cherenkov radiation, the “ACC fire” condition is far more selective since it requires particles to be traveling fast enough to radiate. This leads to a very pure pion signal with negligible contamination, attributing < 1% systematic uncertainty.

Fixed Width/Mean Gaussians and Background Effects

For $p_T \geq 3$ GeV/c, low statistics cause the means and widths of particle distributions to vary across bins in $d\phi$. Because of this, all $d\phi$ bins are summed for a given p_T bin and are fit as a whole in order to fix a constant mean and width for each particle

species. In doing so, only the heights of the Gaussians are allowed to vary. In practice, this method tends to undercount particles. When the means of particle distributions deviate from the model-fixed values of the Gaussian models it causes only the regions that fall under the Gaussians to be counted, largely missing regions of the distribution that are not encompassed by the curve. This accounts for a 7% under-counting in these bins.

Additionally, background tracks for the very last p_T bin are strong enough to contribute to error. The TOFW along with the PC3 allows for very strong background rejection thanks to the two detectors' high precision tracking and distance from the event vertex. Only tracks with five matching points are accepted for analysis, that is: 2 hits in the DC, 1 matched hit in the PC1 within $2 - \sigma$, 1 matched hit in the TOFW within $3 - \sigma$, and 1 matched hit in the PC3 to $3 - \sigma$. This leads to a negligible background for high statistics analyses. For $4 \leq p_T \leq 4.5$, the numbers of detected particles are low enough that the background may contribute 1 out of every 10 tracks counted for each particle species. This leads to a 10% systematic error for this last bin from background.

8.4 Detector Acceptance

Detectors occupy a limited and constant range in space. The ability of a detector to cover a range in space is called its *acceptance*. Additionally, detectors are imperfect, there are dead channels, hot channels, edge effects, and other phenomena that can ruin the efficiency of a detector and add holes to its acceptance. Because of this, acceptance limitations of detectors can affect measurements in various analyses, however, for reasons

I will discuss, a flow analysis is at best negligibly affected by detector acceptance effects. Analyses where acceptance effects are strongest are those where the coordinate system is “static”. By this I mean that the production of analyzed tracks are studied in the lab frame coordinate system and any repeatedly missed tracks in a hole in acceptance are missed indefinitely and completely. Since event characteristics are random, by the necessity of event plane determination there is a statistical “smearing” that happens from the Q-vector normalization and the event plane flattening. Any holes in azimuthal coverage due to detector limitations in the lab coordinate system are smeared over by this normalization and flattening since we are performing the analysis in the event plane coordinate system which is statistically distributed and normalized. Furthermore, collaborators have studied the systematics of acceptance on v_2 measurements[47] by comparing v_2 measurements made with charged hadrons detected in TOF.E and TOF.W (45° per arm) with charged hadrons detected in full central arm acceptance (90° per arm). They found that a two-fold increase in azimuthal acceptance resulted in less than 2% difference in flow measurements.

8.5 Summary

The particle yield is binned in six bins of $d\phi$ which therefore means that there are six points that can be perturbed systematically. In order to study the propagation of the yield uncertainty to the measured flow coefficient I take the known values of yield in $d\phi$ and perturb them up or down by the percentages quantified in this chapter. The changed yield vs $d\phi$ distribution is re-fit and a new flow coefficient is calculated. This new v_2 is compared

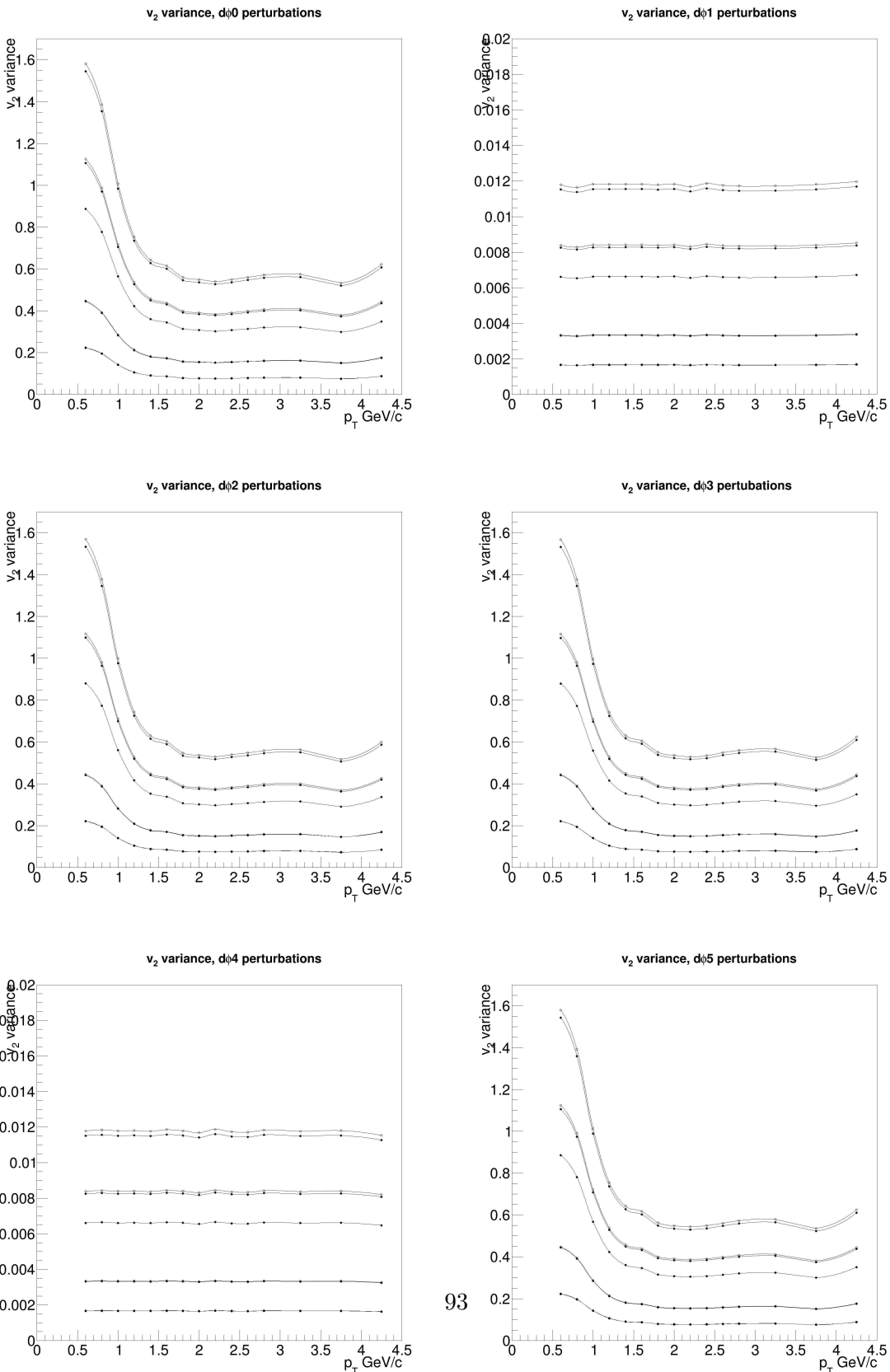
Table 8.2: My caption

Source of Error	Transverse Momentum Bin Range (GeV/c)							
	0.5-0.7	0.7-0.9	0.9-1.1	1.1-1.3	1.3-1.5	1.5-1.7	1.7-1.9	1.9-2.1
Event Plane Resolution	23.40%	23.40%	23.40%	23.40%	23.40%	23.40%	23.40%	23.40%
Detector Acceptance	<2%	<2%	<2%	<2%	<2%	<2%	<2%	<2%
Centrality Determination	5%	5%	5%	5%	5%	5%	5%	5%
PID uncertainty (pion)	22%	20%	14%	11%	9%	17%	16%	15%
PID uncertainty (kaon)	22%	20%	14%	11%	9%	17%	16%	15%
PID uncertainty (proton)	22%	20%	14%	10%	9%	8%	8%	7%

to the original one in order to determine systematic errors on the final measurement which are caused by sources within the process of measuring it. Since the identified track flow follows the behavior of the individual particle flows I will use it for this study and for completeness, perturbations both up and down were be studied.

In practice, of these six points, four contribute strongly to the overall shape of the yield distribution, these are: the two end points and the two center points. This is shown by the significantly smaller systematic error in bins 1 and 4 in fig 8.4. Additionally, the direction of perturbation makes a negligible difference; up and down perturbations line up very well on the plots. Yield systematics have the strongest effect on the lower p_T bins. This is because their significantly higher statistics correspond to a larger loss or gain of counted particles with which to skew the flow coefficient.

Figure 8.4: Effects of Systematic Shifts in Yield on v_2 . 1%, 2%, 4%, 5%, 7%, and 10% perturbations are applied to each yield for a particular bin of $d\phi$ and the corresponding v_2 is calculated. Closed circles are downward perturbations, open circles, upward perturbations.



Chapter 9

Summary and Conclusions

9.1 Discussion

9.2 Conclusions

Appendix A

PHENIX Coordinate System

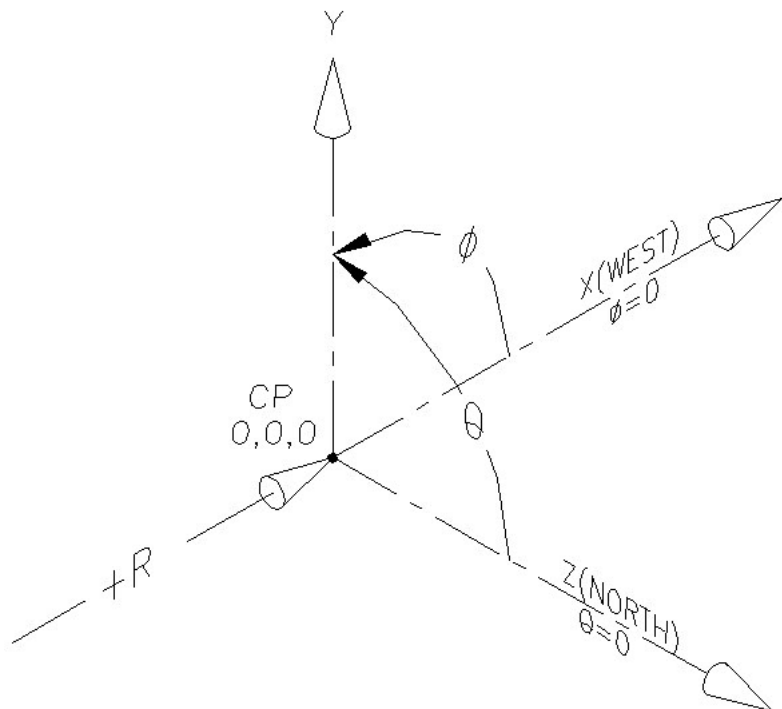


Figure A.1: PHENIX coordinate system

The PHENIX coordinate system in Cartesian coordinates is defines the beam line as the z-axis with the north side of the detector being the positive going direction, due west being the positive going x-axis, and straight up being the positive going y-axis. For spherical coordinates, the azimuthal angle ϕ spans 2π about the z axis with $\phi = 0$ pointing due west, i.e. along the x-axis. The polar angle θ is often converted to pseudorapidity for analysis. Pseudorapidity (η), often referred to colloquially as “rapidity,” (not to be confused with the true rapidity, y) is defined as:

$$\eta = -\ln \left[\tan \left(\frac{\theta}{2} \right) \right]. \quad (\text{A.1})$$

where small values of η refer to processes and measurements in the central arms and larger values of η refer to the forward muon arm regions.

Appendix B

Nuclear Modification Factor

Since heavy ion systems are comprised of many nucleons colliding, we would like to differentiate between phenomena from singular nucleon-nucleon collisions and phenomena created from interactions of nuclear matter. It is therefore convenient to define a quantity that describes how different a system of N colliding nucleons differs from a system of two colliding nucleons scaled up by N , often referred to as *Binary Scaling*. For example, consider the system created with Au+Au collisions. If we wanted to know how pion production was affected by nuclear matter we would be interested in how different pion production was in the collision of 197 nucleons with another 197 nucleons compared to pion production in p+p scaled up by a factor of 197. This quantity is called a *Nuclear Modification Factor* and is usually denoted with the letter R and two subscripts defining what kind of Nuclear Modification Factor it is:

$$R_{AA}(p_T) = \frac{1}{\langle N_{coll} \rangle} \frac{dN_{AA}/dp_T}{d\sigma_{pp}/dp_T}, \quad (\text{B.1})$$

where dN_{AA}/dp_T is the differential yield in the system, $d\sigma_{pp}/dp_T$ is the differential cross section in proton-proton collisions, and $\langle N_{coll} \rangle$ is the number of binary collisions. Given this definition if $R_{AA} = 1$ then we expect no new phenomena in the system, that is, the system comprised of N colliding nucleons behaves exactly as we'd expect N proton-proton collisions to behave. If $R_{AA} > 1$ it is said that interactions with the nuclear material enhances production and vice versa with $R_{AA} < 1$, production is suppressed.

Appendix C

Event and Track Selection Cuts

This is a summary of cuts made on event selection and accepted tracks used for this analysis. For a detailed discussion of the choices for these cuts see chapters 3 and 4

Appendix D

Analysis Data and Plots

D.1 Charged Track Elliptic Flow

Figure D.1: $\frac{dN}{d\phi}$ vs $d\phi$, 0-5% centrality, each plot represents a 0.2 GeV slice in transverse momentum space.

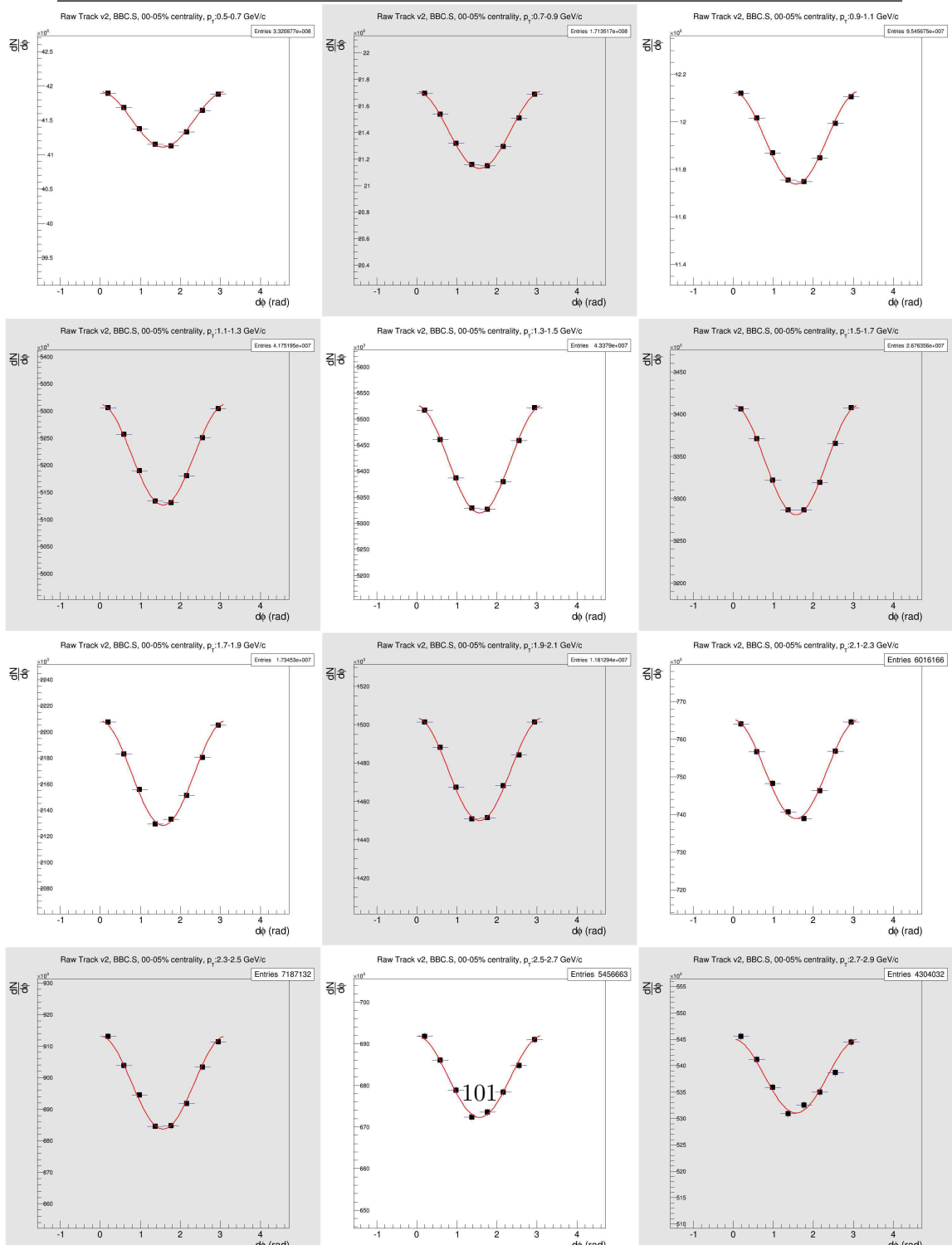


Figure D.2: $\frac{dN}{d\phi}$ vs $d\phi$, 5-10% centrality, each plot represents a 0.2 GeV slice in transverse momentum space.

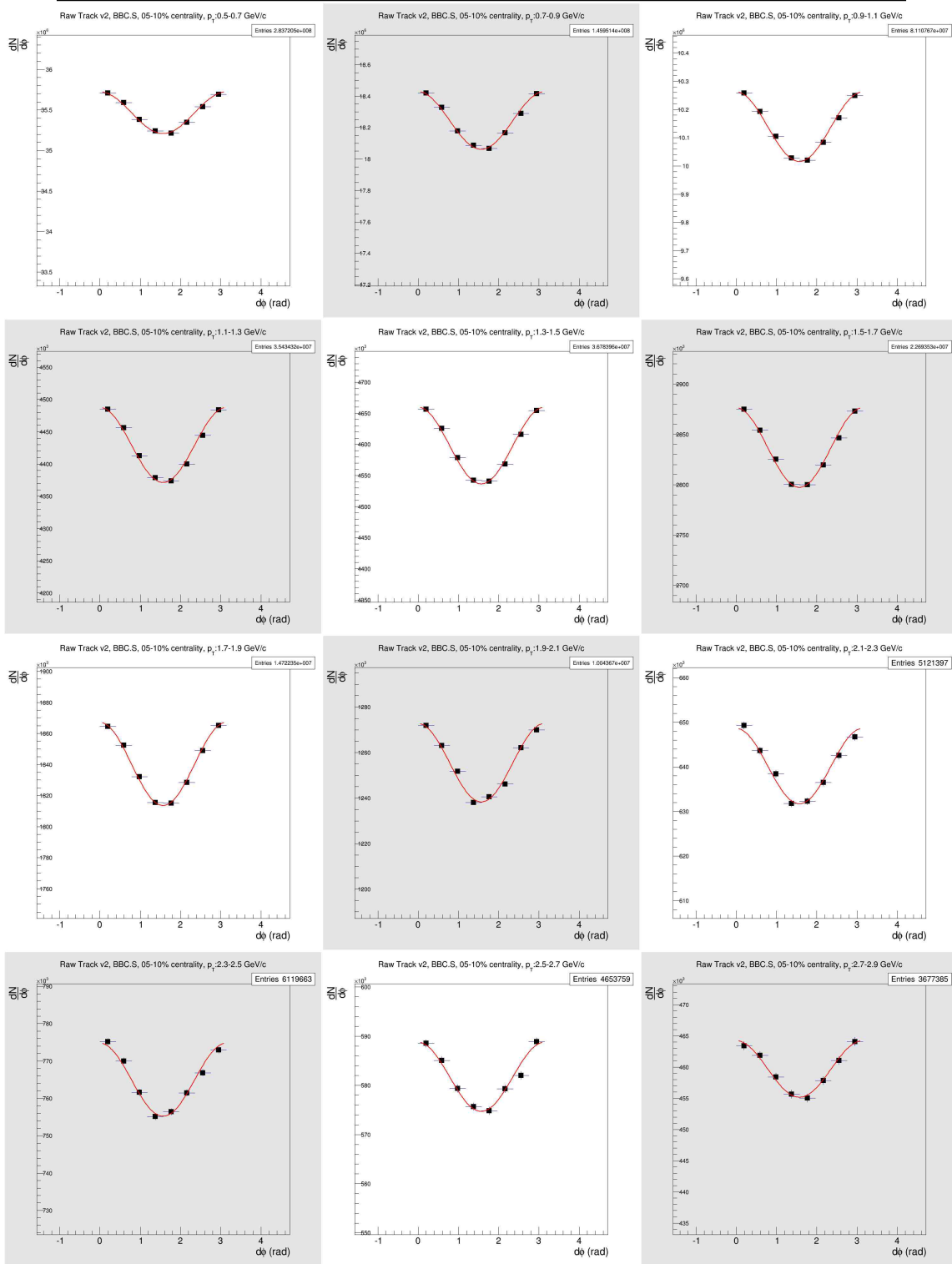


Figure D.3: $\frac{dN}{d\phi}$ vs $d\phi$, 10-15% centrality, each plot represents a 0.2 GeV slice in transverse momentum space.

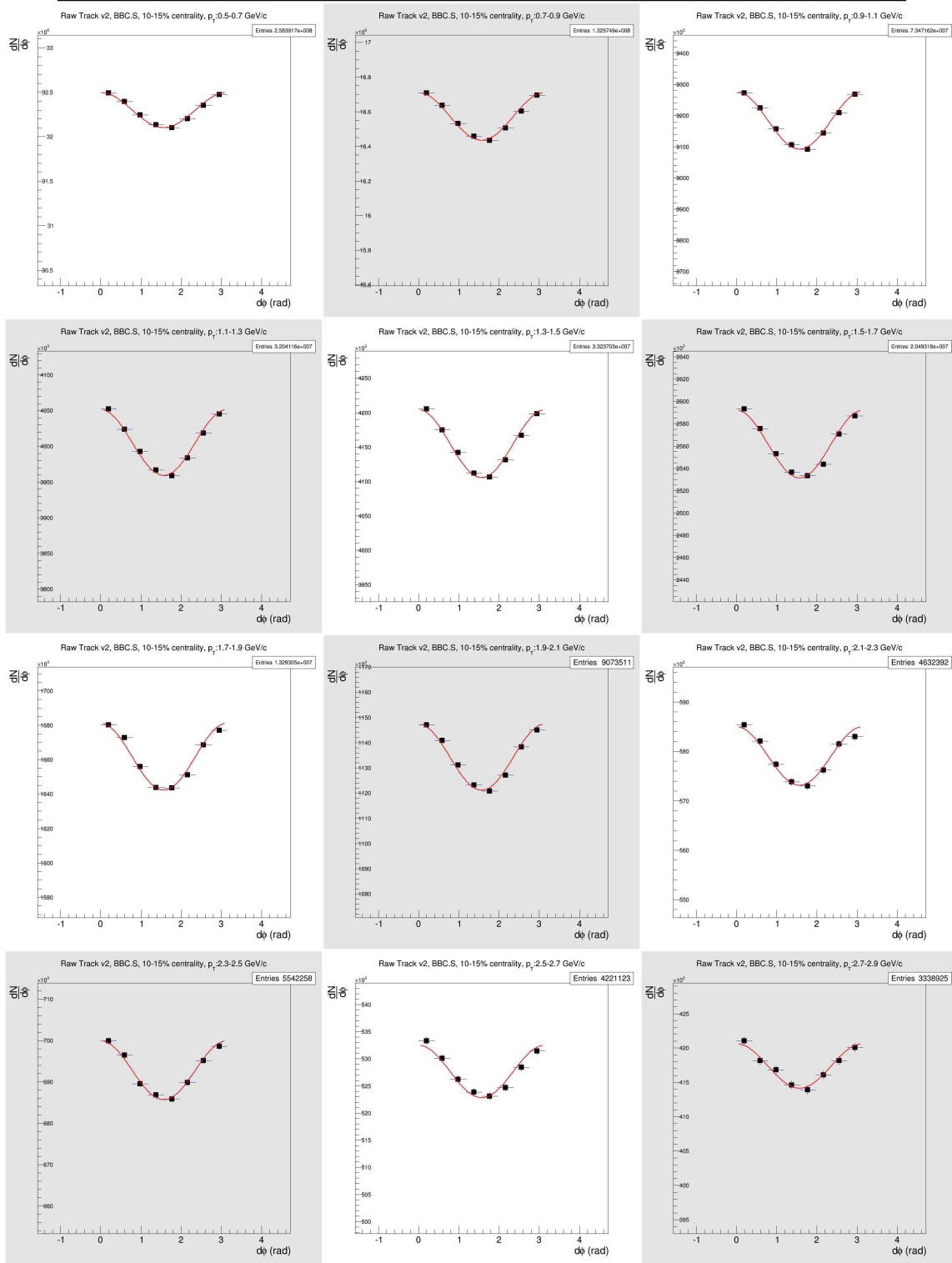
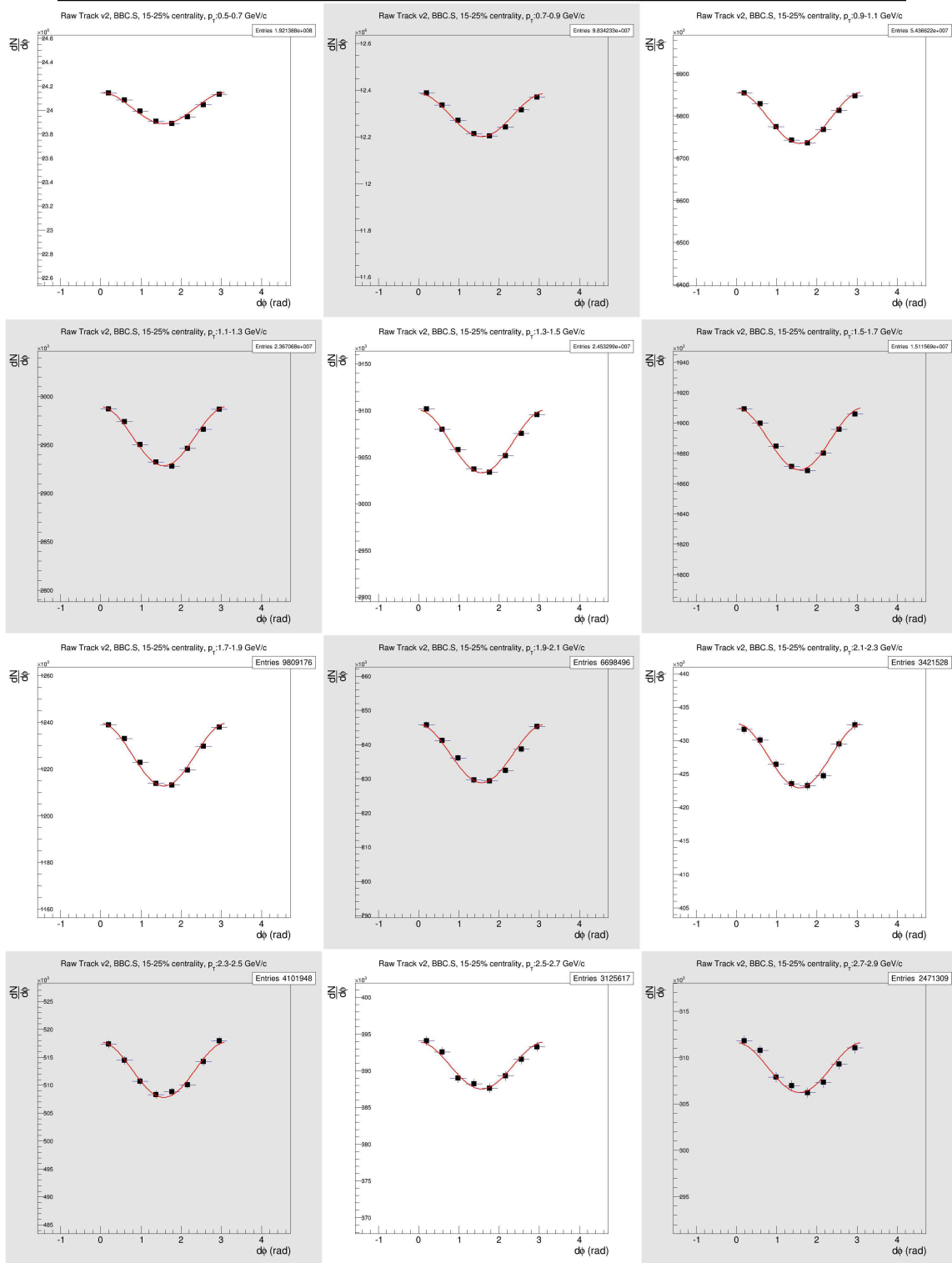


Figure D.4: $\frac{dN}{d\phi}$ vs $d\phi$, 15-25% centrality, each plot represents a 0.2 GeV slice in transverse momentum space.



D.2 Particle Identification: TOFW

D.2.1 Single Gaussian fits, $p_T=0.5\text{-}1.3 \text{ GeV}/c$, TOF.W, negative charged tracks

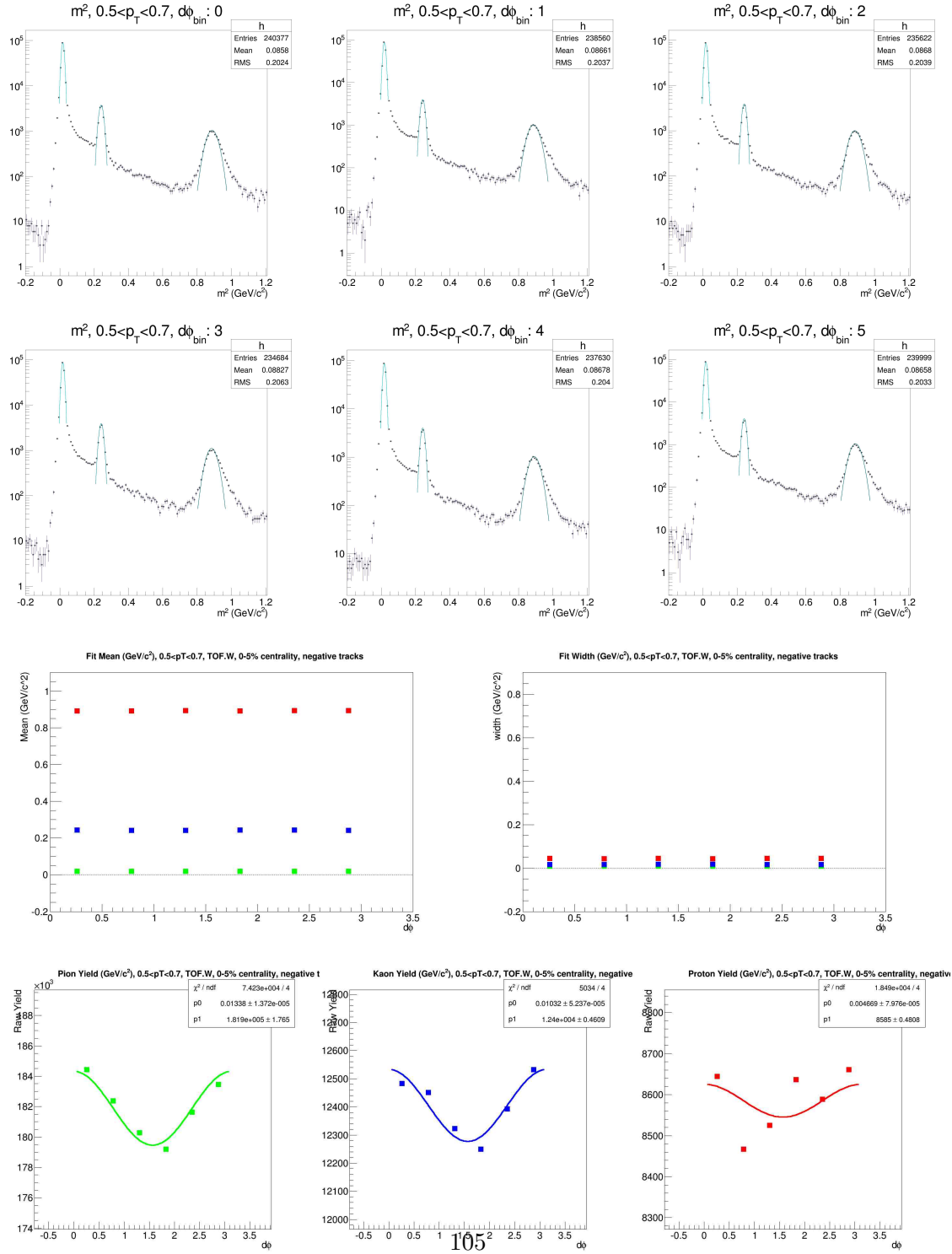


Figure D.5: m^2 Gaussian fits for PID and resulting Yield vs $d\phi$ for $p_T=0.5\text{-}0.7 \text{ GeV}/c$, TOF.W, negative particles

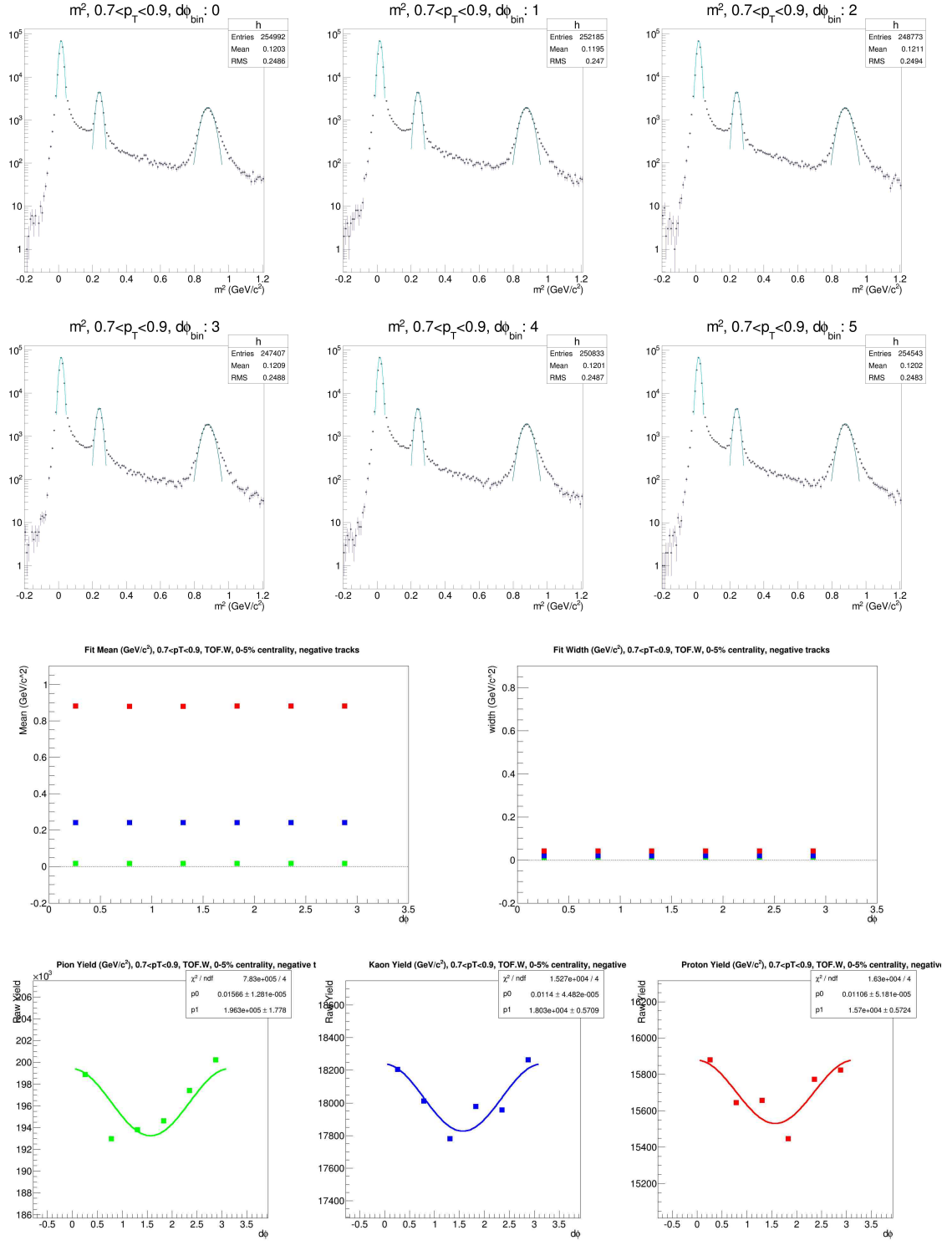


Figure D.6: m^2 Gaussian fits for PID and resulting Yield vs $d\phi$ for $p_T = 0.7-0.9 \text{ GeV}/c$, TOF.W, negative particles

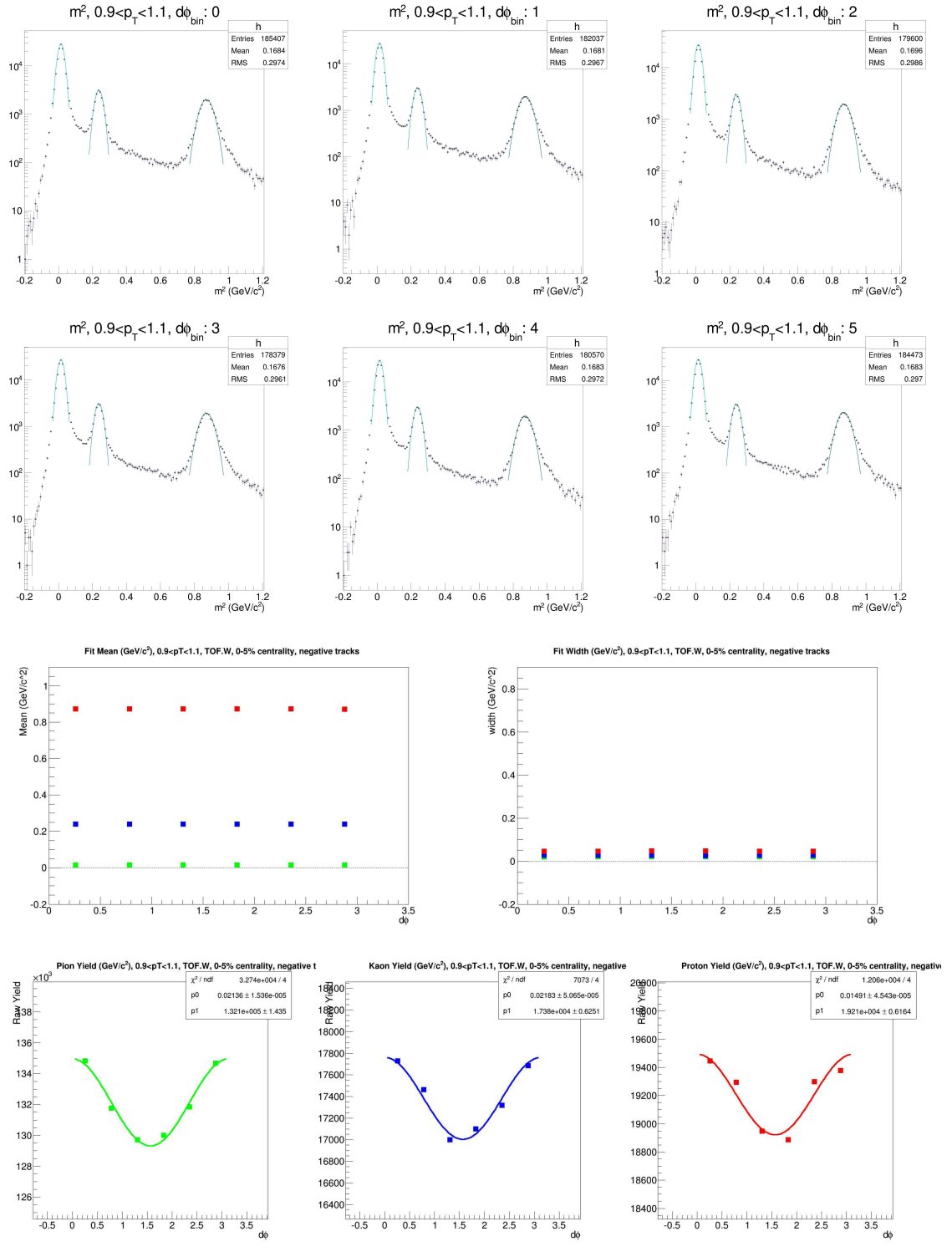


Figure D.7: m^2 Gaussian fits for PID and resulting Yield vs $d\phi$ for $p_T = 0.9$ - 1.1 GeV/c , TOF.W, negative particles

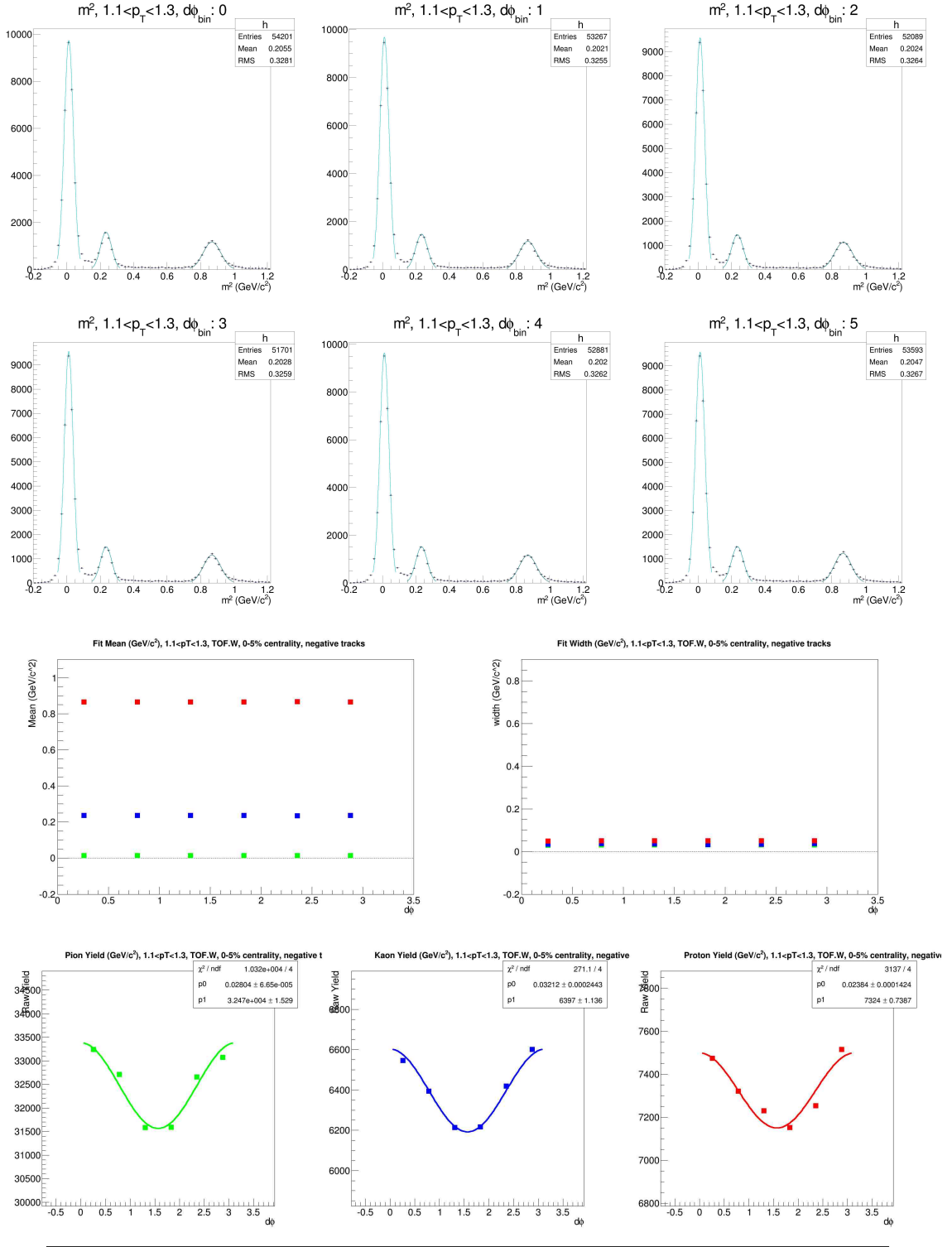


Figure D.8: m^2 Gaussian fits for PID and resulting Yield vs $d\phi$ for $p_T = 1.1 - 1.3 \text{ GeV}/c$, TOF.W, negative particles

D.2.2 Single Gaussian fits, $p_T=0.5\text{-}1.3 \text{ GeV}/c$, TOF.W, positive charged tracks

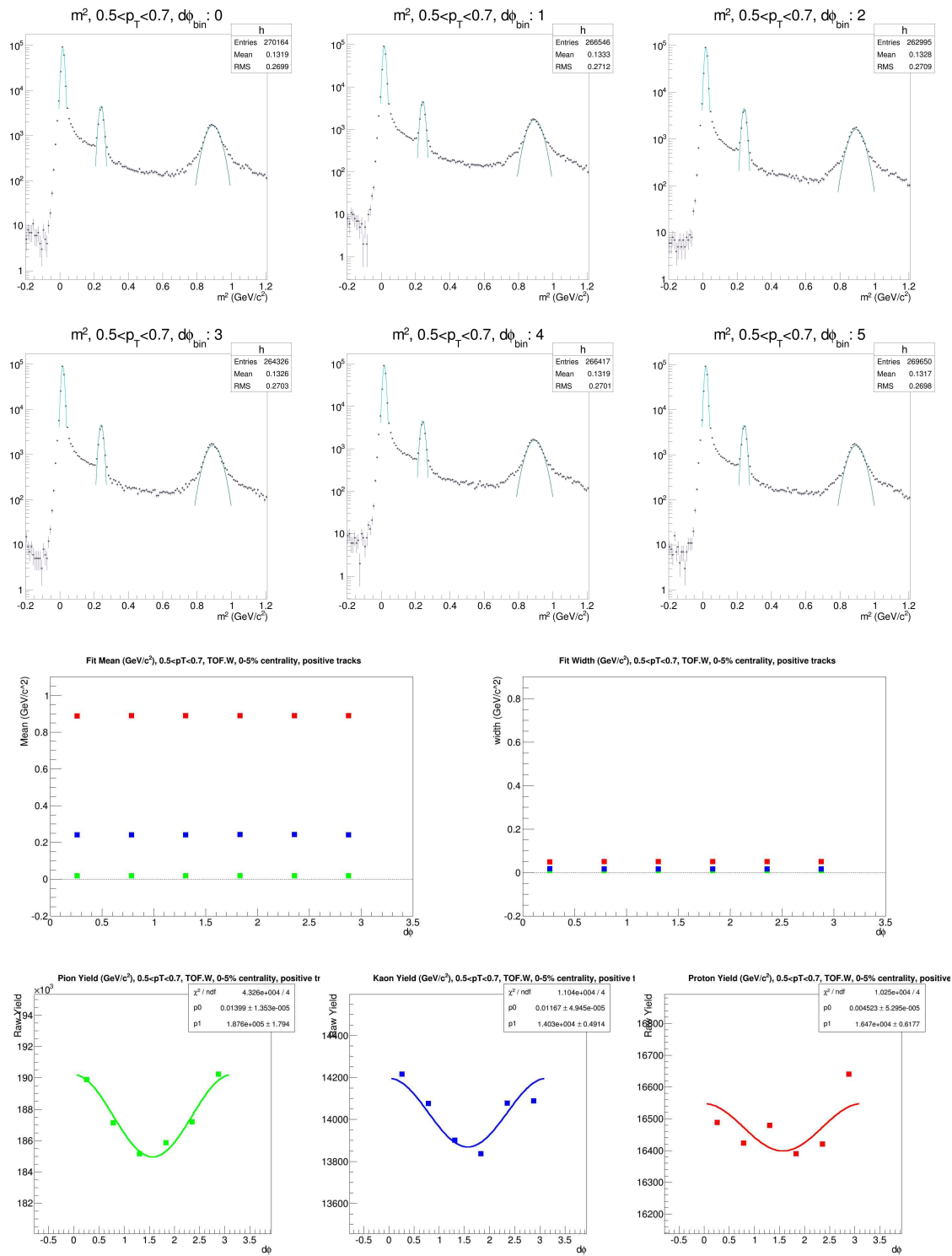


Figure D.9: m^2 Gaussian fits for PID and resulting Yield vs $d\phi$ for $p_T = 0.5\text{-}0.7 \text{ GeV}/c$, TOF.W, positive particles¹⁰⁹

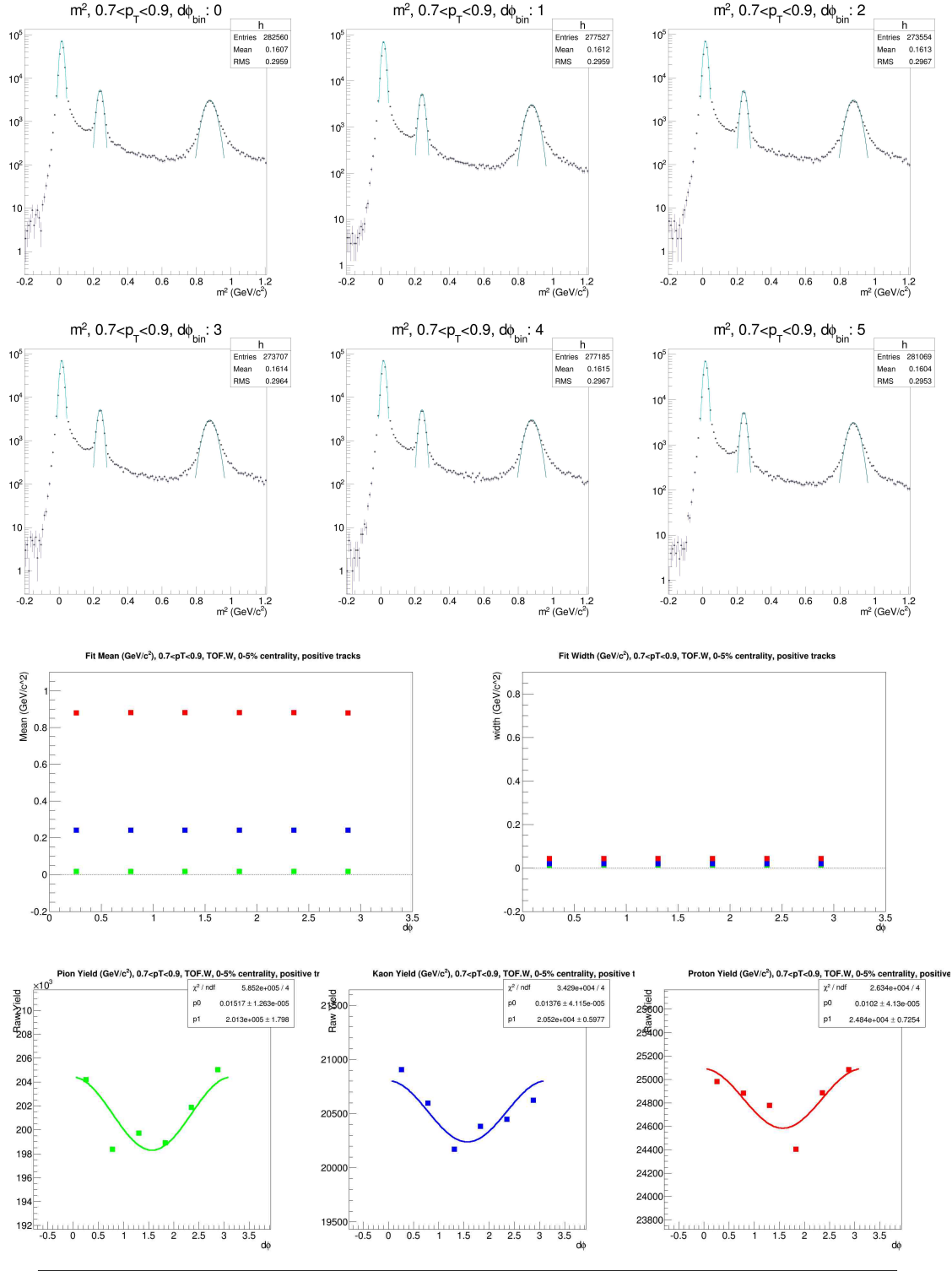


Figure D.10: m^2 Gaussian fits for PID and resulting Yield vs $d\phi$ for $p_T = 0.7\text{-}0.9 \text{ GeV}/c$, TOF.W, positive particles

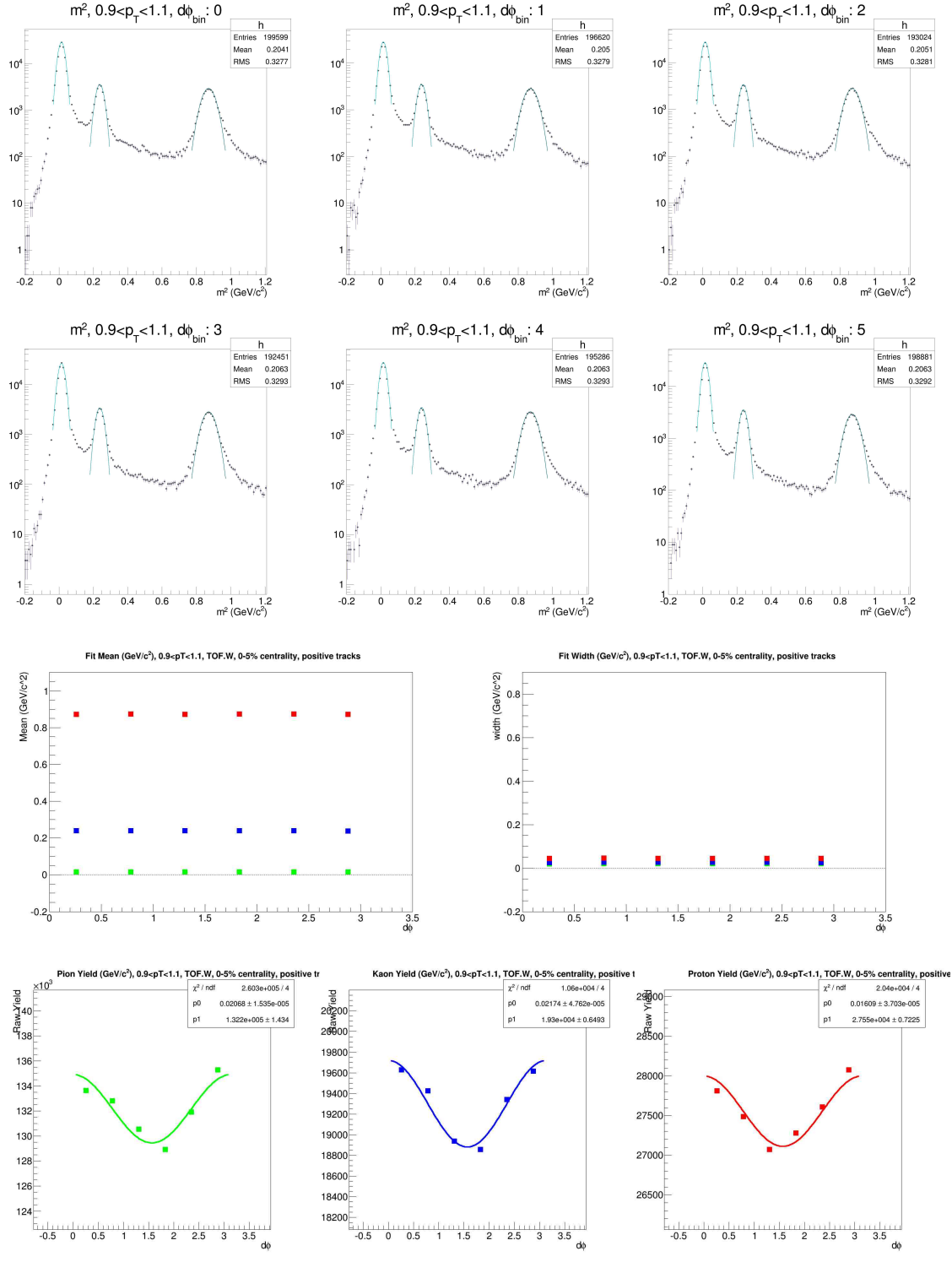


Figure D.11: m^2 Gaussian fits for PID and resulting Yield vs $d\phi$ for $p_T = 0.9-1.1 \text{ GeV}/c$, TOF.W, positive particles

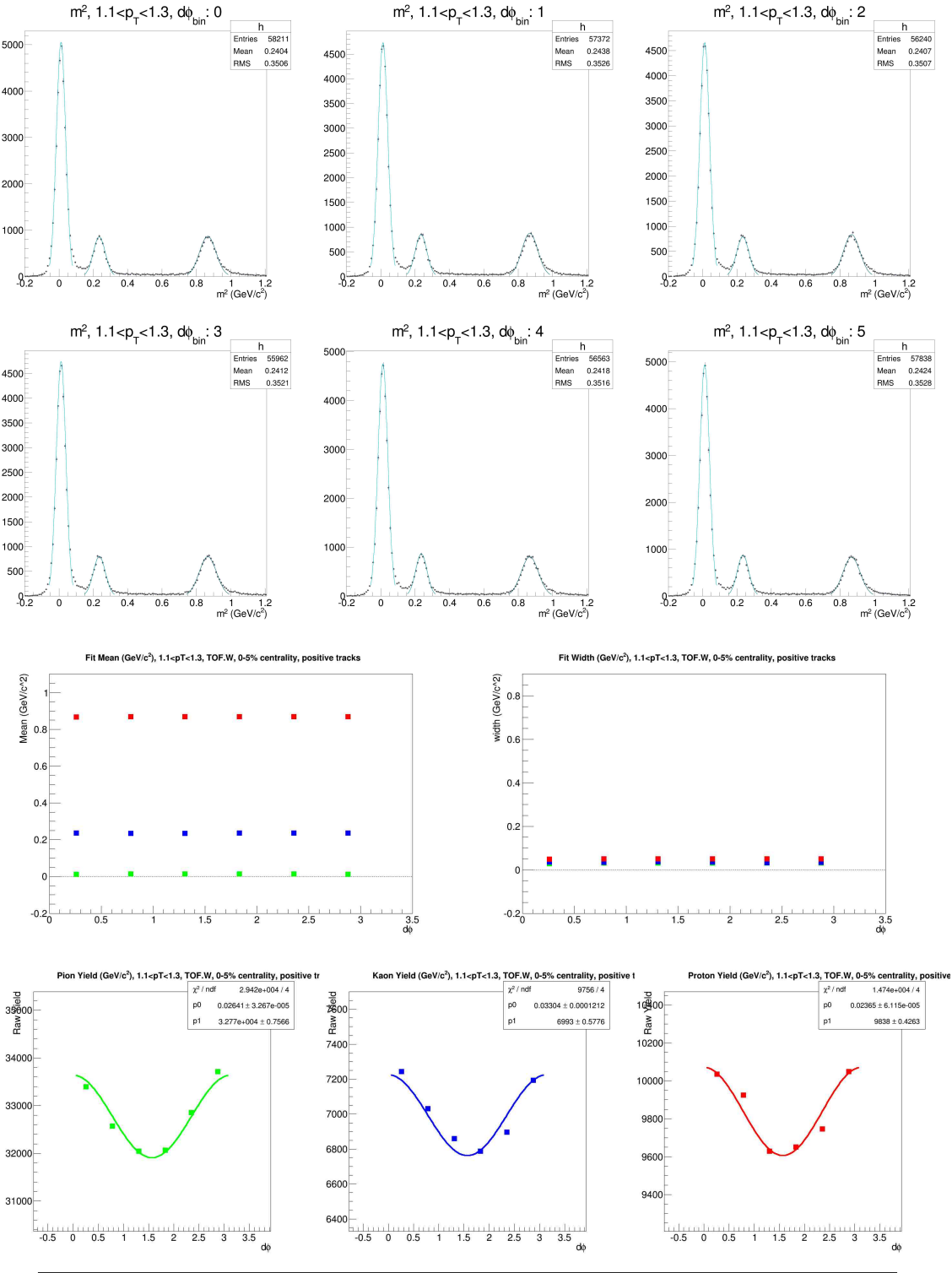


Figure D.12: m^2 Gaussian fits for PID and resulting Yield vs $d\phi$ for $p_T = 1.1-1.3 \text{ GeV}/c$, TOF.W, positive particles

D.2.3 Mixed Gaussian fits, $p_T=1.3\text{-}2.1$ GeV/c, TOF.W, negative charged tracks

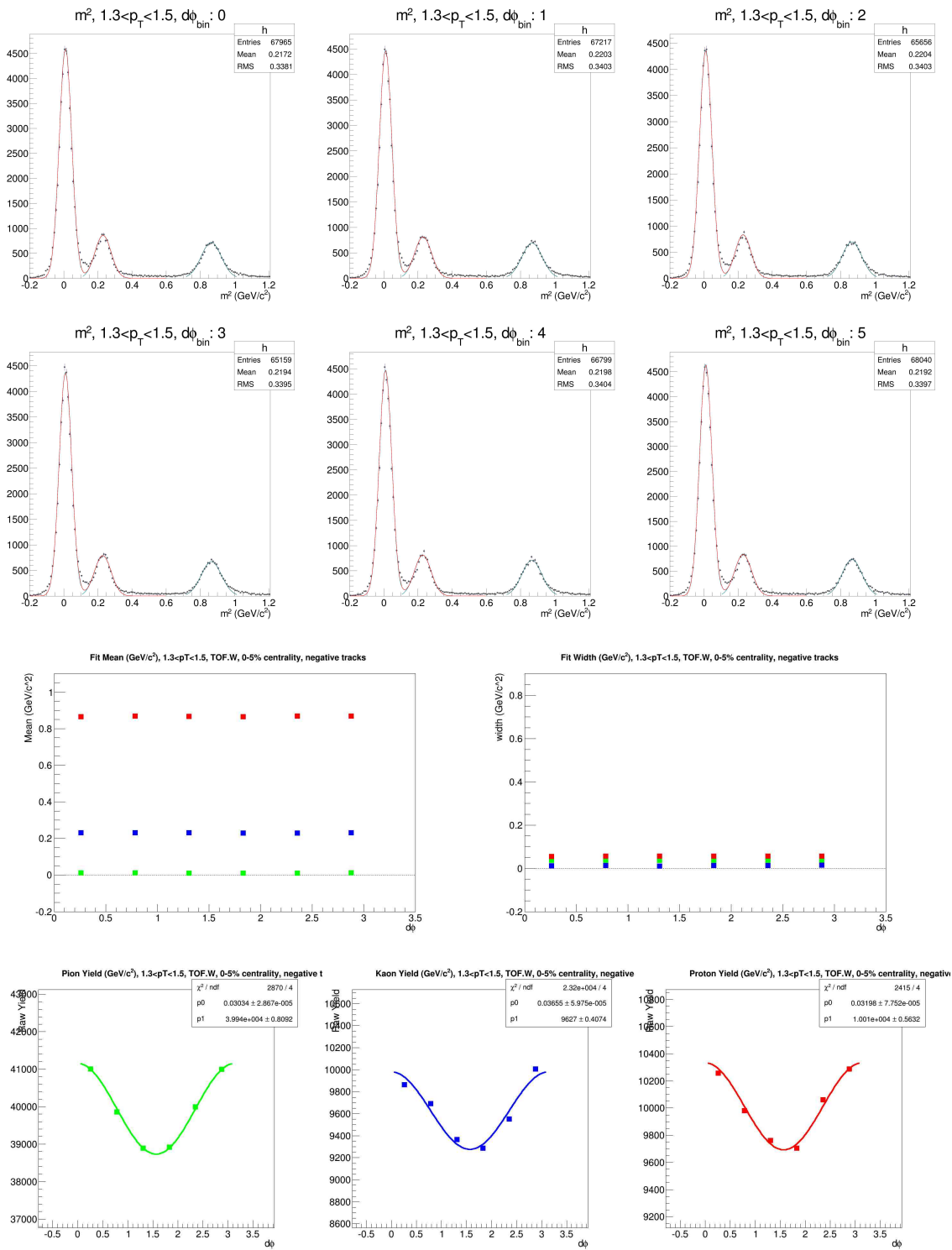


Figure D.13: m^2 Gaussian fits for PID and resulting Yield vs $d\phi$ for $p_T=1.3\text{-}1.5$ GeV/c, TOF.W, negative particles

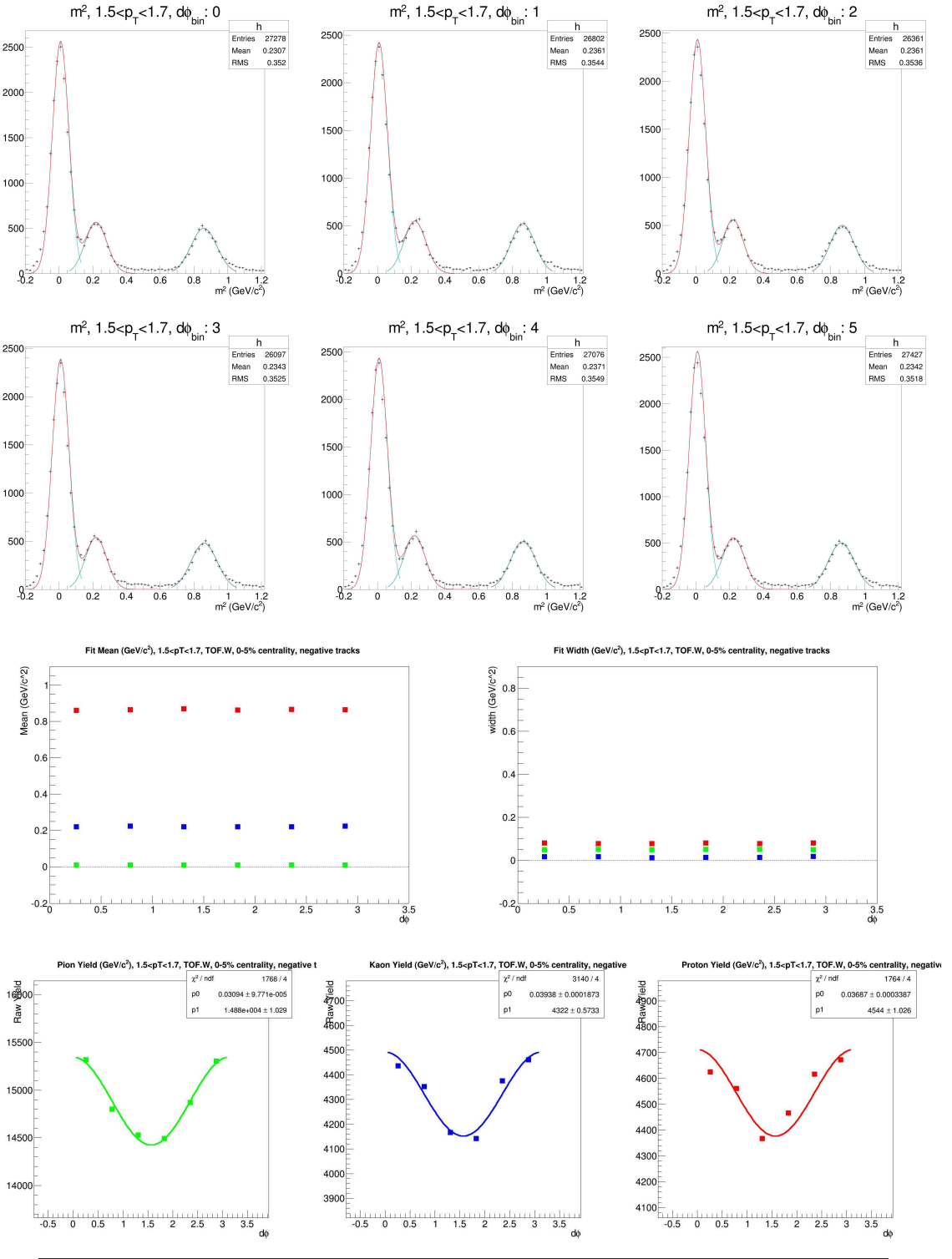


Figure D.14: m^2 Gaussian fits for PID and resulting Yield vs $d\phi$ for $p_T=1.5-1.7$ GeV/c, TOF.W, negative particles

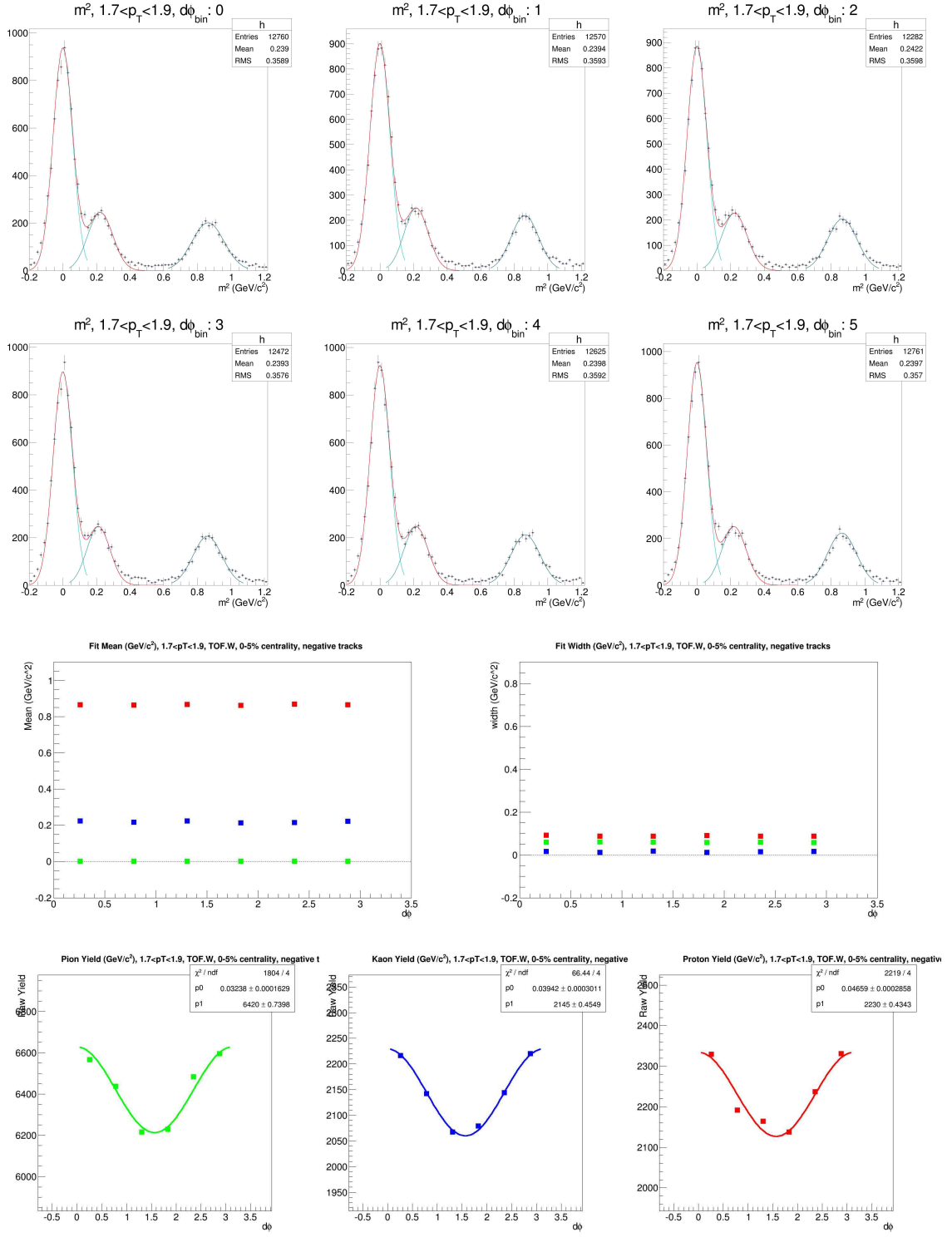


Figure D.15: m^2 Gaussian fits for PID and resulting Yield vs $d\phi$ for $p_T = 1.7-1.9 \text{ GeV}/c$, TOF.W, negative particles

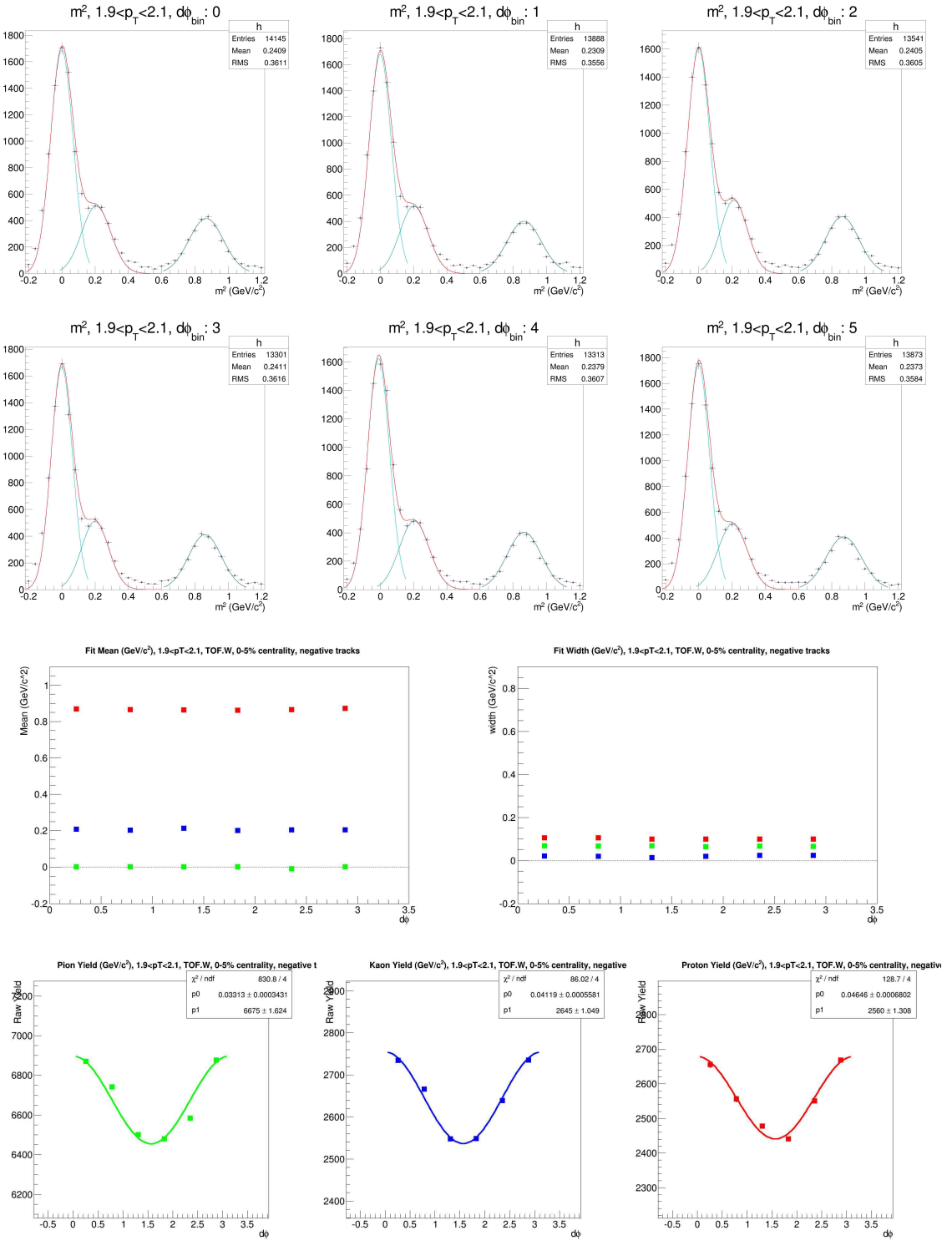


Figure D.16: m^2 Gaussian fits for PID and resulting Yield vs $d\phi$ for $p_T = 1.9-2.1 \text{ GeV}/c$, TOF.W, negative particles

Mixed Gaussian fits, $p_T=1.3\text{-}2.1$ GeV/c, TOF.W, positive charged tracks

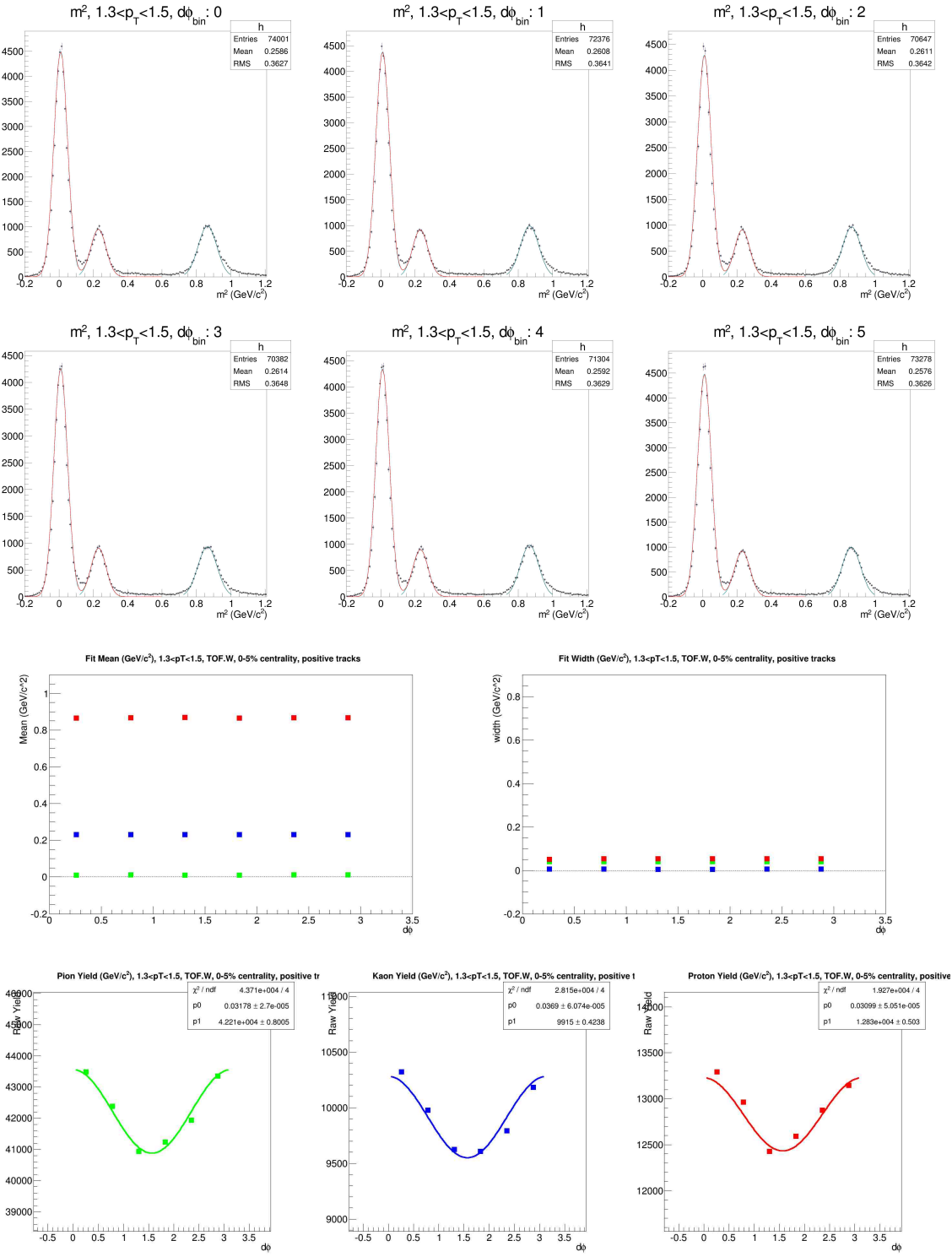


Figure D.17: m^2 Gaussian fits for PID and resulting Yield vs $d\phi$ for $p_T=1.3\text{-}1.5$ GeV/c, TOF.W, positive particles

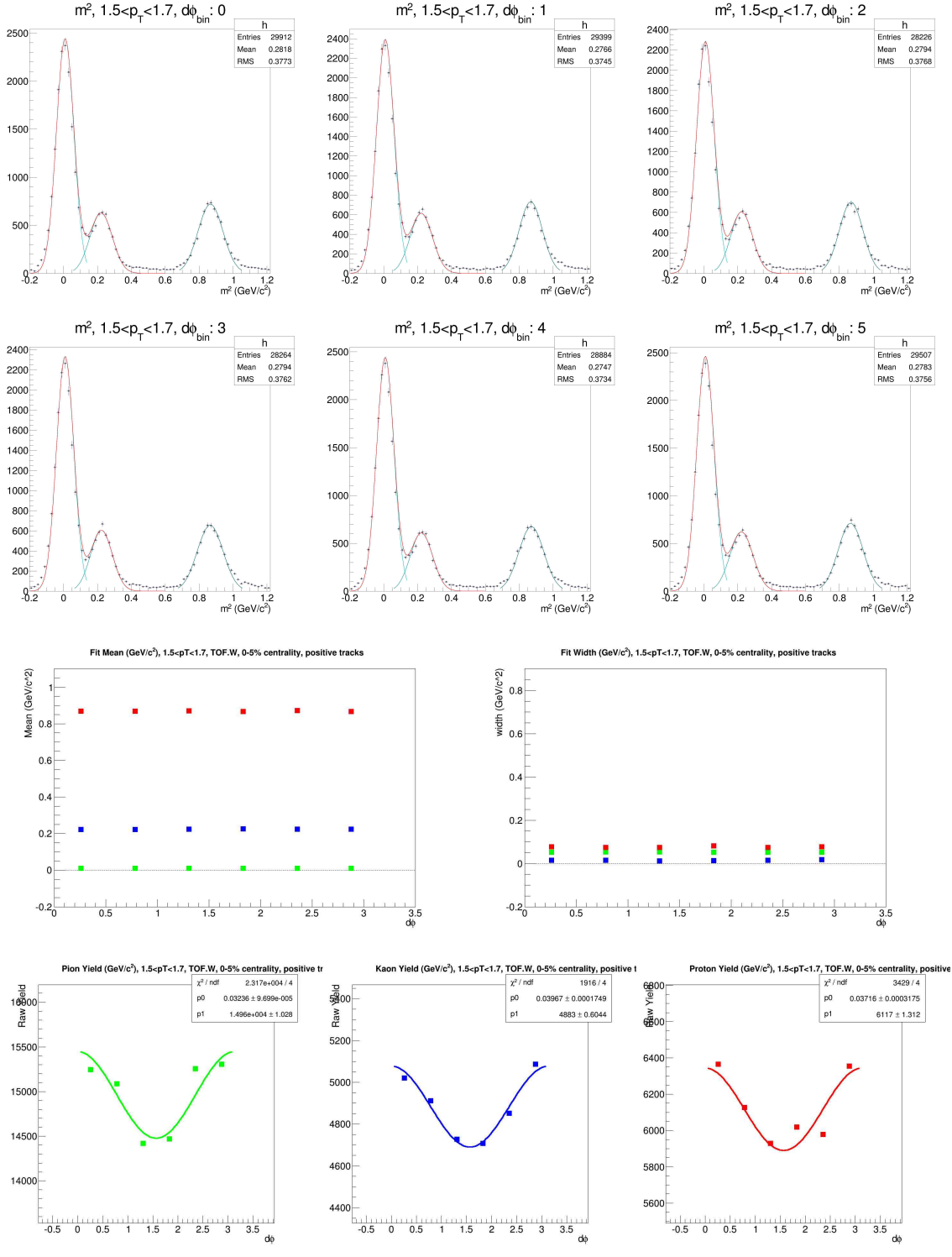


Figure D.18: m^2 Gaussian fits for PID and resulting Yield vs $d\phi$ for $p_T = 1.5-1.7 \text{ GeV}/c$, TOF.W, positive particles

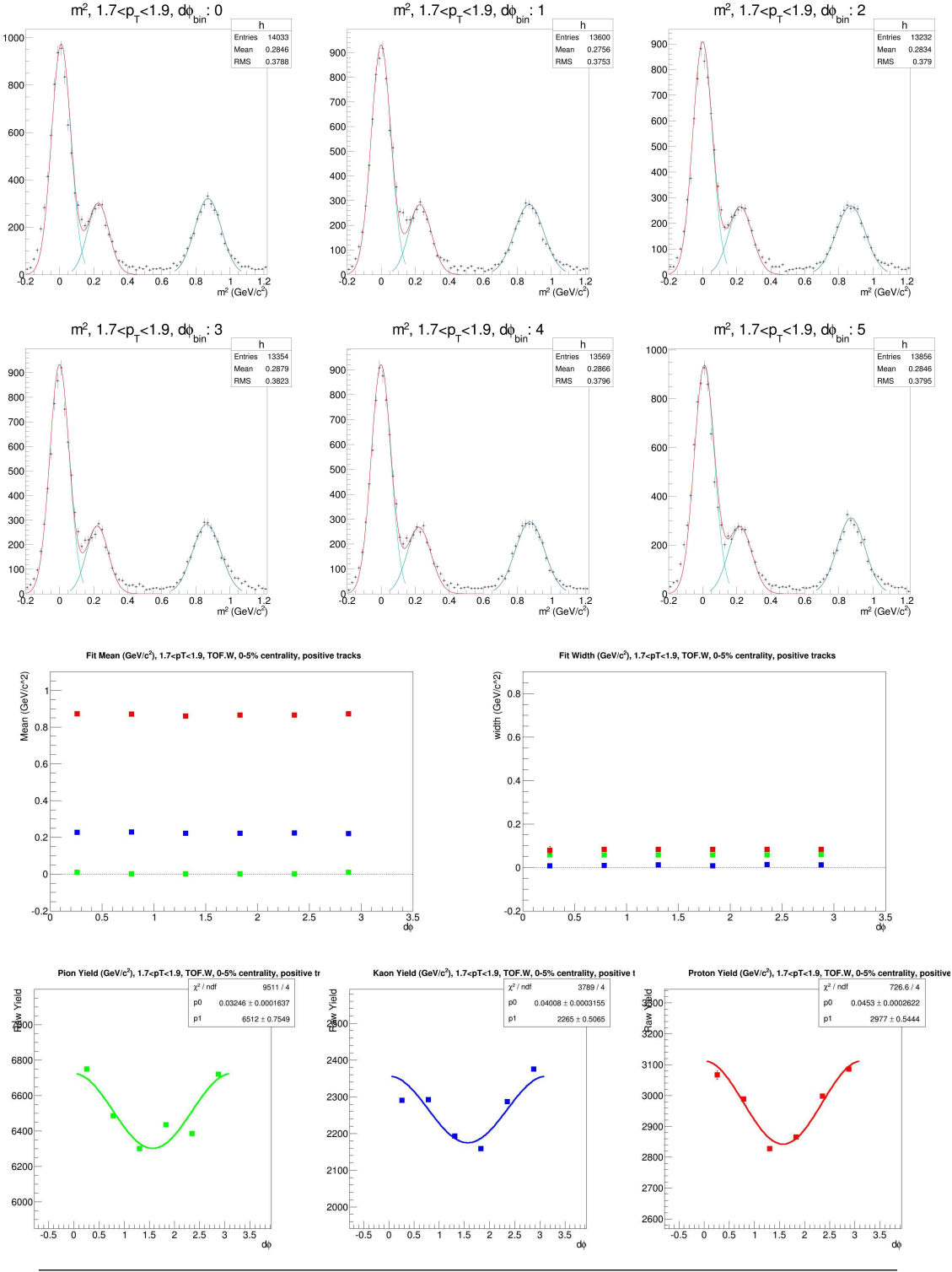


Figure D.19: m^2 Gaussian fits for PID and resulting Yield vs $d\phi$ for $p_T = 1.7-1.9 \text{ GeV}/c$, TOF.W, positive particles

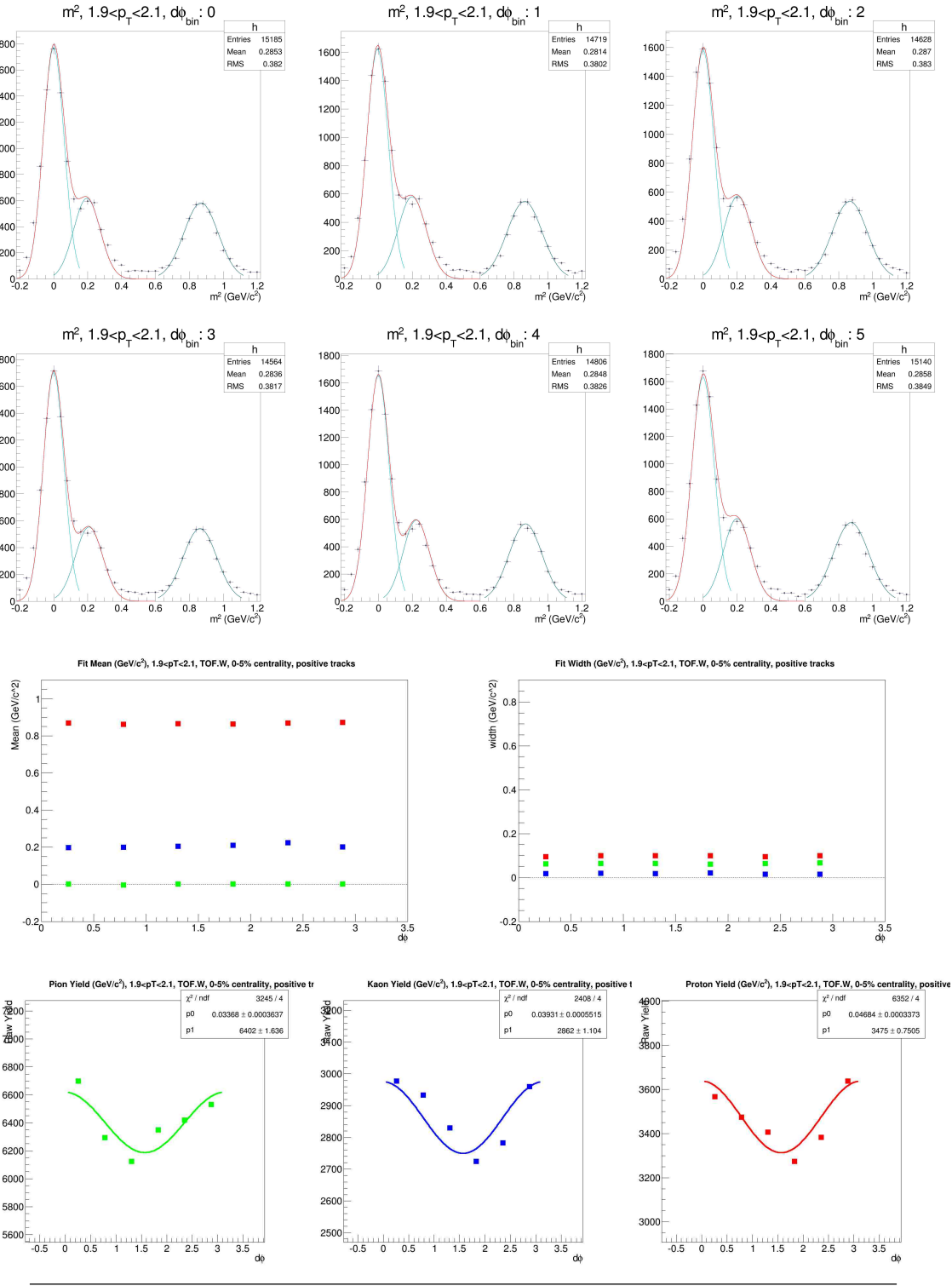
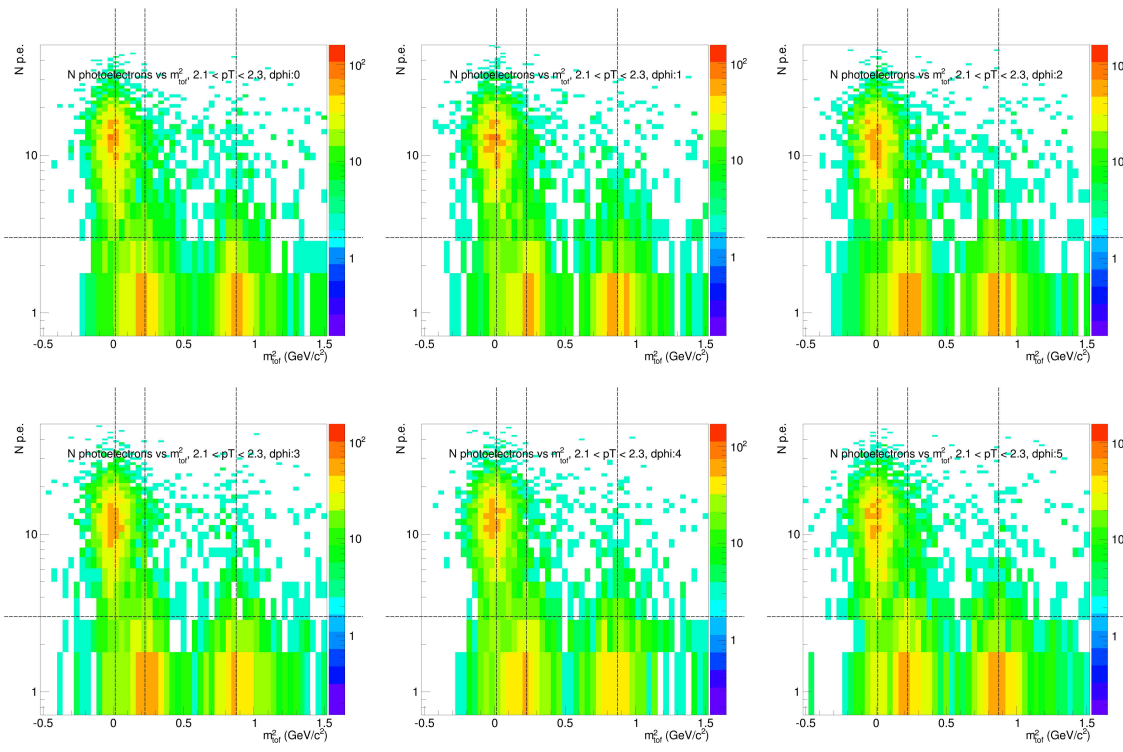
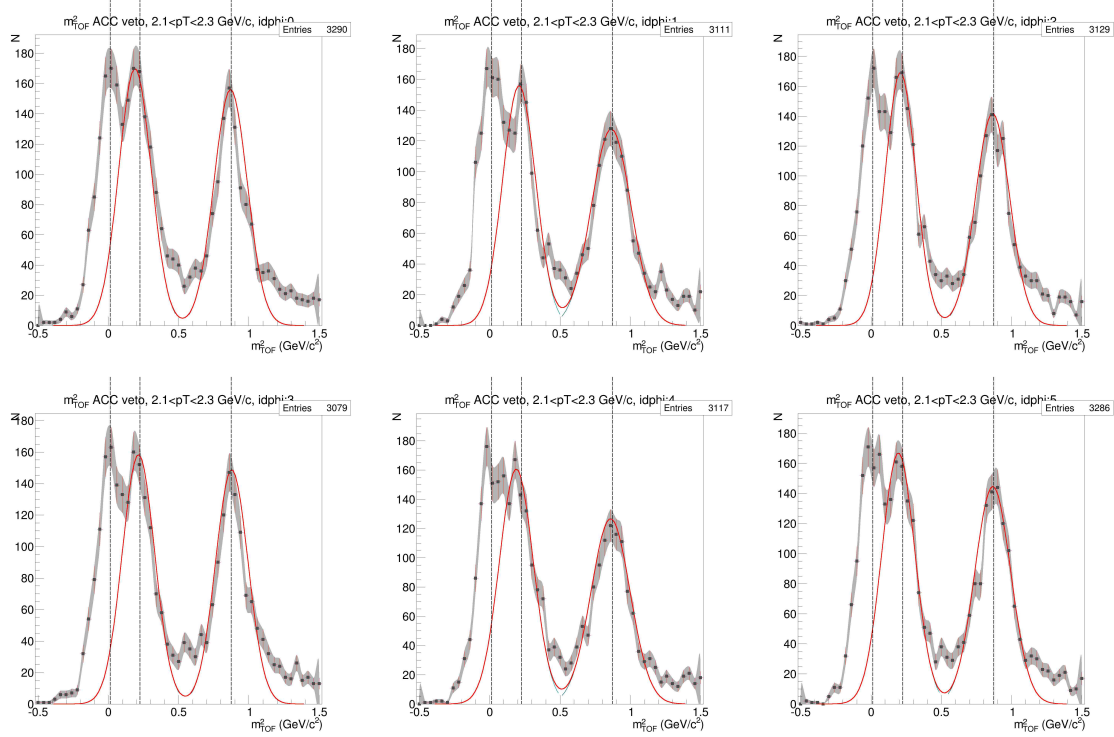


Figure D.20: m^2 Gaussian fits for PID and resulting Yield vs $d\phi$ for $p_T = 1.9-2.1 \text{ GeV}/c$, TOF.W, positive particles

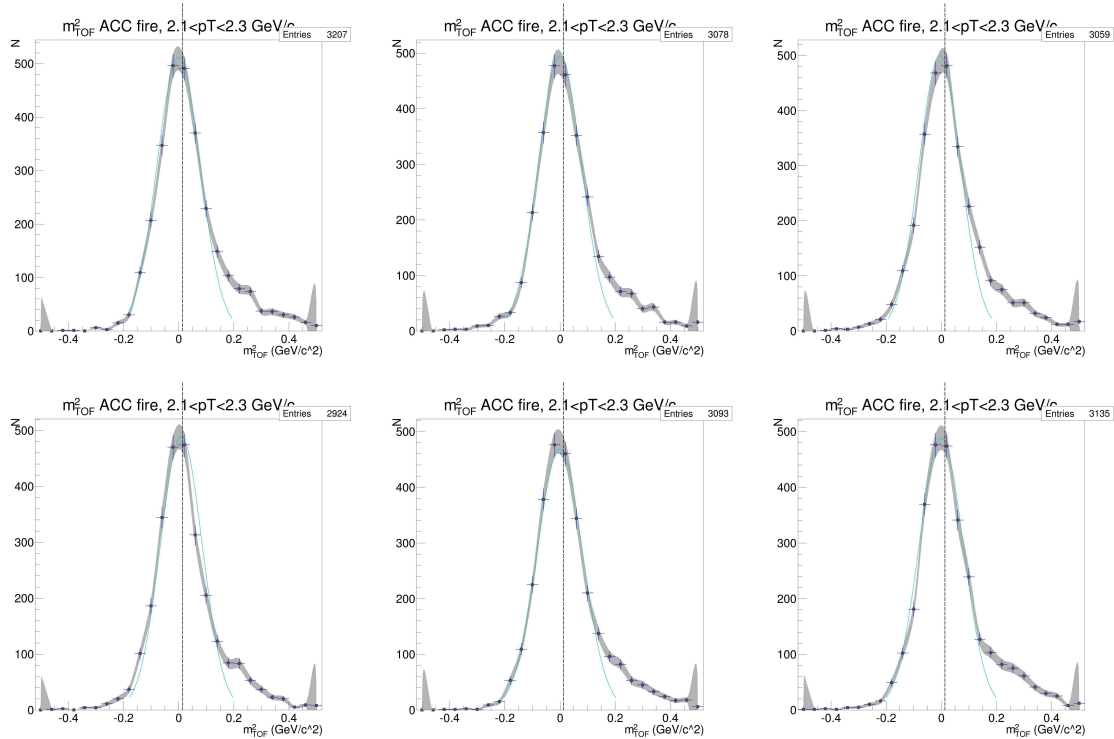
D.2.4 TOF.W and ACC, $p_T=2.1\text{-}3.5$ GeV, negative charged tracks



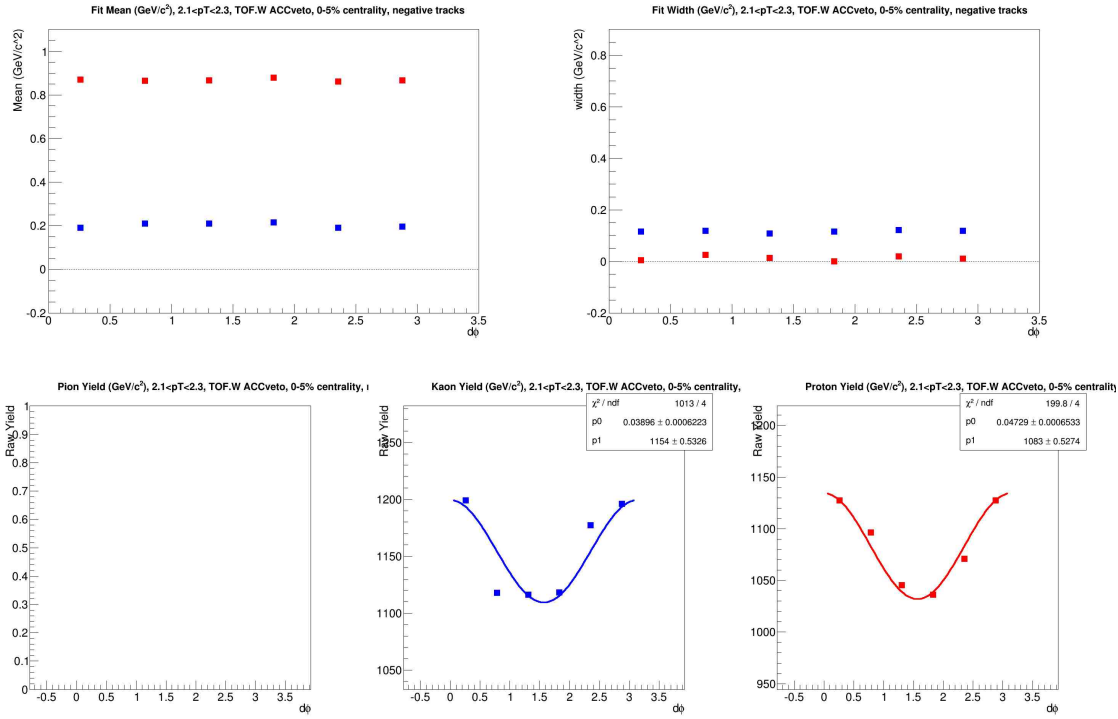
(a) $N_{p.e.}$ vs m^2



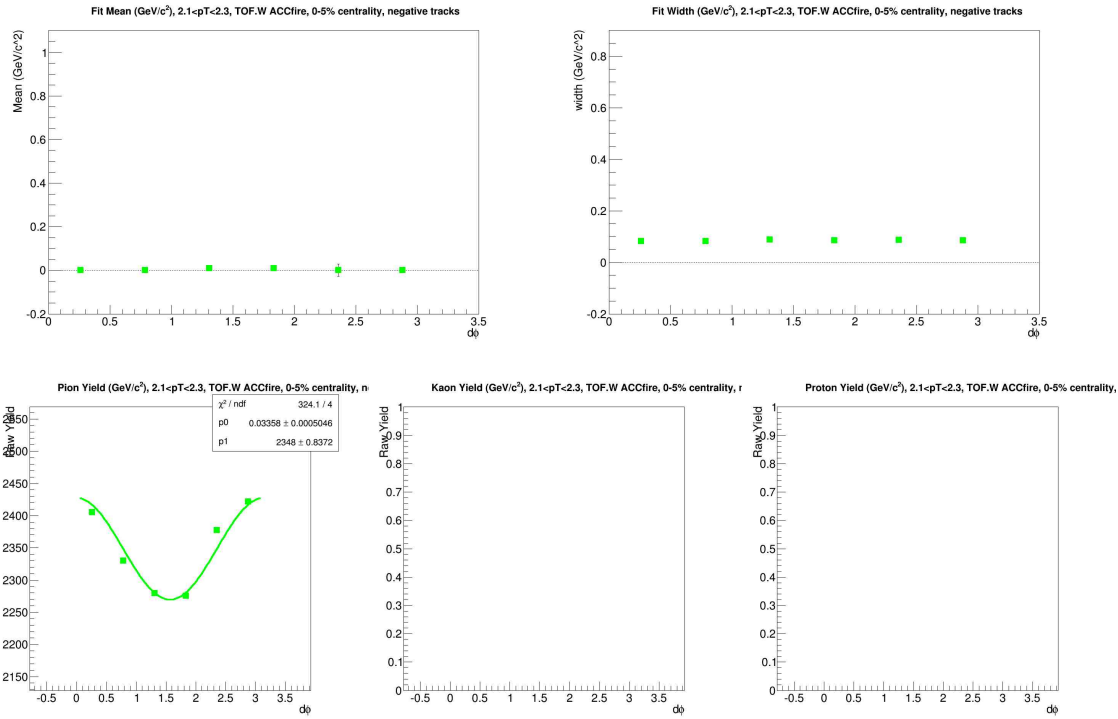
(b) m^2 for ACC vetoed tracks



(c) m^2 for ACC fired tracks

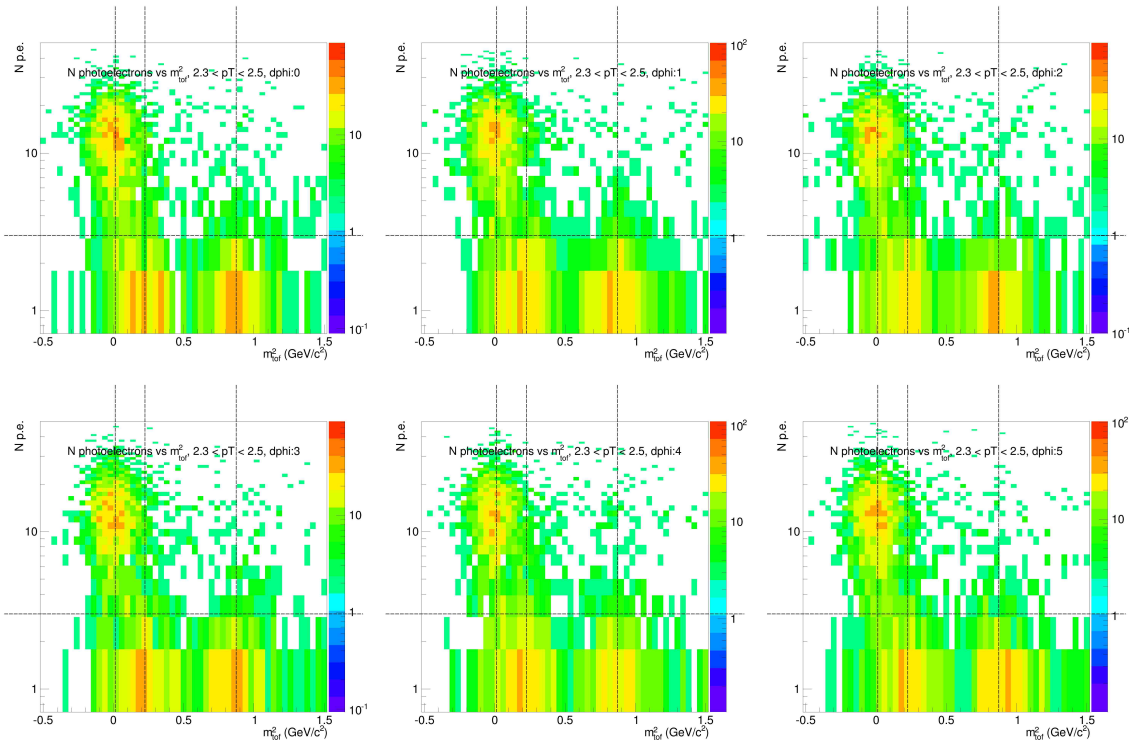


(d) PID parameters and Yields for ACC vetoed tracks

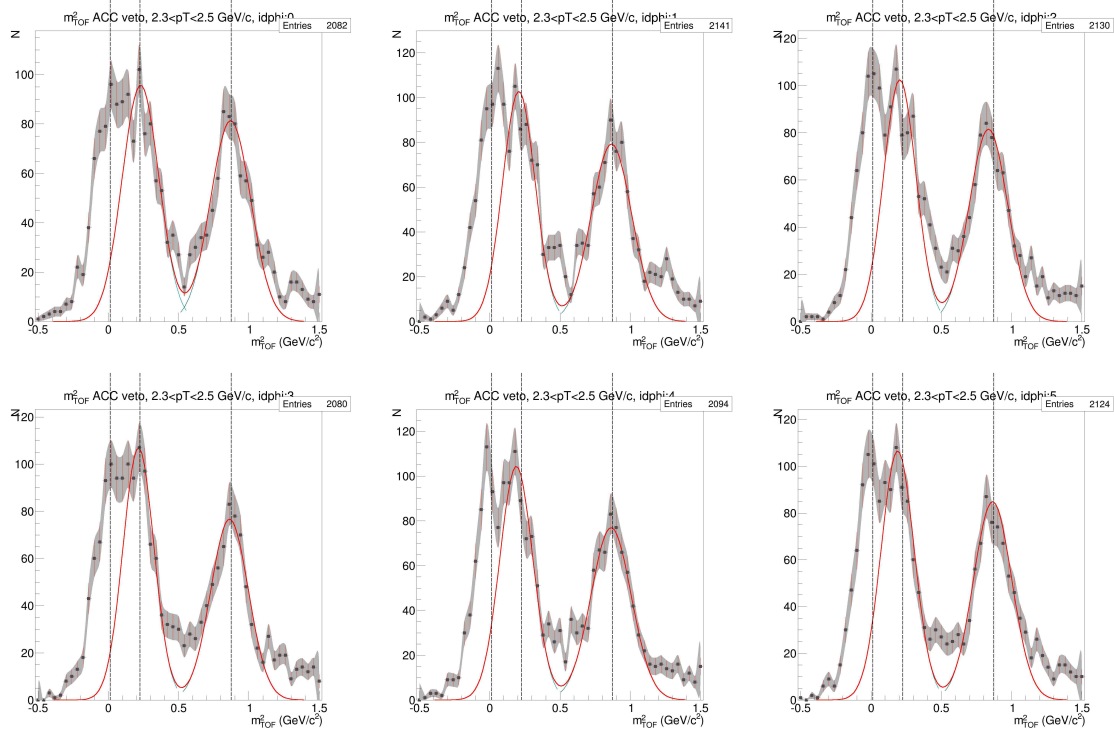


(e) PID parameters and Yields for ACC fired tracks

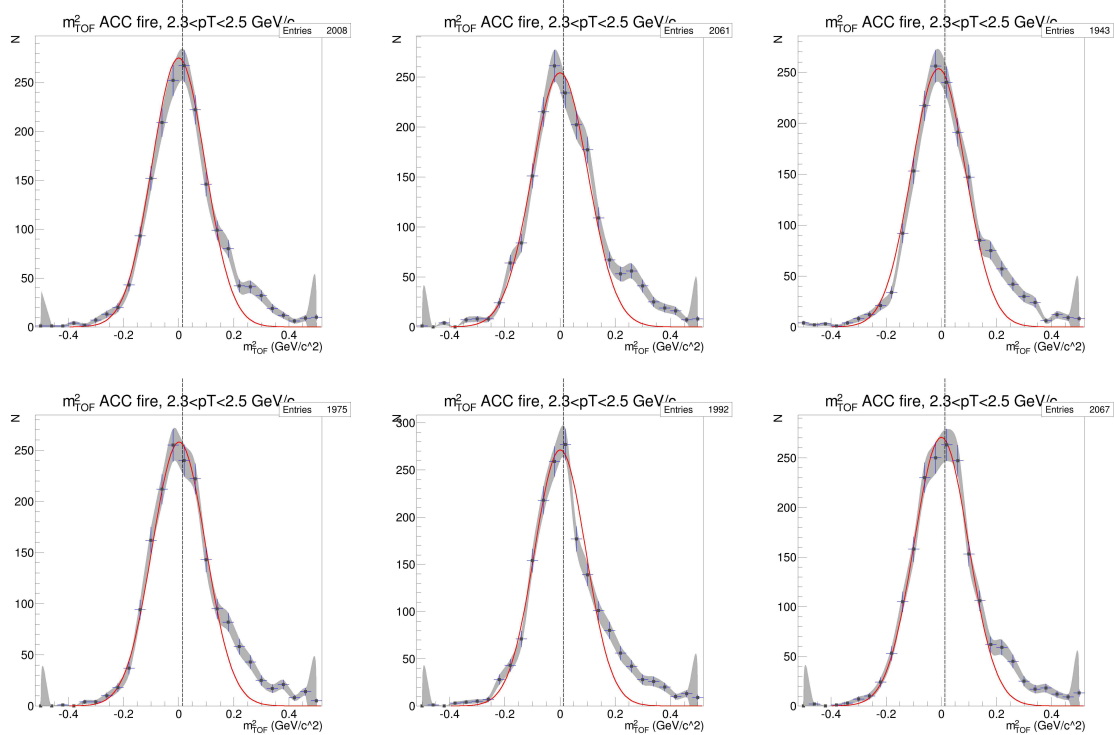
Figure D.21: ACC $N_{p.e.}$ vs m_2 , PID fits, and Yield vs $d\phi$ for $p_T=2.1-2.3$ GeV/c , TOF.W, negative particles



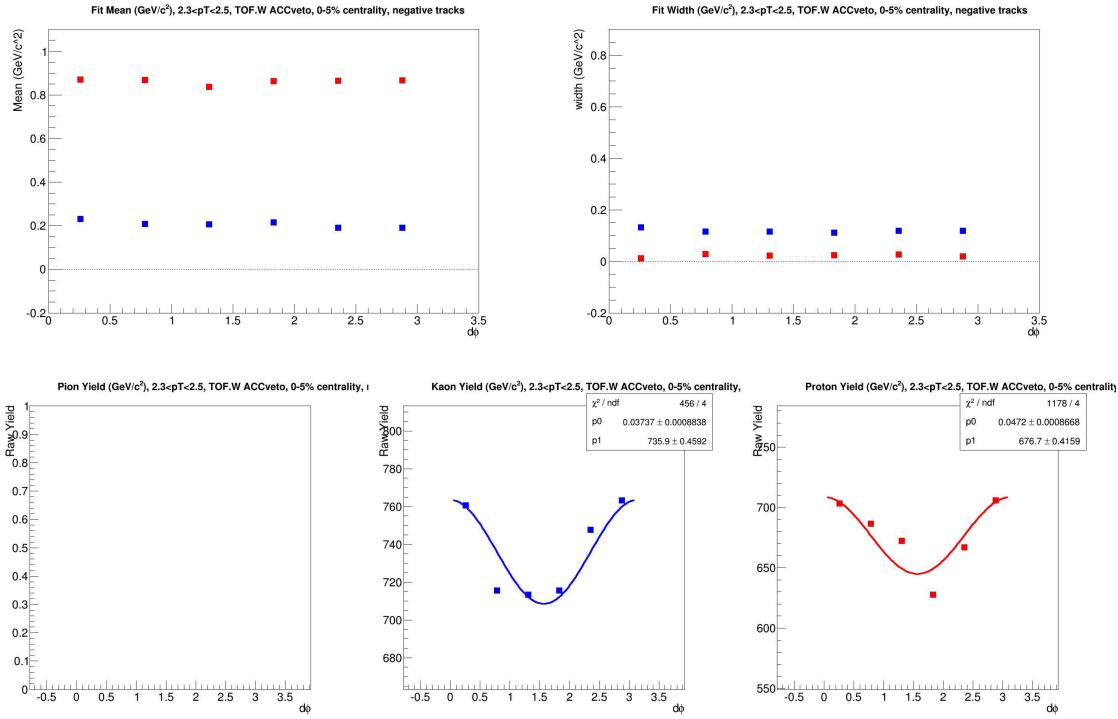
(a) $N_{p.e.}$ vs m^2



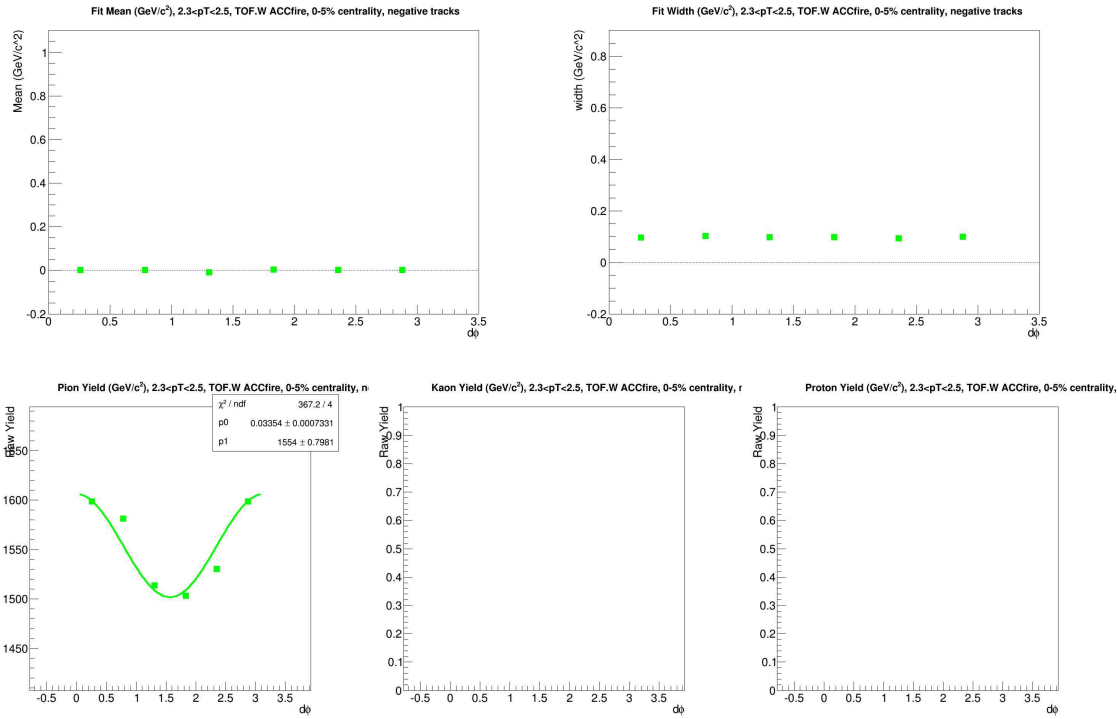
(b) m^2 for ACC vetoed tracks



(c) m^2 for ACC fired tracks

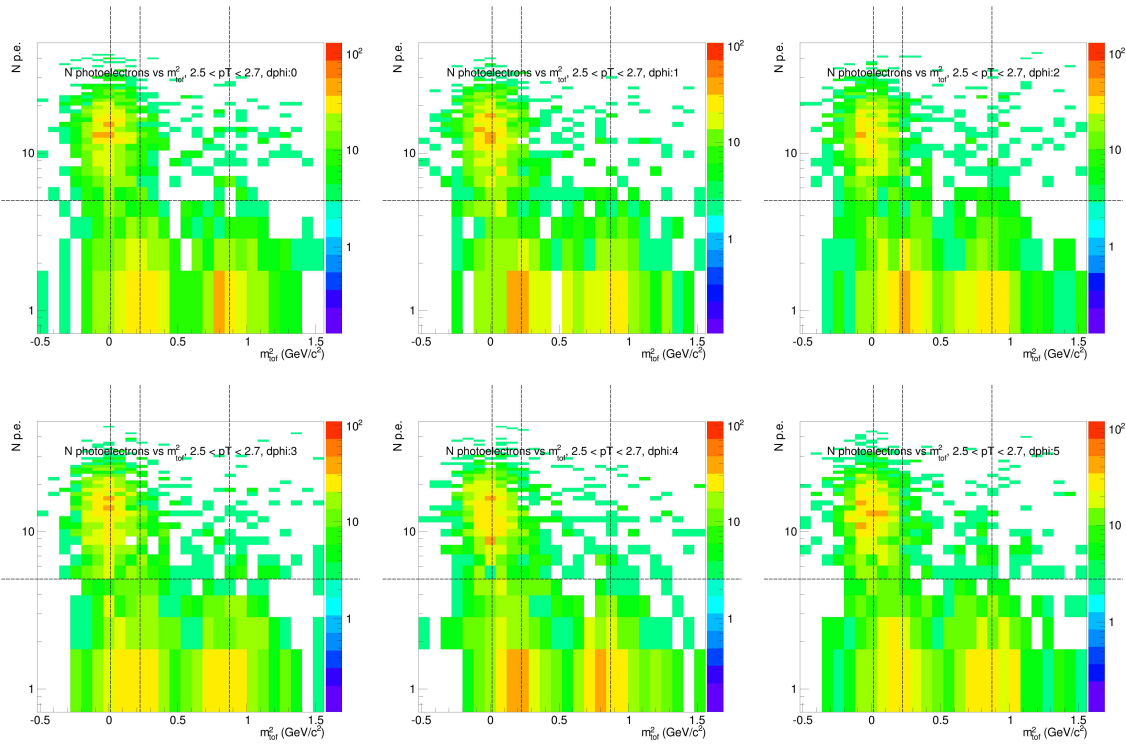


(d) PID parameters and Yields for ACC vetoed tracks

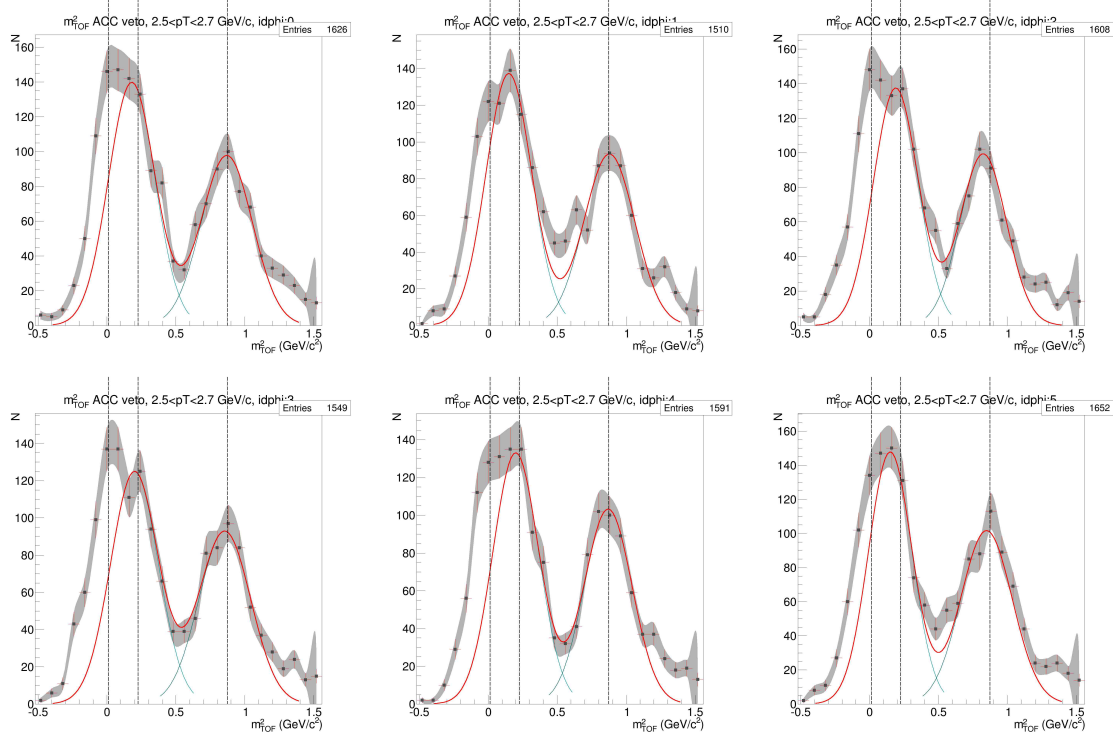


(e) PID parameters and Yields for ACC fired tracks

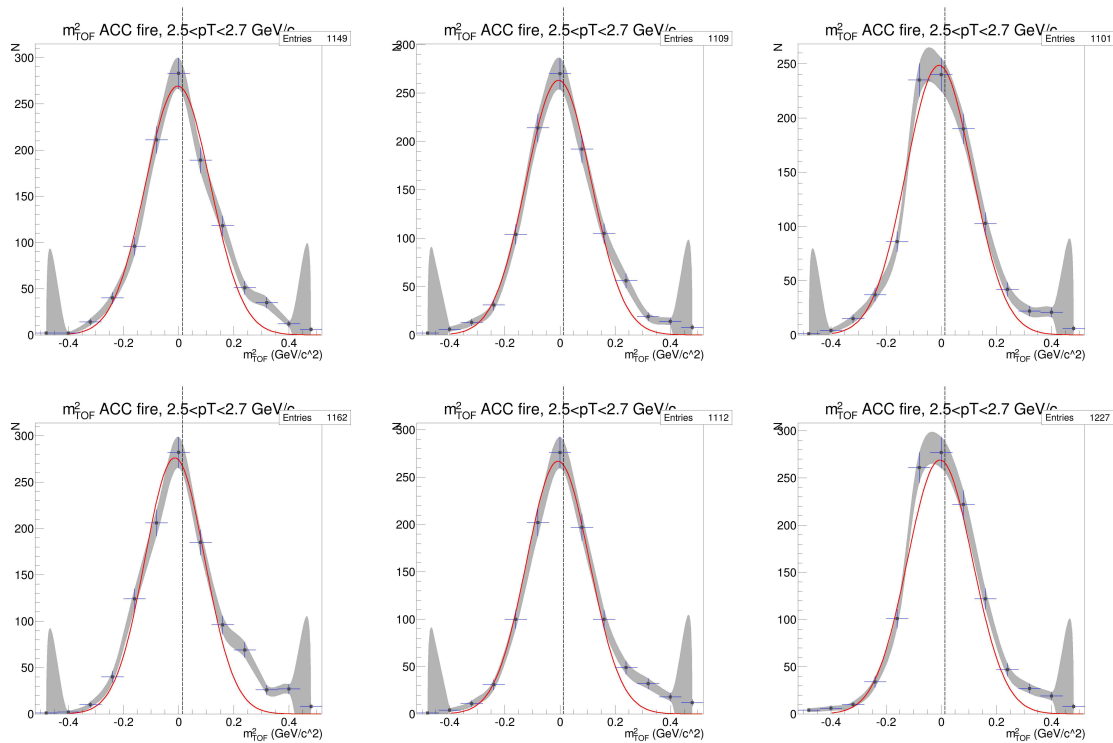
Figure D.22: ACC $N_{p.e.}$ vs m_2 , PID fits, and Yield vs $d\phi$ for $p_T=2.3-2.5$ GeV/c , TOF.W, negative particles



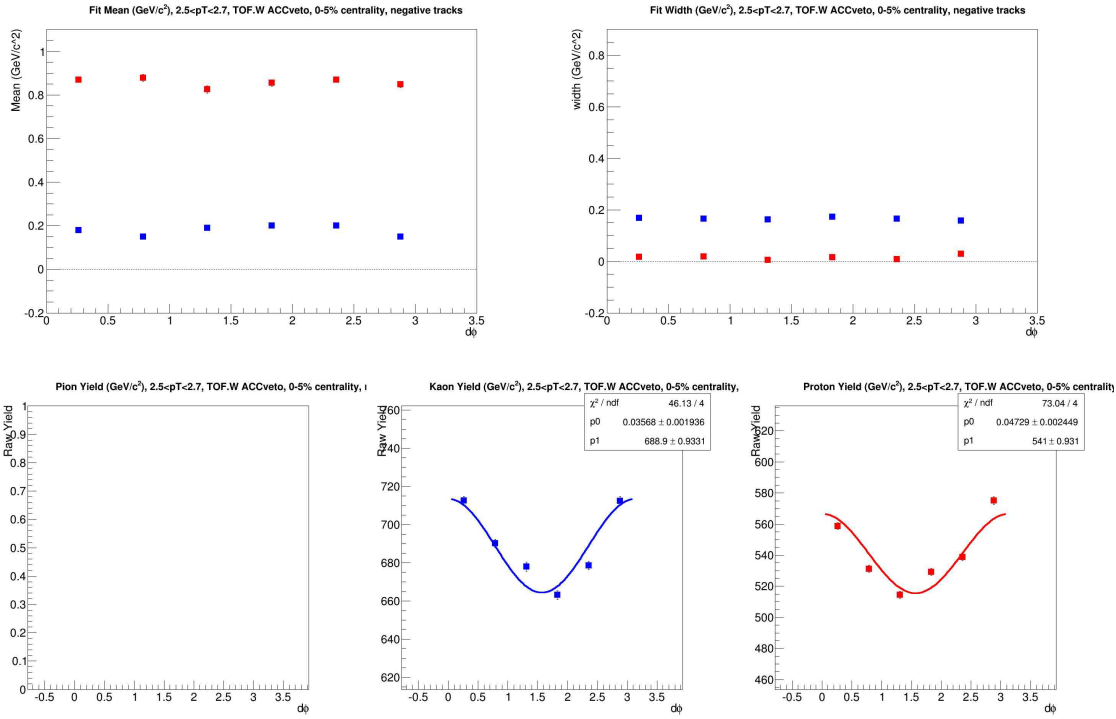
(a) $N_{p.e.}$ vs m^2



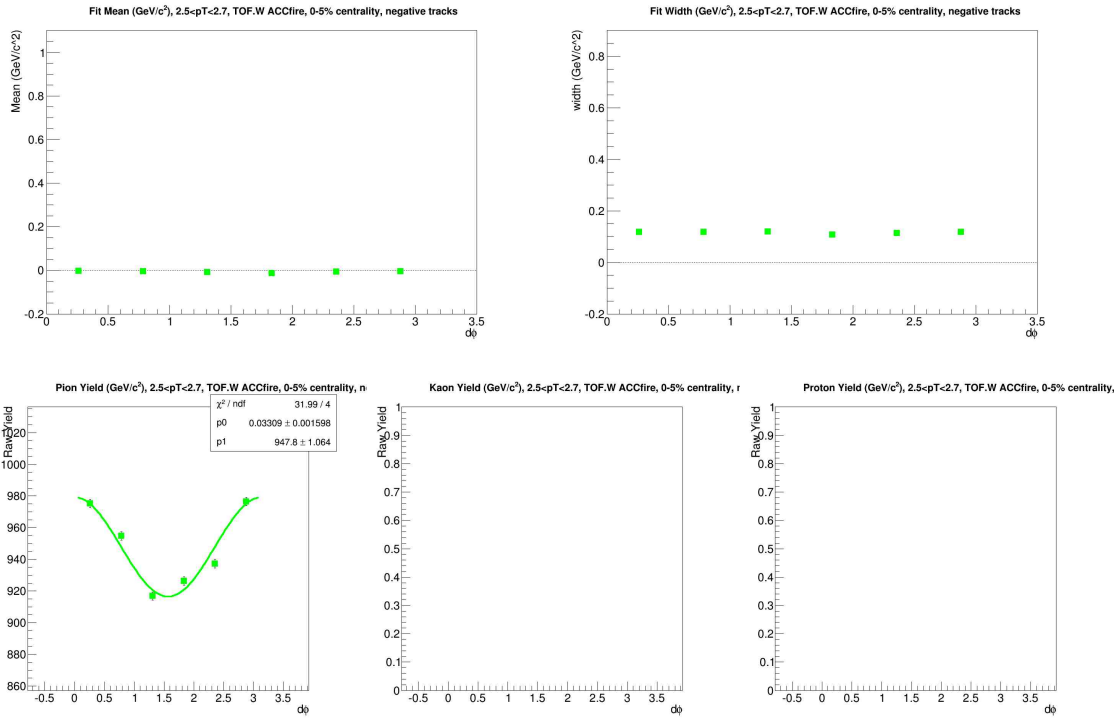
(b) m^2 for ACC vetoed tracks



(c) m^2 for ACC fired tracks

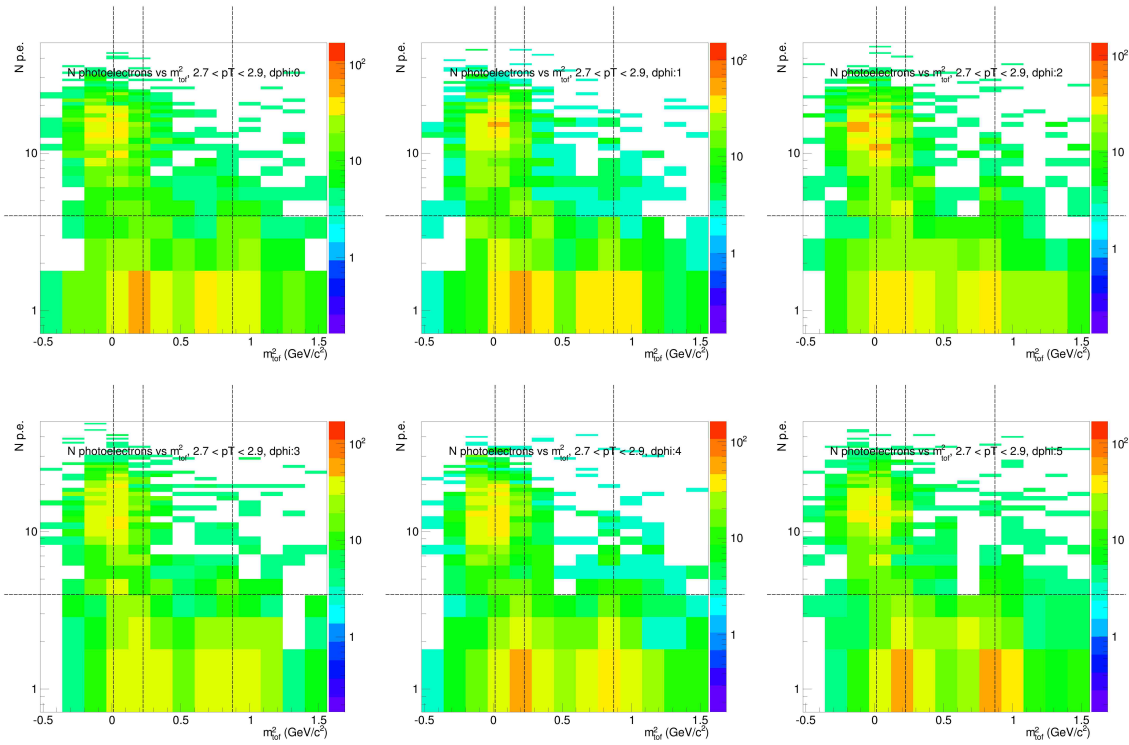


(d) PID parameters and Yields for ACC vetoed tracks

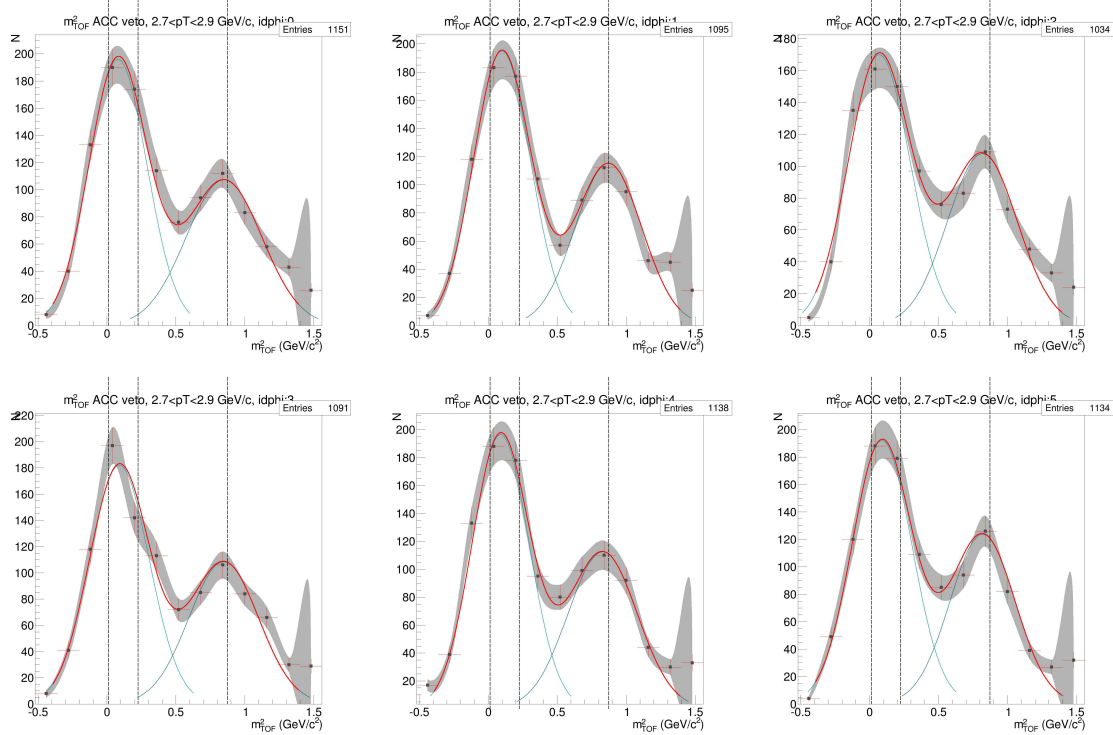


(e) PID parameters and Yields for ACC fired tracks

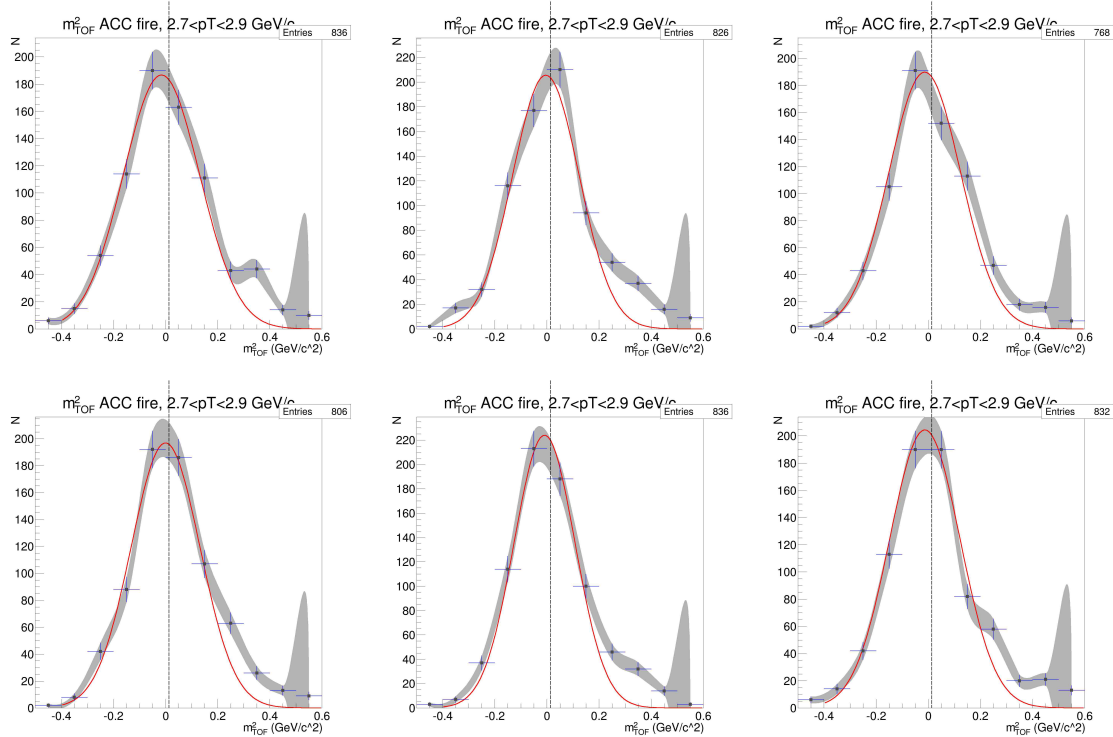
Figure D.23: ACC $N_{p.e.}$ vs m_2 , PID fits, and Yield vs $d\phi$ for $p_T=2.5-2.7$ GeV/c , TOF.W, negative particles



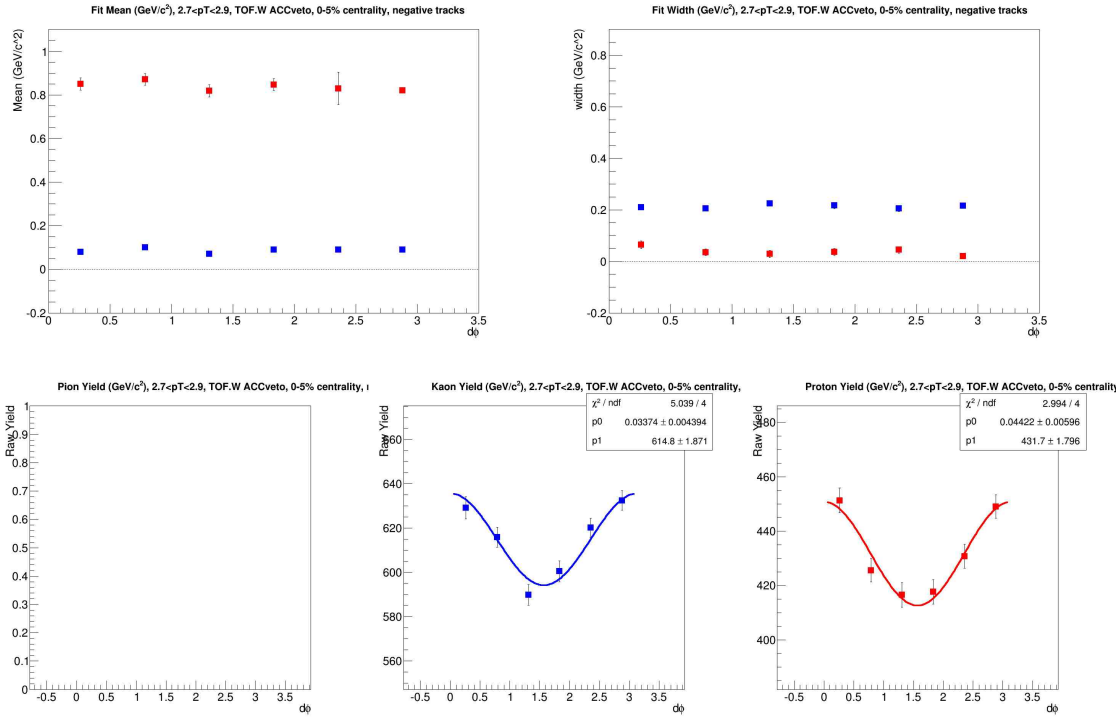
(a) $N_{p.e.}$ vs m^2



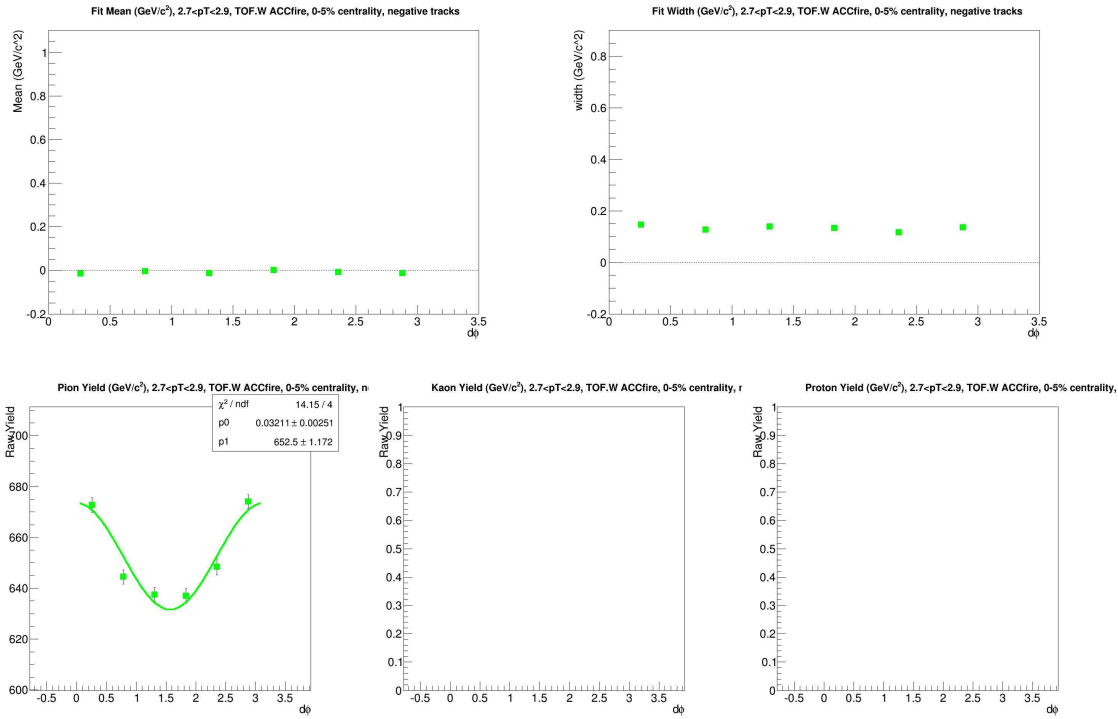
(b) m^2 for ACC vetoed tracks



(c) m^2 for ACC fired tracks

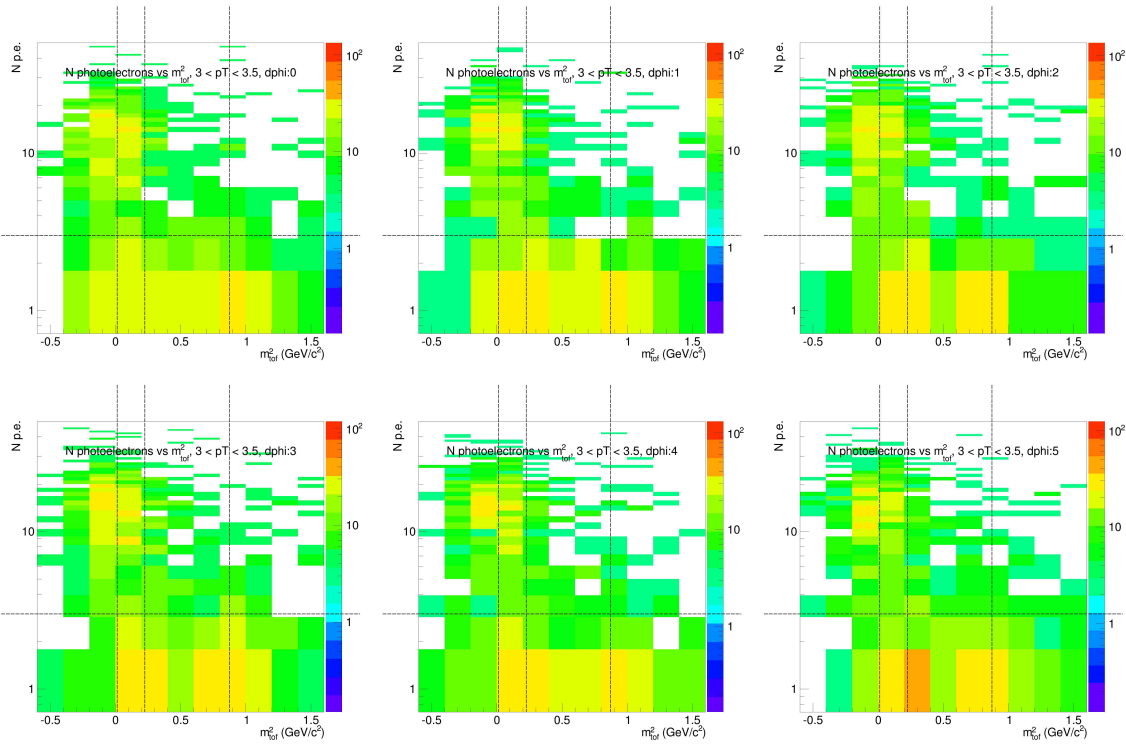


(d) PID parameters and Yields for ACC vetoed tracks

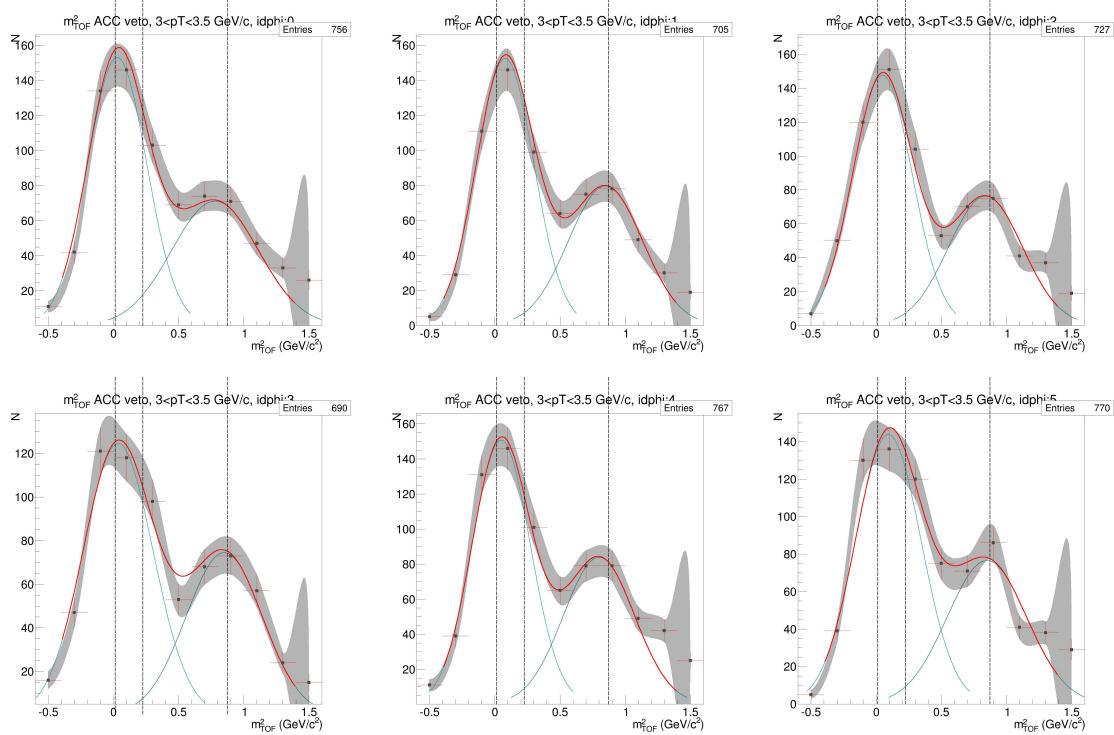


(e) PID parameters and Yields for ACC fired tracks

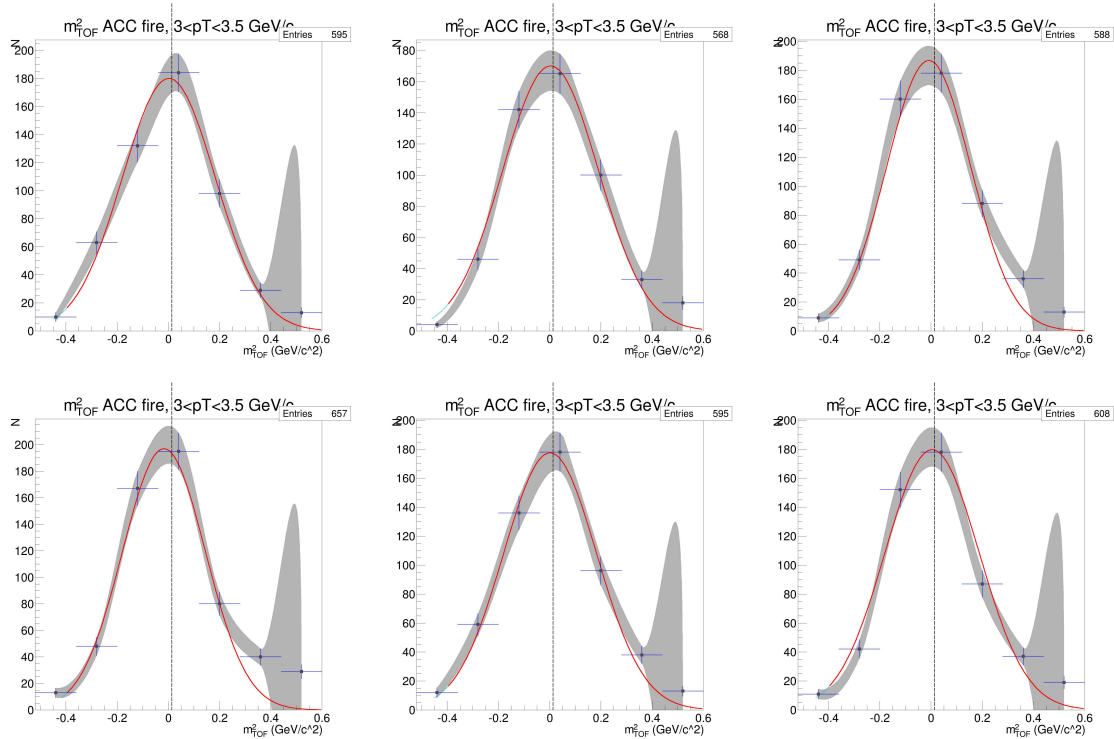
Figure D.24: ACC $N_{p.e.}$ vs m_2 , PID fits, and Yield vs $d\phi$ for $p_T = 2.7$ - 2.9 GeV/c , TOF.W, negative particles

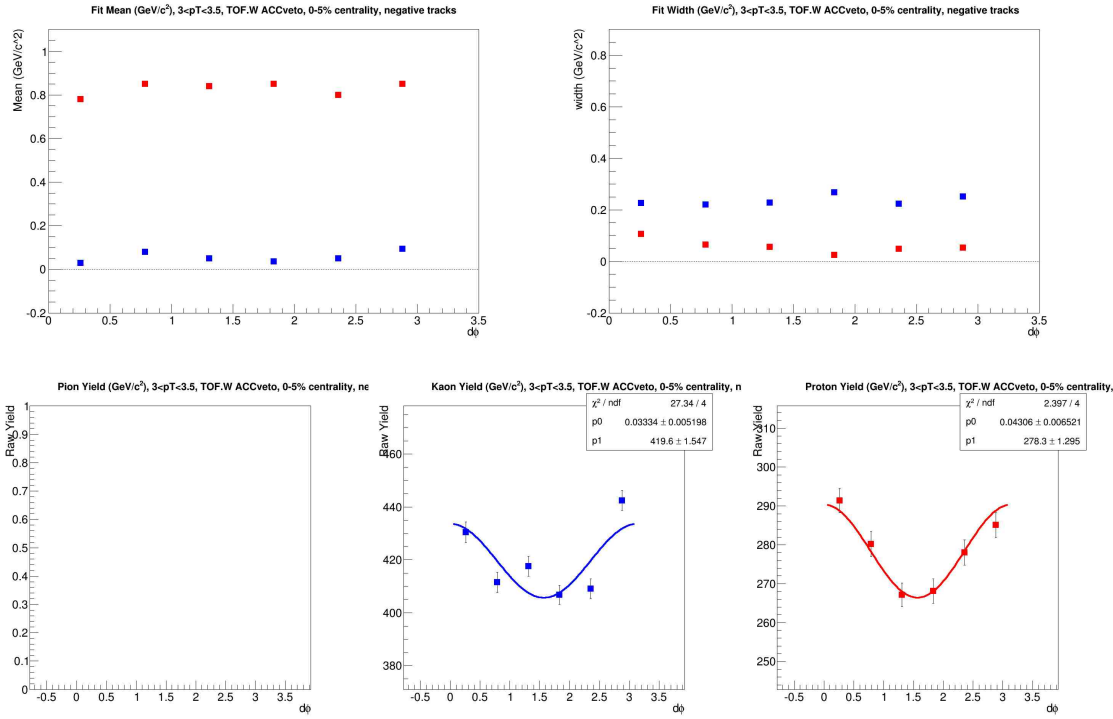


(a) $N_{p.e.}$ vs m^2

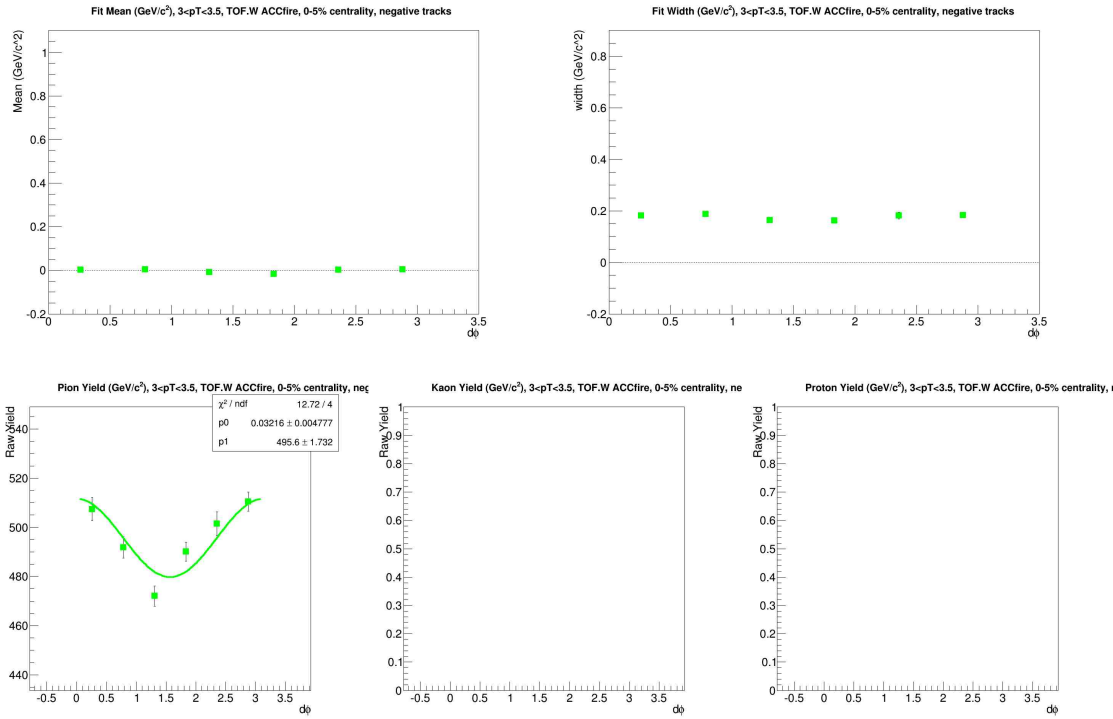


(b) m^2 for ACC vetoed tracks



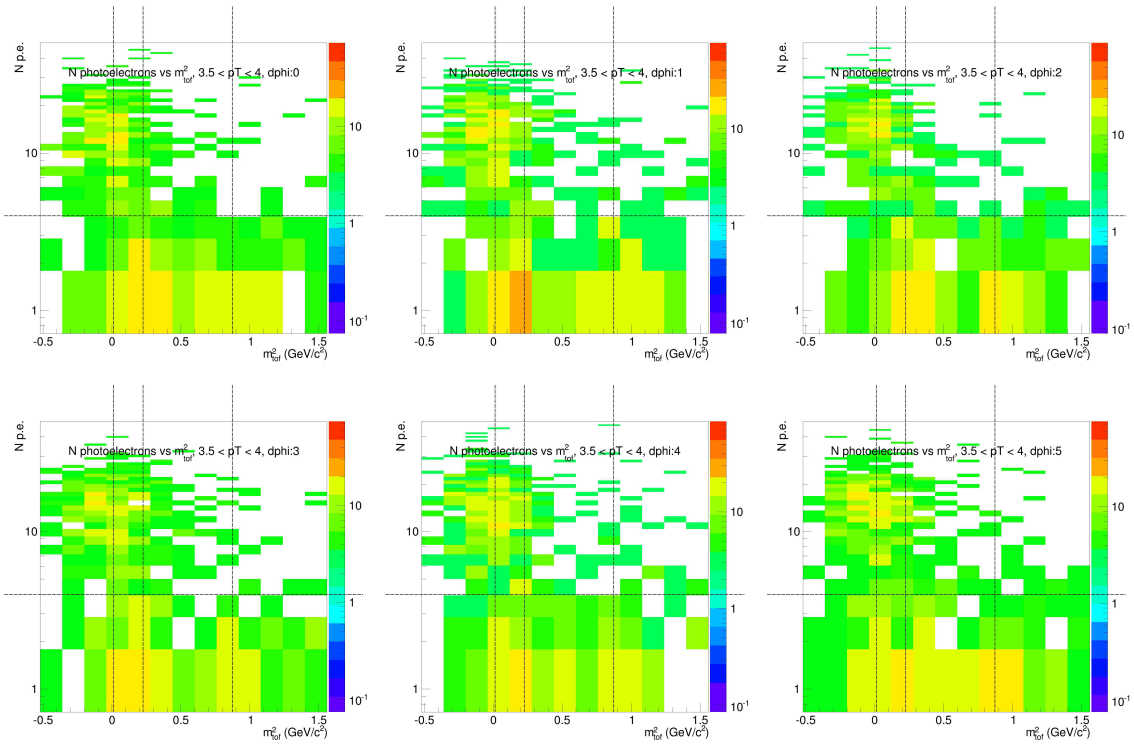


(d) PID parameters and Yields for ACC vetoed tracks

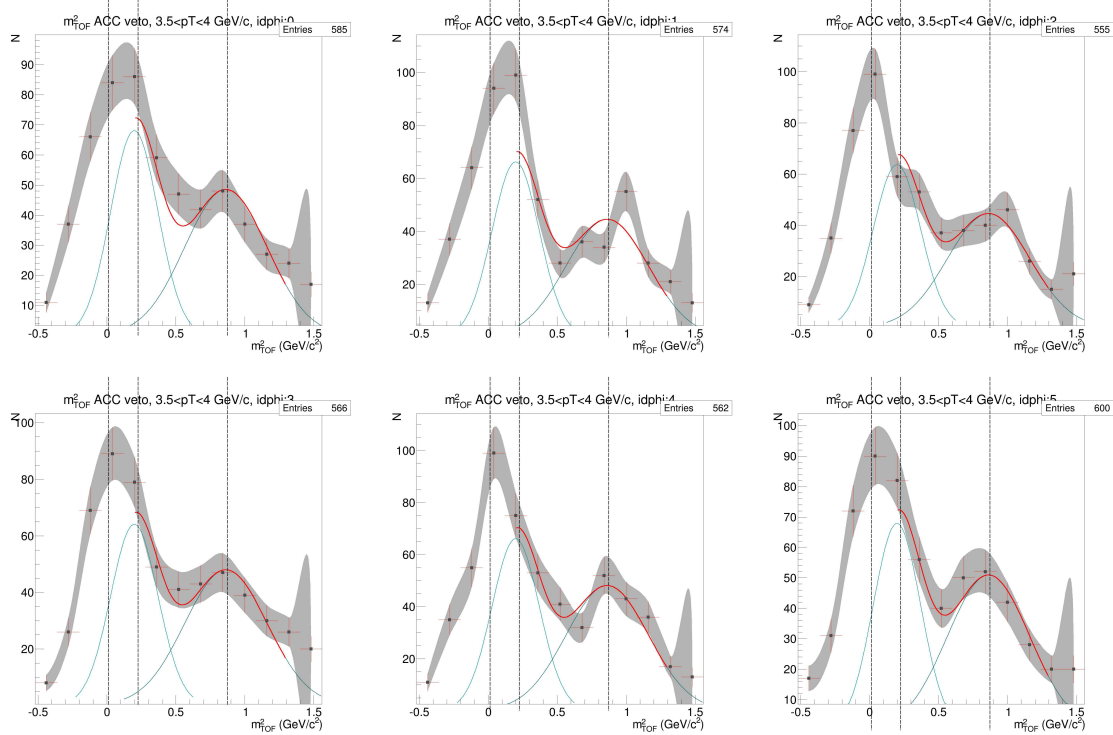


(e) PID parameters and Yields for ACC fired tracks

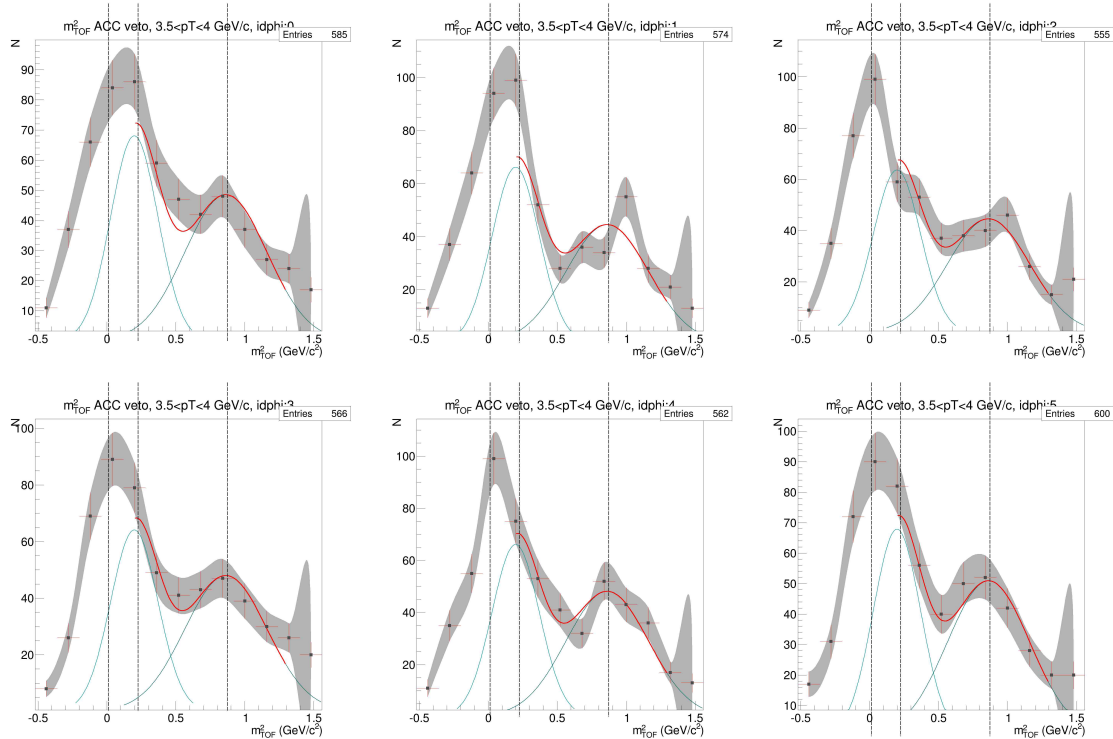
Figure D.25: ACC $N_{p.e.}$ vs m_2 , PID fits, and Yield vs $d\phi$ for $p_T=3.0-3.5$ GeV/c , TOF.W, negative particles



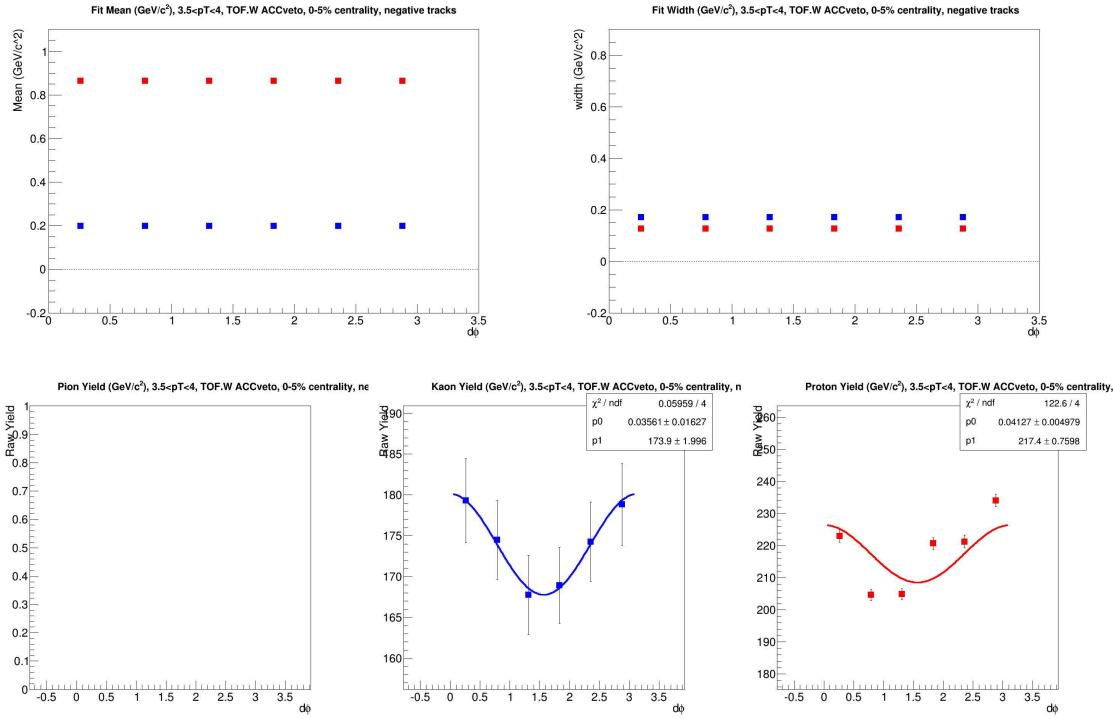
(a) $N_{p.e.}$ vs m^2



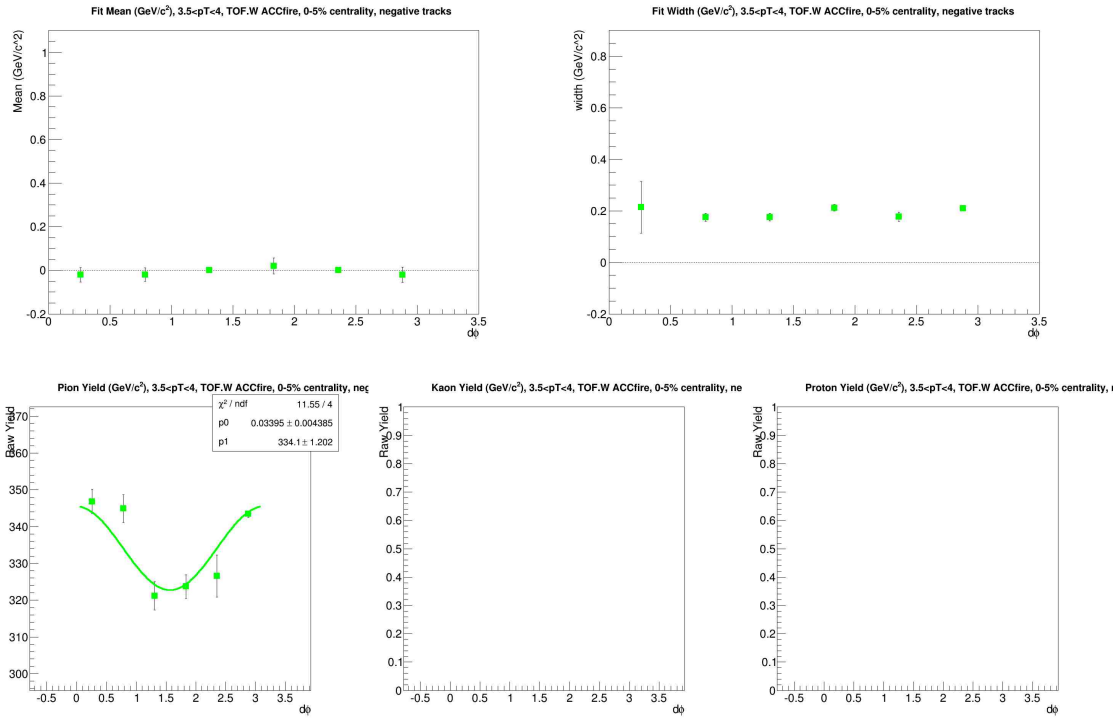
(b) m^2 for ACC vetoed tracks



(c) m^2 for ACC fired tracks

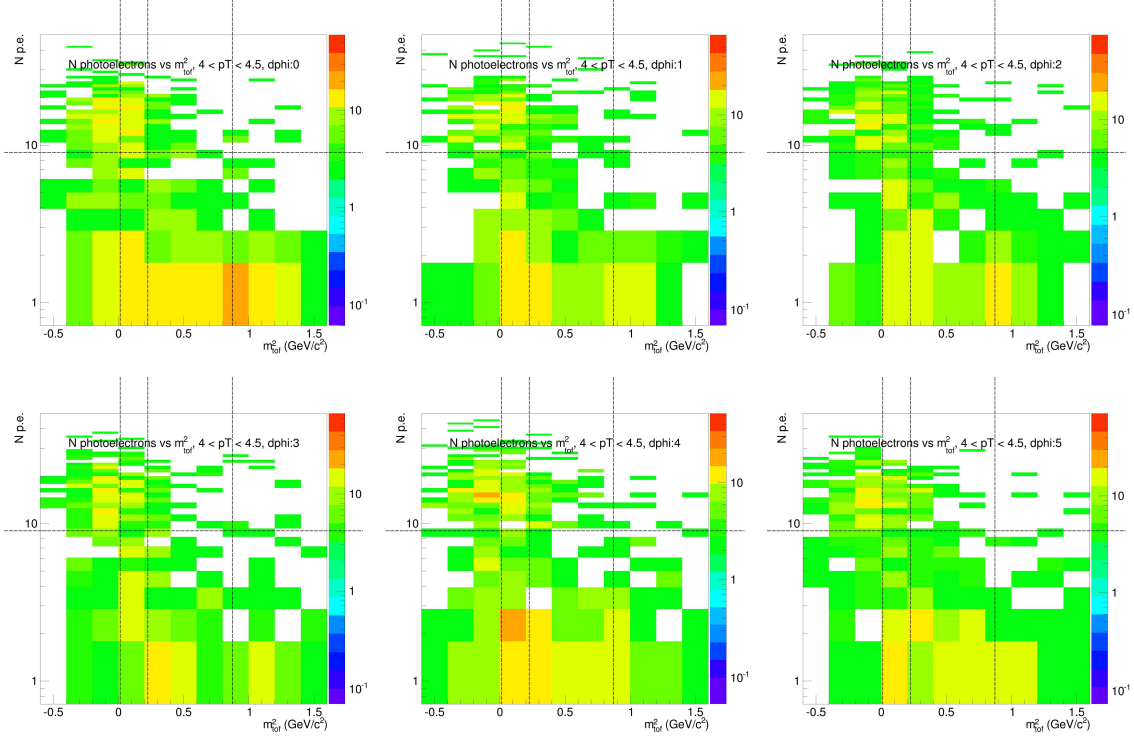


(d) PID parameters and Yields for ACC vetoed tracks

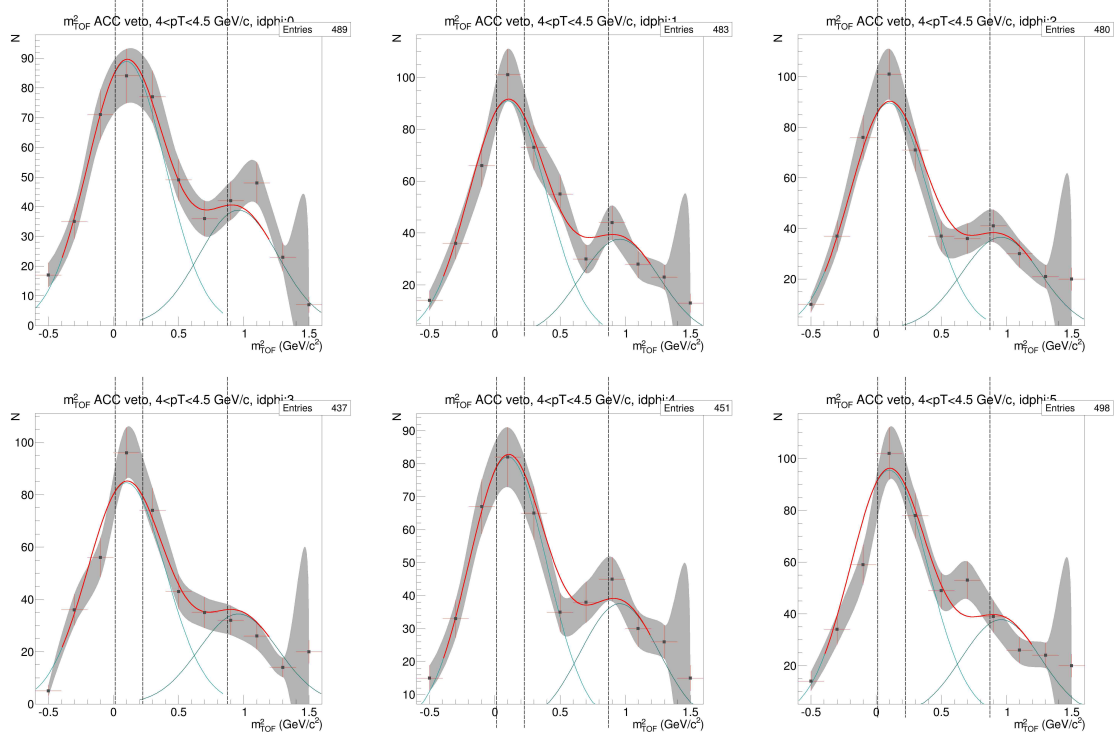


(e) PID parameters and Yields for ACC fired tracks

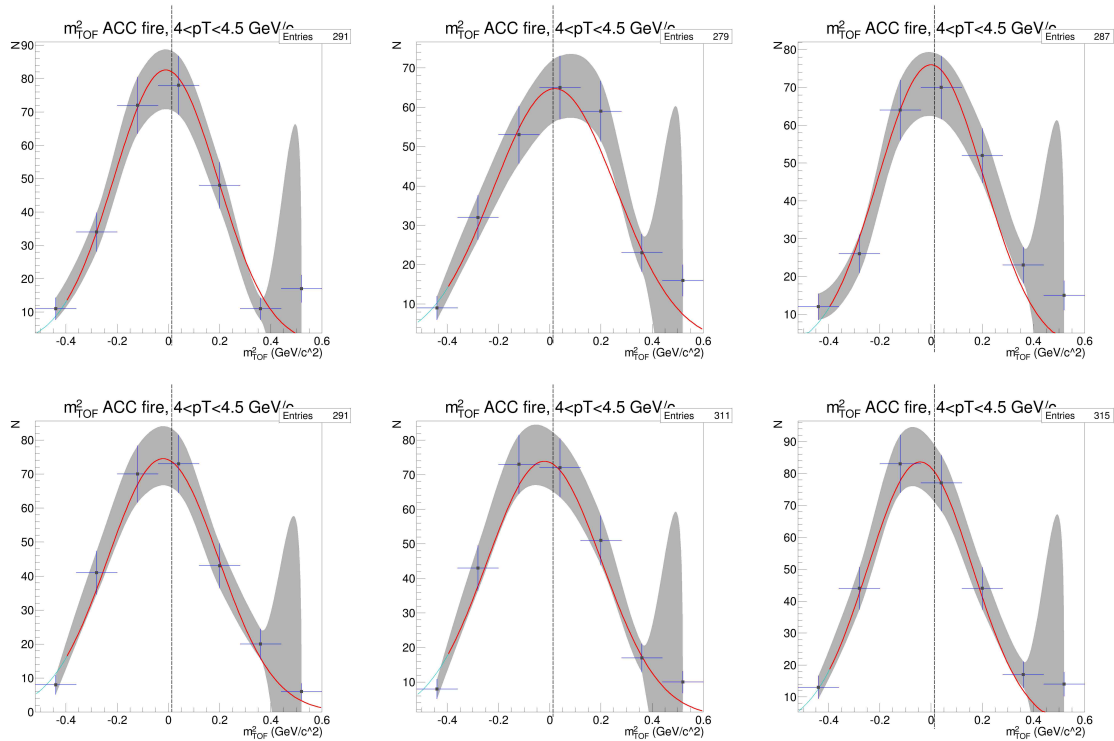
Figure D.26: ACC $N_{p.e.}$ vs m_2 , PID fits, and Yield vs $d\phi$ for $p_T=3.5-4.0$ GeV/c , TOF.W, negative particles



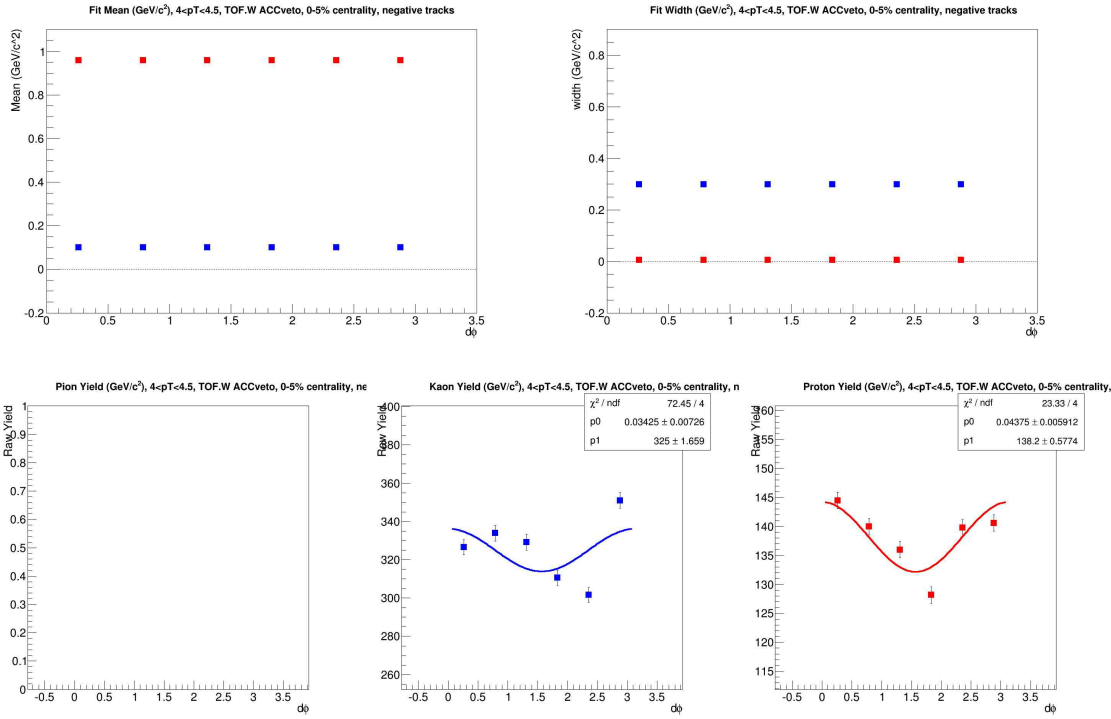
(a) $N_{p.e.}$ vs m^2



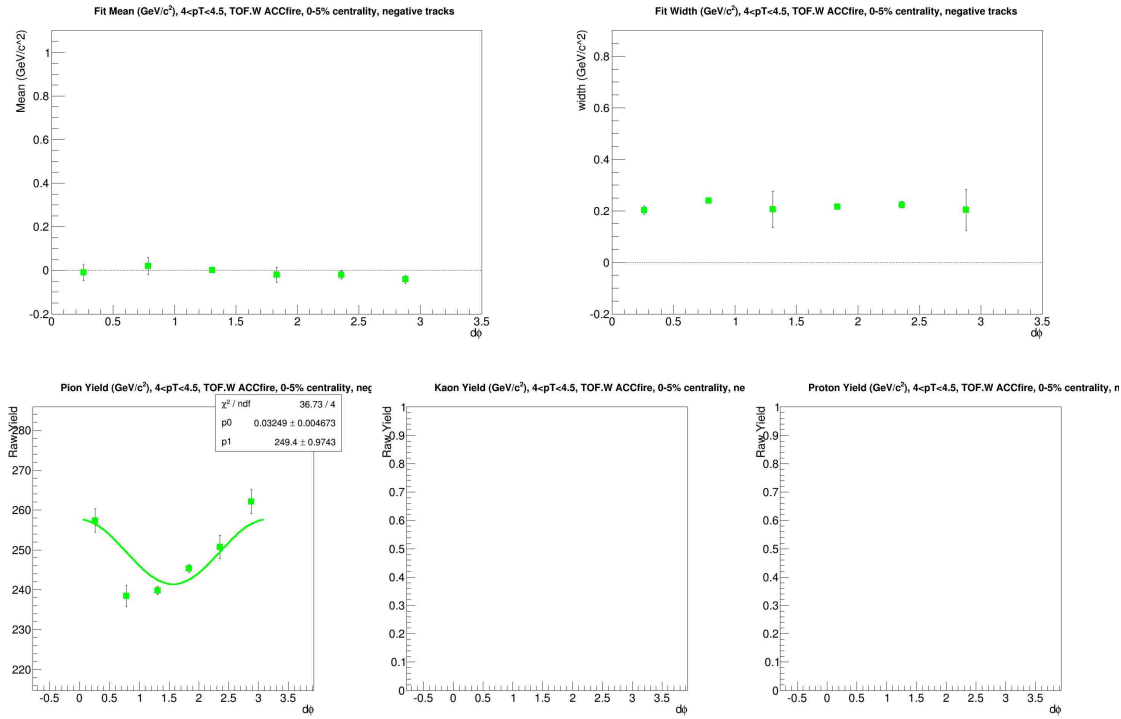
(b) m^2 for ACC vetoed tracks



(c) m^2 for ACC fired tracks



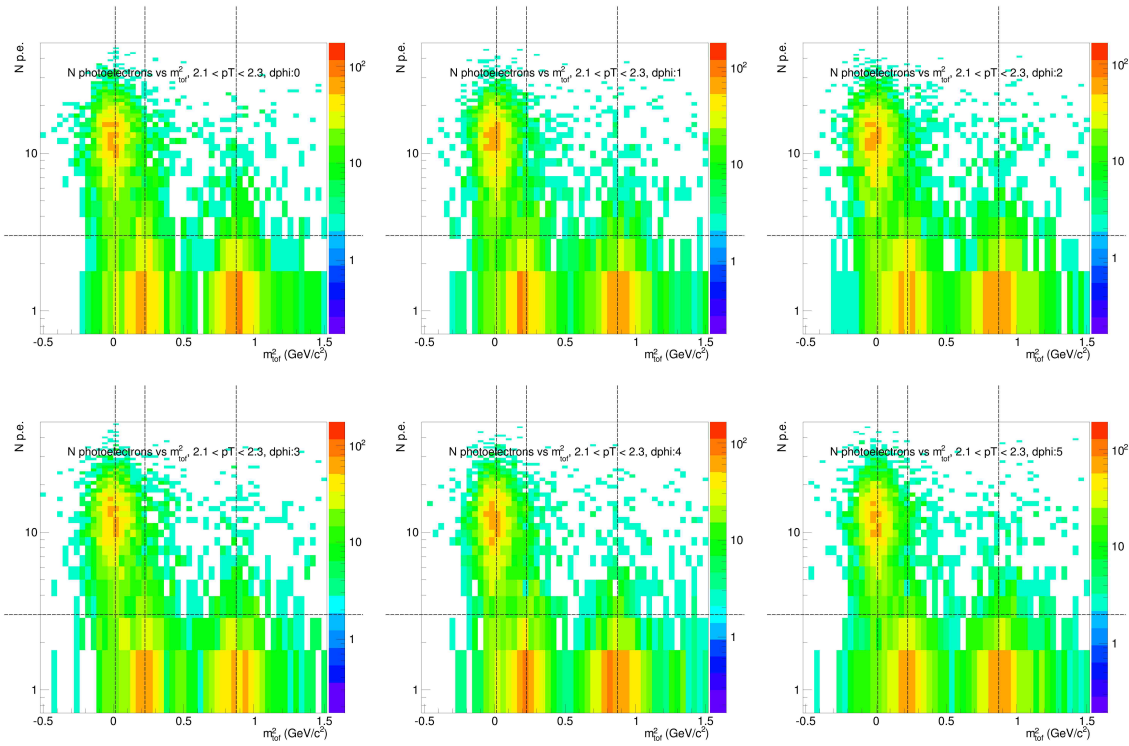
(d) PID parameters and Yields for ACC vetoed tracks



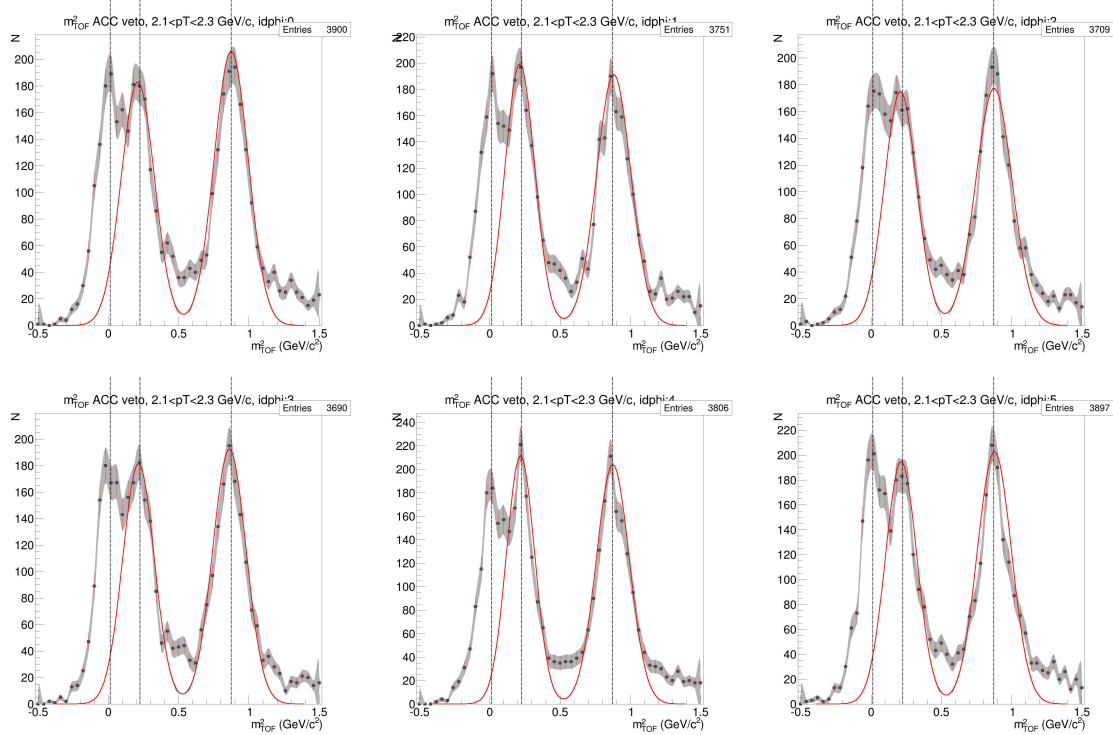
(e) PID parameters and Yields for ACC fired tracks

Figure D.27: ACC $N_{p.e.}$ vs m_2 , PID fits, and Yield vs $d\phi$ for $p_T = 4.0-4.5$ GeV/c, TOF.W, negative particles

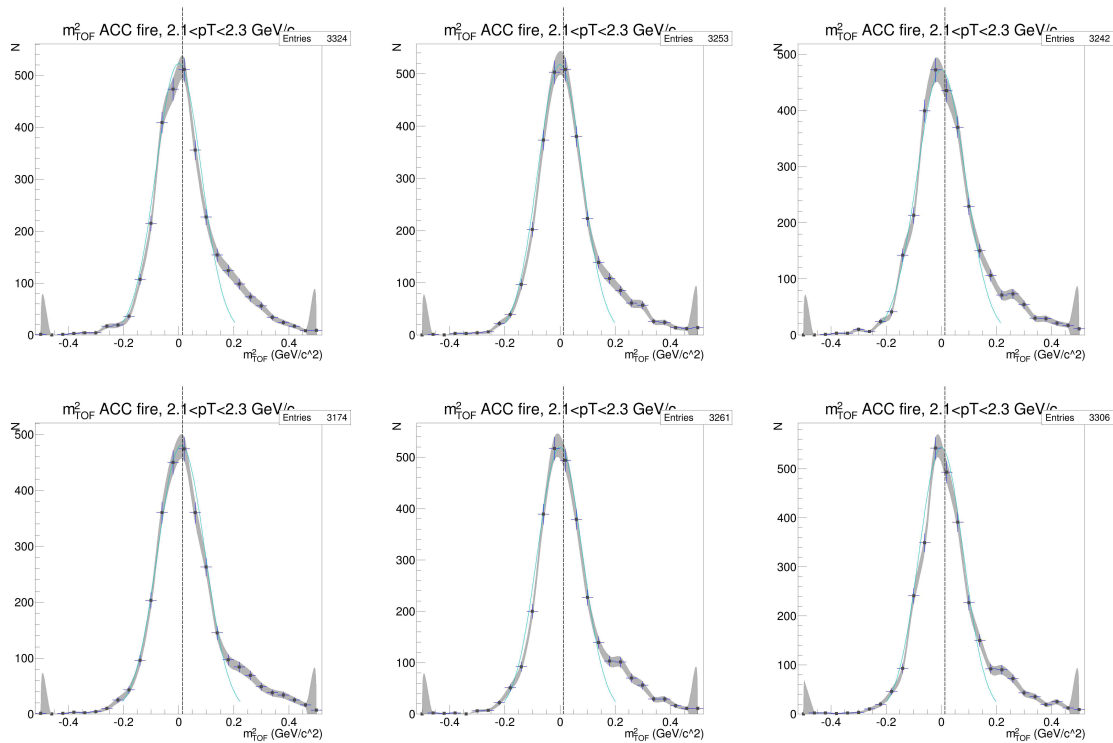
D.2.5 TOF.W and ACC, $p_T=2.1\text{-}3.5$ GeV, positive charged tracks



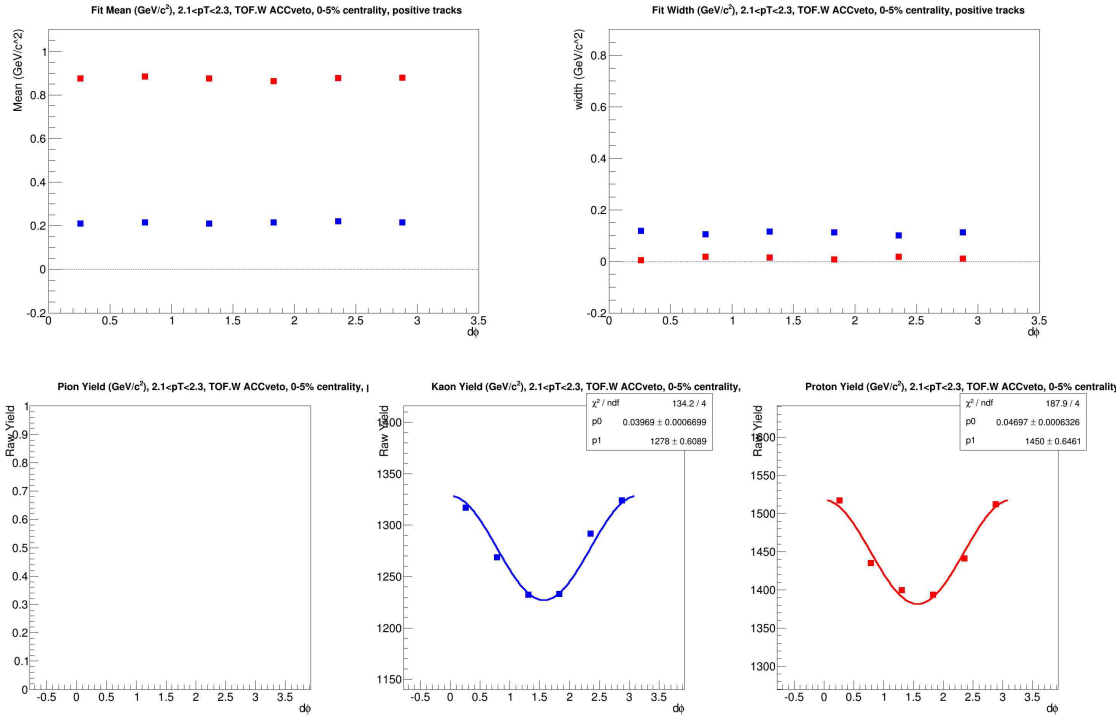
(a) $N_{p.e.}$ vs m^2



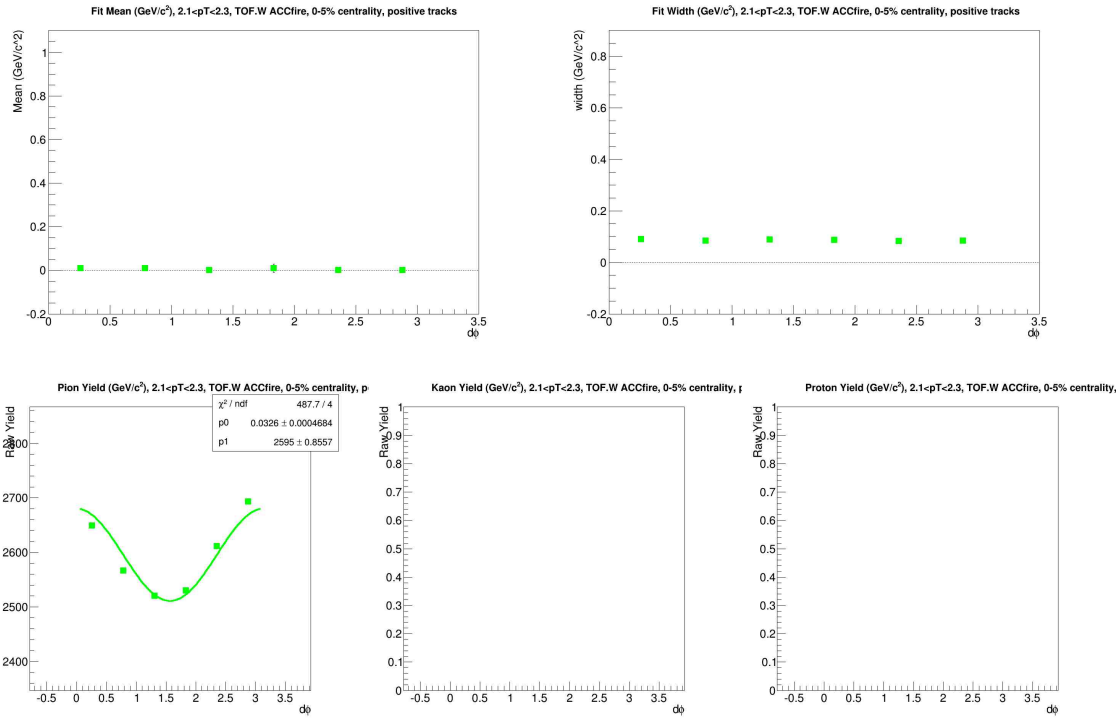
(b) m^2 for ACC vetoed tracks



(c) m^2 for ACC fired tracks

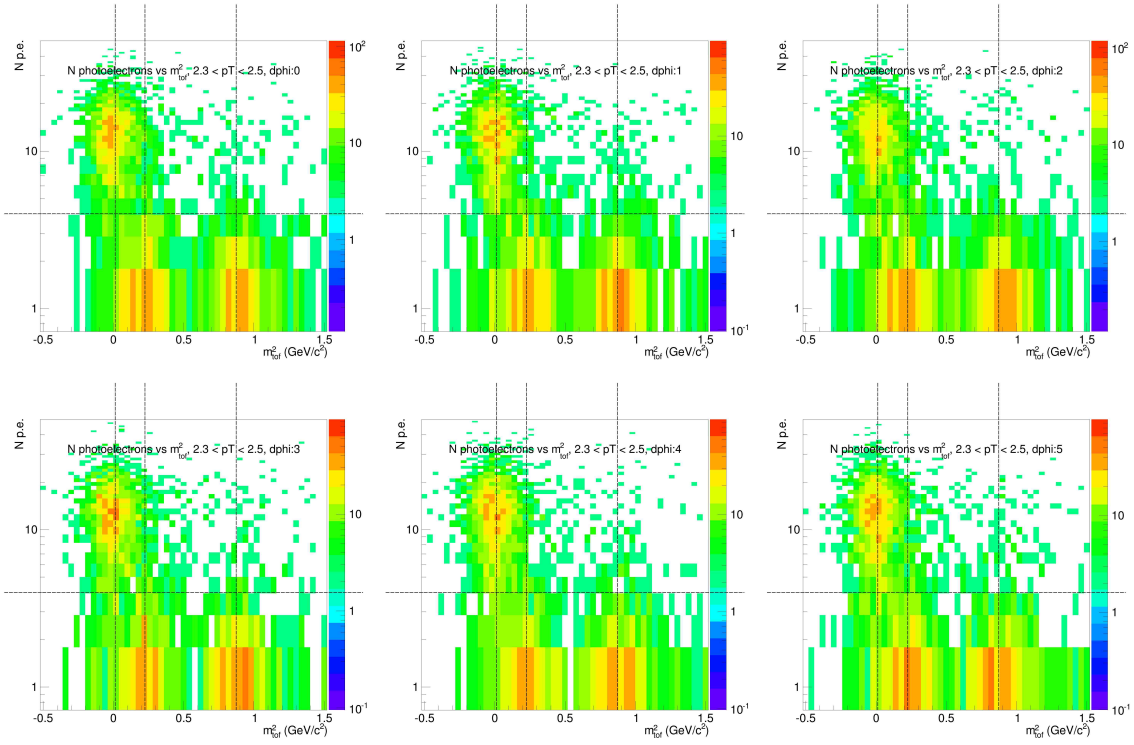


(d) PID parameters and Yields for ACC vetoed tracks

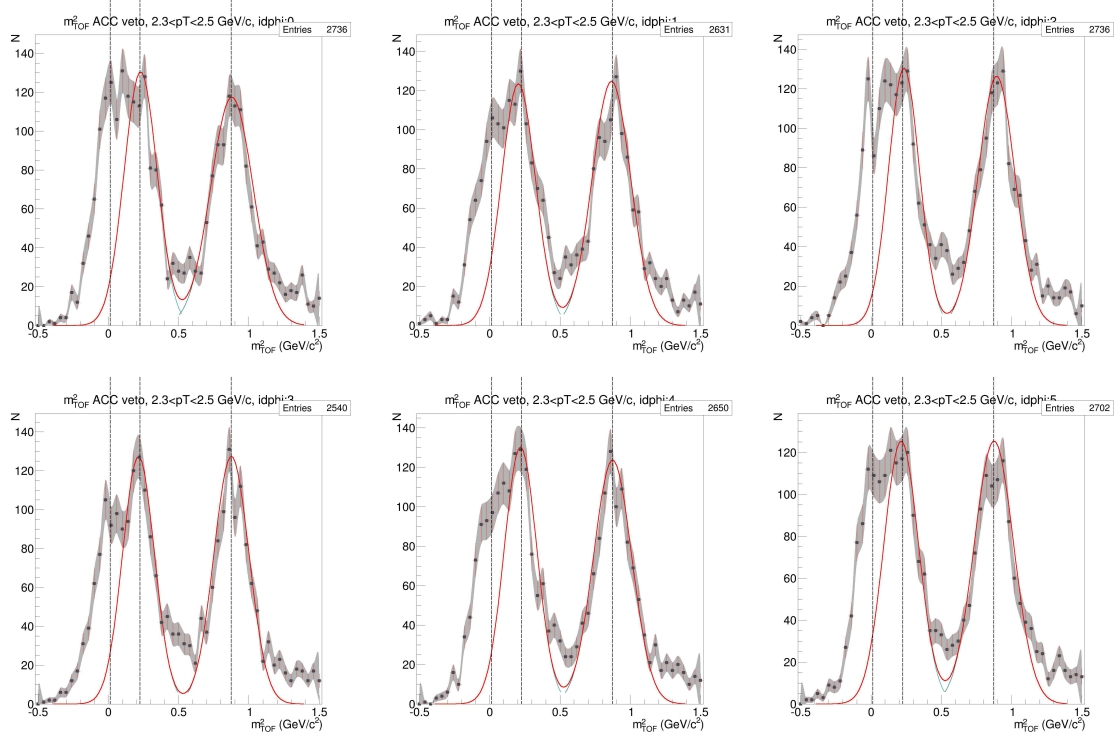


(e) PID parameters and Yields for ACC fired tracks

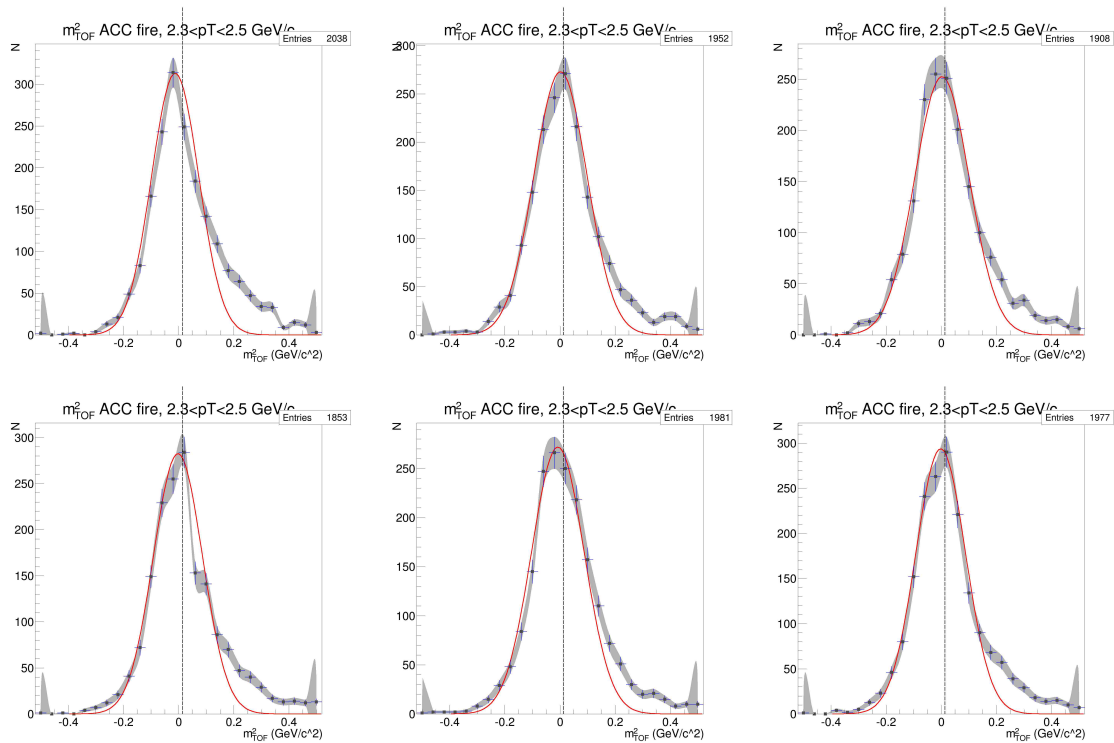
Figure D.28: ACC $N_{p.e.}$ vs m_2 , PID fits, and Yield vs $d\phi$ for $p_T=2.1-2.3$ GeV/c , TOF.W, positive particles



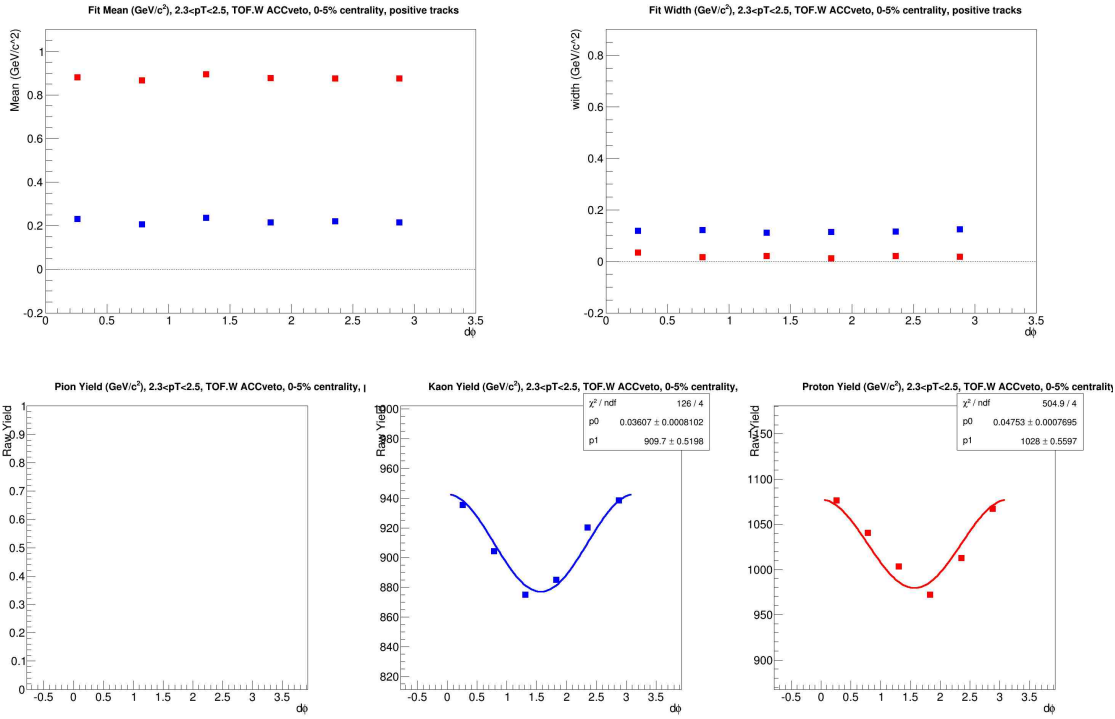
(a) $N_{p.e.}$ vs m^2



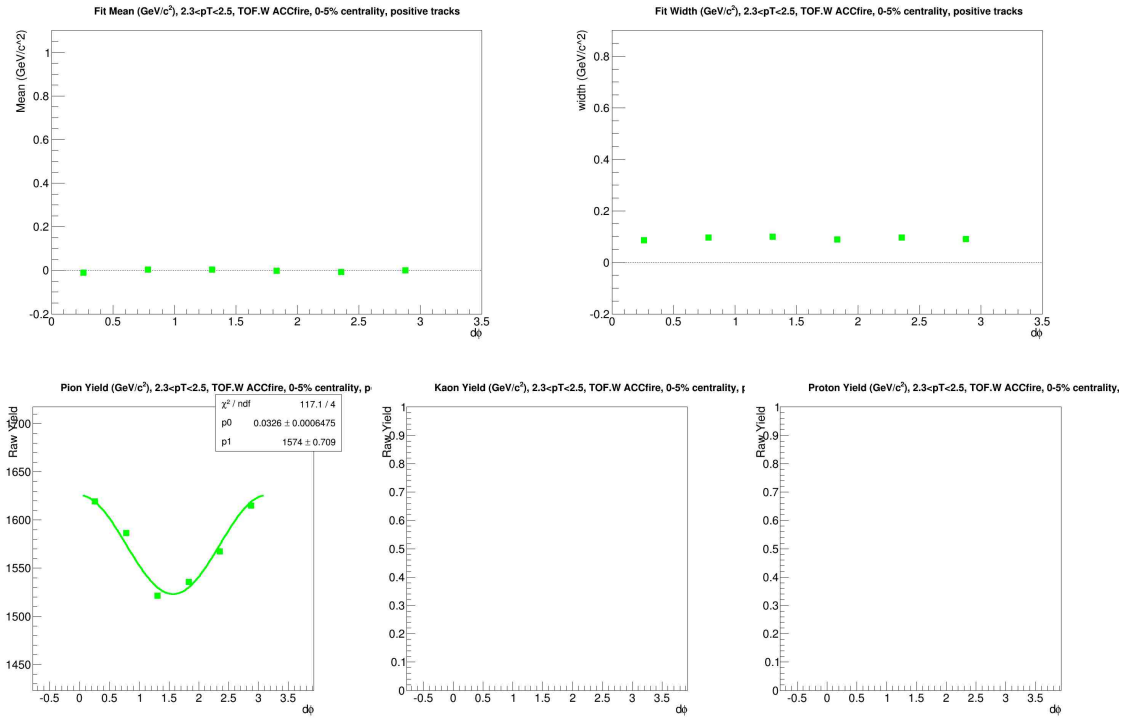
(b) m^2 for ACC vetoed tracks



(c) m^2 for ACC fired tracks

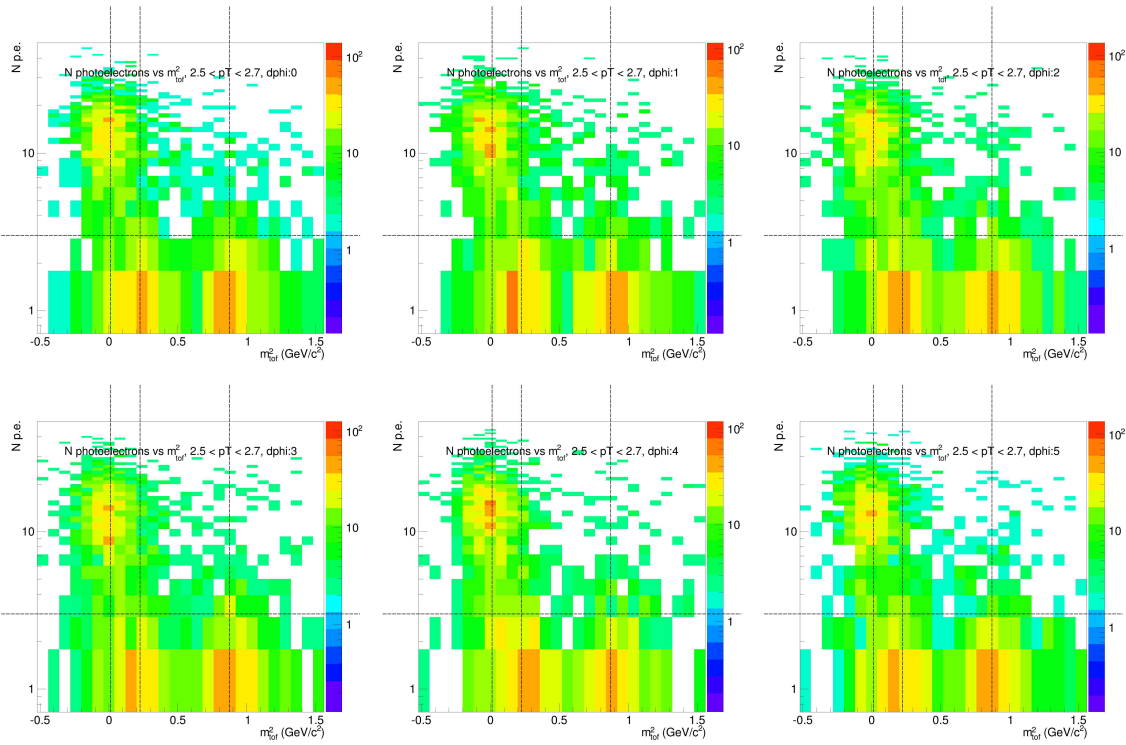


(d) PID parameters and Yields for ACC vetoed tracks

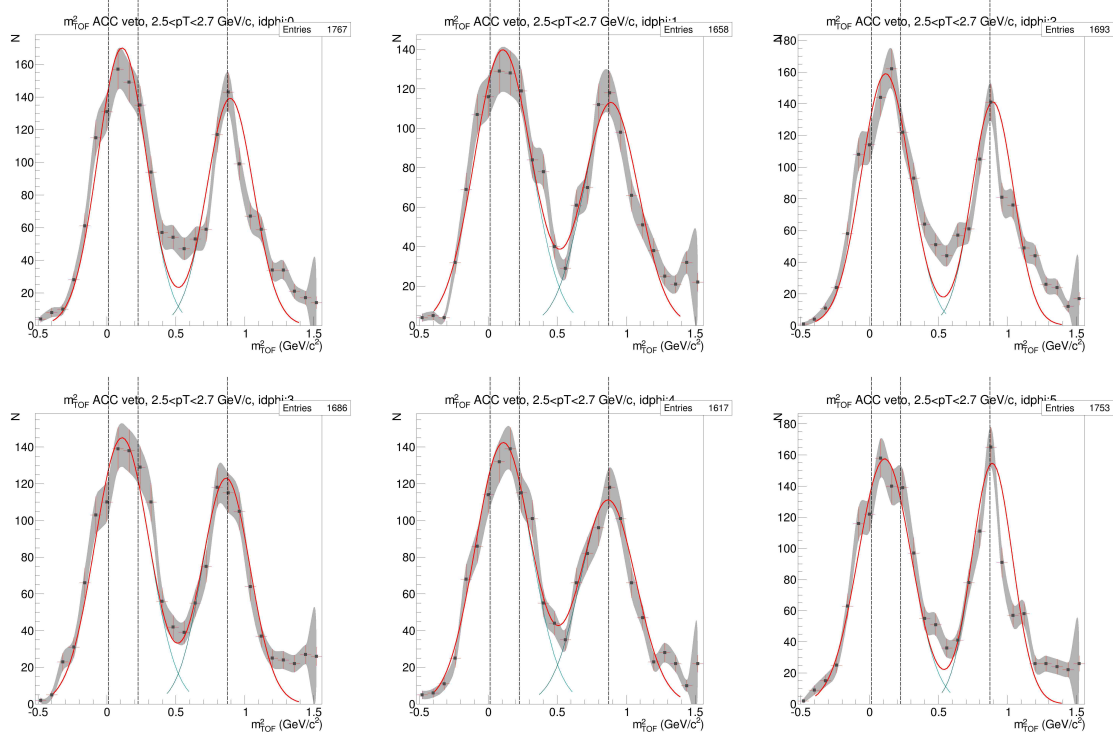


(e) PID parameters and Yields for ACC fired tracks

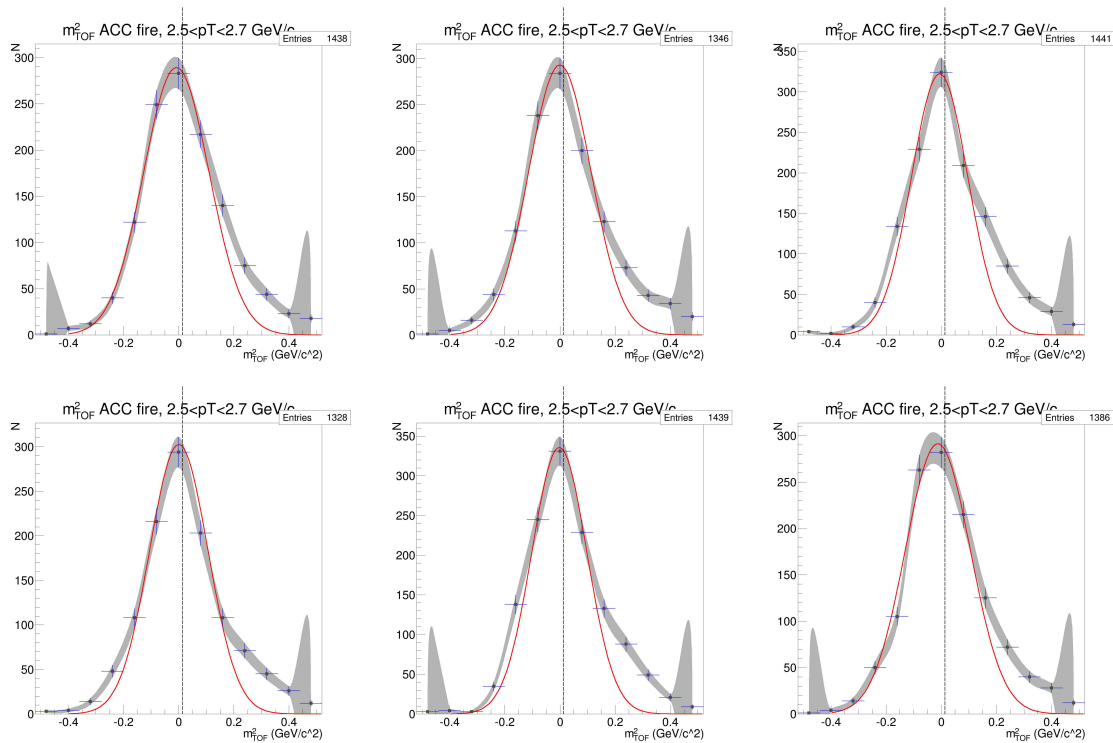
Figure D.29: ACC $N_{p.e.}$ vs m_2 , PID fits, and Yield vs $d\phi$ for $p_T=2.3-2.5$ GeV/c , TOF.W, positive particles



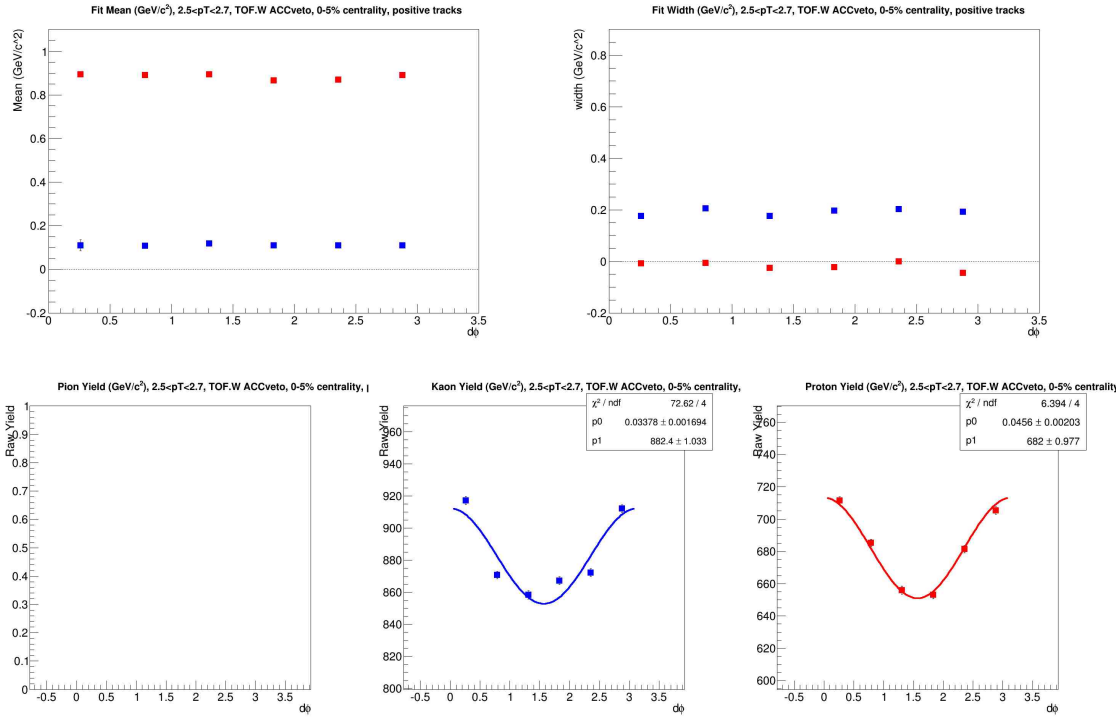
(a) $N_{p.e.}$ vs m^2



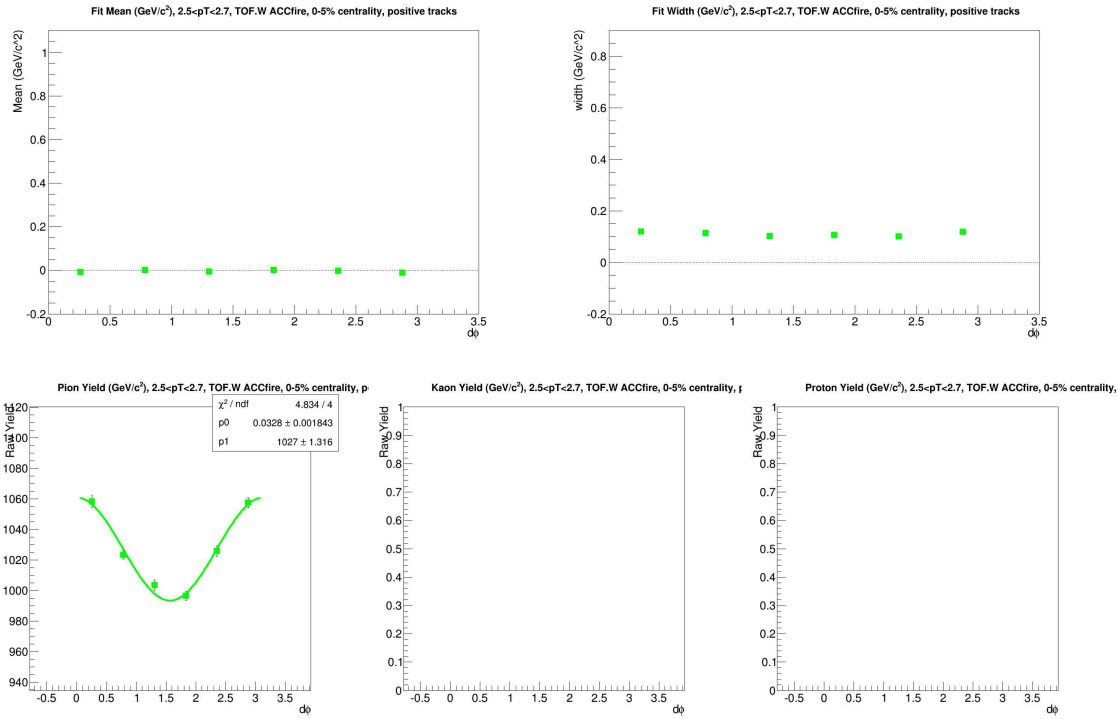
(b) m^2 for ACC vetoed tracks



(c) m^2 for ACC fired tracks

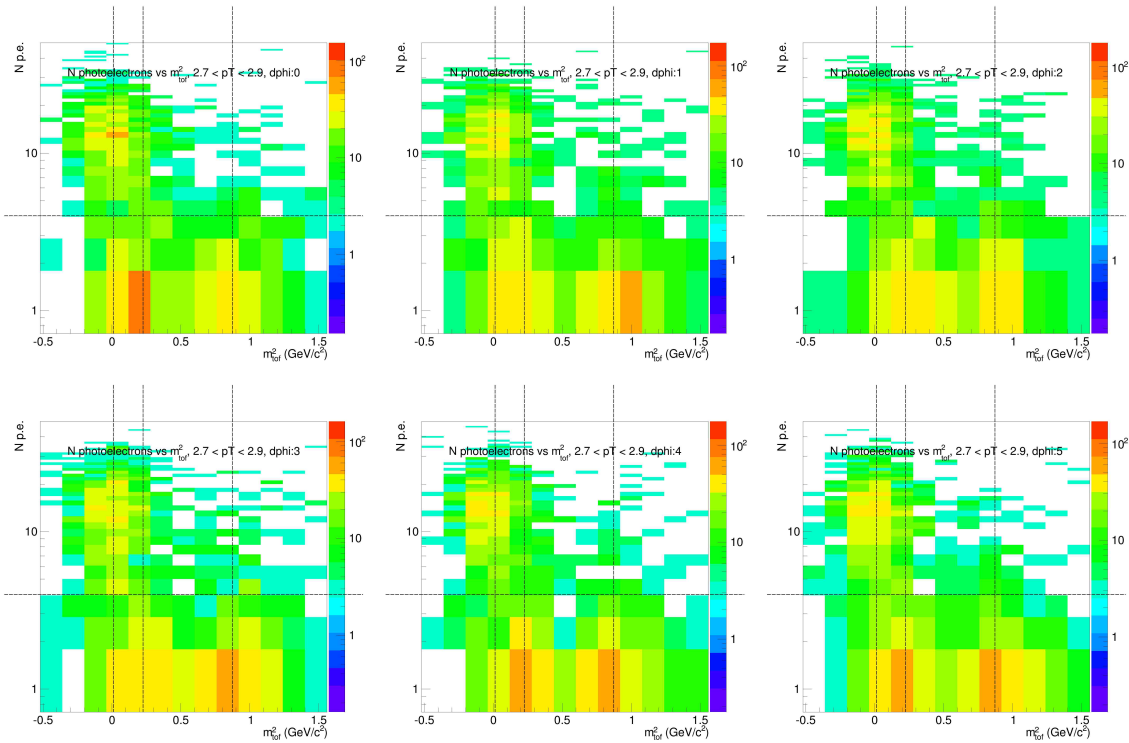


(d) PID parameters and Yields for ACC vetoed tracks

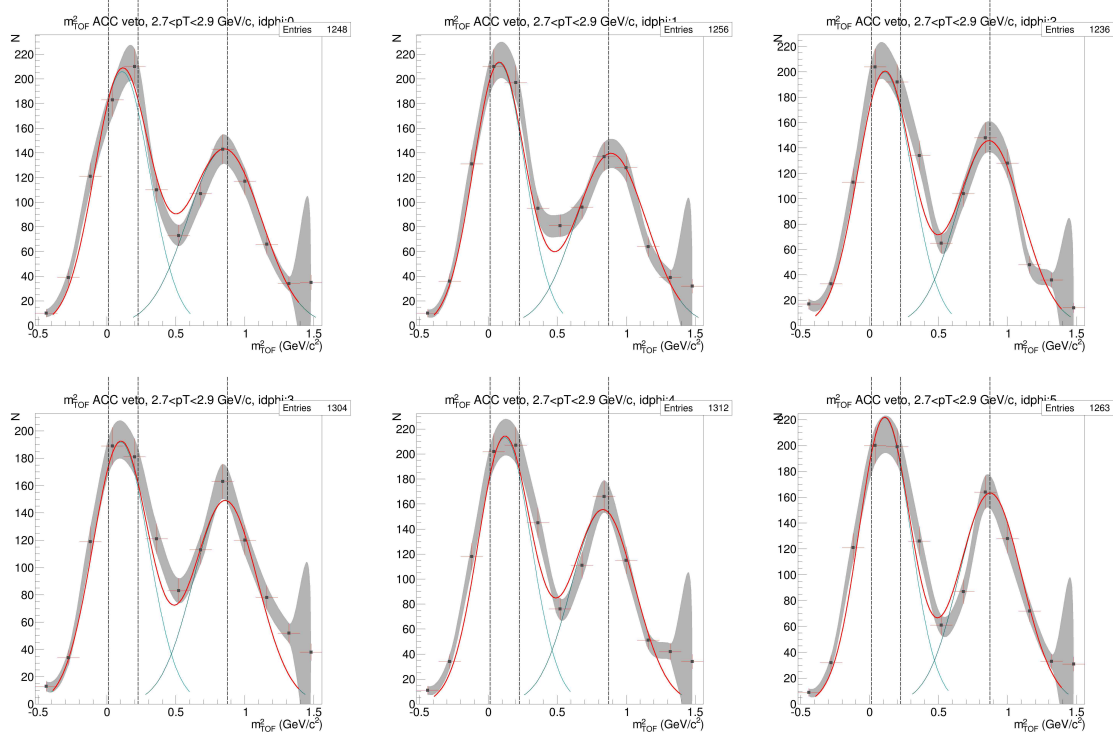


(e) PID parameters and Yields for ACC fired tracks

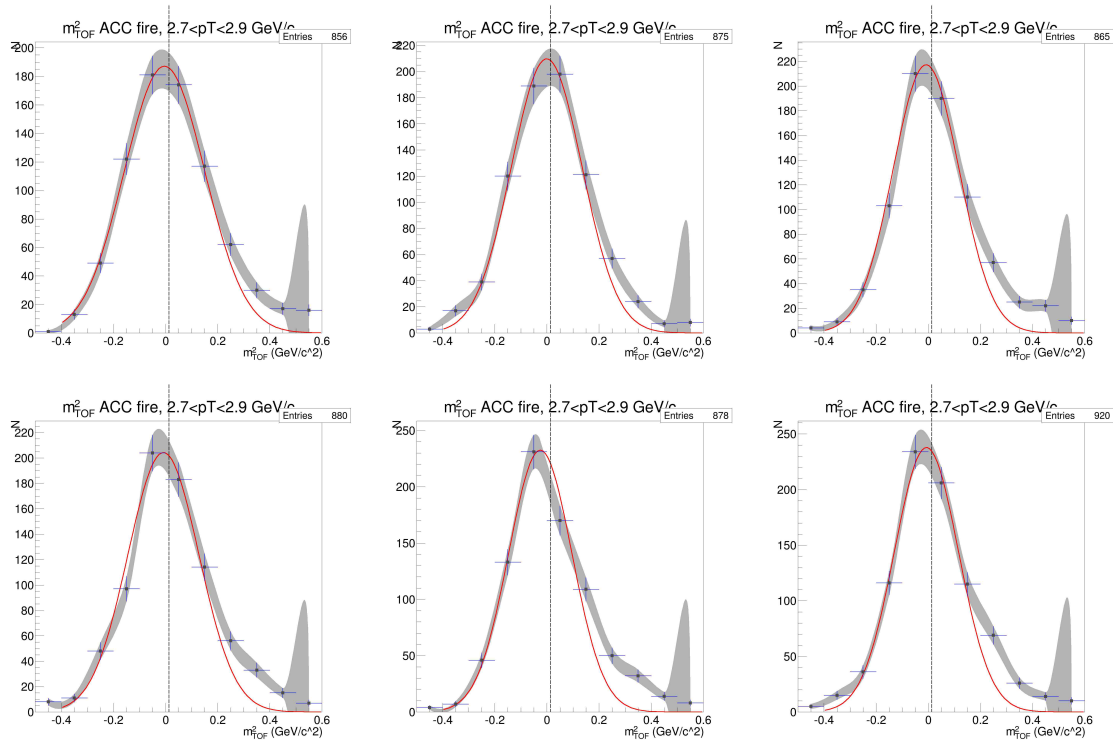
Figure D.30: ACC $N_{p.e.}$ vs m_2 , PID fits, and Yield vs $d\phi$ for $p_T = 2.5$ - 2.7 GeV/c, TOF.W, positive particles



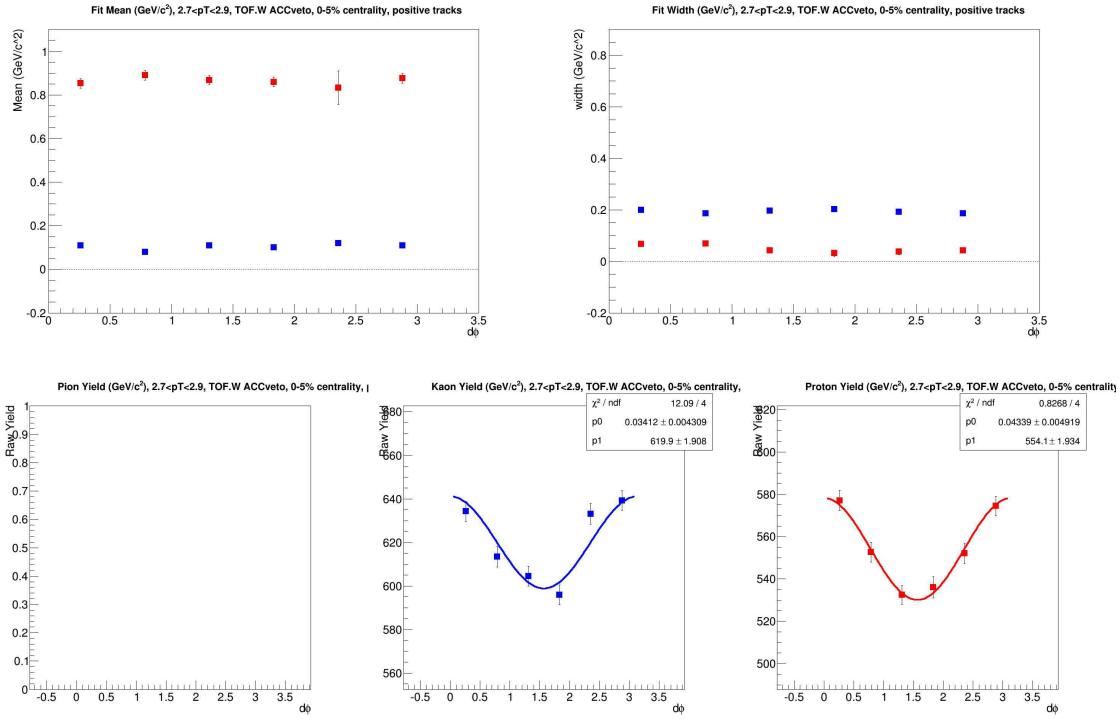
(a) $N_{p.e.}$ vs m^2



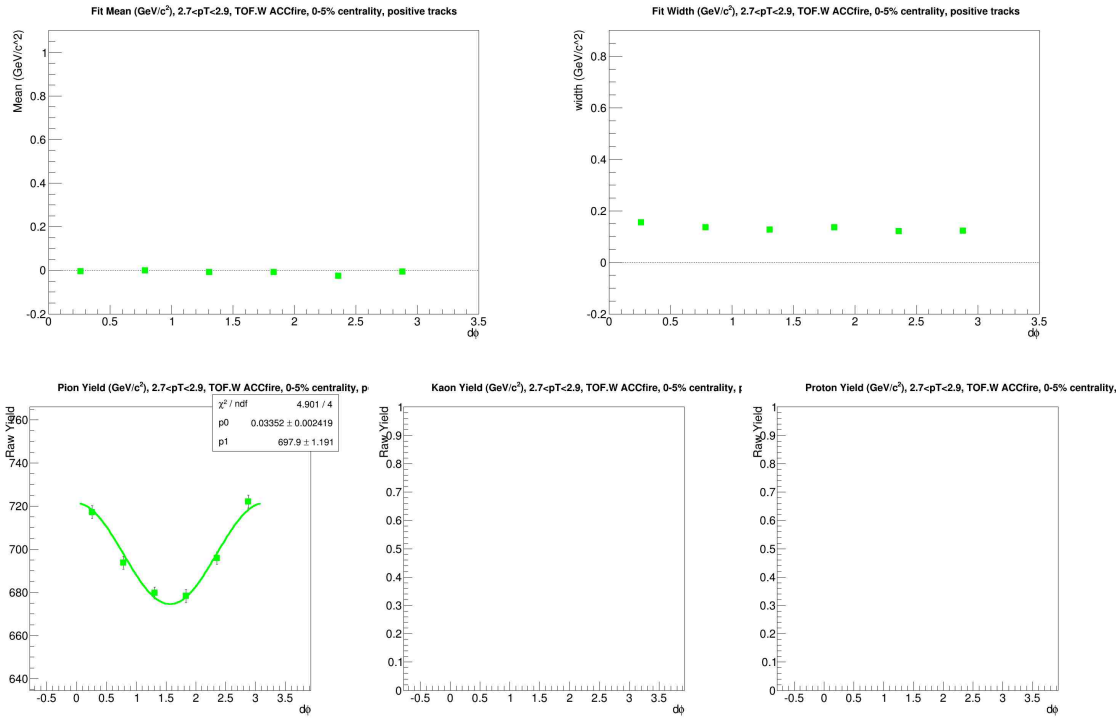
(b) m^2 for ACC vetoed tracks



(c) m^2 for ACC fired tracks

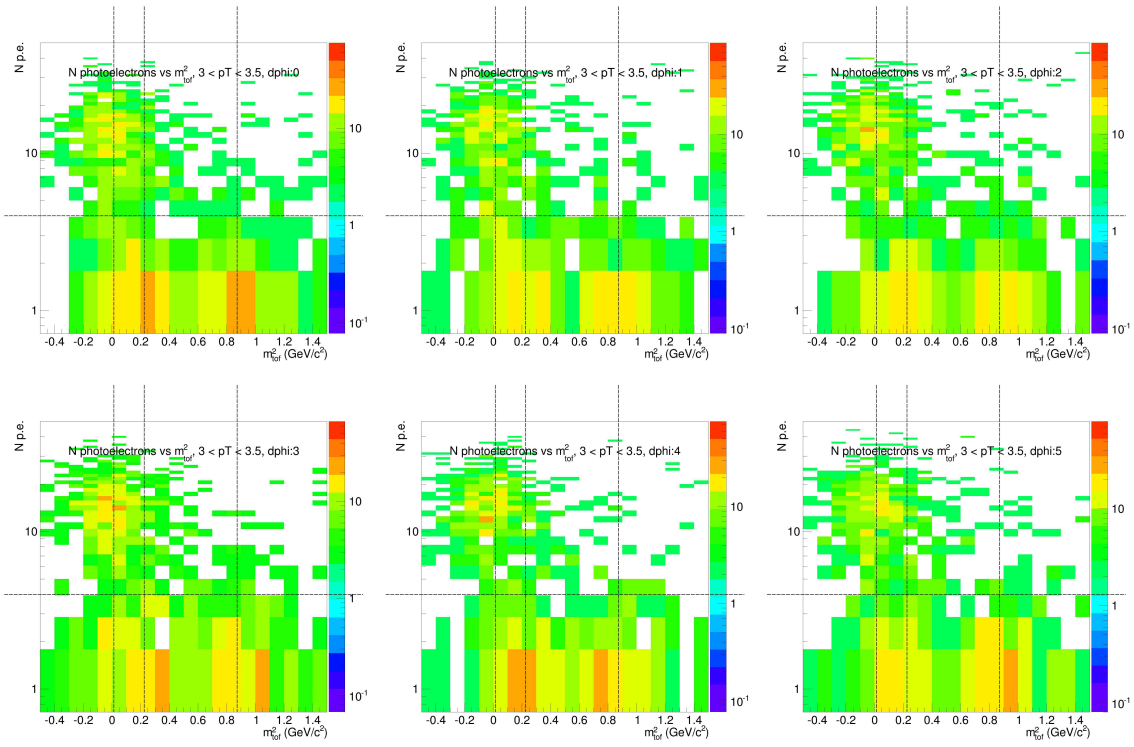


(d) PID parameters and Yields for ACC vetoed tracks

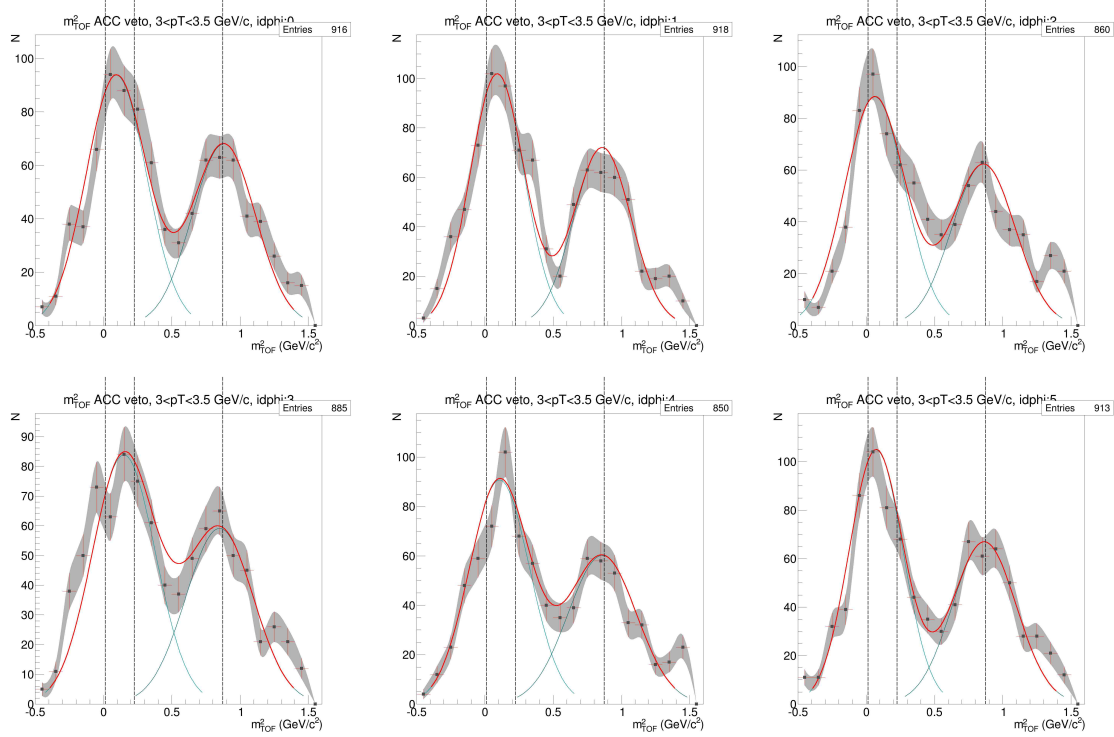


(e) PID parameters and Yields for ACC fired tracks

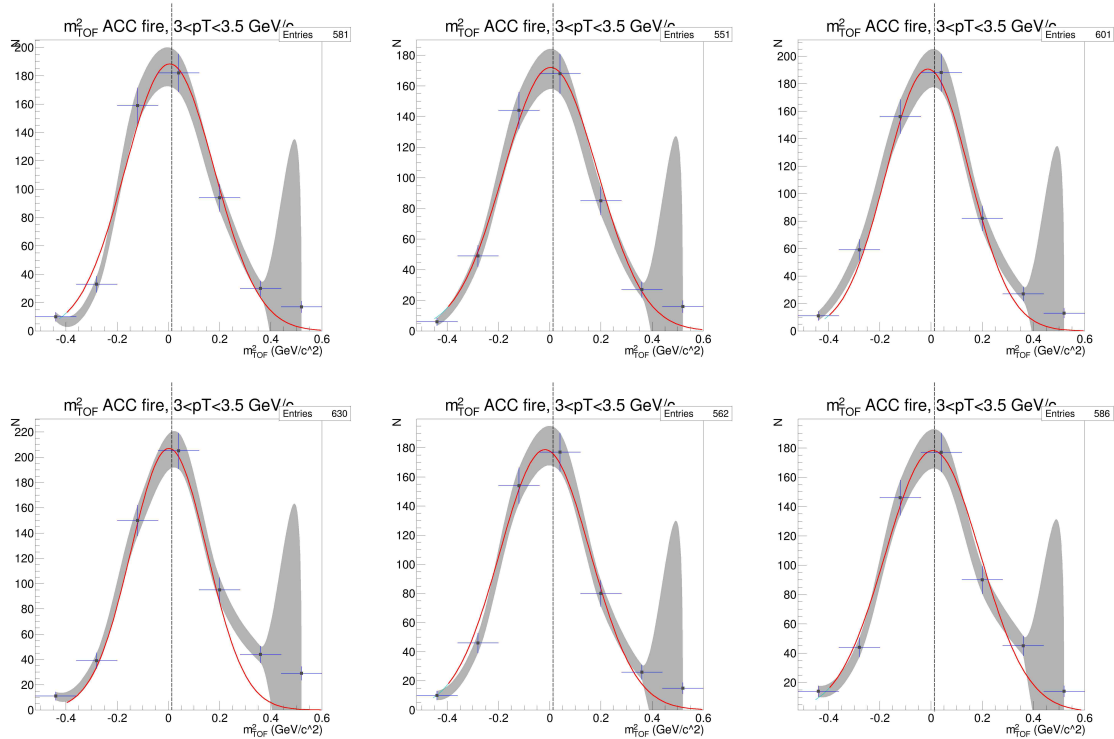
Figure D.31: ACC $N_{p.e.}$ vs m_2 , PID fits, and Yield vs $d\phi$ for $p_T = 2.7$ - 2.9 GeV/c , TOF.W, positive particles



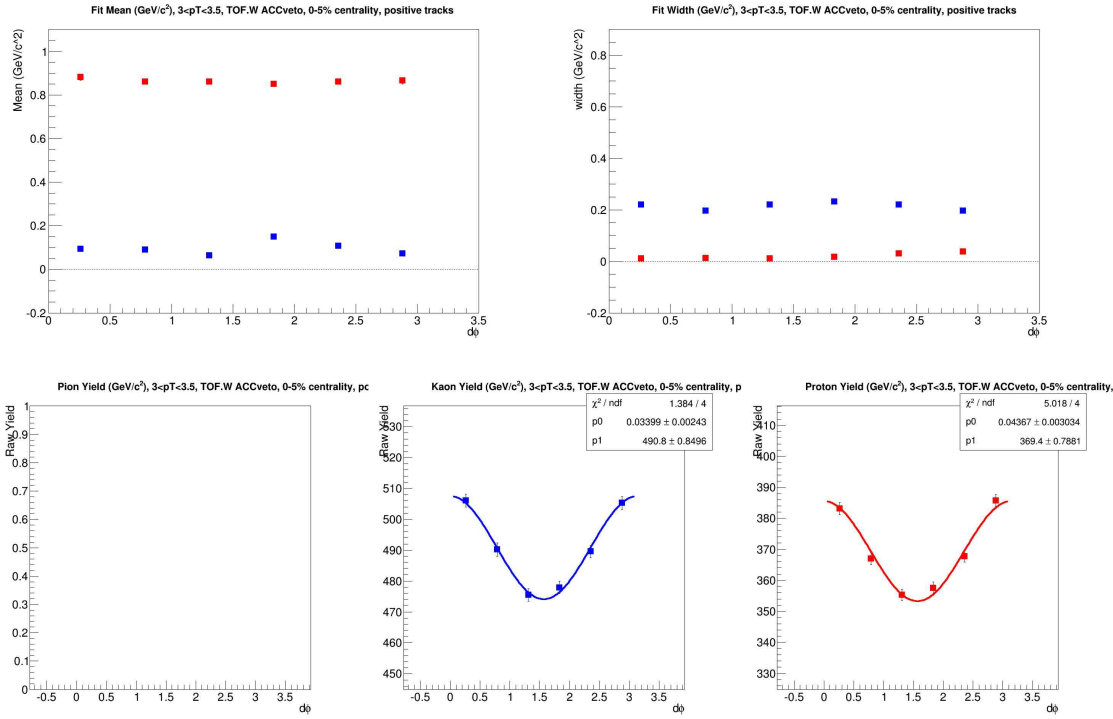
(a) $N_{p.e.}$ vs m^2



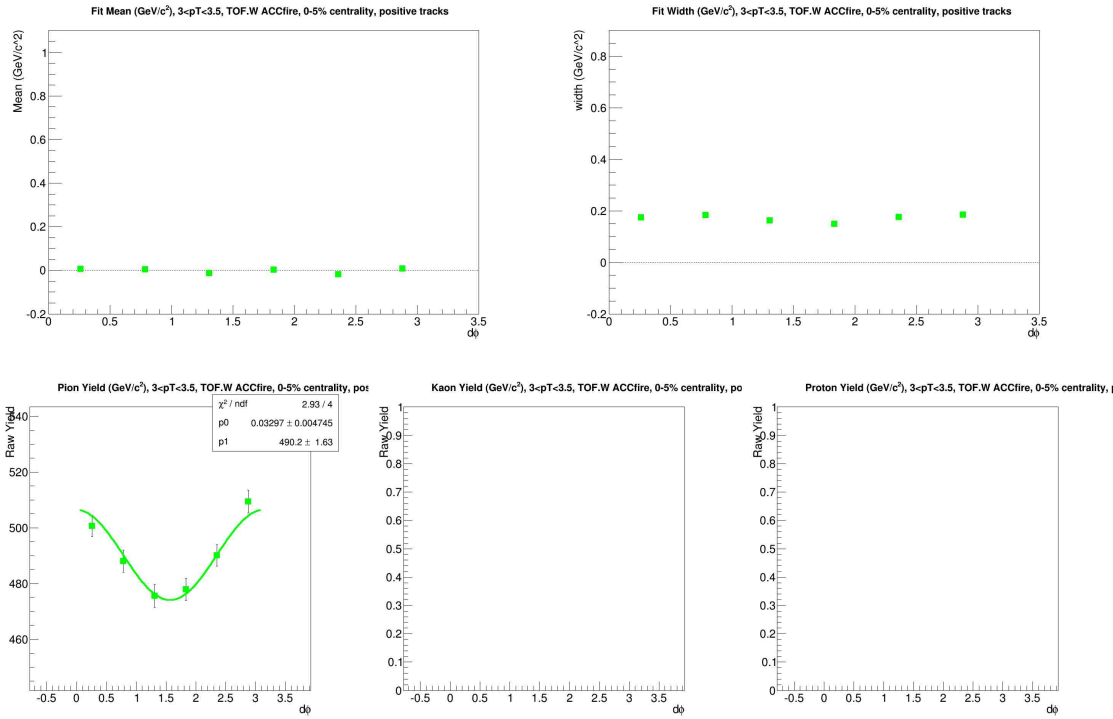
(b) m^2 for ACC vetoed tracks



(c) m^2 for ACC fired tracks

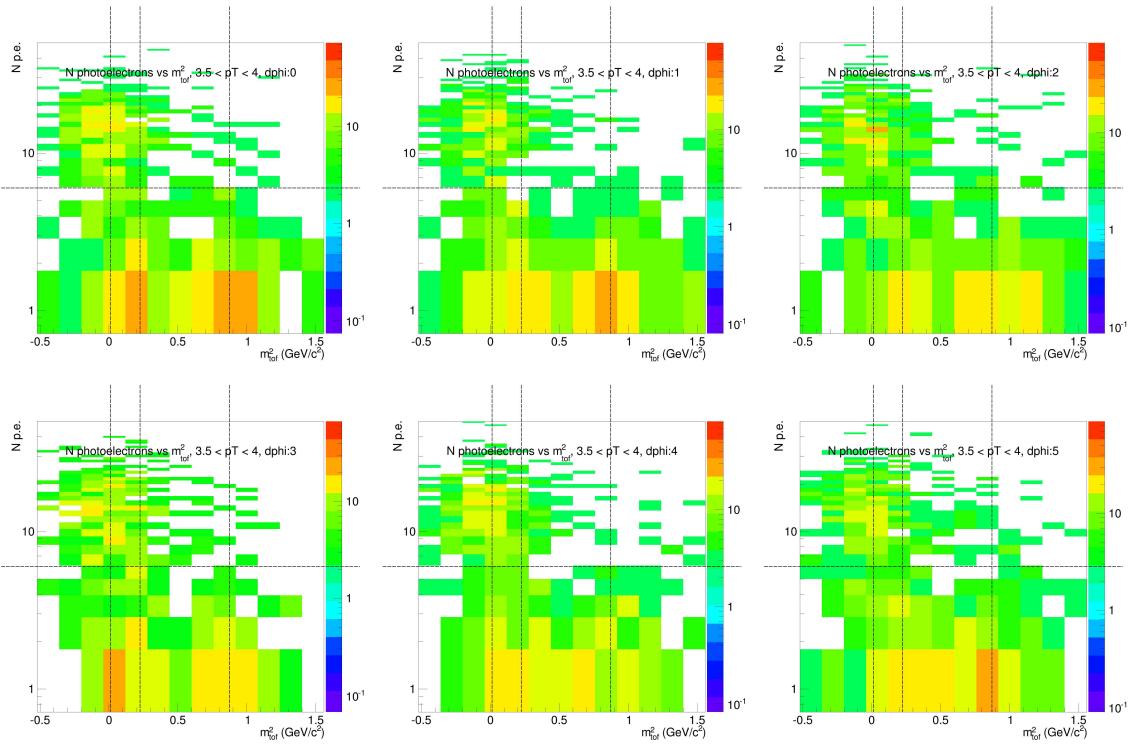


(d) PID parameters and Yields for ACC vetoed tracks

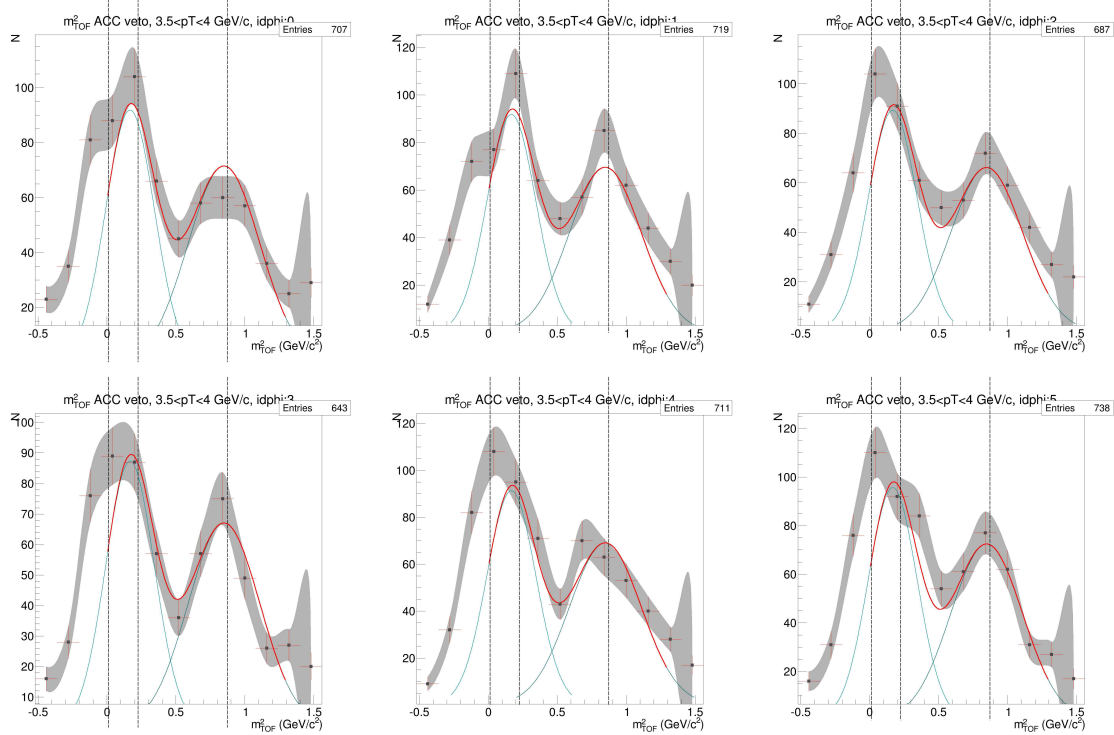


(e) PID parameters and Yields for ACC fired tracks

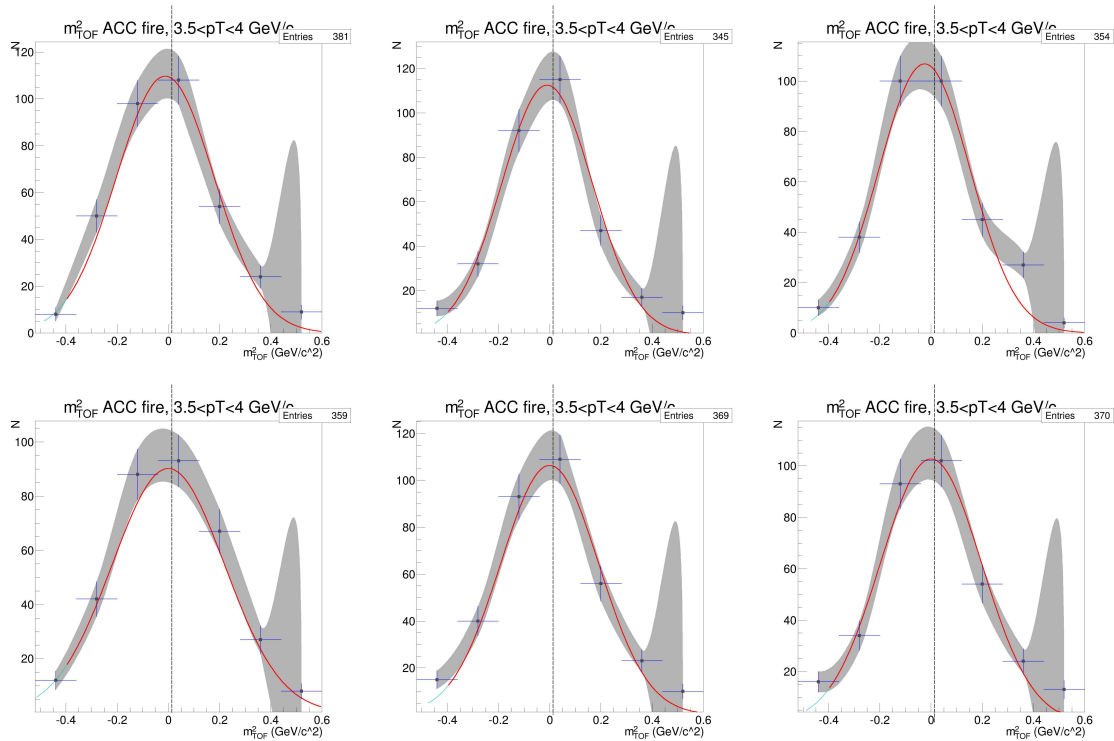
Figure D.32: ACC $N_{p.e.}$ vs m_2 , PID fits, and Yield vs $d\phi$ for $p_T=3.0-3.5$ GeV/c , TOF.W, positive particles



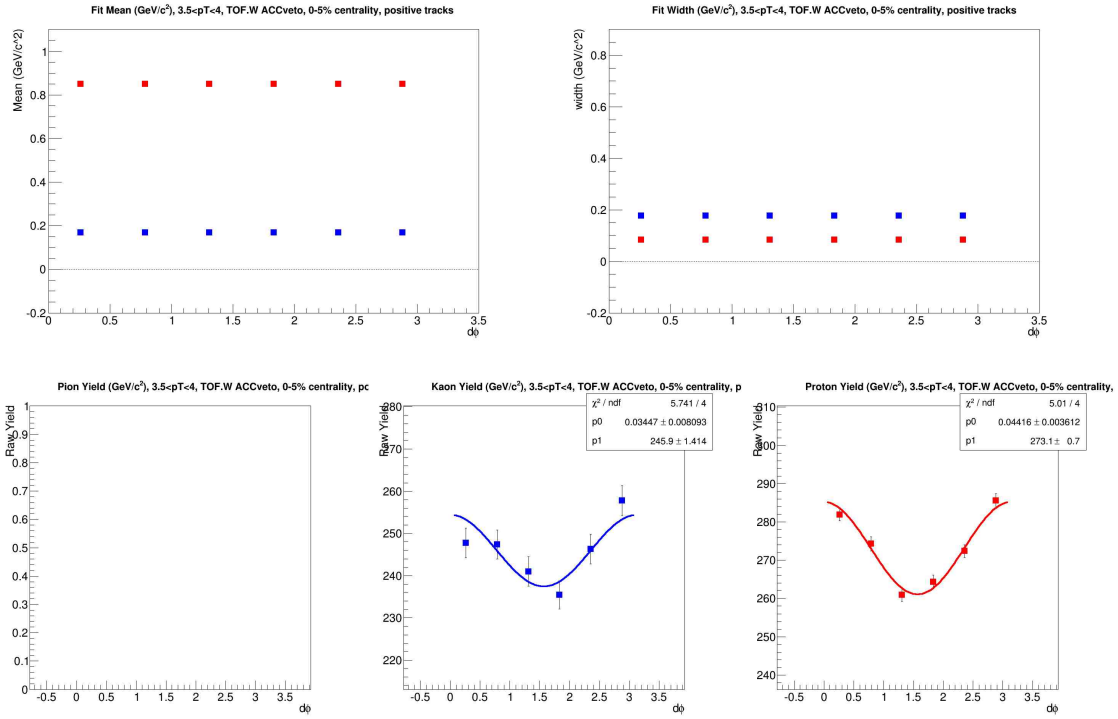
(a) $N_{p.e.}$ vs m^2



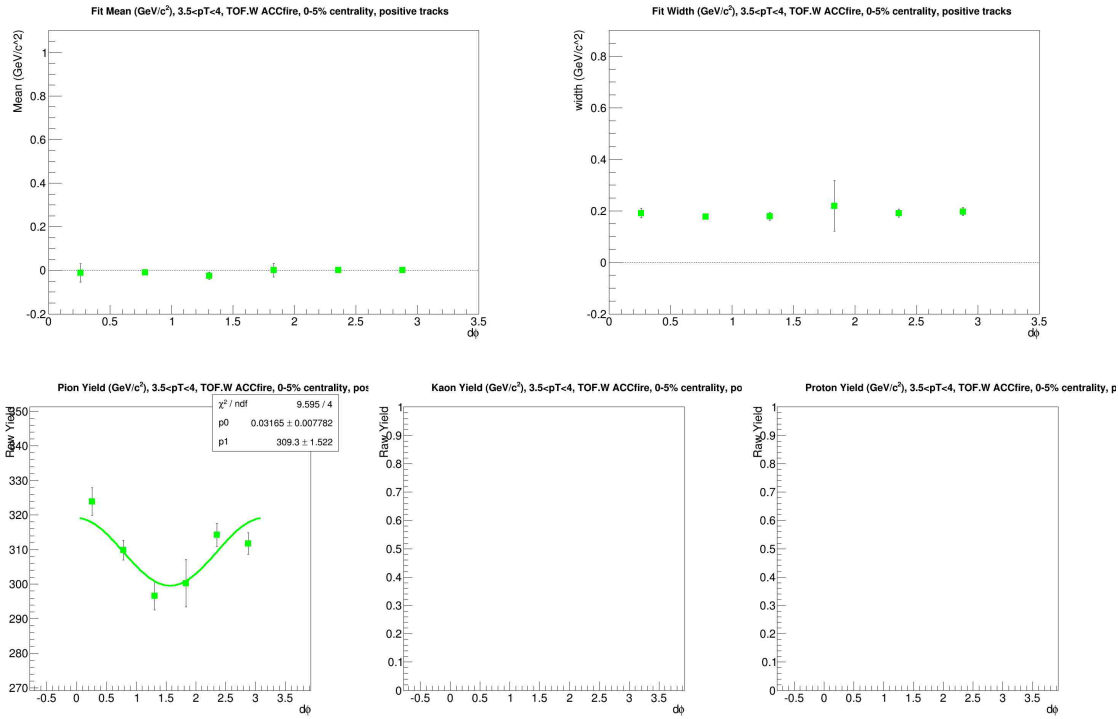
(b) m^2 for ACC vetoed tracks



(c) m^2 for ACC fired tracks

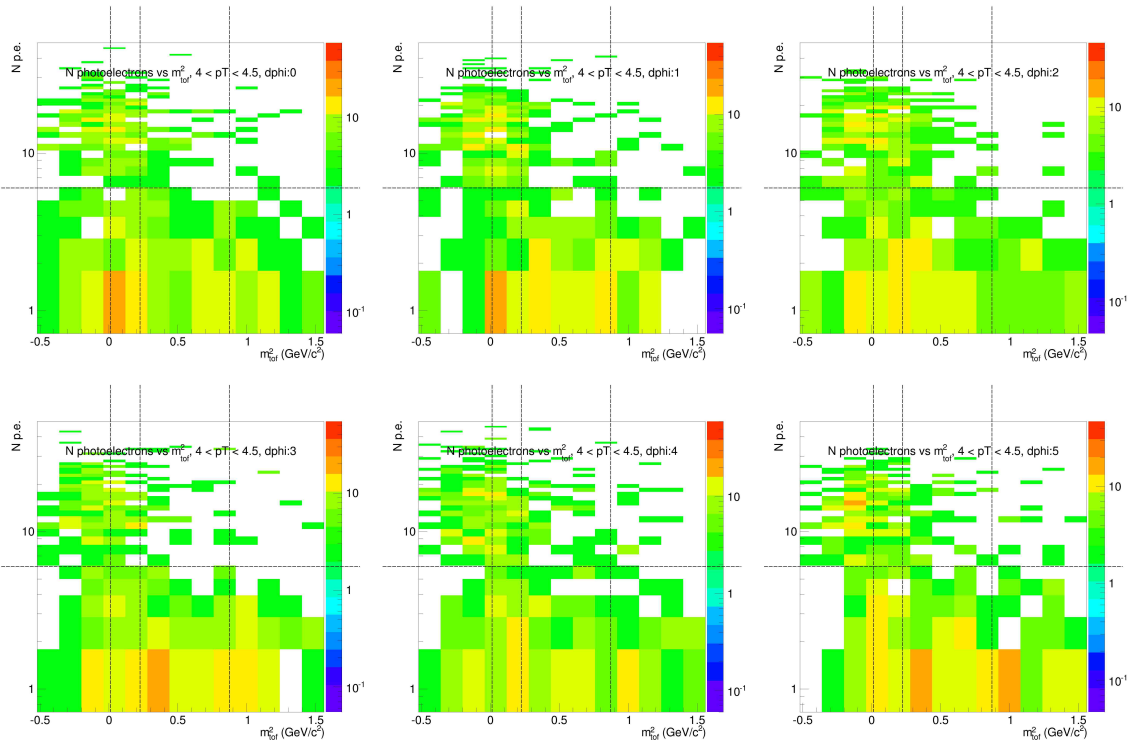


(d) PID parameters and Yields for ACC vetoed tracks

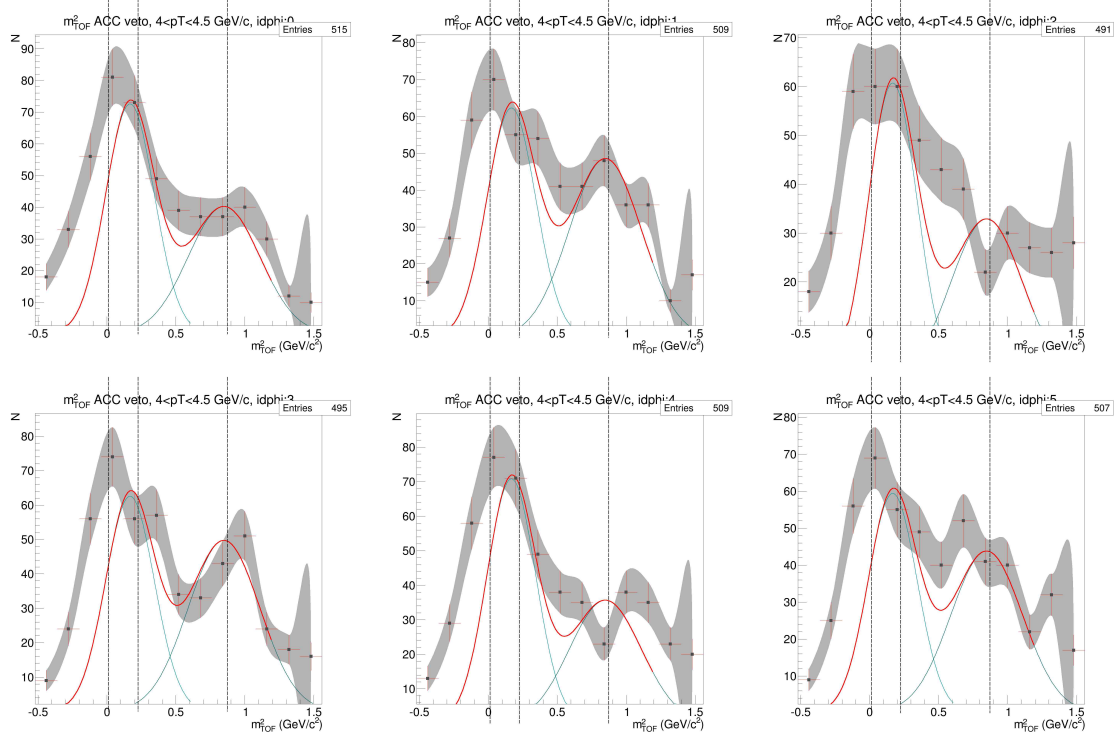


(e) PID parameters and Yields for ACC fired tracks

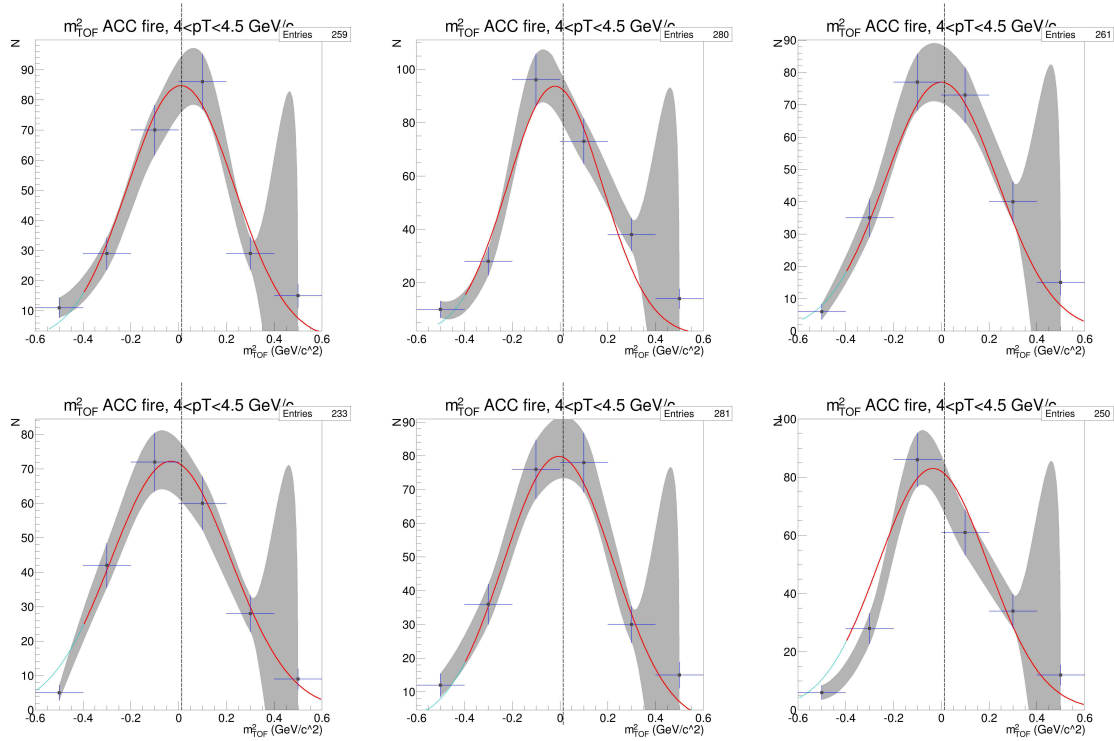
Figure D.33: ACC $N_{p.e.}$ vs m_2 , PID fits, and Yield vs $d\phi$ for $p_T=3.5-4.0$ GeV/c , TOF.W, positive particles



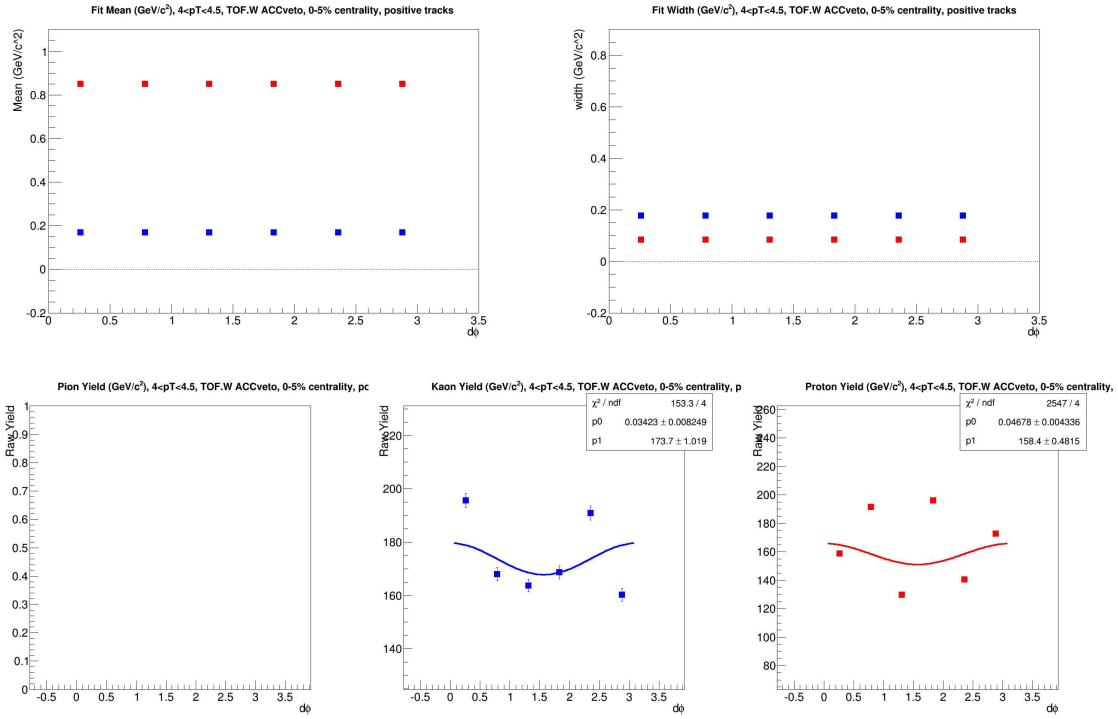
(a) $N_{p.e.}$ vs m^2



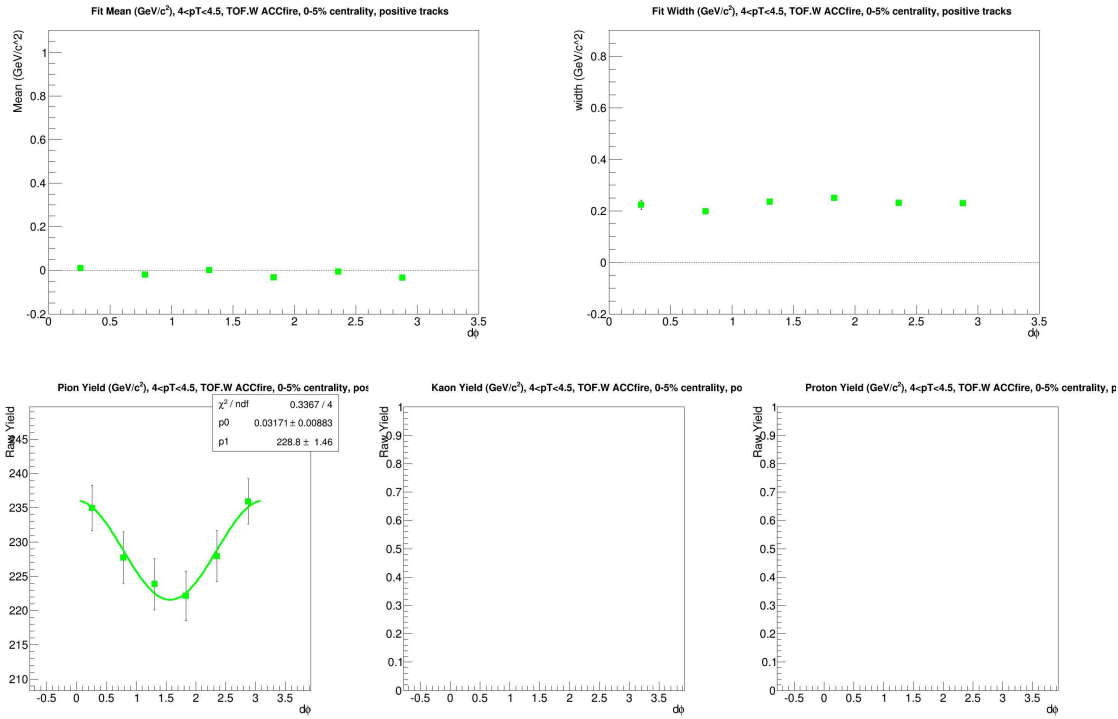
(b) m^2 for ACC vetoed tracks



(c) m^2 for ACC fired tracks



(d) PID parameters and Yields for ACC vetoed tracks



(e) PID parameters and Yields for ACC fired tracks

Figure D.34: ACC $N_{p.e.}$ vs m_2 , PID fits, and Yield vs $d\phi$ for $p_T=4.0-4.5$ GeV/c , TOF.W, positive particles

Bibliography

- [1] T. Abbott, Y. Akiba, D. Alburger, D. Beavis, R. R. Betts, L. Birstein, M. A. Bloomer, P. D. Bond, C. Chasman, Y. Y. Chu, B. A. Cole, J. B. Costales, H. J. Crawford, J. B. Cumming, R. Debbe, E. Duek, J. Engelage, S. Y. Fung, L. Grodzins, S. Gushue, H. Hamagaki, O. Hansen, S. Hayashi, S. Homma, H. Z. Huang, Y. Ikeda, S. Katcoff, S. Kaufman, K. Kimura, K. Kitamura, K. Kurita, R. J. Ledoux, M. J. Levine, Y. Miake, R. J. Morse, S. Nagamiya, J. Olness, C. G. Parsons, L. P. Remsberg, M. Sarabura, A. Shor, P. Stankus, S. G. Steadman, G. S. F. Stephans, T. Sugitate, M. J. Tannenbaum, M. Torikoshi, J. H. van Dijk, F. Videbaek, M. Vient, P. Vincent, E. Vulgaris, V. Vutsadakis, W. A. Watson, H. E. Wegner, D. S. Woodruff, Y. D. Wu, and W. A. Zajc. Kaon and pion production in central si+au collisions at 14.6 A gev/ c . *Phys. Rev. Lett.*, 64:847–850, Feb 1990.
- [2] B. I. Abelev, M. M. Aggarwal, Z. Ahammed, B. D. Anderson, M. Anderson, D. Arkhipkin, G. S. Averichev, Y. Bai, J. Balewski, O. Barannikova, L. S. Barnby, J. Baudot, S. Bekele, V. V. Belaga, A. Bellingeri-Laurikainen, R. Bellwied, F. Benedosso, S. Bhardwaj, A. Bhasin, A. K. Bhati, H. Bichsel, J. Bielcik, J. Bielcikova, L. C. Bland, S-L. Blyth, B. E. Bonner, M. Botje, J. Bouchet, A. V. Brandin, A. Bravar, T. P. Burton, M. Bystersky, R. V. Cadman, X. Z. Cai, H. Caines, M. Calderón de la Barca Sánchez, J. Castillo, O. Catu, D. Cebra, Z. Chajecki, P. Chaloupka, S. Chattopadhyay, H. F. Chen, J. H. Chen, J. Cheng, M. Cherney, A. Chikanian, W. Christie, J. P. Coffin, T. M. Cormier, M. R. Cosentino, J. G. Cramer, H. J. Crawford, D. Das, S. Das, S. Dash, M. Daugherty, M. M. de Moura, T. G. Dedovich, M. DePhillips, A. A. Derevschikov, L. Didenko, T. Dietel, P. Djawotho, S. M. Dogra, W. J. Dong, X. Dong, J. E. Draper, F. Du, V. B. Dunin, J. C. Dunlop, M. R. Dutta Mazumdar, V. Eckardt, W. R. Edwards, L. G. Efimov, V. Emelianov, J. Engelage, G. Eppley, B. Erazmus, M. Estienne, P. Fachini, R. Fatemi, J. Fedorisin, P. Filip, E. Finch, V. Fine, Y. Fisyak, J. Fu, C. A. Gagliardi, L. Gaillard, M. S. Ganti, V. Ghazikhanian, P. Ghosh, J. E. Gonzalez, Y. G. Gorbunov, H. Gos, O. Grebenyuk, D. Grosnick, S. M. Guertin, K. S. F. F. Guimaraes, N. Gupta, T. D. Gutierrez, B. Haag, T. J. Hallman, A. Hamed, J. W. Harris, W. He, M. Heinz, T. W. Henry, S. Heppermann, B. Hippolyte, A. Hirsch, E. Hjort, A. M. Hoffman, G. W. Hoffmann, M. J. Horner, H. Z. Huang, S. L. Huang, E. W. Hughes, T. J. Humanic, G. Igo, P. Jacobs, W. W. Jacobs, P. Jakl, F. Jia, H. Jiang, P. G. Jones, E. G. Judd, S. Kabana, K. Kang, J. Kapitan, M. Kaplan, D. Keane,

A. Kechechyan, V. Yu. Khodyrev, B. C. Kim, J. Kiryluk, A. Kisiel, E. M. Kislov, S. R. Klein, A. Kocoloski, D. D. Koetke, T. Kollegger, M. Kopytine, L. Kotchenda, V. Kouchpil, K. L. Kowalik, M. Kramer, P. Kravtsov, V. I. Kravtsov, K. Krueger, C. Kuhn, A. I. Kulikov, A. Kumar, A. A. Kuznetsov, M. A. C. Lamont, J. M. Landgraf, S. Lange, S. LaPointe, F. Laue, J. Lauret, A. Lebedev, R. Lednický, C-H. Lee, S. Lehocká, M. J. LeVine, C. Li, Q. Li, Y. Li, G. Lin, X. Lin, S. J. Lindenbaum, M. A. Lisa, F. Liu, H. Liu, J. Liu, L. Liu, Z. Liu, T. Ljubicic, W. J. Llope, H. Long, R. S. Longacre, W. A. Love, Y. Lu, T. Ludlam, D. Lynn, G. L. Ma, J. G. Ma, Y. G. Ma, D. Magestro, D. P. Mahapatra, R. Majka, L. K. Mangotra, R. Manweiler, S. Margetis, C. Markert, L. Martin, H. S. Matis, Yu. A. Matulenko, C. J. McClain, T. S. McShane, Yu. Melnick, A. Meschanin, J. Millane, M. L. Miller, N. G. Minaev, S. Mioduszewski, C. Mironov, A. Mischke, D. K. Mishra, J. Mitchell, B. Mohanty, L. Molnar, C. F. Moore, D. A. Morozov, M. G. Munhoz, B. K. Nandi, C. Nattrass, T. K. Nayak, J. M. Nelson, N. S. Nepali, P. K. Netrakanti, L. V. Nogach, S. B. Nurushev, G. Odyniec, A. Ogawa, V. Okorokov, M. Oldenburg, D. Olson, M. Pachr, S. K. Pal, Y. Paneratsev, S. Y. Panitkin, A. I. Pavlinov, T. Pawlak, T. Peitzmann, V. Perevozchikov, C. Perkins, W. Peryt, S. C. Phatak, R. Picha, M. Planinic, J. Pluta, N. Poljak, N. Porile, J. Porter, A. M. Poskanzer, M. Potekhin, E. Potrebenikova, B. V. K. S. Potukuchi, D. Prindle, C. Pruneau, J. Putschke, G. Rakness, R. Raniwala, S. Raniwala, R. L. Ray, S. V. Razin, J. Reinnarth, D. Relyea, A. Ridiger, H. G. Ritter, J. B. Roberts, O. V. Rogachevskiy, J. L. Romero, A. Rose, C. Roy, L. Ruan, M. J. Russcher, R. Sahoo, T. Sakuma, S. Salur, J. Sandweiss, M. Sarsour, P. S. Sazhin, J. Schambach, R. P. Scharenberg, N. Schmitz, J. Seger, I. Selyuzhenkov, P. Seyboth, A. Shabetai, E. Shahaliev, M. Shao, M. Sharma, W. Q. Shen, S. S. Shimanskiy, E. P. Sichtermann, F. Simon, R. N. Singaraju, N. Smirnov, R. Snellings, G. Sood, P. Sorensen, J. Sowinski, J. Speltz, H. M. Spinka, B. Srivastava, A. Stadnik, T. D. S. Stanislaus, R. Stock, A. Stolpovsky, M. Strikhanov, B. Stringfellow, A. A. P. Suaide, N. L. Subba, E. Sugarbaker, M. Sumbera, Z. Sun, B. Surrow, M. Swanger, T. J. M. Symons, A. Szanto de Toledo, A. Tai, J. Takahashi, A. H. Tang, T. Tarnowsky, D. Thein, J. H. Thomas, A. R. Timmins, S. Timoshenko, M. Tokarev, T. A. Trainor, S. Trentalange, R. E. Tribble, O. D. Tsai, J. Ulery, T. Ullrich, D. G. Underwood, G. Van Buren, N. van der Kolk, M. van Leeuwen, A. M. Vander Molen, R. Varma, I. M. Vasilevski, A. N. Vasiliev, R. Vernet, S. E. Vigdor, Y. P. Viyogi, S. Vokal, S. A. Voloshin, W. T. Waggoner, F. Wang, G. Wang, J. S. Wang, X. L. Wang, Y. Wang, J. W. Watson, J. C. Webb, G. D. Westfall, A. Wetzler, C. Whitten, H. Wieman, S. W. Wissink, R. Witt, J. Wood, J. Wu, N. Xu, Q. H. Xu, Z. Xu, P. Yepes, I-K. Yoo, V. I. Yurevich, W. Zhan, H. Zhang, W. M. Zhang, Y. Zhang, Z. P. Zhang, Y. Zhao, C. Zhong, R. Zoukarneev, Y. Zoukarneeva, A. N. Zubarev, and J. X. Zuo. Identified baryon and meson distributions at large transverse momenta from Au + Au collisions at $\sqrt{s_{NN}} = 200$ GeV. *Phys. Rev. Lett.*, 97:152301, Oct 2006.

- [3] M. C. Abreu et al. Evidence for deconfinement of quarks and gluons from the J / psi

suppression pattern measured in Pb + Pb collisions at the CERN SPS. *Phys. Lett.*, B477:28–36, 2000.

- [4] A. Adare, S. Afanasiev, C. Aidala, N. N. Ajitanand, Y. Akiba, H. Al-Bataineh, J. Alexander, A. Angerami, K. Aoki, N. Apadula, Y. Aramaki, E. T. Atomssa, R. Averbeck, T. C. Awes, B. Azmoun, V. Babintsev, M. Bai, G. Baksay, L. Baksay, K. N. Barish, B. Bassalleck, A. T. Basye, S. Bathe, V. Baublis, C. Baumann, A. Bazilevsky, S. Belikov, R. Belmont, R. Bennett, A. Berdnikov, Y. Berdnikov, J. H. Bhom, A. A. Bickley, D. S. Blau, J. S. Bok, K. Boyle, M. L. Brooks, H. Buesching, V. Bumazhnov, G. Bunce, S. Butsyk, C. M. Camacho, S. Campbell, A. Caringi, C.-H. Chen, C. Y. Chi, M. Chiu, I. J. Choi, J. B. Choi, R. K. Choudhury, P. Christiansen, T. Chujo, P. Chung, O. Chvala, V. Cianciolo, Z. Citron, B. A. Cole, Z. Conesa del Valle, M. Connors, P. Constantin, M. Csanad, T. Cs org , T. Dahms, S. Dairaku, I. Danchev, K. Das, A. Datta, G. David, M. K. Dayananda, A. Denisov, A. Deshpande, E. J. Desmond, K. V. Dharmawardane, O. Dietzsch, A. Dion, M. Donadelli, O. Drapier, A. Drees, K. A. Drees, J. M. Durham, A. Durum, D. Dutta, L. D’Orazio, S. Edwards, Y. V. Efremenko, F. Ellinghaus, T. Engelmore, A. Enokizono, H. En’yo, S. Esumi, B. Faadem, D. E. Fields, M. Finger, M. Finger, F. Fleuret, S. L. Fokin, Z. Fraenkel, J. E. Frantz, A. Franz, A. D. Frawley, K. Fujiwara, Y. Fukao, T. Fusayasu, I. Garishvili, A. Glenn, H. Gong, M. Gonin, Y. Goto, R. Granier de Cassagnac, N. Grau, S. V. Greene, G. Grim, M. Grosse Perdekamp, T. Gunji, H.-Å. Gustafsson, J. S. Haggerty, K. I. Hahn, H. Hamagaki, J. Hamblen, R. Han, J. Hanks, E. P. Hartouni, E. Haslum, R. Hayano, X. He, M. Heffner, T. K. Hemmick, T. Hester, J. C. Hill, M. Hohlmann, W. Holzmann, K. Homma, B. Hong, T. Horaguchi, D. Hornback, S. Huang, T. Ichihara, R. Ichimiya, J. Ide, Y. Ikeda, K. Imai, M. Inaba, D. Isenhower, M. Ishihara, T. Isobe, M. Issah, A. Isupov, D. Ivanischev, Y. Iwanaga, B. V. Jacak, J. Jia, X. Jiang, J. Jin, B. M. Johnson, T. Jones, K. S. Joo, D. Jouan, D. S. Jumper, F. Kajihara, S. Kametani, N. Kamihara, J. Kamin, J. H. Kang, J. Kapustinsky, K. Karatsu, M. Kasai, D. Kawall, M. Kawashima, A. V. Kazantsev, T. Kempel, A. Khanzadeev, K. M. Kijima, J. Kikuchi, A. Kim, B. I. Kim, D. H. Kim, D. J. Kim, E. Kim, E.-J. Kim, S. H. Kim, Y.-J. Kim, E. Kinney, K. Kiriluk, . Kiss, E. Kistenev, D. Kleinjan, L. Kochenda, B. Komkov, M. Konno, J. Koster, D. Kotchetkov, A. Kozlov, A. Kr l, A. Kravitz, G. J. Kunde, K. Kurita, M. Kurosawa, Y. Kwon, G. S. Kyle, R. Lacey, Y. S. Lai, J. G. Lajoie, A. Lebedev, D. M. Lee, J. Lee, K. Lee, K. B. Lee, K. S. Lee, M. J. Leitch, M. A. L. Leite, E. Leitner, B. Lenzi, X. Li, P. Lichtenwalner, P. Liebing, L. A. Linden Levy, T. Li ka, A. Litvinenko, H. Liu, M. X. Liu, B. Love, R. Luechtenborg, D. Lynch, C. F. Maguire, Y. I. Makdisi, A. Malakhov, M. D. Malik, V. I. Manko, E. Mannel, Y. Mao, H. Masui, F. Matathias, M. McCumber, P. L. McGaughey, D. McGlinchey, N. Means, B. Meredith, Y. Miake, T. Mibe, A. C. Mignerey, P. Mike , K. Miki, A. Milov, M. Mishra, J. T. Mitchell, A. K. Mohanty, H. J. Moon, Y. Morino, A. Morreale, D. P. Morrison, T. V. Moukhanova, T. Murakami, J. Murata, S. Nagamiya, J. L. Nagle, M. Naglis, M. I. Nagy, I. Nakagawa, Y. Nakamiya, K. R. Nakamura, T. Nakamura, K. Nakano, S. Nam,

J. Newby, M. Nguyen, M. Nihashi, R. Nouicer, A. S. Nyanin, C. Oakley, E. O'Brien, S. X. Oda, C. A. Ogilvie, M. Oka, K. Okada, Y. Onuki, A. Oskarsson, M. Ouchida, K. Ozawa, R. Pak, V. Pantuev, V. Papavassiliou, I. H. Park, J. Park, S. K. Park, W. J. Park, S. F. Pate, H. Pei, J.-C. Peng, H. Pereira, V. Peresedov, D. Yu. Peressounko, R. Petti, C. Pinkenburg, R. P. Pisani, M. Proissl, M. L. Purschke, A. K. Purwar, H. Qu, J. Rak, A. Rakotozafindrabe, I. Ravinovich, K. F. Read, S. Rembeczki, K. Reygers, V. Riabov, Y. Riabov, E. Richardson, D. Roach, G. Roche, S. D. Rolnick, M. Rosati, C. A. Rosen, S. S. E. Rosendahl, P. Rosnet, P. Rukoyatkin, P. Ružička, B. Sahlmueller, N. Saito, T. Sakaguchi, K. Sakashita, V. Samsonov, S. Sano, T. Sato, S. Sawada, K. Sedgwick, J. Seele, R. Seidl, A. Yu. Semenov, R. Seto, D. Sharma, I. Shein, T.-A. Shibata, K. Shigaki, M. Shimomura, K. Shoji, P. Shukla, A. Sickles, C. L. Silva, D. Silvermyr, C. Silvestre, K. S. Sim, B. K. Singh, C. P. Singh, V. Singh, M. Slunečka, R. A. Soltz, W. E. Sondheim, S. P. Sorensen, I. V. Sourikova, N. A. Sparks, P. W. Stankus, E. Stenlund, S. P. Stoll, T. Sugitate, A. Sukhanov, J. Szklai, E. M. Takagui, A. Taketani, R. Tanabe, Y. Tanaka, S. Taneja, K. Tanida, M. J. Tannenbaum, S. Tarafdar, A. Taranenko, P. Tarján, H. Themann, D. Thomas, T. L. Thomas, M. Togawa, A. Toia, L. Tomášek, H. Torii, R. S. Towell, I. Tserruya, Y. Tsuchimoto, C. Vale, H. Valle, H. W. van Hecke, E. Vazquez-Zambrano, A. Veicht, J. Velkovska, R. Vértesi, A. A. Vinogradov, M. Virius, V. Spectra and ratios of identified particles in au+au and d+au collisions at $\sqrt{s_{NN}} = 200$ gev. *Phys. Rev. C*, 88:024906, Aug 2013.

- [5] K. Adcox et al. Formation of dense partonic matter in relativistic nucleus-nucleus collisions at RHIC: Experimental evaluation by the PHENIX collaboration. *Nucl. Phys.*, A757:184–283, 2005.
- [6] A. Akindinov et al. The multigap resistive plate chamber as a time-of-flight detector. *Nucl. Instrum. Meth.*, A456:16–22, 2000.
- [7] D. M. Alde, H. W. Baer, T. A. Carey, G. T. Garvey, A. Klein, C. Lee, M. J. Leitch, J. W. Lillberg, P. L. McGaughey, C. S. Mishra, J. M. Moss, J. C. Peng, C. N. Brown, W. E. Cooper, Y. B. Hsiung, M. R. Adams, R. Guo, D. M. Kaplan, R. L. McCarthy, G. Danner, M. J. Wang, M. L. Barlett, and G. W. Hoffmann. Nuclear dependence of the production of Υ resonances at 800 gev. *Phys. Rev. Lett.*, 66:2285–2288, May 1991.
- [8] F. Antinori et al. Production of strange and multistrange hadrons in nucleus nucleus collisions at the SPS. *Nucl. Phys.*, A661:130–139, 1999.
- [9] Jean Barrette. Anisotropic azimuthal distributions of identified particles in Au + Au collisions at 11.5/A-GeV/c. *Nucl. Phys.*, A661:329–332, 1999.
- [10] Abby Bickley. The physics of the reaction plane detector. *FOCUS Talk*, February 2007.
- [11] CAD @ BNL. Rhic accelerators. *BNL website*, July 2016.

- [12] Peter Braun-Munzinger and Johanna Stachel. Dynamics of ultrarelativistic nuclear collisions with heavy beams: An Experimental overview. *Nucl. Phys.*, A638:3–18, 1998.
- [13] Henner Buesching. The electromagnetic calorimeter. *FOCUS Talk*, February 2003.
- [14] Sergey Butsyk. Phenix drift chamber operation principles. *FOCUS Talk*, January 2003.
- [15] Chin-Hao Chen, Gabor David, Shengli Huang, and Takao Sakaguchi. Measurement of second-order fourier coefficients of the emission angle dependent pi0 yields in run8 d+au collisions. *PHENIX Internal Analysis Note*, AN1164, April 2014.
- [16] Mickey Chiu. Phenix focus: Zero degree calorimeter. *FOCUS Talk*, December 2003.
- [17] John C. Collins and M. J. Perry. Superdense Matter: Neutrons Or Asymptotically Free Quarks? *Phys. Rev. Lett.*, 34:1353, 1975.
- [18] M. D. Corcoran et al. Evidence for multiple scattering of high-energy partons in nuclei. *Phys. Lett.*, B259:209–215, 1991.
- [19] J. W. Cronin, H. J. Frisch, M. J. Shochet, J. P. Boymond, P. A. Piroué, and R. L. Sumner. Production of hadrons at large transverse momentum at 200, 300, and 400 gev. *Phys. Rev. D*, 11:3105–3123, Jun 1975.
- [20] Sidney D. Drell and Tung-Mow Yan. Massive lepton-pair production in hadron-hadron collisions at high energies. *Phys. Rev. Lett.*, 25:316–320, Aug 1970.
- [21] A. Pikin et al. Rhic ebis: basics of design and status of commissioning. *Journal of Instrumentation*, 5(C09003), September 2010.
- [22] T. Fields and M. D. Corcoran. Nuclear rescattering effects in massive dihadron production. *Phys. Rev. Lett.*, 70:143–145, Jan 1993.
- [23] K.F. Read for PHENIX collab. *15th Winter Workshop on Nuclear Dynamics*, Park City, Utah, January 1999.
- [24] Tarun Kanti Ghosh, K. Adcox, S. S. Adler, N. Ajitanand, Y. Akiba, J. Alexander, L. Aphecetche, Y. Arai, S. H. Aronson, R. Averbeck, T. C. Awes, K. N. Barish, P. D. Barnes, J. Barrette, B. Bassalleck, S. Bathe, V. Baublis, A. Bazilevsky, S. Belikov, F. G. Bellaiche, S. T. Belyaev, M. J. Bennett, Y. Berdnikov, S. Botelho, M. L. Brooks, D. S. Brown, N. Bruner, D. Bucher, H. Buesching, V. Bumazhnov, G. Bunce, J. Burward-Hoy, S. Butsyk, T. A. Carey, P. Chand, J. Chang, W. C. Chang, L. L. Chavez, S. Chernichenko, C. Y. Chi, J. Chiba, M. Chiu, R. K. Choudhury, T. Christ, T. Chujo, M. S. Chung, P. Chung, V. Cianciolo, B. A. Cole, D. G. D’Enterria, G. David, H. Delagrange, A. Denisov, A. Deshpande, E. J. Desmond, O. Dietzsch, B. V. Dinesh, A. Drees, A. Durum, D. Dutta, K. Ebisu, Y. V. Efremenko, K. El Chenawi, H. En’yo, S. Esumi, L. Ewell, T. Ferdousi, D. E. Fields, S. L. Fokin, Z. Fraenkel, A. Franz, A. D.

Frawley, S-Y Fung, S. Garpman, T. K. Ghosh, A. Glenn, A. L. Godoi, Y. Goto, S. V. Greene, M. Grosse Perdekamp, S. K. Gupta, W. Guryn, H-Å Gustafsson, J. S. Haggerty, H. Hamagaki, A. G. Hansen, H. Hara, E. P. Hartouni, R. Hayano, N. Hayashi, X. He, T. K. Hemmick, J. Heuser, J. C. Hill, D. S. Ho, K. Homma, B. Hong, A. Hoover, T. Ichihara, K. Imai, M. S. Ippolitov, M. Ishihara, B. V. Jacak, W. Y. Jang, J. Jia, B. M. Johnson, S. C. Johnson, K. S. Joo, S. Kametani, J. H. Kang, M. Kann, S. S. Kapoor, S. Kelly, B. Khachaturov, A. Khanzadeev, J. Kikuchi, D. J. Kim, H. J. Kim, S. Y. Kim, Y. G. Kim, W. W. Kinnison, E. Kistenev, A. Kiyomichi, C. Klein-Boesing, S. Klinksiek, L. Kochenda, D. Kochetkov, V. Kochetkov, D. Koehler, T. Kohama, A. Kozlov, P. J. Kroon, K. Kurita, M. J. Kweon, Y. Kwon, G. S. Kyle, R. Lacey, J. G. Lajoie, J. Lauret, A. Lebedev, D. M. Lee, M. J. Leitch, X. H. Li, Z. Li, D. J. Lim, M. X. Liu, X. Liu, Z. Liu, C. F. Maguire, J. Mahon, Y. I. Makdisi, V. I. Manko, Y. Mao, S. K. Mark, S. Markacs, G. Martinez, M. D. Marx, A. Masaike, F. Matathias, T. Matsumoto, P. L. McGaughey, E. Melnikov, M. Merschmeier, F. Messer, M. Messer, Y. Miake, T. E. Miller, A. Milov, S. Mioduszewski, R. E. Mischke, G. C. Mishra, J. T. Mitchell, A. K. Mohanty, D. P. Morrison, J. M. Moss, F. Mühlbacher, M. Muniruzzaman, J. Murata, S. Nagamiya, Y. Nagasaka, J. L. Nagle, Y. Nakada, B. K. Nandi, J. Newby, L. Nikkinen, P. Nilsson, S. Nishimura, A. S. Nyanin, J. Nystrand, E. O'Brien, C. A. Ogilvie, H. Ohnishi, I. D. Ojha, M. Ono, V. Onuchin, A. Oskarsson, L. Österman, I. Otterlund, K. Oyama, L. Paffrath, A. P. T. Palounek, V. S. Pantuev, V. Papavassiliou, S. F. Pate, T. Peitzmann, A. N. Petridis, C. Pinkenburg, R. P. Pisani, P. Pitukhin, F. Plasil, M. Pollack, K. Pope, M. L. Purschke, I. Ravinovich, K. F. Read, K. Reygers, V. Riabov, Y. Riabov, M. Rosati, A. A. Rose, S. S. Ryu, N. Saito, A. Sakaguchi, T. Sakaguchi, H. Sako, T. Sakuma, V. Samsonov, T. C. Sangster, R. Santo, H. D. Sato, S. Sato, S. Sawada, B. R. Schlei, Y. Schutz, V. Semenov, R. Seto, T. K. Shea, I. Shein, T-A Shibata, K. Shigaki, T. Shiina, Y. H. Shin, I. G. Sibiriak, D. Silvermyr, K. S. Sim, J. Simon-Gillo, C. P. Singh, V. Singh, M. Sivertz, A. Soldatov, R. A. Soltz, S. Sorensen, P. W. Stankus, N. Starinsky, P. Steinberg, E. Stenlund, A. Ster, S. P. Stoll, M. Sugioka, T. Sugitate, J. P. Sullivan, Y. Sumi, Z. Sun, M. Suzuki, E. M. Takagui, A. Taketani, M. Tamai, K. H. Tanaka, Y. Tanaka, E. Taniguchi, M. J. Tannenbaum, J. Thomas, J. H. Thomas, T. L. Thomas, W. Tian, J. Tojo, H. Torii, R. S. Towell, I. Tserruya, H. Tsuruoka, A. A. Tsvetkov, S. K. Tuli, H. Tydesjö, N. Tyurin, T. Ushiroda, H. W. van Hecke, C. Velissaris, J. Velkovska, M. Velkovsky, A. A. Vinogradov, M. A. Volkov, A. Vorobyov, E. Vznuzdaev, H. Wang, Y. Watanabe, S. N. White, C. Witzig, F. K. Wohn, C. L. Woody, W. Xie, and et al. First results from rhic-phenix. *Pramana*, 57(2):355–369, 2001.

- [25] Judy Goldhaber. Bevalac had 40-year record of historic discoveries. *Berkeley Lab Science Articles Archive*, October 1992.
- [26] H. A. Gustafsson, H. H. Gutbrod, B. Kolb, H. Löhner, B. Ludewigt, A. M. Poskanzer, T. Renner, H. Riedesel, H. G. Ritter, A. Warwick, F. Weik, and H. Wieman. Collective flow observed in relativistic nuclear collisions. *Phys. Rev. Lett.*, 52:1590–1593, Apr 1984.

- [27] Ulrich W. Heinz and Barbara V. Jacak. Two particle correlations in relativistic heavy ion collisions. *Ann. Rev. Nucl. Part. Sci.*, 49:529–579, 1999.
- [28] C. Hohne. Strangeness production in nuclear collisions: Recent results from experiment NA49. *Nucl. Phys.*, A661:485–488, 1999.
- [29] Rudolph C. Hwa and C. B. Yang. Final-state interaction as the origin of the cronin effect. *Phys. Rev. Lett.*, 93:082302, Aug 2004.
- [30] Rudolph C. Hwa and C. B. Yang. Recombination of shower partons at high p_T in heavy-ion collisions. *Phys. Rev. C*, 70:024905, Aug 2004.
- [31] Akio Kiyomichi. Identified charged hadron spectra and particle ratios at $\sqrt{s}=200$ gev for qm2002. *PHENIX internal analysis notes*, AN148, 2002.
- [32] David William Kleinjan. *Measurement of the Transverse Single Spin Asymmetry and the Invariant Cross Section of Inclusive Eta Mesons Produced from Transversely Polarized Proton-Proton Collisions at Center of Mass Energy of 200 GeV*. PhD thesis, University of California, Riverside, 2014.
- [33] J. H. Kühn. Nucleon-number dependence of large-transverse-momentum reactions and multiple scattering. *Phys. Rev. D*, 13:2948–2953, Jun 1976.
- [34] J. M. Brennan M. Blaskiewicz and K. Mernick. Three-dimensional stochastic cooling in the relativistic heavy ion collider. *Phys. Rev. Lett.*, 105(094801), August 2010.
- [35] Hiroshi Masui. Phenix focus: Time of flight. *FOCUS Talk*, February 2004.
- [36] J. T. Mitchell et al. Event reconstruction in the PHENIX central arm spectrometers. *Nucl. Instrum. Meth.*, A482:491–512, 2002.
- [37] Jamie Nagle, Shawn Beckman, Javier Orjuela-Koop, and Anne Sickles. Phenix run-08 dau a 200 gev centrality categorization: Addendum. *PHENIX internal analysis notes*, AN1087, February 2013.
- [38] Mattias Ohlsson, Carsten Peterson, and Alan L. Yuille. Track finding with deformable templates the elastic arms approach. *Computer Physics Communications*, 71(1):77 – 98, 1992.
- [39] Anders Oskarsson. The pad chambers. *FOCUS Talk*, January 2003.
- [40] A. M. Poskanzer and S. A. Voloshin. Methods for analyzing anisotropic flow in relativistic nuclear collisions. *Phys. Rev. C*, 58:1671–1678, Sep 1998.
- [41] Eric Richardson. The phenix trigger system. *FOCUS Talk*, April 2004.
- [42] Eric Richardson. The reaction plane detector. *FOCUS Talk*, January 2007.

- [43] ARTHUR L. ROBINSON. Nuclear squeeze at lawrence berkeley lab. *Science*, 224(4651):857–858, 1984.
- [44] Sky Deva Rolnick. *Measurement of Dielectron Continuum in $p + p$ at $\sqrt{s} = 200$ GeV as a Baseline study for Chiral Symmetry Restoration*. PhD thesis, University of California, Riverside, 2015.
- [45] Brennan C. Schaefer. *Measurements of directed, elliptic, and triangular flow of charged hadrons from Cu+Au collisions at $\sqrt{s} = 200$ GeV with PHENIX at RHIC*. PhD thesis, Vanderbilt University, 2016.
- [46] Edward V. Shuryak. Quantum Chromodynamics and the Theory of Superdense Matter. *Phys. Rept.*, 61:71–158, 1980.
- [47] A. Taranenko and Roy A. Lacey. Systematic study of azimuthal anisotropy of charged hadrons in au+au collisions. *PHENIX internal analysis notes*, AN957, January 2011.
- [48] Lucas Taylor. Resistive plate chambers. *CMS Detectors Web Page*, November 2011.
- [49] Alberica Toia. Participants and spectators at the heavy-ion fireball. *CERN Courier*, April 2013.
- [50] Sebastian White. RHIC/PHENIX hosted group page, 2003.
- [51] F. Wojciech. *Phenomenology of Ultra-relativistic Heavy-ion Collisions*. World Scientific.